UNIVERSITÀ DEGLI STUDI DI MILANO

Scuola di Dottorato in Fisica, Astrofisica e Fisica Applicata

Dipartimento di Fisica

Corso di Dottorato in Fisica, Astrofisica e Fisica Applicata

Ciclo XXX

Searching for Dark Matter in the Mono-Jet and Mono-Photon Channels with the ATLAS Detector

Settore Scientifico Disciplinare FIS/01-FIS/04

Tesi di dottorato di :

Maria Giulia RATTI

Supervisori: Dott.ssa Silvia RESCONI

Prof. Leonardo CARMINATI

Coordinatore: Prof. Franceso RAGUSA

Anno Accademico 2016-2017

Commission of the final examination:

External Referees:
Marie-Hélène GENEST (CNRS/IN2P3)
Albert DE ROECK (CERN and Universiteit Antwerpen)

External Members:
Alessia TRICOMI (Università degli Studi di Catania)
Klaus MÖNIG (DESY and Humboldt-Universität zu Berlin)
Marco CIRELLI (CNRS and Université Paris-Sorbonne)

Final examination:

Date: January 29^{th}, 2018
Università degli Studi di Milano, Dipartimento di Fisica, Milano, Italy

Contents

Introduction

The dark matter problem is among the most compelling and open questions in physics today. The existence of a non-baryonic, non-luminous component of matter, which constitutes a large part of the mass content of the Universe, is inferred from its gravitational effects on the galaxies. However, it is still essentially unknown whether the dark matter interacts with the particles of the Standard Model other than gravitationally.

One attractive explanation to the dark matter problem is given by the WIMP hypothesis: dark matter is assumed to be made of particles with a mass around the scale of the electroweak symmetry breaking and to couple weakly to the particles of the Standard Model. Such weakly interacting massive particles, WIMPs, naturally have a relic abundance of the correct order of magnitude to account for the amount of dark matter observed by cosmological experiments. Moreover, many extensions of the Standard Model predict the existence of particles with these characteristics, thus making the WIMP very attractive from the theoretical point of view.

If dark matter is made of WIMPs, it could be produced at colliders. The Run 2 of the Large Hadron Collider (LHC), with the increased center-of-mass energy and larger statistics compared to the Run 1, constitutes a unique opportunity to access the electroweak scale in laboratory conditions and thoroughly test the WIMP hypothesis.

Detecting dark matter at a collider experiment, such as ATLAS, is challenging, because the WIMPs, being electrically neutral and weakly interacting, once produced, would escape the detector without leaving any visible traces. Conservation of momentum can be used as a handle to detect these elusive particles: since the initial transverse momentum prior to the collision is close to zero, an imbalance in the visible transverse momenta of the collision products, missing transverse momentum, $E_{\mathrm{T}}^{\mathrm{miss}}$, can be indicative of the presence of dark matter particles.

One way to look for WIMPs at the LHC is given by signatures characterized by the presence of a large $E_{\mathrm{T}}^{\mathrm{miss}}$ recoiling against a high-momentum detectable object, X, called 'mono-X' or '$E_{\mathrm{T}}^{\mathrm{miss}}$ + X'.

This work concentrates on the search for dark matter particles in the mono-jet and mono-photon signatures. The mono-photon is a clean channel, characterized by a low level of background from Standard Model processes. The mono-jet is the most abundant reaction among the mono-X and the most sensitive to many scenarios beyond the Standard Model.

Searches for dark matter in the mono-jet and mono-photon final states which make use of the data collected by the ATLAS detector during the Run 2 of the LHC are performed and presented. The key aspect of these searches is the precise estimation of the background coming from the processes of the Standard Model; several elements of novelty on this topic are introduced and discussed.

It is clear that a robust reconstruction and precise measurement of the $E_{\mathrm{T}}^{\mathrm{miss}}$ is a crucial aspect in the search for dark matter at colliders. An important part of this thesis is devoted to the optimization of the $E_{\mathrm{T}}^{\mathrm{miss}}$ reconstruction and to the assessment of the $E_{\mathrm{T}}^{\mathrm{miss}}$ performance at the ATLAS experiment in Run 2.

A wealth of particle physics models has been proposed to describe the production of dark matter particles in the mono-X signatures and interpret the results of the searches. Two simplified models and a model of effective field theory are adopted. Part of this work is devoted to the characterization and simulation of one of these simplified models, the $t-$ channel model, which yields a mono-jet signature. The interpretation of the $t-$ channel model is introduced in an ATLAS analysis for the first time.

The results of the mono-photon and mono-jet searches are interpreted in the context of these dark matter models and a comparison with the results from non-collider dark matter experiments is presented, highlighting the importance of collider results in the hunt for dark matter.

This thesis starts with an introduction to the basic concepts of the Standard Model in Chapter 1, followed by a discussion of the dark matter problem and the strategies to detect dark matter in Chapter 2. The focus then shifts to the description of the experimental facilities to collect the data in Chapter 3, followed by a discussion of the ATLAS event reconstruction and performance of the physics objects in Chapter 4. Chapter 5 is dedicated to the $E_{\mathrm{T}}^{\mathrm{miss}}$ reconstruction and performance. Chapter 6 deals with the characterization of the dark matter models employed in the mono-photon and mono-jet searches. The core of the thesis is constituted by Chapters 7 and 8 which discuss the methods and the results of the searches for dark matter in the mono-photon and mono-jet final states, respectively. The conclusions of this work are drawn at the end.

Contributions

This thesis is the result of my work. As I am part of a large experimental collaboration, my activity also relies on the activity of a large number of researchers and analysis groups. Unless explicit reference is made, the results are obtained by me or constitute a part of a publication to which I contributed primarily. My leading contributions are listed below, divided by chapter.

Chapter 5: $E_{\mathrm{T}}^{\mathrm{miss}}$ Reconstruction and Performance

I completed the qualification task to become ATLAS author by studying the performance of the reconstruction of the $E_{\mathrm{T}}^{\mathrm{miss}}$. My work focused on comparing the performance of different $E_{\mathrm{T}}^{\mathrm{miss}}$ calculations: a calorimeter-based and a track-based computation. I took the responsibility of maintaining the code for the performance studies. I studied in details the $E_{\mathrm{T}}^{\mathrm{miss}}$ performance as a function of different jet multiplicities, topologies, detector and data-taking conditions. The studies were made public in [1]. I also contributed to the assessment of the performance of $E_{\mathrm{T}}^{\mathrm{miss}}$ in the early 2015 data [2]. These results constituted the basis for recommending the *Track Soft Term* (TST) computation to ATLAS physics analyses.

Chapter 6: Particle Dark Matter Models

I characterized the 't-channel' dark matter model, which I later introduced in the mono-jet analysis. I crucially contributed to the optimization of the generation procedure and I studied the kinematics predicted by the model as a function of its free parameters. I quantified the level of overlap between the $t-$ channel model and a similar supersymmetric model. I also studied the predicted relic density, as well as the sensitivity of the mono-jet search to this model. I performed the validation needed for the generation of the official ATLAS samples, reported in Appendix A, and I later interpreted the results of the mono-jet search in terms of the parameters of this model.

Chapter 7: Mono-Photon Search with 2015 Data

I was the main analyzer of the search with the 2015 data [3] throughout all the process. I was in charge of almost all aspects of the analysis, starting from the optimization of the data format, through the development of the analysis tools, including those for the statistical interpretation, to the presentation of the results during the review. I studied an optimal strategy for the estimation of the major backgrounds and for the validation of the full background estimation. I performed detailed studies on the systematic uncertainties. I developed a dedicated photon cleaning to suppress beam-induced background, which has also been adopted by other analyses, and I contributed to the estimation of jet-to-photon background. I estimated the trigger efficiency and performed cross-checks for the derivation of the limits. For the analysis performed on the 2015 and 2016 data [4], I remained in the analysis team for code support and advice.

Chapter 8: Mono-Jet Search with 2015 and 2016 Data

I was a leading analyzer of the search with the 2015 and 2016 data [5]. I took the responsibility of many aspects of the analysis: from the code validation and maintenance, to the production, delivery and presentation of the analysis results at most stages of the review process.
A novel approach for the calculation of the theoretical uncertainties for the $V+$jets processes has been used for this analysis, thanks to which the precision of the background estimation has approximately halved. I crucially contributed to the optimization of the major backgrounds estimation and fitting strategy, to the optimization of the control regions definition, to the improved understanding of both theoretical and experimental uncertainties. I performed numerous cross-checks needed at the various stages of the approval process and I finally interpreted the results of the search by setting model-independent limits and limits in the context of several dark matter models.

CHAPTER 1

Introduction to the Standard Model

The Standard Model (SM) of particle physics is a quantum field theory that describes the elementary constituents of matter and their interactions. It has proven capable of extremely accurate predictions, that have been tested to an impressive level of accuracy and in a wide range of energies by the experiments performed in the last decades.

This chapter is meant to provide an introduction to the basic concepts of the SM: a description of the building blocks of the SM will be followed by the illustration of the principle of gauge invariance and its application in the formulation of the theory of strong and electroweak interactions. The Higgs mechanism will also be explained, given the relevance that its discovery has had in the establishment and confirmation of the Standard Model. Some of the most important theoretical issues and open points that arise from the formulation of the SM are briefly discussed at the end of the chapter.

An in-depth discussion of the theory of the Standard Model is beyond the scope of this document; the interested reader can refer to the well-known book by Peskin and Shroeder [6].

1.1 Building a theory: particles and interactions

The SM is a quantum field theory that describes three of the known interactions in nature: electromagnetic, weak and strong forces.

The ingredients to build such a theory are two:

Particles: particles are irreducible representations of the Poincaré group. The Casimir operators of this group (those which commute with all generators of the group) identify the two quantum numbers based on which the elementary particles can be classified: spin and mass. Additional symmetries permit further classifications, for example the charge.

Interactions: the dynamics is obtained from the most general Lagrangian which is compatible with the rules of quantum mechanics and of special relativity, and it must satisfy a set of symmetries, which are usually inferred experimentally. The

form of the interactions arises from requiring the invariance of the Lagrangian under this set of symmetries. The representations of these transformations are the generators of the associated symmetry group, which manifest themselves as gauge bosons. The symmetry group of the SM is $SU(3)_C \times SU(2)_L \times U(1)_Y$.

1.2 Fundamental building blocks of the SM

From what is stated above, it is clear that the building blocks that constitute the known matter today are categorized into two: interacting particles on the one hand, which are fermions, and mediators of the forces which control the interactions, on the other hand, the gauge bosons.

In this paragraph a brief description of the particles and mediators of the SM is given, together with their most important properties. These can be also visualized in Figure 1.1.

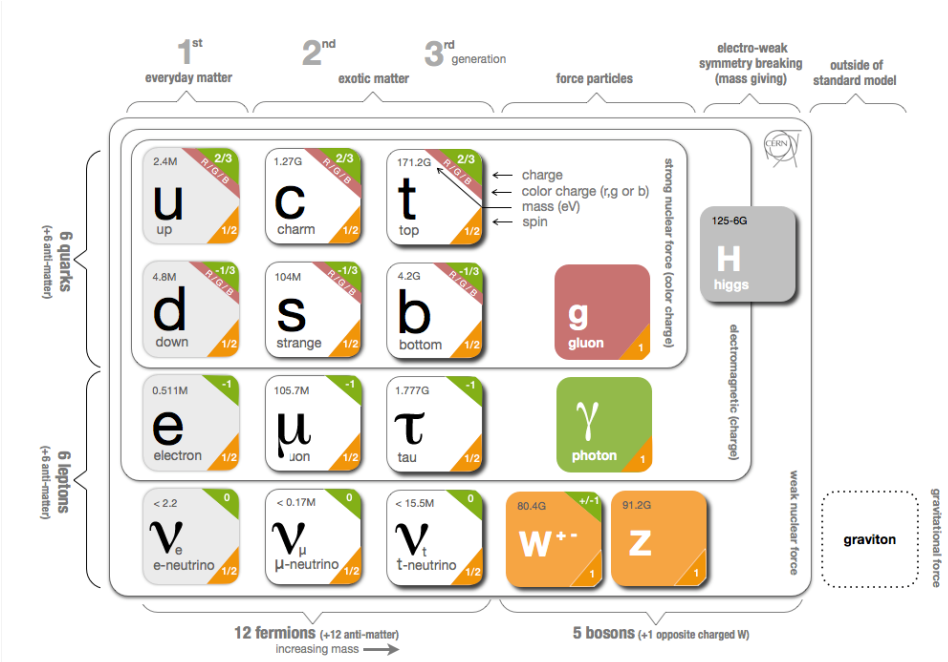

Figure 1.1: An illustration of the fundamental particles and interactions of the Standard Model [7].

Fermions

The elementary particles which constitute matter are the fermions; all fundamental fermion particles have spin $s = \frac{1}{2}$. Fermions are further subdivided into *leptons* and *quarks*. While leptons interact only via the electroweak force, quarks can also interact via the strong force and are characterized by an additional quantum number, color.

Fermions are classified in three generations of increasing mass. The first generation cor-

responds to what exists in common matter, while the second and third generations are accessible at higher energies.

For each generation, quarks further exist in two types, up and down. The two types differ in their electromagnetic charge, where up-type quarks (anti-quarks) have a charge of 2/3 (-2/3) while down-type quarks (anti-quarks) have a charge of -1/3 (1/3).

Leptons can be separated in charged leptons, with charge +1 or -1, and neutrinos, which are neutral.

For every fermion there is a corresponding antifermion which has the same mass and spin of the fermion, but opposite charge. For neutrinos, it is not yet known whether neutrinos and antineutrinos are distinct particles or not.

Gauge bosons

The mediators of the fundamental interactions are the gauge bosons.

The photon is the mediator of the electromagnetic force. It couples to all charged particles. It is massless, electromagnetically neutral, and has spin $s = 1$.

The gluons are the mediators of the strong force. They are massless, have spin $s = 1$ and carry the color charge. Color has three degrees of freedom (red, green, blue) which express themselves in eight different gluons. Gluons couple to quarks and to themselves.

The W^+, W^- and Z bosons are the three mediators of the weak interaction. The W bosons have +1 or -1 electric charge and are each other's antiparticles. The Z boson is electrically neutral and is its own antiparticle. The three particles have a spin $s = 1$. Differently from the other gauge bosons, they are not massless and acquire their mass via the spontaneous symmetry breaking mechanism. The weak gauge bosons couple both to quarks and to leptons. Boson-boson interactions are also possible.

1.3 The power of symmetries: the example of QED

The simplest way to illustrate the role of gauge invariance in the foundations of the Standard Model is the case of Quantum Electrodynamics (QED). One starts from the Dirac Lagrangian, which describes the motion of a free fermion field $\psi(x)$ defined in each point of space-time:

$$\mathcal{L}^{Dirac} = \bar{\psi}(x)(i\gamma^\mu \partial_\mu - m)\psi(x)\,. \tag{1.1}$$

One can require the invariance of this Lagrangian under a local (or *gauge*) transformation of the field through a generic function $\alpha(x)$:

$$\psi(x) \to \psi'(x) = e^{i\alpha(x)}\psi(x)\,. \tag{1.2}$$

Such invariance can be obtained by substituting the derivative in Eq. 1.1 with a covariant derivative $\mathcal{D}_\mu = \partial_\mu + ieA_\mu$, where we have introduced the gauge field A_μ which is defined by its gauge transformation property:

$$A_\mu \to A'_\mu = A_\mu - \partial_\mu \alpha(x)\,, \tag{1.3}$$

where e is the dimensionless coupling coupling strength of electrodynamics.

When using the covariant derivative in Eq. 1.1, the Lagrangian takes the form:

$$\mathcal{L} = \bar{\psi}(x)(i\gamma^\mu \partial_\mu - m)\psi(x) - e(\bar{\psi}\gamma^\mu \psi)A_\mu \,. \tag{1.4}$$

It is easy to show that this Lagrangian is invariant under the gauge transformation defined by Eqs. 1.2 and 1.3.
A gauge-invariant kinematic term for A_μ can then be introduced to describe its free propagation; given the field strength

$$F^{\mu\nu} = \partial^\mu A^\nu - \partial^\nu A^\mu \,, \tag{1.5}$$

the free Lagrangian for electrodynamics is

$$\mathcal{L}_{gauge} = -\frac{1}{4} F^{\mu\nu} F_{\mu\nu} \,. \tag{1.6}$$

The full Lagrangian describing QED can then be finally obtained as:

$$\mathcal{L}_{QED} = \bar{\psi}(x)(i\gamma^\mu \partial_\mu - m)\psi(x) - e(\bar{\psi}\gamma^\mu \psi)A_\mu - \frac{1}{4} F^{\mu\nu} F_{\mu\nu} \,. \tag{1.7}$$

It is interesting to notice that gauge invariance does not allow for a mass term of the form $m_A^2 A^\mu A_\mu$.
The formalism of gauge invariance can be used with more complicated symmetries such as $SU(3)_C$ which governs Quantum Chromodynamics.

1.4 Lagrangian of QCD

Among the fundamental fermions, only the quarks interact via the strong interaction. The strong interactions are described by the theory of Quantum Chromodynamics (QCD). The symmetry group of the strong interaction is $SU(3)_C$, where C indicates the color; there are 8 generators for this group, corresponding to as many gluons. The generators do not commute with each other ($[T_a, T_b] = i\lambda_{abc} T_c$) and therefore QCD is developed as a non-Abelian gauge theory.
The field which interacts is a multiplet

$$\psi = \begin{pmatrix} \psi_1 \\ \psi_2 \\ \psi_3 \end{pmatrix} \tag{1.8}$$

obeying the free Dirac Lagrangian as in 1.1, where m is a mass matrix instead of a single number. The gauge transformation takes the form:

$$\psi \to \psi' = U(\overrightarrow{\theta}(x))\psi = (e^{ig\sum_a \theta_a(x) T_a})\psi \,. \tag{1.9}$$

In order to get the Lagrangian invariance one must:

- introduce gauge fields G_a^μ, transforming as $G_a^\mu \to G_a'^\mu \approx G_a^\mu - \partial^\mu \theta_a - g\lambda_{abc}\theta_b G_c^\mu$ for small θ_a, where g is the dimensionless coupling strength of the strong interaction;

- introduce the covariant derivative $\mathcal{D}^\mu \stackrel{\text{def}}{=} \partial^\mu + igT_aG_a^\mu$;
- introduce the field strengths $F_a^{\mu\nu} \stackrel{\text{def}}{=} (\partial^\mu G_a^\nu) - (\partial^\nu G_a^\mu) - g\lambda_{abc}G_b^\mu G_c^\nu$.

The full invariant Lagrangian is then:

$$\mathcal{L}_{QCD} = \underbrace{\bar{\psi}(i\gamma^\mu\partial_\mu - m)\psi}_{free\ fermion\ propagator} \underbrace{- g(\bar{\psi}\gamma_\mu T_a\psi)G_a^\mu}_{interaction} \underbrace{- \frac{1}{4}(\partial^\mu G_a^\nu - \partial^\nu G_a^\mu)(\partial_\mu G_{a\nu} - \partial_\nu G_{a\mu})}_{gauge\ boson\ propagator}$$
$$+ \underbrace{\frac{1}{2}g\lambda_{abc}G_b^\mu G_c^\nu(\partial_\mu G_{a\nu} - \partial_\nu G_{a\mu}))}_{triple\ gauge\ coupling} \underbrace{- \frac{1}{4}g^2\lambda_{abc}\lambda_{ars}G_b^\mu G_c^\nu G_{r\mu}G_{s\nu}}_{quadruple\ gauge\ coupling} . \tag{1.10}$$

It can be noticed that differently from the case of QED, there are terms (triple and quadruple gauge couplings) which involve the self-coupling of the gluons; this implies that the gluons, unlike the photon which is electrically neutral, carry the color charge.

Another characteristic of QCD which makes it substantially different from QED is the behavior of its coupling constant in different energy regimes. The strong coupling constant $\alpha_S \stackrel{\text{def}}{=} \frac{g^2}{4\pi}$ is relatively small at high energies (i.e. at small distances), and it increases at lower energies. This means that QCD is almost a free theory at high energies (and this is the only regime where it is perturbative), while it creates very strongly bound states at lower energies, meaning at higher distances. This is responsible for the phenomenon of *color confinement*, which means that colored particles cannot be found isolated. In fact, when for example a system constituted by a quark and an antiquark is separated, at some point it becomes favorable for a new quark-antiquark pair to form.

1.5 Electroweak theory

The theory of electroweak interactions was born from the attempts to produce a gauge theory for the weak force, in analogy with QED. Such a theory should be able to describe on the one hand the weak charged current interactions, such as the β decay, and at the same time neutral current interactions, such as neutrino scattering. In the 1960s Glashow, Salam and Weinberg independently found a gauge invariant theory which described the weak charged and neutral currents and incorporated the QED.

In electroweak theory, it becomes relevant to introduce left and right components of the fields, which are obtained from the full field as follows:

$$\psi_{R,L} = P_{R,L}\psi = \frac{1}{2}(1 \pm \gamma^5)\psi\,. \tag{1.11}$$

The symmetry of the electroweak theory is $SU(2)_L \times U(1)_Y$, which calls for four gauge fields and as many generators. The generators are the weak isospin $\mathbf{T}$ and the weak hypercharge Y, which are related to the electric charge Q by

$$Y = 2(Q - T^3). \tag{1.12}$$

Left-handed fermions are paired in isospin doublets with $T = 1/2$ and $T^3 = \pm 1/2$, while right-handed fermions are isospin singlets ($T = 0$, $T^3 = 0$):

$$\psi_L = \begin{pmatrix} u_L \\ d_L \end{pmatrix}, \qquad \psi_R = (u_R), (d_R)\,. \tag{1.13}$$

The gauge fields of the $SU(2)_L \times U(1)_Y$ group are W^1, W^2, W^3 (for $SU(2)$) and B (for $U(1)$).
The gauge transformation of this group for the ψ field is

$$\psi \to \psi' = (e^{i\frac{g'}{2}\alpha_0 Y} \cdot e^{ig\alpha_k T^k})\psi\,, \tag{1.14}$$

where the dimensionless coupling strenghts g and g' have been introduced.
The covariant derivative for this gauge transformation is

$$\mathcal{D}^\mu = (\partial^\mu + igT_k W_k^\mu + i\frac{g'}{2} Y B^\mu)\,. \tag{1.15}$$

By requiring the gauge invariance, the Lagrangian of the electroweak interactions takes the form:

$$\mathcal{L}_{EW}^{int} = -\frac{g'}{2}(\bar{\psi}\gamma_\mu Y \psi)B^\mu - g(\bar{\psi}\gamma_\mu T^k \psi)W^{k\mu}\,, \tag{1.16}$$

which is expressed in terms of the gauge fields and the ψ field. $\mathcal{L}_{EW}^{int}$ can be written in terms of the fields associated with the observed bosons (the three weak bosons W^+, W^-, Z, and the photon A) by introducing a rotation of angle θ_W between the gauge fields:

$$\begin{array}{rcl} B &=& A\cos\theta_W - Z\sin\theta_W\,, \\ W^3 &=& A\sin\theta_W + Z\cos\theta_W\,, \\ W^{1(2)} &=& \frac{W^- \pm W^+}{\sqrt{2}}\,. \end{array} \tag{1.17}$$

The Weinberg angle θ_W is defined by relating the coupling strengths through:

$$e = g\sin\theta_W = g'\cos\theta_W\,. \tag{1.18}$$

With these substitutions, $\mathcal{L}_{EW}^{int}$ then takes the form:

$$\begin{aligned} \mathcal{L}_{EW}^{int} = &-\frac{g}{\sqrt{2}}\underbrace{[\bar{u}_L \not{W}^- d_L + \bar{d}_L \not{W}^+ u_L]}_{weak\,charged} - \quad e \quad \underbrace{\bar{\psi}\not{A} Q\psi}_{electromagnetic} \\ &- \frac{e}{2\sin\theta_W\cos\theta_W}\underbrace{\bar{\psi}\not{Z}[T^3 - 2Q\sin^2\theta_W - T_L^3\gamma^5]\psi}_{weak\,neutral} \end{aligned} \tag{1.19}$$

where the definition $\not{X} \stackrel{\text{def}}{=} \gamma^\mu X_\mu$ has been introduced to simplify the notation. The contributions of weak charged, neutral and electromagnetic currents are stressed and the chiral structure of the theory is manifest: the charged currents act only on the left-handed components of the fields, while the neutral current acts on both left-handed and right-handed components.

It was already mentioned in Section 1.3 how mass terms of the gauge bosons are in general prohibited by gauge invariance; in the case of electroweak interaction, also the mass terms for fermions are prohibited, as a consequence of the chiral structure of Eq. 1.19. A mechanism which gives mass to the fermions and to the electroweak bosons is thus required which preserves the gauge invariance and the chiral symmetry.

1.6 Higgs Mechanism

The Higgs mechanism was introduced by the work of Higgs [8] and of Englert and Brout [9], and later used by Weinberg with the aim of providing the mass terms of the weak bosons and of the fermions in a gauge-invariant way.
The idea behind such a mechanism is that it realizes a spontaneous symmetry breaking (SSB), which means that the theory does not contain an explicit breaking of the gauge symmetry, but mass terms arise from the choice of a minimal configuration of the potential of a new *ad hoc* field, called Higgs field.
The minimal way to realize SSB is by introducing in the SM Lagrangian a complex scalar field Φ with Lagrangian:

$$\mathcal{L}_{\mathcal{H}} = (\mathcal{D}^{\mu}\Phi)^{\dagger}(\mathcal{D}_{\mu}\Phi) - V(\Phi) \tag{1.20}$$

where the $V(\Phi)$ describes the potential for the Φ field. Since Φ must couple to the $W^{\pm}$ fields to give them mass, Φ must be an isospin doublet; minimally, the field can be an isospin doublet of complex scalar fields. At the same time, Φ must not couple to the A field, which is massless; therefore Φ must be such to have $Q = 0$. Recalling the relation 1.12 between isospin and charge, this implies that there is a gauge where one of the two components of Φ must be zero.

$$\Phi = \begin{pmatrix} \Phi^{+} \\ \Phi^{0} \end{pmatrix} = \begin{pmatrix} 0 \\ \phi \end{pmatrix} . \tag{1.21}$$

The potential introduced in Eq. 1.20 is of the form:

$$V(\Phi) = \lambda(\Phi^{\dagger}\Phi)^2 + \mu^2(\Phi^{\dagger}\Phi) \, , \tag{1.22}$$

where $\lambda > 0$, to guarantee the presence of a ground state. According to the sign of μ^2, the ground state can be unique or degenerate, as illustrated in Figure 1.2.
If $\mu^2 > 0$ the potential presents a single minimum at 0, while if $\mu^2 < 0$ the potential has a contour of minima at $\frac{\mu^2}{\lambda^2} \stackrel{\text{def}}{=} \frac{1}{2}v^2$.
The interesting case is that of $\mu^2 < 0$, which permits the realization of SSB. In this case, the field acquires a vacuum expectation value:

$$\langle 0|\Phi|0\rangle = \frac{v}{\sqrt{2}} \, . \tag{1.23}$$

When written as an expansion around the ground state, Φ takes the form:

$$\Phi = \frac{1}{\sqrt{2}} \begin{pmatrix} 0 \\ v + h(x) \end{pmatrix} . \tag{1.24}$$

Until now, it can be seen that starting from a symmetric potential as that of Eq. 1.22, the choice of a particular gauge has naturally brought to choosing a specific form for the ground state. Rewriting the Lagrangian in terms of the expanded Φ will make appear the required mass terms for the gauge bosons as a direct consequence.

1.6.1 Mass of the weak bosons

Starting from Eq. 1.20, substituting the expansion defined in Eq. 1.24, and defining the covariant derivative

$$\mathcal{D}_\mu \stackrel{\text{def}}{=} \partial_\mu + i\frac{g'}{2}B_\mu Y + igW_\mu^k T^k \,, \tag{1.25}$$

the Lagrangian $\mathcal{L}_\mathcal{H}$ takes the form:

$$\mathcal{L}_\mathcal{H} = \underbrace{|i\frac{g'}{2}B\Phi + i\frac{g}{2}T^k W^k \Phi|^2}_{bosons\,masses\,\&\,bosons-Higgs\,int.} + \underbrace{|\partial\Phi|^2 - V(\Phi)}_{Higgs\,kinetic\,\&\,self-interaction} \,. \tag{1.26}$$

When developing the first term to include the rotations defined in Eq. 1.17, the following mass terms for the gauge bosons appear:

$$\left(\frac{gv}{2}\right)^2 W^+W^-, \quad \frac{1}{2}\left(\frac{gv}{2\cos\theta_W}\right)^2 Z^2 \,, \tag{1.27}$$

and the masses of the gauge bosons are then:

$$m_W = \frac{gv}{2}, \quad m_Z = \frac{gv}{2\cos\theta_W} = \frac{m_W}{\cos\theta_W} \,. \tag{1.28}$$

1.6.2 Mass of the fermions

As noted in Section 1.5, the explicit mass terms in the free Dirac Lagrangian for fermions violate the chiral symmetry of the electroweak sector since there would be a term where right and left components of the fields appear mixed:

$$m(\bar{\psi}_L\psi_R + \bar{\psi}_R\psi_L). \tag{1.29}$$

The scalar sector introduced to provide mass to the gauge bosons can be used to generate terms in the Lagrangian which represent the masses of the fermions while fulfilling the chiral symmetry. This is done by introducing Yukawa terms of the form:

$$\mathcal{L}_{Yukawa} = -\frac{1}{\sqrt{2}}\left[g_d(v+h)d_L^\dagger d_R + (h.c.) + g_u(v+h)u_L^\dagger u_R + (h.c.)\right] \,, \tag{1.30}$$

where the fermionic fields have been written in terms of their left and right components as defined in Eq. 1.13. Here mass terms can be identified:

$$m_{u,d} = \frac{1}{\sqrt{2}}vg_{u,d} \tag{1.31}$$

where the Yukawa couplings $g_{u,d}$ set the relation between the masses of the fermions and v.

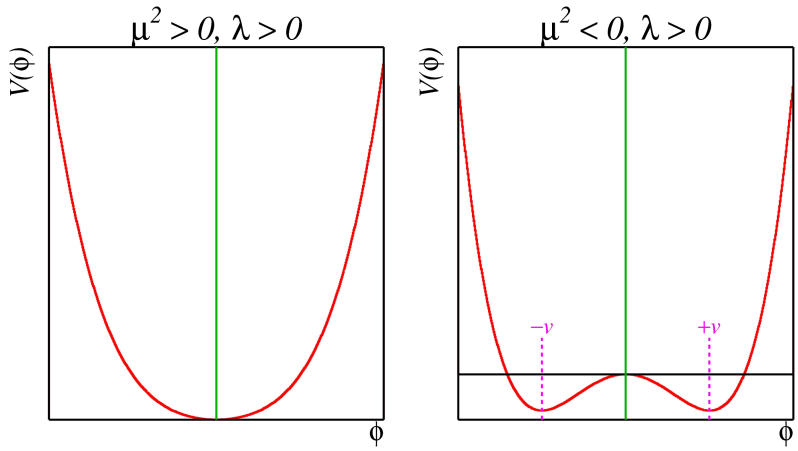

Figure 1.2: Illustration of the shape of the Higgs potential in presence of a single ground state (left) and in presence of more than a single ground state (right), as obtained for $\mu^2 > 0$ and $\mu^2 < 0$, respectively.

1.7 Open issues of the Standard Model

The discovery of the Higgs boson was a great experimental and theoretical success, which has completed the picture of the Standard Model formulation and once again demonstrated the high predictivity of this theory.
Despite the fact that measurements are increasingly providing confidence in its solidity, the SM is not believed to be a complete theory. On the one hand, there are well-established experimental facts which do not find an explanation within the SM; on the other hand, the theory presents some features which are not easily understood or explicable. Below are mentioned some of the open and compelling questions in particle physics.

Dark matter and dark energy: the SM does not provide a particle candidate that can account for the non-luminous matter, known as Dark Matter (DM), which constitutes the majority of the matter present in the Universe. The evidence for DM, the formalism to describe it in the context of particle physics, and the strategies employed to detect it are the topic of the next chapter.
The SM does not give any hint regarding dark energy, the hypothesized energy which evenly permeates space-time and which is needed to explain the observed accelerated expansion of the Universe.

Hierarchy: among the most debated question of the SM is the so-called 'hierarchy problem'. This is related to the large difference between the electroweak scale, which is $\mathcal{O}(100)$ GeV, and the Planck scale, the scale at which it is expected that the gravitational interaction dominates over the others, of the order of $\mathcal{O}(10^{19})$ GeV.
An effect of these two highly-separated scales is the fact that the bare value of the

Higgs mass μ^2 receives large radiative corrections from the fermions interacting with the Higgs field:

$$\delta\mu^2 = -\frac{\lambda_f^2}{8\pi^2}\Lambda_{UV}^2 \,, \tag{1.32}$$

where λ_f^2 is the Yukawa coupling of a given fermion to the Higgs, and Λ_{UV} is an energy cutoff until which the SM is expected to be valid.

If there is no new physics between the electroweak scale and the Planck scale, Λ_{UV} would be close to the latter and, as a consequence, the Higgs mass would be extremely large; given that this is not the case, this means either that the parameters of the Standard Model are fine-tuned in a way that prevents these large corrections or that there is a new sector of particles at a scale between the electroweak and the Planck scales which provides the cancellation.

Baryon asymmetry: in the Universe today a large predominance of matter over anti-matter is observed. This constitutes a problem from the cosmological point of view, because it is not easy to explain how from the thermal equilibrium established after the Big Bang, most of the anti-matter disappeared.
The Cabibbo-Kobayashi-Maskawa matrix of the quarks, which transforms the electroweak eigenstates into mass eigenstates, provides terms which can partially account for matter-antimatter asymmetry, but not enough to justify the observed asymmetry today.

Gravity: the SM does not provide a description of the gravitational interactions. The unification between SM and general relativity would require the quantization of gravity. In particle interactions at the energies accessible today, the effect of gravity is neglected, given it is much smaller compared to the other interactions; gravity is expected to play a role at a much higher energy scale, the already mentioned Planck scale.

CHAPTER 2

The Dark Matter Problem

Particle dark matter constitutes a paradigm to explain the astrophysical observations of missing mass at various scales; while it is not the only paradigm that has been proposed, it is commonly considered to be the most successful at describing the observations and it is the one embraced in this work. Particle dark matter has not been observed yet and this constitutes the main motivation of this thesis.

This chapter first introduces the concepts at the basis of the dark matter problem, then gives an overview of the famous particle candidates proposed to solve it and finally explains the experimental strategies which have been deployed to detect dark matter particles.

The reader interested in a complete review of the dark matter problem can refer to the book edited by Bertone [10].

2.1 Introduction

Evidence for a non-baryonic dark matter (DM) component in the Universe derives from an impressive range of unrelated astrophysical observations, covering distances from the galactic to the cosmological scales. The observations based on the spectrum of the Cosmic Microwave Background anisotropies can be explained by a model in which the total mass-energy of the universe consists in ordinary matter for approximately 5%, dark matter for around 27%, the rest being a dark and unknown component of energy. The most important evidences for DM will be explained in Section 2.2.

While astrophysical observations provide evidence for the existence of DM through the gravitational effects on the ordinary matter, how DM particles fit into the Standard Model or even whether they interact with SM particles otherwise than gravitationally, is still essentially a mystery.

One of the most attractive explanations is provided by the 'WIMP hypothesis': DM is assumed to consist of hypothetical stable particles with masses around the scale of electroweak symmetry breaking, in the 10 GeV - 1 TeV range, whose interactions with other elementary particles have a strength similar to the weak interactions of the Standard Model. Such weakly massive interacting particles, WIMPs, naturally have a relic abundance of the correct order of magnitude to account for the observed dark matter, making

them very appealing from a theoretical and observational point of view. The WIMP miracle in standard cosmology is explained in more detail in Section 2.3.

Many extensions of the SM contain particles which can be identified as WIMP dark matter candidates, including super-symmetry (SUSY) and theories of large extra dimensions (LED). While the WIMP has been the largest focus in the literature, non-WIMP candidates are also possible, as discussed in Section 2.4.

If DM is made of WIMPs, we should be able to detect it in various ways, as schematically illustrated in Figure 2.1. The principle for direct detection experiments (see Section 2.5) is the measurement of the recoil of the nucleons scattered by the WIMPs in large underground detectors. Alternatively, we could detect the products of annihilation of these particles or their decay: with this aim, a wide range of indirect detection experiments (see Section 2.6) are deployed which look for radiation and particles coming from suitable regions of the Universe, such as the galactic center.

Another way of detecting WIMPs (see Section 2.7) is when they are directly produced at colliders through the annihilation of SM particles. Once produced, WIMPs would escape the detector without interacting, leading to a momentum imbalance, or 'missing momentum', signature. In this scenario they could be observed only when recoiling against a detectable object. This is the kind of signature that is analyzed in this work.

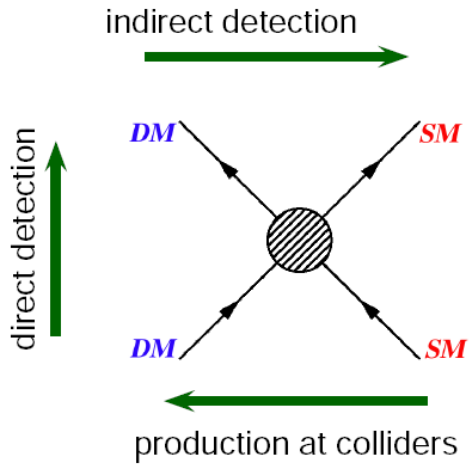

Figure 2.1: Schema illustrating different strategies for dark matter particle detection. Depending on the direction of the time axis, different types of searches can be recognized.

2.2 Evidence for Dark Matter

Evidence for dark matter has built over the years from a number of unrelated astrophysical measurements; a selection of the most famous evidences are presented in this Section.

Missing mass in the Coma cluster The first hint of dark matter in the modern sense was provided by the measurements of the velocity dispersion of the galaxies in the Coma cluster performed by Zwicky [11]: by the application of the virial theorem, he inferred the dynamical mass of the system and found that it was approximately 100 times larger than that inferred from the luminosity of the galaxy, thus pointing out the necessity of invisible mass to explain the observations.

Rotation curves of galaxies Among the most direct evidences for dark matter are the observations of the rotation curves of spiral galaxies, i.e. the measurements of the circular velocity of the stars around the galactic center as a function of their distance r from it, which were pioneered by Rubin and Ford [12]. According to newtonian dynamics, the circular velocity should be determined by:

$$v(r)^2 = \frac{GM(r)}{r} \quad \text{with} \quad M(r) = 4\pi \int \rho(r) r^2 dr, \tag{2.1}$$

where $\rho(r)$ represents the radial density profile of the galaxy. The expectation would be that, given that most of the stars are concentrated in the galactic center, at very high radii the circular velocity should decrease, with a trend $\propto 1/r^{1/2}$. The observations turned out to be in contrast with this expectation and the observed rotation curves show a flat behavior at large distances from the galactic center. The fact that $v(r)$ is approximately constant at large radii suggests that there is a halo of dark matter distributed with $\rho_{halo} \propto 1/r^2$ at large radii. Figure 2.2 shows the observed rotation curves for a few galaxies compared to the fitted distribution assuming a spherical dark matter halo and no coupling between dark matter and visible components. The fits show a good compatibility of the data with the hypothesis of a dark matter halo and it is found that the visible matter dominates the mass distribution within the optically bright disc for brighter galaxies [13], while the dark component is everywhere dominant in low-luminosity galaxies.

Gravitational lensing Another class of important evidence for dark matter is provided by the observation of gravitational lensing at the scale of galaxies and cluster of galaxies. Gravitational lensing is a phenomenon arising from the modification of the space-time curvature produced by mass concentrations and is one of the early predictions of general relativity. Gravitational fields deflect the path of photons and modify the apparent shape of astronomical sources, such as galaxies and quasars. From the properties of the images of the lensed sources, the properties of the lenses can be extracted, in particular their mass. For Einstein rings and particularly giant arcs (strong gravitational lensing), appearing around a cluster of galaxies, the total mass of the lens can be estimated; for example, for the cluster Abell 370, measurements show M/L[1] ratios of approximately 300, which indicates that the cluster of galaxies is dominated by the dark matter component [14]. An optical image of this cluster of galaxies is reported in Figure 2.3.

[1] M and L indicate the mass and the luminosity of the cluster in units of solar masses and luminosity, respectively.

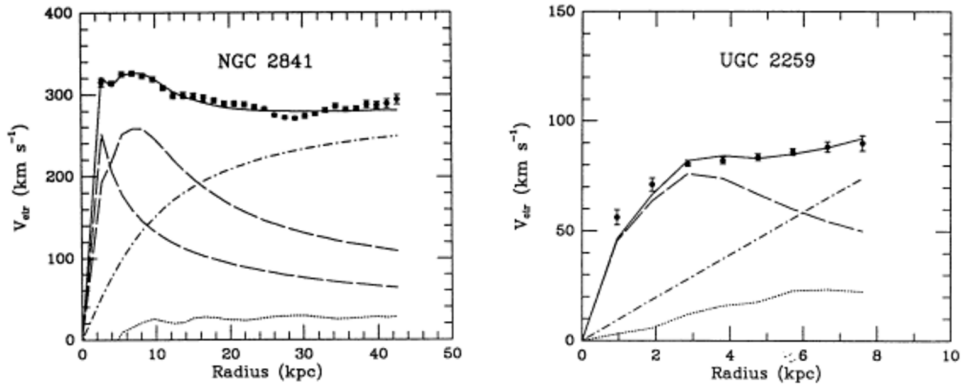

Figure 2.2: Rotation curves of the NGC 2841 (a high-luminosity galaxy, left) and UGC 2259 (a low-luminosity galaxy, right). The circular velocity is shown as a function of the distance from the galactic center as observed in data (black circles). The solid line is the result of the fit to the data; the dotted curve represents the gas component of the fit, the dashed curve represents the visible matter component, while the dash-dotted line represents the dark matter halo component [13].

As opposed to strong lensing, studies of weak lensing infer the property of dark matter from the effects that a number of galaxies and astrophysical objects have on the image of deep astronomical sources. Such distortions are analyzed statistically and, together with strong lensing, can be used to test detailed predictions of the cosmological model, such as the radial mass profile of the dark matter halos.
Among the most spectacular results obtained with weak lensing is the analysis of the Bullet Cluster. In this cluster of galaxies, the joint mass reconstruction from weak and strong gravitational lensing shows two massive substructures that are offset with respect to the baryon distribution observed in X-rays by Chandra [15], as shown in Figure 2.4. The offset between the gas and the inferred mass distribution would result from a violent merging by two clusters, with the dark matter haloes being decoupled from the plasma. In this scenario, the separation would imply that dark matter is collisionless and limits on the dark matter self-interaction can be derived [16].

CMB spectrum Among the most compelling evidences for dark matter are the measurements of the cosmological parameters performed on the Cosmic Microwave Background (CMB) spectrum. The CMB is the radiation originating from the propagation of photons in the early Universe, when they decoupled from matter. Its spectrum follows that of a black body with temperature $T = 2.726\,K$ and is largely isotropic. The analysis of CMB temperature anisotropies enables to test the predictions of the cosmological model and put the best constraints to date on its parameters.

The CMB temperature anisotropy spectrum is usually expanded as a series of spherical

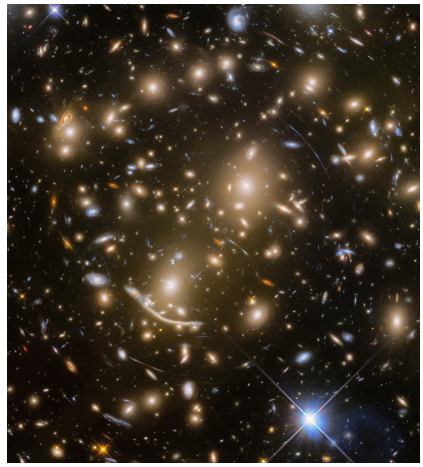

Figure 2.3: Image of the massive galaxy cluster Abell 370 taken by the NASA/ESA Hubble Space Telescope, where giant arcs due to gravitational lensing can be clearly seen [17].

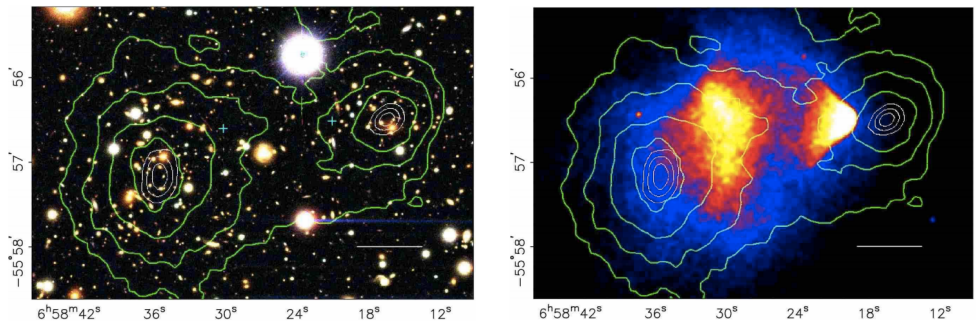

Figure 2.4: Images of the Bullet Cluster in the visible (left) and x-ray (right) obtained with Chandra. The contours overlaid show the gravitational map reconstructed by the joint weak and strong lensing analysis. Both images show the offsets between the distribution of baryons and that of the reconstructed gravitations field [18].

harmonics $Y_{\ell m}(\theta, \phi)$ with coefficients $a_{\ell m}$:

$$\delta T(\theta, \phi) = \sum_{\ell=2}^{+\infty} \sum_{m=-\ell}^{+\ell} a_{\ell m} Y_{\ell m}(\theta, \phi). \tag{2.2}$$

The information that defines the measured spectrum is contained in the values of the coefficients $a_{\ell m}$ and the coefficients that are usually plotted are:

$$\mathcal{D}_\ell = \frac{\ell(\ell+1)C_\ell}{2\pi} = \sum_{m=-\ell}^{+\ell} |a_{\ell m}|^2 \tag{2.3}$$

These coefficients can be predicted by a given formulation of the cosmological model: the spectrum is fitted to the data and the best-fit values are compared with the prediction in order to determine the cosmological parameters. Figure 2.5 shows the angular power spectrum of the CMB anisotropies measured by Planck [19]. The measured baryon and dark matter densities are determined to be respectively:

$$\Omega_b h^2 = 0.02226 \pm 0.00023 \quad \Omega_{DM} h^2 = 0.1186 \pm 0.0020\,. \tag{2.4}$$

These measurements translate into an estimated fraction of matter equal to 30.8% compared to the total mass-energy of the Universe, and a 4.8% fraction of baryons. Planck data confirms the standard cosmological model, without highlighting any significant deviation from it.

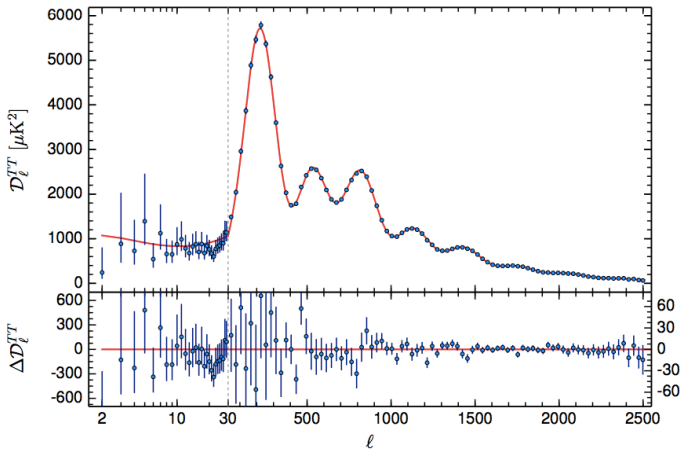

Figure 2.5: Planck 2015 power spectrum of the CMB anisotropies. The data points (blue dots) are fitted to the spectrum predicted by a baseline ΛCDM model (red line). The lower panel shows the residuals with respect to the best-fit spectrum [19].

2.3 Relic density and the WIMP miracle

Our understanding of the history of the Universe is embedded in the already mentioned standard cosmological model, which describes the Universe as evolving from a singular

state about 10^{10} years ago. It allows to explain the thermal history, the abundance of elements, the cosmological relic radiation, the large scale structure and other properties of the Universe [20]. The description of the early Universe is based on the extrapolation of the known physics to the energy scales which occurred at the beginning of the history of the Universe.

In the early Universe, after the baryogenesis, DM and SM particles are thought to be in thermal equilibrium with each others and with the photon bath. Thermal equilibrium consists of chemical equilibrium, which indicates that DM particles annihilate into SM at the same rate at which SM particles annihilate into DM, and kinetic equilibrium, which means that DM and SM exchange kinetic energy via elastic scattering. Assuming $2 \to 2$ interactions, the occurring reactions are:

$$\text{DM DM} \leftrightarrow \text{SM SM} \;\; \text{(inelastic)} \qquad \text{DM SM} \;\to\; \text{DM SM} \;\; \text{(elastic)} \tag{2.5}$$

As the Universe expands, the temperature decreases, the lighter species can no longer produce DM particles; it also becomes harder for the DM particles to annihilate. When the DM annihilation rate drops below the expansion rate of the Universe (Hubble rate), the annihilation processes shut off. At this point, DM is no longer in chemical equilibrium and the DM abundance remains frozen in time (*freeze-out*).

After the freeze-out, DM remains in kinetic equilibrium with the surrounding plasma via the elastic scattering. Eventually, when the scattering rate drops below the Hubble rate, also this reaction stops. Depending whether the DM is non-relativistic (cold dark matter, CDM) or relativistic (warm dark matter, WDM), the kinetic decoupling happens after or by the same time of the annihilation. This influences the structure formation in the Universe: the more relativistic is the DM, the more suppressed is the structure formation at small scales [21]. Current observations favor CDM over WDM scenarios.

In order to understand more quantitatively how the freeze-out occurs in the CDM scenario, the evolution of the DM number density n can be tracked down by the Boltzmann equation in its covariant form. Assuming that kinetic equilibrium is maintained and that the SM particles are in thermal equilibrium with the photon bath, the equation takes the form:

$$\frac{dn}{dt} + 3Hn = -\langle \sigma v \rangle \left(n^2 - n_{eq}^2 \right) \, . \tag{2.6}$$

The term $3Hn$ describes the decrease of the density with the expansion of the Universe at the Hubble rate H; the term on the r.h.s is the collision term, governed by the velocity-averaged annihilation cross-section $\langle \sigma v \rangle$ and by the number density at thermal equilibrium n_{eq}. From the form of 2.6 it can be seen that for $n < n_{eq}$, the DM density increases, while for $n > n_{eq}$, the DM density decreases.

It is useful to rewrite the equation in terms of the comoving number density $Y = n/s$, with s the total entropy of the Universe:

$$\frac{dY}{dx} = -\frac{\langle \sigma v \rangle s}{Hx} \left(Y^2 - Y_{eq}^2 \right) \tag{2.7}$$

where x is defined from a rescaled time variable $x = m_\chi / T$, with m_χ is the mass of the DM particle and T is the temperature. In this form, the expansion effect is absorbed in

the definition of Y and the behavior of the number density as a function of the collision term is more evident.

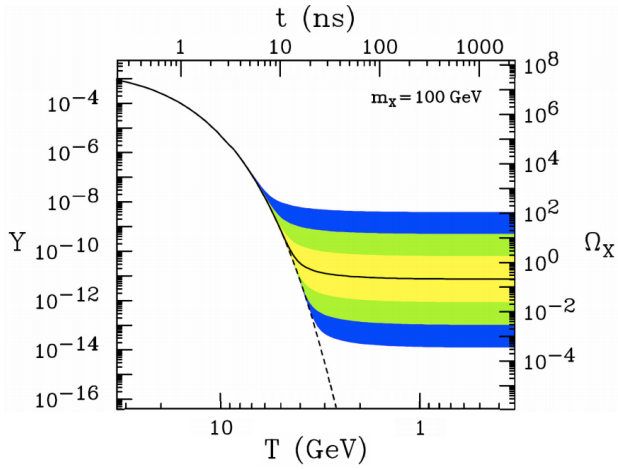

Figure 2.6: The comoving number density Y and resulting thermal relic density for a 100 GeV dark matter as a function of temperature or time. The solid line corresponds to the solution of the Boltzmann equation which yields the correct relic density and the colored regions correspond to a cross section that differ by 10,100,1000 from this value. The shaded line indicates the solution for a particle that remains in thermal equilibrium [22].

There is no analytic solution to the equation; the numerical solution is of the kind depicted in Figure 2.6. While $T \gtrsim m_\chi$, thermal equilibrium is maintained, and the DM density becomes Boltzmann suppressed; if there was no expansion, it would keep falling as indicated by the dashed line. However, as the Universe expands, the temperature decreases; when the annihilation rate cannot keep up with the expansion, thermal equilibrium is lost and the DM density in the comoving volume becomes approximately constant in time until today, as illustrated by the solid line.

The fall off from thermal equilibrium can be expressed by the condition:

$$n\langle\sigma v\rangle \sim H, \tag{2.8}$$

which, expressed in terms of the observed DM density Ω_{DM}, becomes:

$$\Omega_{DM}h^2 = \frac{m_{DM}n}{\rho_c} \sim \frac{m_{DM}H}{\rho_c\langle\sigma v\rangle}\,, \tag{2.9}$$

where ρ_c is the critical density, which is the average energy density required for a flat Universe. By substituting the numerical values for H and ρ_c, and taking the annihilation cross section as $\langle\sigma v\rangle \sim \alpha^2/m^2$, one can obtain:

$$\Omega_{DM}h^2 = 0.1\left(\frac{0.01}{\alpha}\right)^2\left(\frac{m_\chi}{100\,\text{GeV}}\right)^2 \tag{2.10}$$

which yields the observed value observed today by Planck, when assuming $\alpha \sim 0.01$ and mass $m_{DM} \sim 100$ GeV. The fact that a DM particle with typical weak scale mass

and couplings gives the correct relic abundance observed today is known as the 'WIMP miracle'.

2.4 Dark Matter candidates

2.4.1 Candidates from ordinary matter

As indicated by the CMB anisotropies, it is rather well established that DM cannot (at least not entirely) be made of standard baryons, which would stay unseen because they do not emit electromagnetic radiation. Astrophysical objects of this kind include dark planets, brown dwarfs, black holes and neutron stars, and are collectively called machos (Massive Compact Halo Objects). The presence of these objects can be detected through micro-lensing effects. Several dedicated experiments, such as EROS [23] and MACHO [24], have systematically searched for machos in our galaxy. As shown in Figure 2.7, the latest results from the EROS collaboration exclude that machos in the mass range of $0.6 \times 10^{-7} M_\odot < M < 15 M_\odot$ constitute a large fraction of the dark matter halo. In particular, for macho masses $M \sim 0.4 M_\odot$, the halo fraction allowed by EROS is significantly smaller than allowed by the MACHO measurements.

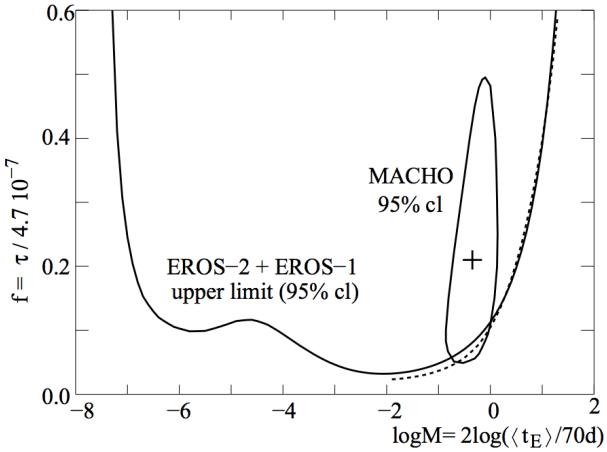

Figure 2.7: Excluded fraction at 95% CL of DM halo constituted by machos, f, as a function of the macho mass, M, for the combined analysis of the EROS surveys. The likelihood contour at 95% CL observed by MACHO is also reported. From Ref. [23].

It has already been mentioned that the success of the standard cosmological model favors the hypothesis that dark matter is non-relativistic. If DM was relativistic, the natural candidate would be the SM neutrino. Stable neutrinos make a contribution to the total energy density of the Universe which is given by:

$$\Omega_\nu h^2 = \frac{m_{tot}}{94\,\text{eV}}\,, \tag{2.11}$$

where m_{tot} indicates the sum of the individual masses of all neutrino species. To fulfill the limit given by the measured DM abundance, it should hold: $m_{tot} \leq 11$ eV. Direct

measurements of the mass of the electron antineutrino currently set an upper bound of $m_\nu < 2.05$ eV [25]. This upper limit applies to all three neutrinos masses, since the mass differences among them must be very small to explain the atmospheric and solar neutrino oscillations. Therefore neutrinos are not abundant enough to be the dominant component of DM. Furthermore, neutrinos have a role in determining the large scale structure of the Universe: being free-streaming, they tend to spread out the large scale structures of matter. The combination of CMB data and galaxy surveys constrains the influence of neutrinos to be small in the structure formation and the sum of the masses to be $m_{tot} < 0.13$ eV [26].

2.4.2 WIMP candidates

The most studied candidate for particle dark matter is the already mentioned WIMP, a particle produced thermally, which interacts weakly with SM particles, with a mass in the GeV-TeV regime, non-relativistic, neutral and stable, constituting approximately 23% of the total mass-energy of the Universe. WIMPs are predicted in a variety of beyond the Standard Model (BSM) theories. These BSM models can be broadly classified based on three different approaches.

Natural theories: theories that solve the hierarchy problem have been proposed, starting from the early proposals of supersymmetry and technicolor through the idea of large extra dimensions. All these theories predict the existence of new states at the TeV scale, responsible for cancelling the Higgs divergences. Because the new states should couple to SM particles, to avoid strong constraints from electroweak precision data and flavor physics, a new symmetry is introduced under which the SM particles are neutral while the BSM particles are charged. In this way the coupling between a single BSM particle and a single SM particle cannot contribute at tree level, thus solving the tension with EW precision data. As a by-product, the new symmetry implies the existence of a new stable particle that provides a dark matter candidate if it is electrically neutral and weakly interacting [27]. The most studied example is by far the supersymmetric neutralino.

Minimal models: more recently, simplified theories have gained momentum, given the tight constraints from the LHC, which make natural theories suffer themselves of a naturalness problem. In the new approach, models do not aim to solve the hierarchy problem, but exclusively address the problem of dark matter. Among these are models which predict an additional scalar doublet in the SM, such as the inert doublet model [28], or the minimal fermionic dark matter approach [29], which introduces a lepton multiplet, the lightest state of which provides a DM candidate.

Simplified Models and EFTs: the advent of the LHC has favored the rise of even more simplified models, each of which usually predicts one DM candidate and an additional particle, the mediator, responsible for the interaction between DM and SM particles. The classification of the models is usually based on the properties of

spin and parity of the mediator. A given simplified model can characterize more signatures, making straightforward the comparison between different channels. Another advantage of simplified models is that, being quite simple, a broad range of models can be scanned in order to capture all DM-motivated signatures. Far from being complete theories, simplified models can provide building blocks for more elaborate models.

The models used as benchmarks for the searches in this work are primarily simplified models not covered by searches for supersymmetry; a more detailed discussion on those relevant for this work is deferred to Chapter 6.

2.4.3 Non-WIMP candidates

While most of the focus in the field of particle Dark Matter has undoubtedly been the WIMP, it is worth to note that there are many well-motivated theories which yield the correct relic density and predict detectable signals. A complete list of these candidates is beyond the scope of this document, but some of the proposals in the literature are briefly discussed.

Some dark matter candidates arise from simple modifications of the WIMP hypothesis: for example it is possible to open up the allowed mass regime for the DM particle by taking a much smaller coupling; this leads to the so-called **WIMPless DM** models [30]. These models usually involve entirely new dark sectors, which include a DM candidate.

A different mechanism, **freeze-in** [31], could be responsible for the DM production, in contrast to the standard picture of thermal relics produced at freeze-out. The idea of freeze-in is based on the assumption that the DM density is negligibly small in the earlier history of the Universe; at this time, the DM would be very weakly coupled to the thermal bath. DM particles would be produced slowly but constantly from annihilations or decays of SM particles, with the dominant production occurring around $T \approx m$, until the expansion rate of the Universe becomes so high that the DM abundance remains fixed. This idea is illustrated in Figure 2.8.

Another idea is that of **Asymmetric DM** [32], which connects the relic abundance of DM with the baryon asymmetry, by assuming a common production mechanism between DM and SM, which provides a justification for the fact that $\Omega_{DM} \approx 5\Omega_b$.

SuperWIMPs are particles which inherit the correct relic density through decays [33]: WIMPs would freeze-out as usual in the early Universe, but later decay to superWIMPs, which would form the DM candidates existing today. This scenario can be realized in many BSM theories; one example is the supersymmetric gravitino, when the gravitino is the lightest SUSY particle (LSP), and the role of the WIMP is played by the next-to-lightest SUSY particle (NLSP).

A possible candidate for dark matter is the **sterile neutrino**, a neutrino that doesn't interact weakly, to which the other families of neutrinos can oscillate. It can be added in a simple extension of the SM as a fermion, singlet under the SM gauge group and only interacting with the SM via a Yukawa coupling with the left-handed lepton doublet and the Higgs. The model contains just two new parameters, the mass of the sterile neutrino

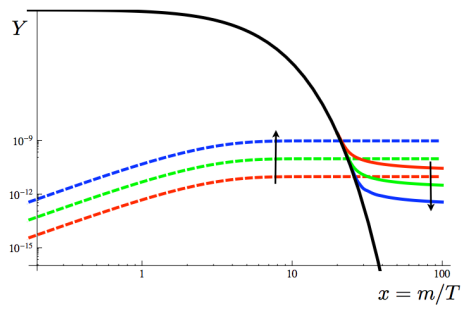

Figure 2.8: Evolution of the comoving relic density for conventional freeze-out (solid) and freeze-in (dashed) as a function of $x = m/T$. To be noted that the freeze-in abundance is dominated by the epoch $x \approx 5$, in contrast to freeze-out which only departs from equilibrium for $x \approx 20-30$ [31].

and the mixing angle. For a recent review on the subject, including the cosmological constraints and the controversial observations in some neutrino oscillation experiments, the reader can refer to [34].

Axions are introduced to explain the strong CP problem; they are electrically neutral, pseudo-scalar and stable particles and thus provide a DM candidate. Axion searches are qualitatively different from the WIMP searches and are not discussed in this document. Axions are already very well constrained: from the combination of accelerator searches, which exploit the coupling between axions and SM particles, astrophysical observations such the evolution of red giant stars and the duration of supernovae, axion masses approximately above 10^{-2} eV are ruled out [35]. Regarding the production mechanism, the axion couples so weakly to other matter, that it never was in thermal equilibrium in the early Universe. There is a considerable uncertainty in the relation between mass and relic density, depending on the several possible sources of axion production [36]; in order to avoid DM over-production, axion masses should be larger than 10^{-5} eV. A summary of constraints on the axion masses is given in Figure 2.9.

2.5 Direct detection

The idea underlying direct detection is that, if the Milky Way galaxy is filled with WIMPs, then a flux of dark matter particles should pass through the Earth and interact with known matter, although with very low cross-section. As WIMPs scatter off nucleons, the energy of recoil of the nuclei should be detectable. Therefore, direct detection experiments are configured as detectors which maximize the probability of interaction and employ various techniques to measure the energy, direction and time modulation of the WIMP flux.

The calculation of the event rate are and the underlying assumptions are discussed first, followed by an overview of the detection techniques currently employed together with the best exclusion limits to date.

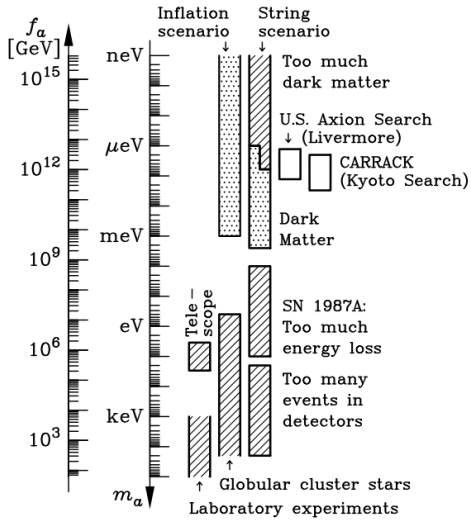

Figure 2.9: Astrophysical and cosmological exclusion regions (hatched) for the axion mass m_a or equivalently, the Peccei-Quinn scale f_a. An 'open end' of an exclusion bar means that it represents a rough estimate. The dotted regions indicate where axions could plausibly be the cosmic dark matter [37].

Event rate calculation

The energy differential event rate, expressed in counts $\mathrm{kg}^{-1}\,\mathrm{day}^{-1}$ for a WIMP mass m_χ and a nucleus with mass m_N is given by [38]:

$$\frac{dR}{dE} = \frac{\rho_0}{m_N m_\chi} \int_{v_{min}}^{\infty} v f(v) \frac{\mathrm{d}\sigma_{\chi N}}{\mathrm{d}E}(v, E)\mathrm{d}v\,, \tag{2.12}$$

where:

- ρ_0 is the **local WIMP density**, for which the canonical value of 0.3 GeV cm^{-3} is used by most experiments. The values obtained can vary by a factor 2 depending on the models used for the Milky Way;
- $f(v)$ is the **WIMP speed distribution** in the detector frame; the standard halo model assumes an isothermal sphere with density profile $\rho(r) \propto r^{-2}$, which yields an isotropic, Gaussian velocity distribution, with the mean given by the time-dependent Earth velocity around the galactic center. While the isothermal halo assumption is a good first approximation, observations and numerical simulations show that it is likely not to be the full model. For time-averaged differential rates, however, which are obtained by integrating $f(v)$, there is only a weak dependence on the shape of $f(v)$ and hence on the details of the halo model.
  The Earth velocity around the galactic center is in principle given by three components: the motion of the local standard of rest (LSR), the Sun's peculiar motion

with respect to the LSR, and the Earth's orbit about the Sun. For experiments not seeking for a time or directional modulation, only the measurement of the velocity of the LSR is important. The local circular velocity obtained by combining a large number of measurements is found to be $v_c = (220 \pm 20)\mathrm{km\,s^{-1}}$;

- E is the **recoil energy** of the nucleon; in the extreme non-relativistic limit, as it is the case at these velocities, the recoil energy due to elastic scattering is calculated in terms of the scattering angle in the center-of-mass frame θ^*:

$$E = \frac{\mu_N^2 v^2 (1 - \cos\theta^*)}{m_N} \tag{2.13}$$

  where μ_N is the WIMP-nucleon reduced mass;

- v_{min} is the lower limit of integration and is due to the **minimum recoil energy** that can be measured by the detector. This sets a lower limit on the WIMP masses that can be measured by a given detector. In fact, the dependence of the event rate on m_χ and E means that for very light WIMPs the rate R will decrease rapidly with increasing energy and the event rate above threshold may be too small to be detected;

- $\frac{\mathrm{d}\sigma_{\chi N}}{\mathrm{d}E}$ is the **WIMP-nucleus differential cross-section**, which encodes the particle and nuclear physics inputs. It is usually expressed in terms of spin-dependent (SD) and spin-independent (SI) contributions as:

$$\frac{\mathrm{d}\sigma_{\chi N}}{\mathrm{d}E} = \frac{m_N}{2\mu_N^2 v^2}\left(\sigma_{SI} F_{SI}^2(E) + \sigma_{SD} F_{SD}^2(E)\right) \tag{2.14}$$

  where the form factors $F(E)$ encode the dependence of the nuclear wavefunctions on the momentum transfer and can be determined by nuclear physics calculations and measurements, while the cross-sections σ_{SD}, σ_{SI}, describe the interaction between the nucleus and the WIMP in the non-relativistic limit. These two are the variables according to which experiments express their limits; this makes direct detection limits largely independent on the particle physics model assumed to describe the WIMP-nucleon interaction.

Detection techniques and current limits

Direct detection experiments are designed with a few common characteristics, dictated by the necessity to detect low interaction rates at low energies. The low WIMP interaction rate requires large detector masses to increase the interaction probability inside the target. In order to measure small nuclear recoil energies, ranging from 1 to 100 keV, which are the typical values expected for WIMP masses between 1 GeV and 1 TeV, detector technologies with low energy thresholds need to be employed. Detectors are usually located in deep underground laboratories in order to suppress large background produced by cosmic rays. To suppress the residual backgrounds coming from the neutrons and gamma rays of the environment and from the detector components themselves,

shielding strategies are employed and the ultra-high purity is a stringent requirement for the detector materials and components.

There are several detector types which are currently employed in direct detection experiments, using one or more detection techniques (mainly ionization, scintillation, phonons). They are listed here with a brief description, while Figure 2.10 provides a non-exhaustive list of experiments categorized according to the detection technique. For an extensive discussion on direct detection experiments, the reader can refer to Chapters 20, 21 and 22 of [10].

Semi-conductors, such as germanium and silicon, are used as ionization detectors. When operating at cryogenic temperatures, they can also be used as bolometers, to enhance the discrimination power between nuclear and electron recoils.

Noble liquids at cryogenic temperatures, such as liquid argon and liquid xenon, are targets with high scintillation and ionization yields. The advantage of these detectors is the promise of scale-up to large masses at modest costs compared to semiconductors. Discrimination from backgrounds in these detectors is based on the pulse shapes of scintillation light and ratios between ionization and scintillation signals.

Crystals, such as sodium and caesium iodides, are used as scintillator detectors. The relative simplicity of this technology allows to operate the detectors over long periods of time for several years; for this reason, crystals are the preferred choice for measuring potential signals with annual modulation.

Superheated liquids close to boiling temperatures can be used as bubble chambers. This technique has the advantage that it has a low sensitivity to low ionizing particles, such as electrons and photons, and thus provide an automatic background suppression.

Gas detectors at room temperatures are employed to reconstruct the full path of the nuclear recoils in directional experiments. Current experiments use the gaseous time projection chamber technology.

As already mentioned, direct detection experiments present their results as limits on WIMP-nucleon interaction cross-sections, σ_{SI} and σ_{SD}, as a function of the DM mass. In principle, each component should be distinguished between neutron and proton. For SI, the limits are presented assuming that they are equal, while for SD, limits are presented separately.

Most of the current direct detection experiments are more sensitive to the SI component, reaching upper limits as low as $10^{-46}\,\mathrm{cm}^{-2}$ for WIMP masses in the range of a few GeV, as shown in Figure 2.11. Projections from a selected numbers of upcoming experiments are also reported. In the plot, the region dominated by the irreducible neutrino background coming from solar and atmospheric neutrinos is also indicated. The uncertainty on these rates is the current major limiting factor for the eventual reach of these experiments.

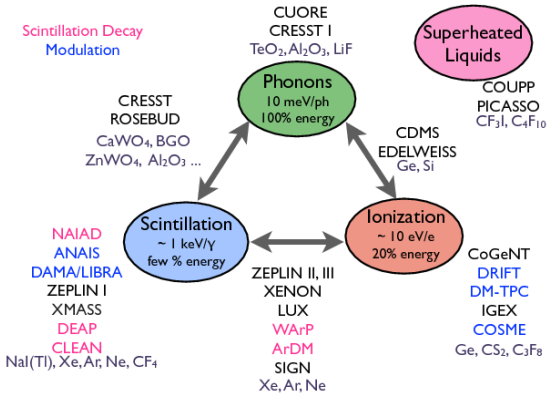

Figure 2.10: Direct detection experiments listed according to their detection strategy [39].

For the SD component, experiments are usually sensitive either to the WIMP-neutron or the WIMP-proton interaction. The best limits are provided by LUX, for the former, and by PICO, for the latter, as illustrated in Figure 2.12. In the plots, also the limits set by several indirect detection and collider experiments are presented.

With the exception of the claim for a signal reported by the DAMA/LIBRA collaboration [40], which is excluded by other experiments, no solid evidence for DM has been provided by direct detection experiments so far.

2.6 Indirect detection

Indirect detection experiments aim at observing the radiation and particles produced by dark matter annihilations, such as gamma rays, highly energetic neutrinos, highly energetic charged particles. Dense regions of the galactic halo, such as the galactic center, may be excellent amplifiers for the purposes of detecting gamma-rays or neutrinos. Other astrophysical objects, such as the Sun or the Earth, could also act as gravitational traps for the WIMPs.

Among the particles produced in DM annihilations, **gamma rays** are particularly interesting since they travel in straight lines and almost unabsorbed and thus do not require an involved calculation of their propagation. If a mono-energetic line in the photon spectrum was observed incompatibly with other astrophysical sources, it would constitute a 'smoking gun' for a DM signal [43].

Gamma rays are detected with large ground-based telescopes, collecting light from atmospheric Cerenkov interactions, such as HESS and MAGIC, and with space telescopes, such as the Fermi Gamma-ray Space Telescope. A possible line at approximately 130 GeV,

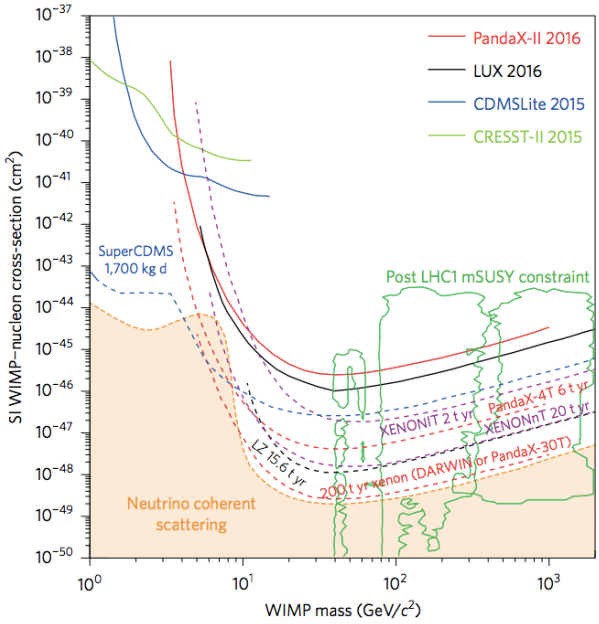

Figure 2.11: Current limits and future projections on the spin-independent WIMP-nucleon cross-section from the direct detection experiments [41].

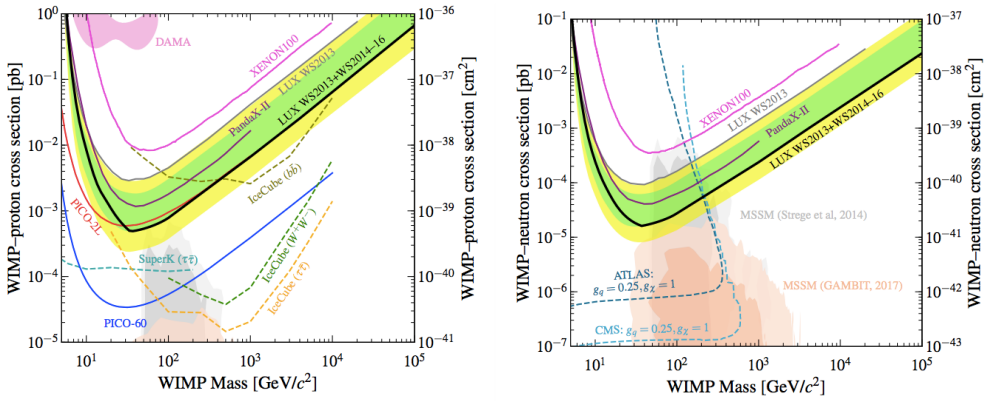

Figure 2.12: Current limits on the WIMP-proton (left) and WIMP-neutron cross-section (right) recently reported by the LUX collaboration [42]. In the case of the WIMP-proton scattering, limits from indirect detection experiments (SuperKamiokande and IceCube) are the most stringent in many regions of the parameter space.

observed by Fermi, was a topic of discussion in recent years; however, subsequent analyses of the Fermi data have shown a reduced significance of the excess, compared to the original observations, and the interpretation as a candidate for dark matter is now disfavored by the Fermi collaboration itself [44].
More recently, another excess of gamma rays has been observed by Fermi and confirmed by subsequent analyses [45]. This excess is concentrated in the galactic center, at energies of a few GeV. Although the excess is firmly detected, an interpretation of this emission as a signal of self-annihilating DM particles is not unambiguously possible due to difficulties in modeling the systematic effects of the gamma rays in the galactic plane [46].

Neutrinos can be secondary products of DM annihilations in the Sun. Over the lifetime of the Sun, a sufficient density of WIMPs can accumulate in its center, so that an equilibrium is established between WIMP capture and their annihilation [47]. Neutrinos generated from the decay of heavy quarks and gauge bosons escape from the Sun with minimal absorption and travel to Earth, where they can be detected using large volume neutrino detectors, such as SuperKamiokande and IceCube. Neutrino telescopes detect Cerenkov radiation from the secondary particles produced in the interactions of high-energy neutrinos with the detector medium. These experiments are usually located deep underground and the detector is made of a large volume of well-shielded water or ice. No excess over the background has been observed yet by the currently operating detectors, and limits on the velocity averaged WIMP annihilation cross-section are set, which can be translated to WIMP-nucleon scattering cross sections and compared to results from the direct detection experiments. Neutrino experiments set stringent limits in the case of spin-dependent interactions, as already shown in Figure 2.12.

Excesses of **charged particles** are challenging signatures of DM annihilations, given the large number of effects which can concur in modifying the propagation of charged particles. Positrons and anti-protons are the usual targets for these experiments, given the subdominant component of anti-matter compared to matter in cosmic rays coming from non DM-sources. Experimental techniques for charged particles range from detectors on balloons, such as ATIC, or in space, such as PAMELA and AMS, to large-area cosmic-ray detectors on the ground, such as Auger.
Several experiments have observed that the positron fraction rises from approximately 10 GeV up to 500 GeV, as shown in Figure 2.13, while conventional expectations for galactic cosmic rays predict a falling spectrum. The observation suggests that there must be a source responsible for the injection of positrons at high energies: both DM annihilations and pulsars have been proposed as possible explanations but, currently, there is not a large consensus in disfavoring one hypothesis or the other. More precise results on the positron fraction and the antiproton-to-proton ratio will help to distinguish between the two; the most recent results from AMS-02 present a remarkably flat behavior in the antiproton-to-proton at high energies, as shown in Figure 2.14, which is thought to be incompatible with secondary production of antiprotons from ordinary cosmic rays and of difficult explanation from pulsar origin [48]. Figure 2.15 shows examples of how the positron fraction and antiproton-to-proton ratio can be fitted to a model which includes the total expected cosmic ray flux and a dark matter component.

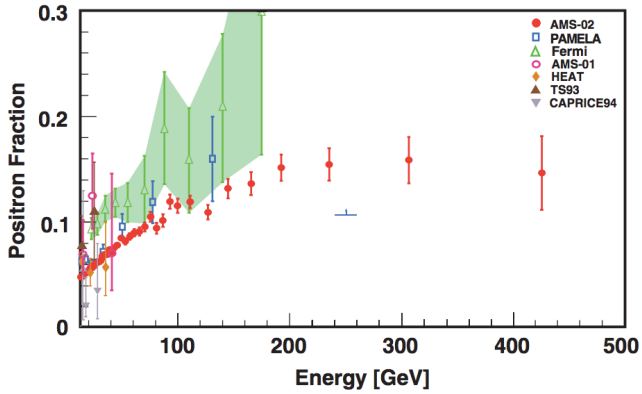

Figure 2.13: The positron fraction above 10 GeV, where it begins to increase, as measured from AMS-02 and compared to the results from other experiments [49].

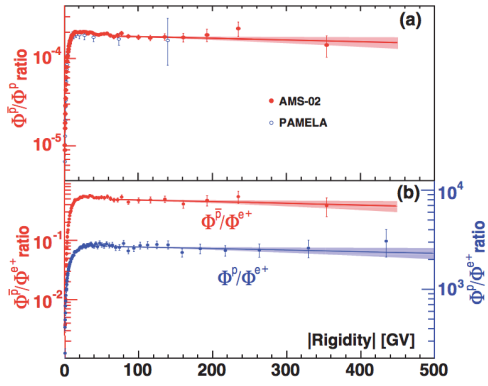

Figure 2.14: Top panel: the $p/\bar{p}$ flux ratio as a function of the rigidity (momentum per unit of charge) from 1 to 450 GV and compared with the results from PAMELA. Bottom panel: the measured $\bar{p}/e^+$ (red) and p/e^+ (blue) flux ratios [50].

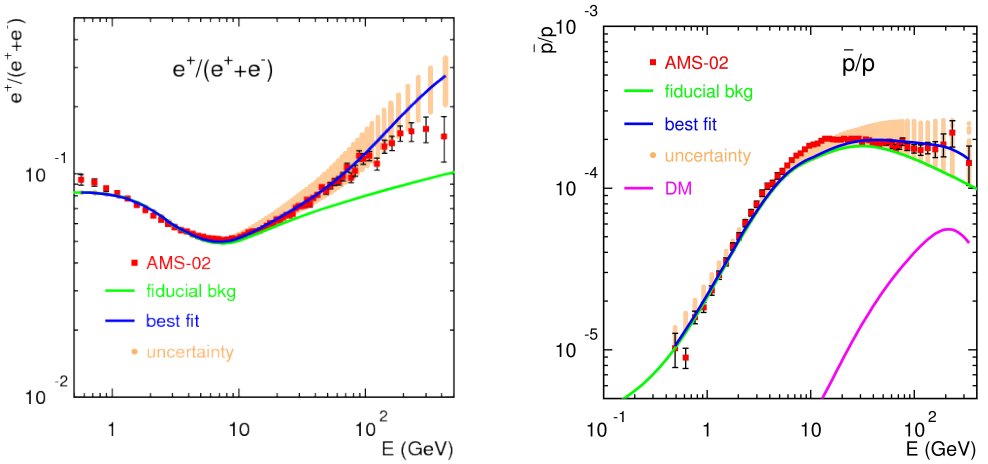

(a) (b)

Figure 2.15: The positron fraction (a) and the $p/\bar{p}$ flux ratio (b) observed by AMS-02 compared to the prediction of the total cosmic ray flux with a dark matter model with parameter values that best fit the AMS-02 data. Two different dark matter models are used in the two cases. The total predicted flux is the sum of the background flux (green solid line) and the dark matter contribution. Orange dots indicate the 2σ confidence region of the prediction. (a) from [51] and (b) from [52].

2.7 Detection at colliders

At colliders DM particles can be produced from the annihilations of SM particles or from the decay of other exotic particles. Since DM must have a stability of the order of the lifetime of the Universe, when produced in a pp collision, DM particles live long enough to escape undetected. Their escape, however, leads to a momentum imbalance in the transverse plane to the collision, where the total momentum is expected to be zero. Missing transverse momentum is thus the primary signature to look for DM particles.

A large program of BSM searches has been deployed by past and present experiments at colliders, characterized by the missing transverse momentum signature. Besides searches optimized to discover supersymmetric processes, one way to search for DM particles is to look for deviations from the SM predictions in events characterized by a large missing transverse momentum recoiling against a visible SM particle, where the latter is needed to tag the event. These kind of signatures are called 'mono-X', where X is a detectable physics object, such as a single jet of hadronic activity, a vector boson or a Higgs. The mono-photon and mono-jet signatures are the focus of this work and will be discussed in detail in Chapters 7 and 8.

CHAPTER 3

The ATLAS Experiment at the LHC

ATLAS (A Toroidal LHC Apparatus) is a high energy physics experiment that detects the products of the collisions of protons accelerated at the Large Hadron Collider (LHC). The analyses described in this thesis are based on the data collected by ATLAS at a center-of-mass energy of 13 TeV in the course of 2015 and 2016, during the Run 2 of the LHC.
In this chapter, after an introduction to the LHC accelerator, the ATLAS detector and its sub-detectors, are described. The bulk of this chapter is based on the References [53] for the LHC and [54] for ATLAS.

3.1 The Large Hadron Collider at CERN

3.1.1 Accelerator complex

The LHC [55, 53], is a circular proton-proton collider built across the border between Switzerland and France, which started its operations in 2009. With its 27 km of circumference and a center-of-mass collision energy of 13 TeV, it is the largest and highest energy particle accelerator ever built. The beams of the LHC are brought into collision inside four detectors: ALICE, ATLAS, CMS and LHCb, which are spread along the circumference of the LHC as shown in Figure 3.1.

Protons in the LHC travel in two counter-rotating beams bent by large magnetic fields and acquire energy at each round; the acceleration relies on radio-frequency cavities which increase the beam energy by around 500 keV at each turn. The binding of the trajectory of the protons throughout the ring is achieved by means of a complex magnet system, which is synchronized with the acceleration frequency. It consists of 1232 superconducting dipole magnets, each 15 m long, which are cooled to 1.9 K using superfluid helium, and are able to generate magnetic fields of 8.33 T. The magnet system includes quadrupole magnets, for the containment and focusing of the transversal oscillations of the beam; four series of quadrupoles are also used to bring the beams into collision at each of the interaction points. The system is completed by sextupole, octupole and decupole magnets, which correct for small imperfections in the magnetic field at the extremities of the dipoles.

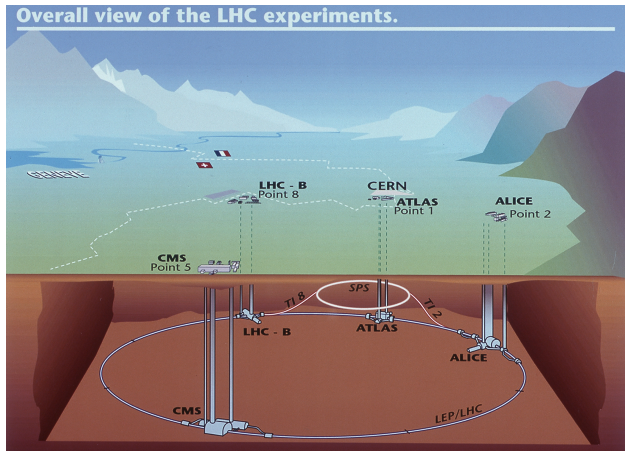

Figure 3.1: The locations of the four LHC experiments shown along the circumference of the LHC [56].

The LHC is just the last stage of a whole acceleration chain; several machines from the CERN accelerator complex provide the first steps of acceleration, as sketched in Figure 3.2. Protons obtained from hydrogen atoms stripped off their electron, are accelerated by the Linac2 up to 50 MeV. The beam is then injected into the Proton Synchrotron Booster (PSB), which accelerates the protons to 1.4 GeV, followed by the Proton Synchrotron (PS), which pushes the beam to 25 GeV. Protons are then sent to the Super Proton Synchrotron (SPS), the second-largest machine in the complex, measuring nearly 7 km in circumference, that operates at up to 450 GeV, the minimum at which the LHC can maintain a stable beam.

3.1.2 Luminosity and pile-up conditions

At particle colliders rare processes are usually looked for, such as the production of particles that had never been detected before. In a scattering process the rate of events per unit time and the cross section are related by a proportionality factor, which is called instantaneous luminosity and is denoted as $\mathcal{L}$:

$$\frac{dN_{events}}{dt} = \mathcal{L}\sigma \tag{3.1}$$

Therefore the instantaneous luminosity is the quantity that needs to be maximized in order to maximize the probability to detect a given process. At a collider the luminosity depends on the beam parameters according to the relations [53]:

$$\mathcal{L} = \frac{f_{rev} N_p^2 N_b \gamma_r}{\mathcal{A}} \mathcal{S} \tag{3.2}$$

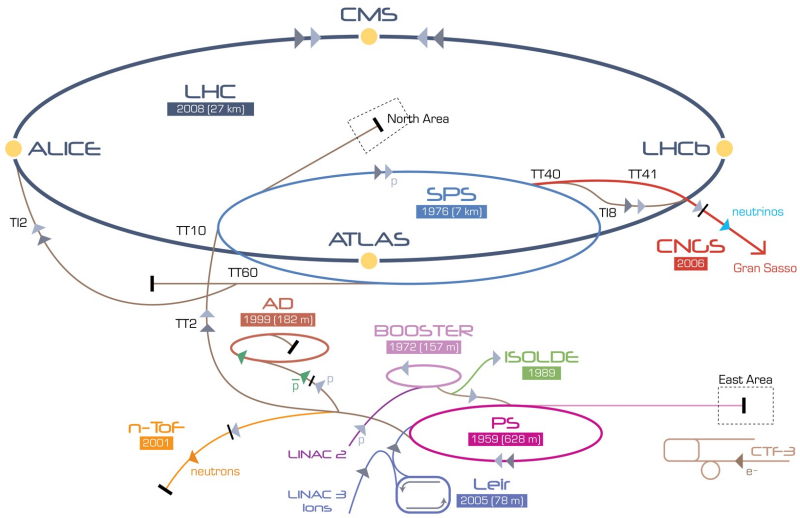

Figure 3.2: A sketch of the LHC accelerator complex at CERN [53].

$$\mathcal{A} = 4\pi\epsilon_n\beta^*, \qquad \mathcal{S} = \left(1 + \left(\frac{\theta_c\sigma_z}{2\sigma^*}\right)^2\right)^{-1/2} \tag{3.3}$$

f_{rev} is the revolution frequency, N_p is the number of particles in each bunch and N_b is the number of bunches per beam, γ_r is the relativistic gamma factor, $\mathcal{A}$ is the effective cross-section area of the beams and $\mathcal{S}$ is a suppression factor which describes the increase of effective interaction area due to the crossing angle at the interaction point (IP). For round and equal beams, $\mathcal{A}$ depends on the normalized transverse beam emittance ϵ_n and on the beta function at the collision point β^*, while $\mathcal{S}$ depends on the crossing angle θ_c, the RMS bunch length σ_z, and on the transverse RMS beam size at the IP as in Equation 3.3.

It is thus clear that an increase in the luminosity can be achieved for example by squeezing the beams and reducing their transverse size, by increasing the number of protons per bunch, or by decreasing the spacing between bunches.

In all cases, the increase in luminosity implies increased experimental challenges in terms of pile-up conditions. The term *pile-up* is used to collectively denote all kind of proton-proton collisions in addition to the collision of interest. Pile-up interactions are recorded as belonging to the same event as that of interest, but are in fact originated by a distinct interaction. In Chapters 4 and 5, while discussing the performance of the reconstruction of the physics objects and of the $E_{\mathrm{T}}^{\mathrm{miss}}$, the importance of pile-up interactions will become more clear.

There are two main components of pile-up:

- *in-time pile-up* denotes the additional pp collisions occurring in the same bunch-crossing as the collision of interest; detectors must be able to distinguish particles from multiple simultaneous interactions to address this component;

- *out-of-time pile-up* denotes the additional pp collisions occurring in bunch-crossings just before and after the collision of interest; this effect is mainly controlled by the distance in time between subsequent bunch crossings; detectors with faster response than the bunch spacing are insensitive to this component;

The amount of pileup activity is typically parametrized in terms of the number of reconstructed primary vertices N_{PV}, which is measured in the tracking detectors on an event-by-event basis, and in terms of the mean number of interactions per bunch crossing $\langle\mu\rangle$, which is an average over a given block of events and is measured by dedicated ultra-fast detectors. [1]

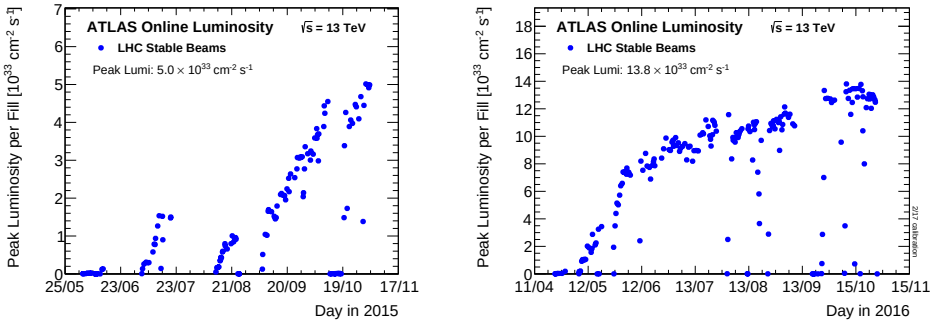

(a) 2015 (b) 2016

Figure 3.3: The peak instantaneous luminosity delivered to ATLAS during stable beams for pp collisions at $\sqrt{s}$ =13 TeV is shown for each LHC fill as a function of time in 2015 (left) and 2016 (right) [58]. The luminosity is determined using counting rates measured by the luminosity detectors, and is based on a preliminary 13 TeV calibration determined using van-der-Meer beam-separation scans.

During the 2015 and 2016 operations the instantaneous luminosity and the associated pile-up conditions were increased as shown in Figure 3.3. Figure 3.4 shows the delivered integrated luminosity in 2015 and 2016 as a function of the average number of interactions per bunch crossing. With an average of $\langle\mu\rangle = 13.7$ over the course of 2015 and $\langle\mu\rangle = 24.9$ over 2016, a total integrated luminosity of 42.7 fb^{-1}was delivered by the LHC. Figure 3.5 shows the integrated luminosity as delivered by the LHC (green) and as accumulated by ATLAS (yellow) during 2015 and 2016.

3.2 Particle detection at the LHC

The challenging luminosity and pile-up conditions at the LHC, which have been discussed in Section 3.1.2, set some common requirements for the various technologies em-

[1] The average number of interactions per bunch crossing $\langle\mu\rangle$ and the instantaneous luminosity $\mathcal{L}$ are linked via the following relation [57]:

$$\mathcal{L} = n_b \frac{\langle\mu\rangle f_{rev}}{\sigma_{inel}} \tag{3.4}$$

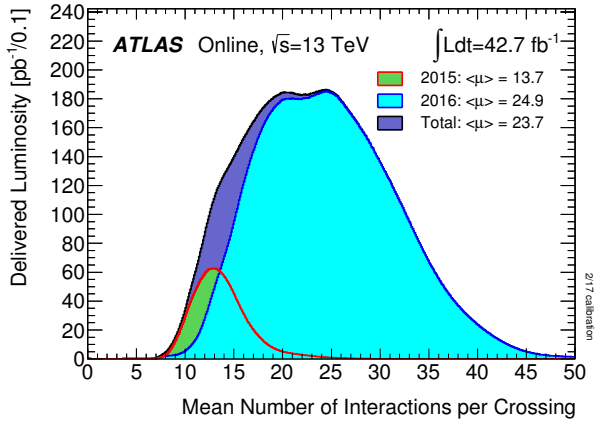

Figure 3.4: Luminosity-weighted distribution of the average number of interactions per crossing for the 2016 and 2015 *pp* collision data at 13 TeV center-of-mass energy [58].

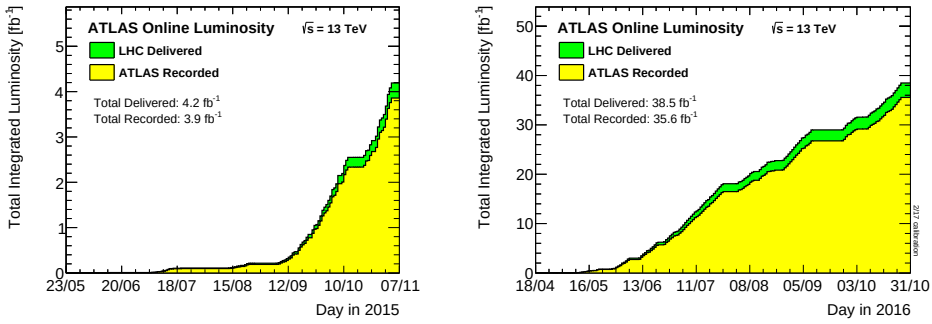

(a) 2015 (b) 2016

Figure 3.5: Integrated luminosity versus time delivered to (green) and recorded by ATLAS (yellow) during stable beams for *pp* collisions at $\sqrt{s}$ =13 TeV in 2015 (left) and 2016 (right) [58].

ployed for the detector components:

- high granularity is needed to resolve the tracks and energy deposits in an environment with a very high density of particles;
- large angular acceptance is essential for the correct reconstruction of the entire event;
- fast response is required to cope with interaction rates of the order of 40 MHz;
- good resistance to high doses and radiation, both in terms of sensor elements and electronics, is essential to guarantee long duration and excellent operations for several years.

Granularity, coverage and response will be further discussed in the description of the ATLAS detector in the next sections, while resistance to radiation and considerations about the shielding will only be touched upon; for a detailed discussion the reader can refer to Chapter 3 of [54].

3.3 Overview of the ATLAS detector

The ATLAS detector is a general purpose collider experiment. As most experiments at beam-beam colliders, ATLAS has a cylindrical layout, with forward-backward symmetry with respect to the interaction point. In order to collect all the products of a proton-proton collision, a very good hermeticity has been aimed, with detectors covering almost the full solid angle around the interaction point.

ATLAS uses a right-handed coordinate system with its origin at the nominal interaction point in the center of the detector and the z-axis along the beam pipe. The x-axis points from the IP to the center of the LHC ring, and the y-axis points upward. Cylindrical coordinates (r, ϕ) are used in the transverse plane, ϕ being the azimuthal angle around the beam pipe. The polar angle is usually expressed in terms of pseudo-rapidity, η, which transforms additively under Lorentz boosts, and is defined as: $\eta = -\ln\tan(\theta/2)$. ATLAS coordinate system is illustrated in Figure 3.6.

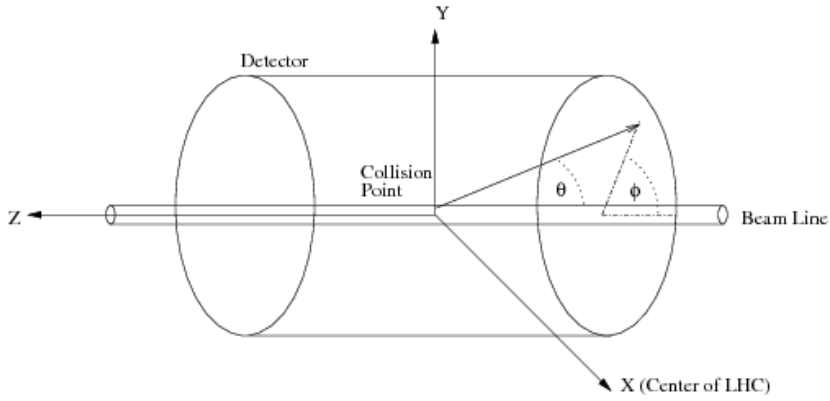

Figure 3.6: ATLAS coordinate system. From [59].

ATLAS is composed of a system of sub-detectors, that are enveloped one within another; an overview of the layout of ATLAS is shown in Figure 3.7. Closest to the beam pipe is the tracking system, which extends up to $|\eta| < 2.5$. It is enclosed by a solenoid magnet, which provides a 2 T magnetic field that bends the trajectories of the particles and allows the measurement of the momentum and charge of the charged particles. Outside the solenoid stand the calorimeters: the electromagnetic and hadronic calorimeters, to measure energy and direction of electrons, photons and of hadrons, respectively. The calorimeter system extends up to $|\eta| < 4.9$. The calorimeters are enclosed by the muon spectrometer, which measures the momenta of muons up to $|\eta| < 2.7$. The high magnetic field required to bend the trajectory of the muons is provided by three large toroidal

magnets, one in the barrel region and two in the end-caps.

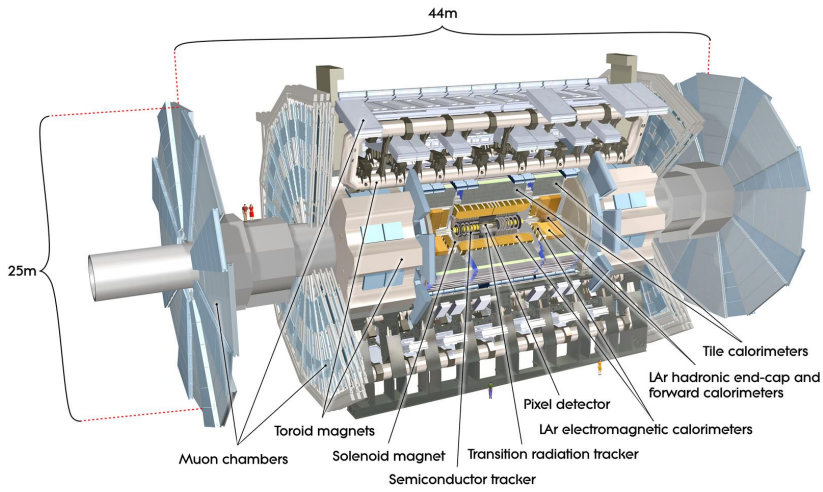

Figure 3.7: General layout of the ATLAS detector [60].

3.4 Magnets

The magnetic system is composed of superconducting magnets with different geometries:

- Central solenoid: a thin solenoid provides a 2 T field in the direction of the beam axis for the inner detector. An important design characteristic for this component is the thickness, which must be as low as possible, in order to minimize the material in front of the calorimeters and achieve the desired calorimeter performance; in total, the solenoid material contributes approximately 0.66 radiation lengths.
- Toroids: a barrel toroid and two end-cap toroids with eight windings each provide a magnetic field of approximately 0.5 T and 1 T for the muon detector in the central region and end-cap region, respectively. Altogether, the toroid system has a size of 22 m in diameter and 26 m in length. The system is air-core and is able to generate a strong bending power in a large volume, while minimizing multiple scattering effects.

A schematic view of the magnet system is depicted in Figure 3.8, while Figure 3.9 illustrates the aspect and size of the central toroid.

3.5 Inner Detector

The Inner Detector (ID) is the inner-most part of ATLAS and occupies a cylindrical volume around the beam pipe. It has a radius of approximately 1.1 m and a length of 6.2

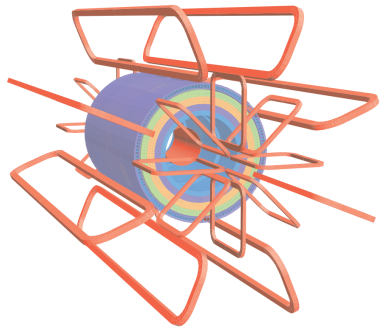

Figure 3.8: Geometry of magnet windings [54]. The coils of each toroid are visible, while the solenoid windings lie inside the calorimeter volume, which is also displayed.

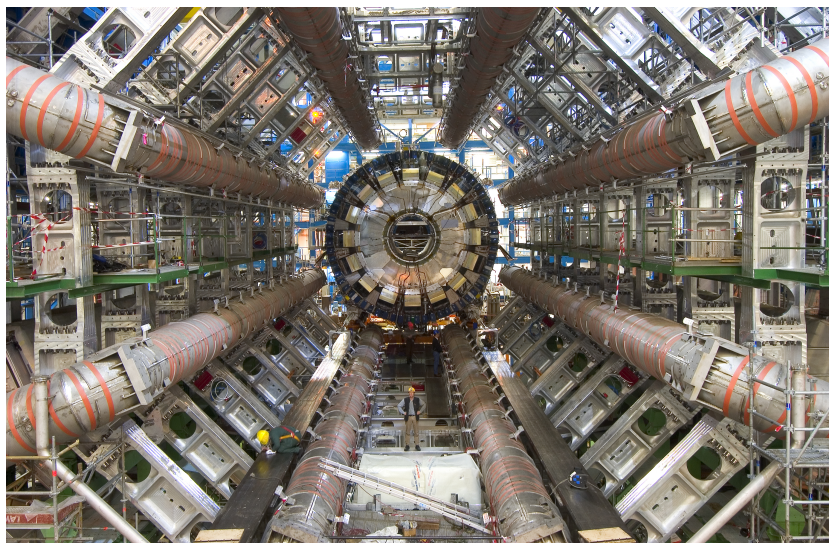

Figure 3.9: The barrel toroidal magnet with the calorimeter before the latter is moved into the middle of the detector [60].

m. With its high granularity, the ID is able to reconstruct the tracks and the vertices of interaction to measure with high accuracy the transverse momenta of charged particles down to 0.1 GeV and within the pseudo-rapidity range $|\eta| < 2.5$.
It is composed of three concentric sub-detectors, each consisting in two parts: in the barrel region the sensors are arranged in cylindrical structures around the beam axis while in the end-caps they are arranged in disks perpendicular to the beam axis. The layout of the ID is shown in figure 3.10.

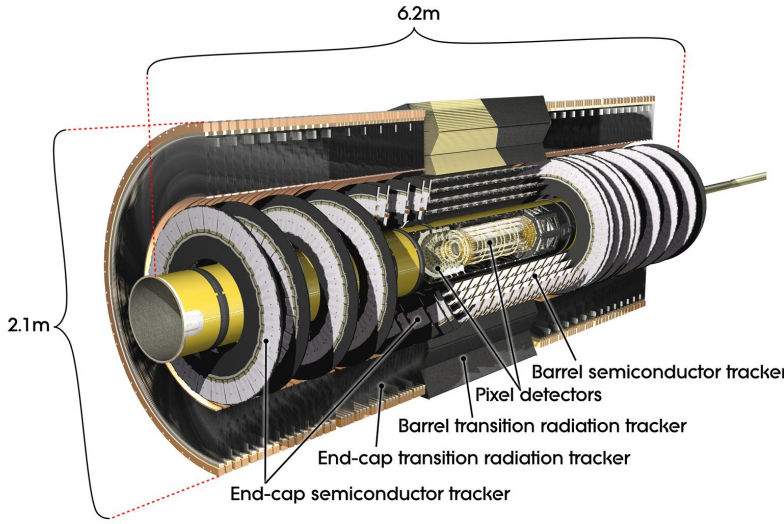

Figure 3.10: Illustration of the ATLAS Inner Detector [60].

- The **pixel detector** is constituted by three layers of silicon sensors (pixels). All pixels are identical and with a size of 50x400 μm^2. The pixels are arranged in 1744 modules with 47232 pixels each. The three layers are located at z of 50.5, 88.5, and 122.5 mm from the interaction point, while the three layers of the end-caps are located at r of 495, 580, and 650 mm from the interaction point. The spatial resolutions provided in a given layer are 10 μm in the transverse (r-ϕ) plane and 115 μm in the axial direction (z, barrel) or radial direction (r, endcaps). Three space-points are provided for the measurement of each track which enable a precise reconstruction of the vertices and the determination of the impact parameter.

  A new innermost layer (**Insertable B-Layer, IBL**) has been inserted since the start of the LHC Run 2; it is constituted by slightly smaller sensor elements with a resolution of 8 μm in the barrel and 40 μm in the end-caps. The IBL is located at z of 33.2 mm from the IP; it provides an additional space-point, thus improving the impact parameter reconstruction and vertexing.

- The **Semiconductor Tracker (SCT)** is a silicon micro-strip detector. The strips are arranged in layers in such a way as to provide four space-points per track within

the pseudo-rapidity range coverage in the ID. The four layers in the barrel are located at z of 299, 371, 443, and 514 mm from the IP. The nine layers in the endcap are located at r of 853.8, 934, 1091.5, 1299.9, 1399.7, 1771.4, 2115.2, 2505, and 2720.2 mm from the IP. The intrinsic resolutions per module are 17 μm in the transverse (r-ϕ) plane and 580 μm in the axial direction (z, barrel) or radial direction (r, endcaps).

- The **Transition Radiation Tracker (TRT)** consists of 4 mm diameter gaseous straw tubes interleaved with transition radiation material; it extends radially from 56 to 107 cm, over $|\eta| < 2.0$. The TRT provides around 36 space-points for each track, with an accuracy of 130 μm. In the barrel region, the straws are parallel to the beam axis and are 144 cm long, with their wires divided into two halves, approximately at $\eta = 0$. In the end-cap region, the straws are arranged in wheels and are 37 cm long.
  The hits in the TRT significantly contribute to the momentum measurement, with the lower precision being compensated by the large number of space-points and the longer track length. Given that it is a transition radiation detector, it also helps in discriminating electrons from pions.

3.6 Calorimeters

The energy of all charged and neutral particles in the event except for muons and neutrinos is directly measured in ATLAS thanks to a highly granular calorimeter system which provides excellent performance in terms of energy and spatial resolution.

The ATLAS calorimeter system is composed of several sub-detectors; the layout of the system is illustrated in Figure 3.11: the electromagnetic calorimeter in the barrel (EMB) and end-cap region (EMEC), the hadronic calorimeter in the barrel (Tile) and end-cap region (HEC), the forward calorimeters (FCal).

The structure of the calorimeter system must be such as to measure at the same time particles which mainly interact electromagnetically and produce electromagnetic showers, such as photons and electrons, and hadrons, which give rise to hadronic showers. The calorimeter depth is an important design consideration, as calorimeters must provide good containment for both electromagnetic and hadronic showers and limit punch-through into the muon system. The thickness of the electromagnetic calorimeter in terms of interaction length X_0 is approximately 22 X_0 in the barrel and 24 X_0 in the end-caps, as illustrated in Figure 3.13. In terms of hadronic interaction length λ_I, the total thickness of $11\lambda_I$ at $\eta = 0$ is adequate to provide good containment for high-energy jets and good missing transverse energy measurement. Figure 3.14 illustrates the thickness of the entire calorimeter system in the various pseudo-rapidity regions of the detector.

A second important design feature is the geometrical coverage: the full calorimetric system covers a pseudo-rapidity range of $|\eta| < 4.9$, which is larger compared to the Inner Detector; an almost full solid angle coverage is an important feature for an optimal reconstruction of the missing transverse momentum. The pseudo-rapidity coverage and the granularity of the various components is indicated in Table 3.12.

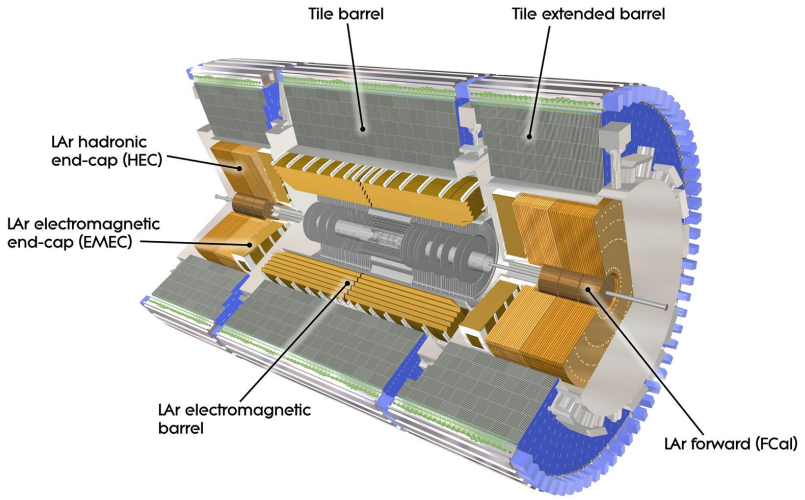

Figure 3.11: Layout of the ATLAS Calorimeter system [60].

	Barrel		End-cap	
EM calorimeter				
Number of layers and $\|\eta\|$ coverage				
Presampler	1	$\|\eta\| < 1.52$	1	$1.5 < \|\eta\| < 1.8$
Calorimeter	3	$\|\eta\| < 1.35$	2	$1.375 < \|\eta\| < 1.5$
	2	$1.35 < \|\eta\| < 1.475$	3	$1.5 < \|\eta\| < 2.5$
			2	$2.5 < \|\eta\| < 3.2$
Granularity $\Delta\eta \times \Delta\phi$ versus $\|\eta\|$				
Presampler	0.025×0.1	$\|\eta\| < 1.52$	0.025×0.1	$1.5 < \|\eta\| < 1.8$
Calorimeter 1st layer	$0.025/8 \times 0.1$	$\|\eta\| < 1.40$	0.050×0.1	$1.375 < \|\eta\| < 1.425$
	0.025×0.025	$1.40 < \|\eta\| < 1.475$	0.025×0.1	$1.425 < \|\eta\| < 1.5$
			$0.025/8 \times 0.1$	$1.5 < \|\eta\| < 1.8$
			$0.025/6 \times 0.1$	$1.8 < \|\eta\| < 2.0$
			$0.025/4 \times 0.1$	$2.0 < \|\eta\| < 2.4$
			0.025×0.1	$2.4 < \|\eta\| < 2.5$
			0.1×0.1	$2.5 < \|\eta\| < 3.2$
Calorimeter 2nd layer	0.025×0.025	$\|\eta\| < 1.40$	0.050×0.025	$1.375 < \|\eta\| < 1.425$
	0.075×0.025	$1.40 < \|\eta\| < 1.475$	0.025×0.025	$1.425 < \|\eta\| < 2.5$
			0.1×0.1	$2.5 < \|\eta\| < 3.2$
Calorimeter 3rd layer	0.050×0.025	$\|\eta\| < 1.35$	0.050×0.025	$1.5 < \|\eta\| < 2.5$
Number of readout channels				
Presampler	7808		1536 (both sides)	
Calorimeter	101760		62208 (both sides)	
LAr hadronic end-cap				
$\|\eta\|$ coverage			$1.5 < \|\eta\| < 3.2$	
Number of layers			4	
Granularity $\Delta\eta \times \Delta\phi$			0.1×0.1	$1.5 < \|\eta\| < 2.5$
			0.2×0.2	$2.5 < \|\eta\| < 3.2$
Readout channels			5632 (both sides)	
LAr forward calorimeter				
$\|\eta\|$ coverage			$3.1 < \|\eta\| < 4.9$	
Number of layers			3	
Granularity $\Delta x \times \Delta y$ (cm)			FCal1: 3.0×2.6	$3.15 < \|\eta\| < 4.30$
			FCal1: $\sim$ four times finer	$3.10 < \|\eta\| < 3.15$,
				$4.30 < \|\eta\| < 4.83$
			FCal2: 3.3×4.2	$3.24 < \|\eta\| < 4.50$
			FCal2: $\sim$ four times finer	$3.20 < \|\eta\| < 3.24$,
				$4.50 < \|\eta\| < 4.81$
			FCal3: 5.4×4.7	$3.32 < \|\eta\| < 4.60$
			FCal3: $\sim$ four times finer	$3.29 < \|\eta\| < 3.32$,
				$4.60 < \|\eta\| < 4.75$
Readout channels			3524 (both sides)	
Scintillator tile calorimeter				
	Barrel		Extended barrel	
$\|\eta\|$ coverage	$\|\eta\| < 1.0$		$0.8 < \|\eta\| < 1.7$	
Number of layers	3		3	
Granularity $\Delta\eta \times \Delta\phi$	0.1×0.1		0.1×0.1	
Last layer	0.2×0.1		0.2×0.1	
Readout channels	5760		4092 (both sides)	

Figure 3.12: Pseudo-rapidity coverage, longitudinal segmentation and granularity of the ATLAS calorimeters [54].

All ATLAS calorimeters are sampling calorimeters, i.e. the calorimeter is composed of alternate layers of absorbing and active material. The absorber is usually made of a dense material, where the shower deposits most of its energy; the active medium is instead used to collect and measure a fraction of the energy of the particles that constitute the shower and is usually made of scintillating material. The use of sampling calorimeters, in contrast to homogeneous calorimeters, which are instead made entirely of active material, yields a slightly degraded energy resolution, but can provide a higher radiation tolerance and a better containment of the showers and lower costs.

Another important feature of the ATLAS calorimeters is the fact that they are non-compensating, i.e. they have a lower response to the hadronic energy deposition compared to the electromagnetic one. This happens mainly because hadronic interaction with the calorimeter may result in invisible energy which is not detected (such as slow nuclear fragments).

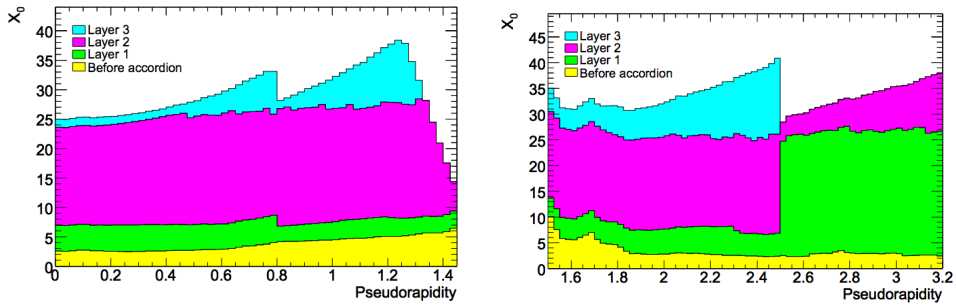

Figure 3.13: Cumulative amounts of material, in units of radiation length X_0, in front of and in the electromagnetic calorimeters, separately for the barrel (left) and for the end-caps (right) [54].

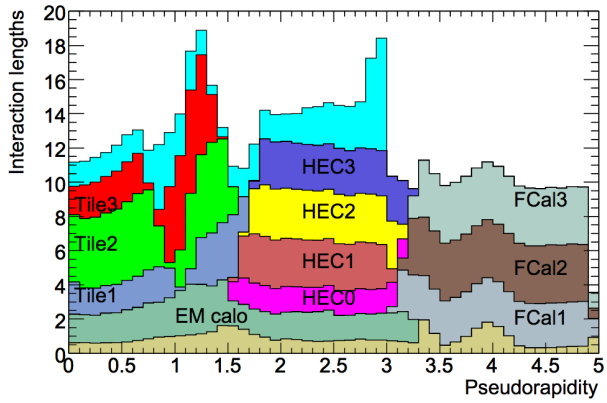

Figure 3.14: Cumulative amounts of material, in units of hadronic interaction length λ_I, in front of the electromagnetic calorimeters, in the electromagnetic calorimeters themselves, in each hadronic layer, and the total amount at the end of the active calorimetry [54].

3.6.1 Electromagnetic calorimeters

The electromagnetic calorimeters (EM) extend up to a radius of 2.25 m and are 6.65 m long. They cover the pseudo-rapidity region of $|\eta| < 3.2$, divided into a barrel part ($|\eta| < 1.475$, EMB) and two end-cap components ($1.375 < |\eta| < 3.2$, EMEC), each placed in their own cryostat.

The EM calorimeters employ lead for the absorber and Liquid Argon (LAr) for the sensitive medium. LAr has been chosen for its linear behavior, its stability of response over time and its radiation hardness. A disadvantage of the LAr technology is the relatively slow response, with a signal integration time of approximately 400 ns.

The geometry of the LAr calorimeters is such to ensure full coverage in ϕ without dead regions: the layers of electrodes and absorbers are bent with accordion shape, as shown in Figure 3.15, and bathed in LAr. The accordion folds run radially in the barrel and axially in the end-caps. The pseudo-rapidity regions where the transition between the barrel and end-caps detectors occurs, called the 'cracks', are less instrumented and typically provide worse measurements; for this reason they are often excluded for the reconstruction and identification of the electrons and photons.

In the longitudinal direction and within $|\eta| < 2.5$ the EM calorimeter is segmented into three sections: the first layer is constituted by finely segmented strips which are important for the discrimination of photons from $\pi^0 \to \gamma\gamma$ decays; the middle layer is constituted by thick towers which collect the majority of the energy of electrons and photons; the back layer is also segmented in towers and collects the tails of the shower. The segmentation in η is highest in the first layer and decreases going towards the back. Figure 3.16 illustrates the geometry of the EM calorimeter along with the segmentation of the three layers at $\eta = 0$.

The EM calorimeters are complemented by a presampler detector within $|\eta| < 1.8$; the presampler consists of a single thin LAr layer, which allows to estimate the energy lost in front of the EM calorimeters.

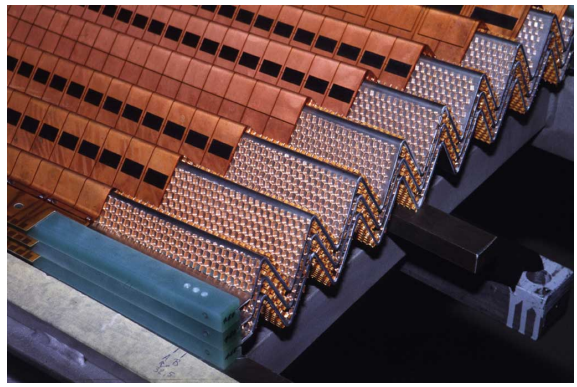

Figure 3.15: Accordion shape of a few layers of absorber and electrodes of the LAr EM calorimeter [60].

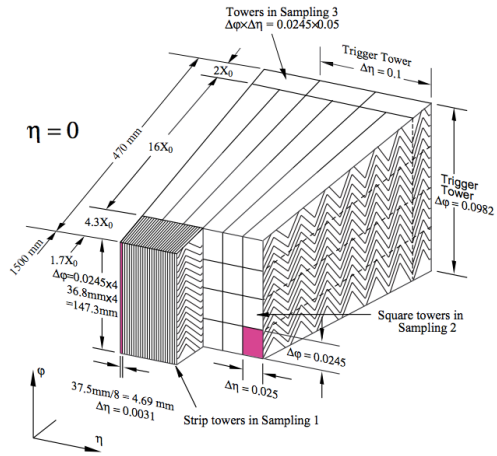

Figure 3.16: Illustration of the geometry of the EM calorimeter at $\eta = 0$ [61].

3.6.2 Hadronic calorimeters

The hadronic calorimeters in the barrel region employ a different technology than LAr, which is instead used for the hadronic calorimeters in the end-caps.

Tile Calorimeter The Tile Calorimeter is placed outside the EM calorimeter and extends radially from 2.28 m to 4.25 m. It is constituted by a 5.8 m long barrel in the region $|\eta| < 1.0$ and two extended barrels, each 2.6 m long, covering $0.8 < |\eta| < 1.7$.

It employs steel as the absorbing material, and plastic scintillator tiles as the active material. This technology for the active material provides maximal radial depth at a lower cost than LAr. Charged particles cross the tiles and scintillation photons are produced which are collected by wavelength-shifting fibres and read through photo-multipliers tubes. Figure 3.17 illustrates the geometry of a tile module. The 64 modules are arranged radially, perpendicularly to the beamline.

In the longitudinal direction, the Tile calorimeter is segmented in three layers, which are approximately 1.5, 4.1 and 1.8 λ_I thick for the barrel and 1.5, 2.6, and 3.3 λ_I for the extended barrel. The η and ϕ segmentation is coarser compared to the EMB, which is motivated by the larger extension of hadronic showers compared to electromagnetic ones.

Hadronic End-cap Calorimeter (HEC) The hadronic end-cap (HEC) calorimeter covers the region $1.5 < |\eta| < 3.2$, which slightly overlaps that of the tile calorimeter. Each end-cap calorimeter consists of two independent wheels, further segmented into two. The wheels are cylindrical, with an outer radius of 2030 mm and are built from 32 wedge-shaped modules each.

The HEC uses copper as absorber and LAr as active material. The high-radiation resistance of copper and Liquid Argon and the granularity allow for a good response to the high-particle fluxes in this η region.

3.6.3 Forward calorimeters

The Forward calorimeters (FCal) complete the calorimeter system, covering the range $3.1 < |\eta| < 4.9$, thus enabling the detection of very forward jets and an optimal coverage for the measurement of the missing transverse momentum.

This region of the detector is exposed to extremely high fluxes of particles; the ability of coping with these conditions drives the design of this component.

The FCal is located at 4.7 m from the interaction point, very close to the end-cap calorimeters, such that only a minimal amount of energy is lost between the two systems and the level of background which punches through the muon system is limited.

Is consists of three longitudinal layers: the first is an electromagnetic calorimeter, while the remaining two are hadronic calorimeters. The active medium for all of them is LAr, while the passive materials employed are different between layers: copper for the electromagnetic layer and tungsten for the other two.

In contrast with the other LAr calorimeters, the gaps between one absorber layer and the other is extremely reduced; this guarantees a fast signal, it helps avoiding problems of ion build-up and at the same time it guarantees the higher possible density for a given volume.

This combination of materials results in 27.6 X_0 of electromagnetic calorimeter material, thus ensuring that no electrons or photons escape longitudinally. Similarly, this combination provides approximately 10 λ_I of material, thus preventing all but the most energetic particles from escaping the FCal. In order to provide even more protection from escaping high-energy particles and shield the muon end-cap region, a large uninstrumented brass plug is placed behind the FCal, as illustrated in Figure 3.18.

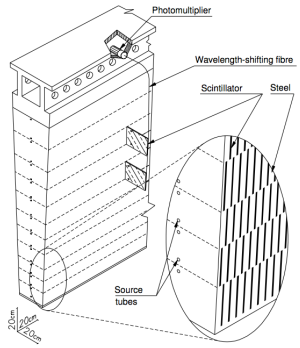

Figure 3.17: Schematic illustration of a tile module: the scintillating tiles, the fibres and the photomultipliers are indicated [61].

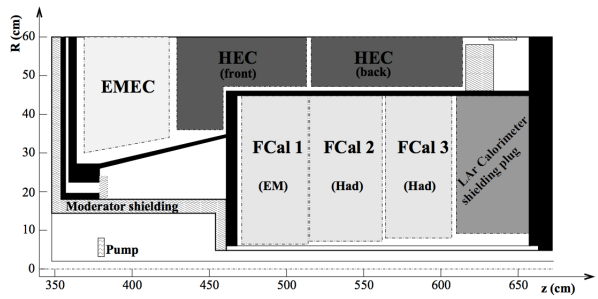

Figure 3.18: Diagram showing the placement of the three FCal modules with respect to the end-cap calorimeters. The shielding plug behind the FCal is also shown [61].

3.7 Muon Spectrometer

Muons are the only detectable particles that can cross the ID and the calorimeters without being stopped; this happens because at the LHC energies they are effectively minimum ionizing particles (MIPs) and therefore they lose only a relatively small amount of energy while crossing the detector material. Therefore they require a dedicated detector, the Muon Spectrometer (MS), which is the outermost part of ATLAS.

The bending of the muon tracks, necessary for the measurement of their momenta, relies on the magnetic field provided by the barrel toroid over the range $|\eta| < 1.4$, by the two end-cap toroids over the range $1.6 < |\eta| < 2.7$ and by a combination of the barrel and end-cap toroids in the transition region. The magnetic field is mostly orthogonal to the muon trajectories.

The measurement of the tracks relies on three layers of detectors, housed inside the toroidal magnets; these are arranged in cylinders around the beam axis at radii of approximately 5 m, 7.5 m, and 10 m in the barrel region. In the transition and end-cap regions, a total of four layers of detectors are arranged in wheels perpendicular to the beam axis, approximately located at $|z| = 7.4$ m, 10.8 m, 14 m, and 21.5 m.

The detector system is composed of high-precision tracking chambers ($|\eta| < 2.7$) complemented by a system of fast trigger chambers ($|\eta| < 2.4$); different technologies are employed in the various sets of detectors.

- **Monitored Drift Tube (MDT)** chambers provide a precise momentum measurement in the bending plane within $|\eta| < 2.7$. The basic detection element is a cylindrical aluminum drift tube, filled with a mixture of gases, and a central wire at high potential. Muon passing in the tubes produce ionization charges that are collected on the wire. These chambers consist of three to eight layers of drift tubes, providing an intrinsic resolution is 35 μm per chamber.

- **Cathode-strip chambers (CSC)** are multi-wire proportional chambers with high rate capability and time resolution, used for the muon momenta measurement in

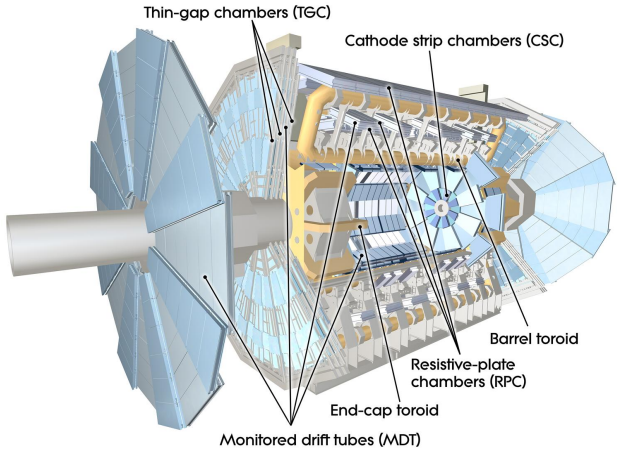

Figure 3.19: Layout of the ATLAS Muon Spectrometer, with the various sub-detectors indicated [54].

		Chamber resolution (RMS) in			Measurements/track		Number of	
Type	**Function**	z/R	ϕ	time	barrel	end-cap	chambers	channels
MDT	tracking	35 μm (z)	—	—	20	20	1088 (1150)	339k (354k)
CSC	tracking	40 μm (R)	5 mm	7 ns	—	4	32	30.7k
RPC	trigger	10 mm (z)	10 mm	1.5 ns	6	—	544 (606)	359k (373k)
TGC	trigger	2–6 mm (R)	3–7 mm	4 ns	—	9	3588	318k

Figure 3.20: Parameters of the four sub-detectors of the muon spectrometer: intrinsic resolutions, number of measurements per track, number of channels and chambers [54].

the forward region ($2 < |\eta| < 2.7$). The cathode planes of these chambers are segmented into strips in orthogonal directions, thus allowing the measurement of both coordinates: the intrinsic resolution in the bending plane is 40 μm and approximately 5 mm in the transverse plane.

- **Trigger** chambers are fast detectors which deliver signals with a spread of 15-25 ns. They include Resistive Plate Chambers (RPC) in the barrel region ($|\eta| < 1.05$), and Thin Gap Chambers (TGC) in the end-caps ($1.05 < |\eta| < 2.4$). Like the MDTs, these are gaseous detectors where the electrons produced in the muon-induced avalanche are read out by two sets of orthogonal strips on each side of the gas gap.

The intrinsic position and time resolution of the various sub-detectors of the muon spectrometer are indicated in Table 3.20, while the layout of the muon spectrometer is shown in Figure 3.19

3.8 Trigger system

3.8.1 Overview

During most of 2015 and for the whole of 2016, the LHC delivered pp collisions with a bunch crossing frequency of 40 MHz; at this level, it would be impossible to record the read-out of all the detector systems for every collision. Considering that a full ATLAS event occupies approximately 1 MB of disk space on average, this would mean recording 40 TB for every second of data taking. The sustainable level of event rate that can be processed and recorded is approximately 1 KHz.

Furthermore, we are not particularly interested in the majority of the events originating from the pp collisions, since they are dominated by soft interactions; while it is important to understand and model correctly these kind of interactions, most interesting are the collisions where a hard scattering between partons happens, resulting in an event with particles at relatively high transverse momenta. Therefore a trigger system which decides whether to keep or not an event is an essential component of any collider experiment.

Usually the criterion to discriminate an interesting event is the presence of a particle with a transverse momentum higher than a given threshold. This kind of triggers are denoted as *primary* triggers, which are optimized for physics analyses and cover all signatures relevant to the ATLAS physics program. They are usually run *unprescaled*, which means that all events firing the trigger are kept, in contrast to *prescaled* triggers, where only a given fraction of events is kept.[2]

The trigger *menu*, which denotes the set of algorithms used for the trigger decision during data taking, their prescale and thresholds, also includes *support* triggers, which are used for efficiency and performance measurements and are typically heavily prescaled, and *calibration* triggers, which are used for the detector calibration and kept at a relatively high rate while storing reduced information on the event. As the LHC conditions change, the trigger menu needs to be changed accordingly in order to meet bandwidth constraints.

3.8.2 Trigger and acquisition system

The Run 2 ATLAS trigger system [62] consists of two levels: the Level-1 trigger (L1) is hardware-based and uses a subset of the detector information to reduce the rate of accepted events to the level of 100 kHz. It is followed by the high-level trigger (HLT) which performs a fast software-based event reconstruction and reduces the rate of recorded events to 1 KHz.

The diagram of Figure 3.21 illustrates the components of the Trigger and Data acquisition system (TDAQ), with emphasis on the components relevant for triggering. The Level-1 Calorimeter trigger (L1Calo) makes use of low granularity information from the electromagnetic and hadronic calorimeters to search for electrons, photons, taus and jets,

[2] For example a trigger with a prescale of 100 means that only 1 event out of 100 is kept.

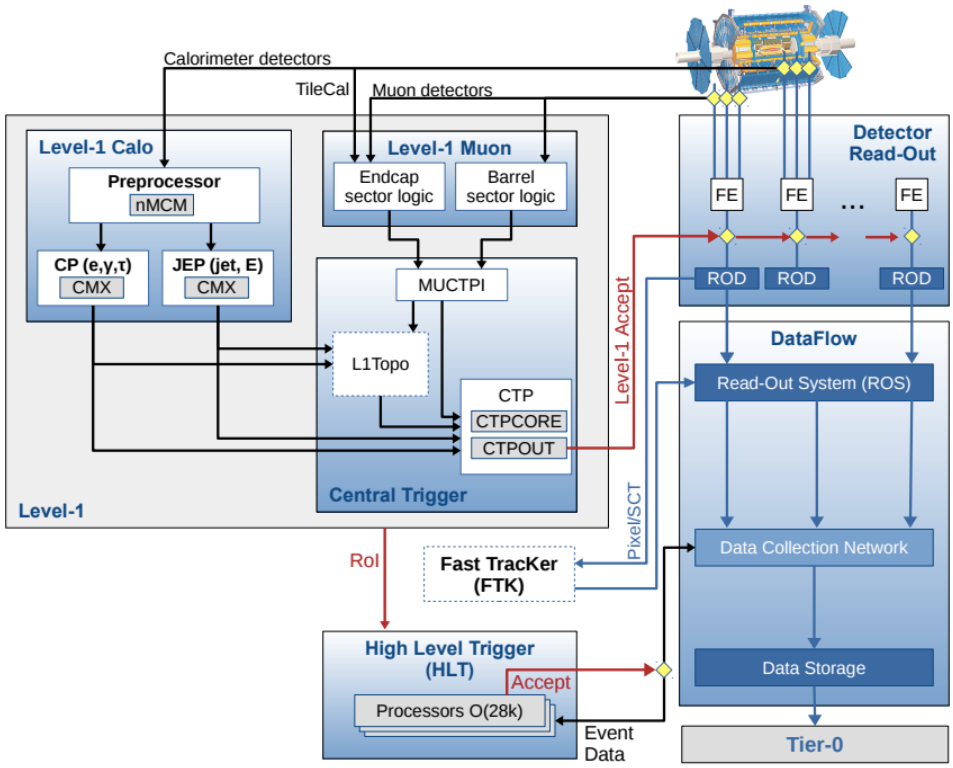

Figure 3.21: The ATLAS TDAQ system in Run 2 with emphasis on the components relevant for triggering. FTK is being commissioned and is not used for the results of this work [62].

as well as high missing transverse energy. The Level-1 Muon trigger system (L1Muon) provides fast trigger signals from the muon detectors. The Level-1 topological trigger (L1Topo) takes as input L1Calo and L1Muon objects and combines them to allow for more complex topological selections. The central trigger processor (CTP) forms the L1 decision based on the information received from the L1Topo, L1Calo and L1Muon and distributes the accept signal and LHC timing signals to the sub-detector readout systems via the Timing,Trigger and Control network (TTC). The total time needed for a L1 decision is approximately 1 μs. The data acquisition system (DAQ) receives and buffers the data from the Read-Out System (ROS) at the L1 trigger rate; the data is then processed by the HLT.

The HLT uses finer-granularity calorimeter information, precision measurements from the MS and tracking information from the ID, which are not available at L1. The HLT algorithms, which are close to those used for offline reconstruction, can be executed either within regions of interest (RoIs) identified at L1 or over the full detector information. The time needed for the HLT decision is of the order of 1 ms. After the events are accepted by the HLT, they are transferred to local storage and exported to the Tier-0 facility at CERN's computing center for offline reconstruction.

CHAPTER 4

ATLAS Event Reconstruction and Performance

When the ATLAS detector records an event from a pp collision, the information on the event is stored in terms of energy deposits in the cells of the calorimeters and hits in the trackers. Advanced reconstruction algorithms are needed to process this information and reconstruct the particles in the event. The outputs of the reconstruction algorithms are called 'physics objects' and are used by the physics analyses to select events with a given experimental signature.

The mono-photon and mono-jet analyses, which are the focus of this work, primarily employ jets, photons and missing transverse momentum, but also make use of electrons and muons. With the exception of the missing transverse momentum, which is the topic of the next chapter, the methods to reconstruct and identify these physics objects and their performance are discussed in the present chapter.

4.1 Clusters, tracks, vertices

Energy clusters are obtained by grouping calorimeters cells around a seed cell with an energy deposition above a certain threshold. Two methods are used in ATLAS to form energy clusters, as described in Ref. [63]: the *topological clustering* is used for the reconstruction of jets, while the *sliding window* algorithm is used for the reconstruction of electrons and photons.

Tracks are instead obtained by fitting sets of clustered hits ('space-points') in the various layers of the tracking detectors. A space-point represents the point where one or more charged particles traversed the detector; track seeds are formed from three space-points and initially fitted with a helix fit; then a combinatorial Kalman filter algorithm is used to build complete track candidates by incorporating additional space-points to the track seeds. A second fit is performed on the obtained track candidates and an ambiguity solving procedure is applied for the many tracks which have space-points in common.

Vertices are reconstructed with an iterative vertex finding algorithm from at least two selected tracks; the primary vertex is selected among the reconstructed vertices as the one with the largest sum of squared of transverse momenta of the tracks associated to it. More details on the reconstruction and performance of tracks and vertices can be found for example in Ref. [64].

4.2 Jets

Hadron collisions are described in terms of quarks and gluons. However, these are never observable in a physics experiment because of the properties of the strong interaction: quarks and gluons undergo fragmentation and hadronization after production and result in a spray of collimated hadrons, with their momenta aligned in the direction of the initial parton. The hadrons coming from the hadronization of a given parton form a *jet*.

4.2.1 Reconstruction

A clear definition of a jet is required both from the theoretical perspective and from the experimental side. Jets must be defined in such a way that the cross-section calculation involving final state partons is finite at all orders in perturbation theory and insensitive to hadronization; this translates into the requirement that jet definitions are infra-red and collinear safe, which means that the emission of a soft parton or a collinear emission must not change the number of reconstructed jets in the event.

Several algorithms can be defined in order to reconstruct jets; a jet algorithm starts from the products of the hadronization of hard scattering partons, groups them into clusters of adjacent particles with an iterative procedure, to finally build a jet.

The most widely used algorithm, and the one used primarily in ATLAS, is the anti-k_t [65] algorithm. In this algorithm the combination of the input particles is ruled by two distance parameters:

$$d_{ij} = min\left(\frac{1}{p_{\mathrm{T}i}^2, p_{\mathrm{T}j}^2}\right)\frac{\Delta_{ij}^2}{R^2} \tag{4.1}$$

$$d_{iB} = \frac{1}{p_{\mathrm{T}i}^2} \tag{4.2}$$

where the angular distance is defined as $\Delta_{ij}^2 = (\eta_i - \eta_j)^2 + (\phi_i - \phi_j)^2$ and the distance parameter R is the value that controls the cone size of the resulting jet. A commonly used value in ATLAS to reconstruct gluon, light quark and b-tagged jets is $R = 0.4$. [1]

The algorithm starts by identifying all possible pairs of input particles and their distance values. If $d_{ij} < d_{iB}$, the objects i and j are combined and removed the from the inputs, while the combined object is added as a new input. If instead $d_{ij} > d_{iB}$, then the object i is selected as a jet and removed from the collection of inputs. At each step the distances d_{ij} and d_{iB} are recomputed and the procedure repeated until no further combination is possible.

Truth jets are jets reconstructed in Monte Carlo (MC) simulated events with such an algorithm, starting from the stable particles obtained from the showering and subsequent hardonization of the hard scattering partons. Truth jets are therefore defined as being measured at the particle-level energy scale.

[1] Values $R = 1.0$ or $R = 1.2$ can be used to reconstruct larger jets, such as those arising from the decay of boosted top quarks or W, Z, or Higgs bosons. The mono-jet and mono-photon analyses only employ small jets with $R = 0.4$ and the present discussion is limited to this type of jets.

Final-state particles interact with the detector material and leave energy deposits in the calorimeters, which are then used as inputs of the jet algorithm for the reconstruction a jet at detector level. It is of primary importance that these inputs reflect the energy of the hadrons at the particle-level, while removing effects coming from the detector noise and pile-up interactions. With this aim, the ATLAS jet reconstruction uses the *topoclustering* algorithm [63]. The idea behind topoclustering is to group neighboring cells that have significant energies compared to the expected noise. Topological clusters are seeded by cells with large signal to noise ratio ($> t_{seed}$), grow by iteratively adding neighboring cells (with signal to noise ratio $> t_{neighbor}$), and finish by including all direct neighbor cells on the outer perimeter (with signal to noise ratio $> t_{cell}$). The values of the thresholds are optimized to find low energy clusters efficiently without being overwhelmed by noise.

After topoclusters are constructed, the energies of the constituent cells are summed to get the total energy of the topocluster; the mass is set to zero, and the direction to match that of the energy-weighted barycenter. The energy of topoclusters is then calibrated at the electromagnetic scale, which correctly reflects the energy of electromagnetic showers, but does not work well for hadronic showers, given the different response of the ATLAS calorimeters to electromagnetic and hadronic energy deposition. In order to account for these differences and provide the correct energy for the resulting jets, a calibration correction is derived, as explained in the following.

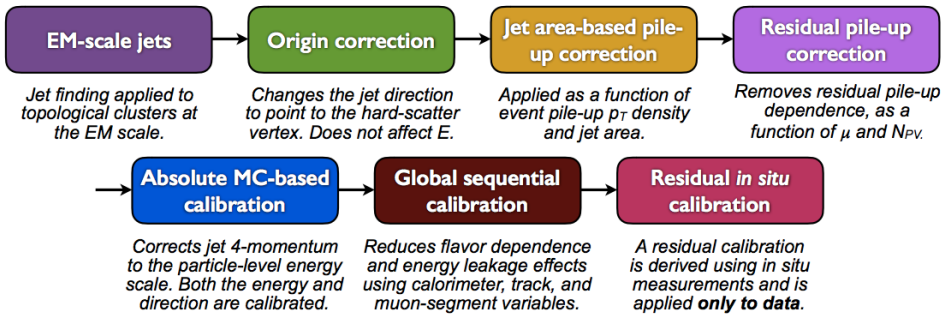

Figure 4.1: The steps of the sequential procedure to calibrate the energy of the jets in ATLAS [66].

4.2.2 Calibration

The procedure to calibrate the energy of the reconstructed jets [66] is articulated in various steps, as illustrated in the diagram of Figure 4.1. This calibration restores the jet energy scale to that of truth jets reconstructed at the particle-level.

Origin correction A correction to the jet direction is applied such that the jet points back to the primary vertex instead of the nominal center of the detector, leading to an improved η resolution.

Pile-up suppression The energy of the jets is corrected to subtract the energy contribution coming from pile-up interactions. First an area-based method subtracts the per-event pile-up contribution to the p_{T} of each jet according to its area. The pile-up contribution is calculated from the median p_{T} density ρ of jets in the $\eta-\phi$ plane; the calculation of ρ uses positive-energy topoclusters limited to $|\eta| < 2$, due to the higher calorimeter occupancy in the forward region. The p_{T} density of each jet is taken to be p_{T}/A, where the area A of a jet is calculated using ghost association [66].

A second pile-up correction is applied to account for residual dependencies of the p_{T} on N_{PV} and μ. These are parametrized by separate coefficients, α and β, derived from linear fits in bins of $p_{\mathrm{T}}^{\mathrm{true}}$ and η on MC samples.

The full correction reads:

$$p_T^{jet,corr} = p_T^{reco} - \rho A - \alpha \times (N_{PV} - 1) - \beta \times \mu. \tag{4.3}$$

Jet energy scale and η calibration The absolute jet energy scale (JES) corrects the reconstructed jet energy to the particle-level energy scale. It is a MC-based correction and is derived starting from the response $\mathcal{R}$ defined as the mean of the Gaussian fit to the core of the E^{reco}/E^{truth} distribution, binned in E^{truth} and η_{det}, the jet η pointing from the geometric center of the detector, in order to remove the ambiguity as to which region of the detector is measuring the jet. The response function is shown in Figure 4.2, where the barrel-endcap and endcap-forward transitions are characterized by a lower energy response due to undetected or absorbed particles in the uninstrumented materials. A numerical inversion is performed to derive the calibration factor which is then applied to correct the E^{reco} of jets, as detailed in Ref. [67].

A second correction is derived as the difference between the reconstructed jet η^{reco} and the truth η^{truth} to account for residual biases in jet η^{reco} and parametrized as functions of E^{truth} and η_{det}. Again a numerical inversion is used to derive the correction factor in E^{reco}.

Jets calibrated with the full jet energy scale and the η calibration are considered to be at the EM+JES scale.

Global sequential calibration Additional corrections are derived to improve the resolution of the JES against fluctuations in the jet particle composition and in the distribution of energy within the jet. Five observables are identified and as many independent corrections are derived and applied sequentially.

In-situ calibration The last steps of the calibration correct the jet energy scale for the discrepancies between reconstructed jets in data and in simulation, which arise from an imperfect description in the MC simulation of the detector and of other effects, such as the underlying event, pile-up and jet formation. Differences between data and MC are quantified by balancing the p_{T} of a jet against other well-measured reference objects.

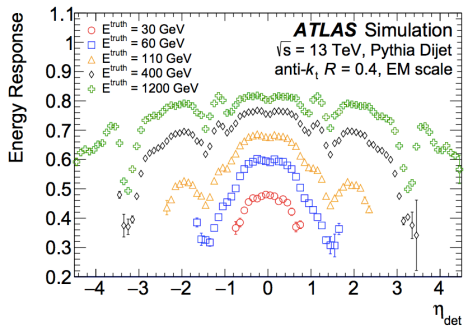

Figure 4.2: The average response of simulated jets as function of the jet η_{det}, shown for several values of E^{truth} [66].

The η-intercalibration corrects the average response of forward jets to that of well-measured central jets using dijet events. Three other *in-situ* calibrations are derived to correct the response of the central jets, each focusing on a different p_{T} region: the first two methods employ $Z(\ell\ell)+$jets and $\gamma+$jets events, respectively, where the leptons and the photon provide well measured reference objects. The $Z(\ell\ell)+$jets calibrations extend in the range $20 < p_{\mathrm{T}}^{Z} < 500$ GeV, while $\gamma+$jets calibrations extend between $36 < p_{\mathrm{T}}^{\gamma} < 950$ GeV. Jets up to 2 TeV are calibrated using the multijet balance technique, where three or more jets are used to balance a high-p_{T} jet. These recoil jets are of sufficiently low p_{T} as to be in the range of Z/γ+jets calibrations.

For each *in-situ* calibration, the response $\mathcal{R}_{insitu}$ is defined in data and MC simulation as the average ratio between the jet p_{T} and the reference object p_{T}, in bins of the reference object p_{T}. The ratio $\mathcal{R}_{insitu}^{\mathrm{data}}/\mathcal{R}_{insitu}^{\mathrm{MC}}$ is inverted to derive the four-momentum correction.

The data-to-MC ratios obtained with the several methods are combined across overlapping regions of jet p_{T}, with the combination favoring the method with greater precision. The combined ratio is shown in Figure 4.3, together with the results obtained from the individual methods.

The *in situ* techniques and the MC-based calibration usually rely on assumptions that are only approximately fulfilled. For every technique, several sources of systematic uncertainties are taken into account and propagated to the calibration factors. These are uncertainties arising from potential mismodelings of physics effects, uncertainties in the measurement of the kinematics of the reference objects, or in the modeling of the p_{T} balance due to the selected event topology. They are captured by using different MC generators, by varying the calibrations and reconstruction efficiency of the physics objects, and by varying the event selections.

The combination of all uncertainties is shown in Figure 4.4 as a function of p_{T} at $\eta = 0$ and as a function of η at $p_{\mathrm{T}} = 80$ GeV. The uncertainty is largest at low p_{T}, starting at

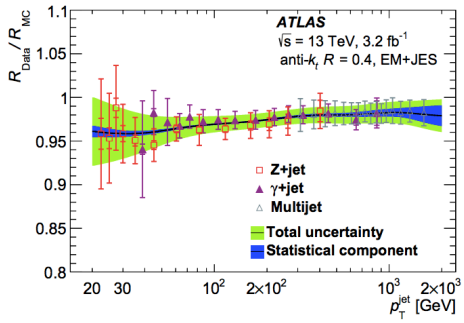

Figure 4.3: Ratio of the jet response in data to that in the MC simulation as a function of the jet p_{T} for $Z(\ell\ell)$ + jets, γ + jets and multijet *in-situ* calibrations. The final derived correction (black line) and its statistical (dark blue) and total (light green) uncertainty bands are also shown [66].

4.5% and decreasing to 1% at 200 GeV; it then rises due to the statistical uncertainties of the *in situ* calibrations.

The full description of the uncertainty on the jet calibration includes 80 nuisance parameters, which are treated as uncorrelated to one another and fully correlated across η and p_{T}; reduced sets of 5 nuisance parameters each are made available, that seek to preserve the possible correlations, while radically reducing the number of independent parameters.

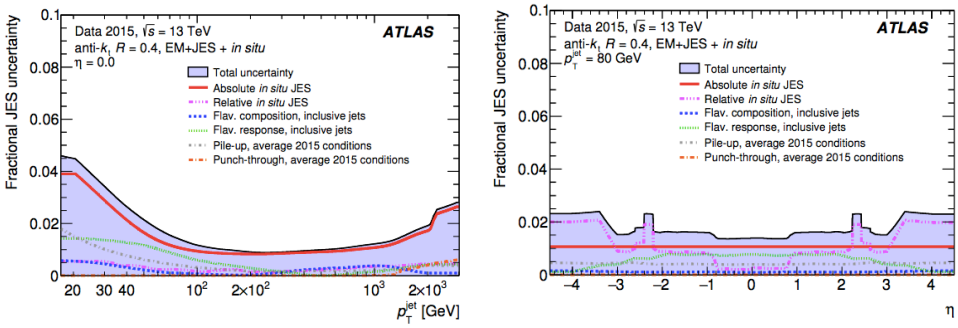

Figure 4.4: Fractional systematic uncertainty on the combined jet energy scale of fully calibrated jets. The various uncertainty components and the combined uncertainty are shown as a function of p_{T} (left) and η (right) of the jet [66].

4.2.3 Jet selection

Pile-up rejection

The LHC environment calls for reconstruction techniques that are able to reject the contribution from pile-up events. As discussed in the previous section, the jet calibration

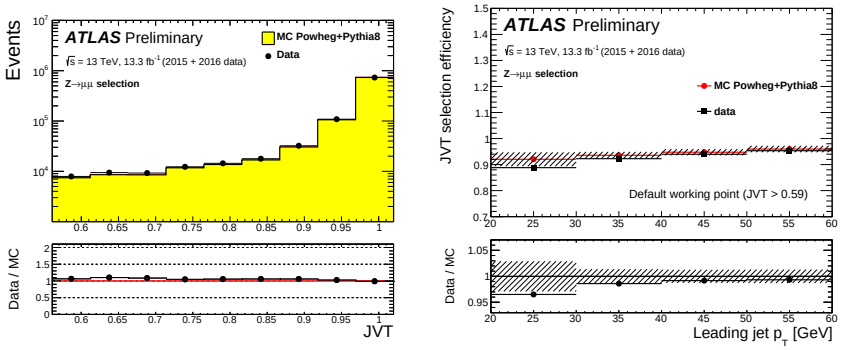

Figure 4.5: Distribution of the Jet Vertex Tagger (left) and the hard scatter jet selection efficiency of the *medium* JVT working point (right) shown for jets balanced against Z bosons decaying to muons [70].

procedure already includes an on-average subtraction of the energy contribution from pile-up; however, pile-up activity may result in spurious reconstructed jets. In Run 2, a new tagger has been introduced to discriminate hard scatter from pile-up jets, primarily based on the fraction of the jet energy as coming from the hard scatter of the interaction. The tagger is denoted as JVT (Jet Vertex Tagger) [68, 69] and is based on the combination of two variables. The first one is the 'corrJVF', which is essentially the fraction of the scalar sum of the p_{T} of the tracks of a jet which are associated to the primary vertex ($\sum_k {p_{\mathrm{T}}}^{trk_k}(\mathrm{PV}_0)$) with respect to the scalar sum of all jet tracks ($\sum_{n\geq 1}\sum_l {p_{\mathrm{T}}}^{trk_l}(\mathrm{PV}_{\mathrm{n}})$). The prefix 'corr' denotes the correction introduced to account for the linear increase of the scalar sum of the jet tracks from pile-up on the number of primary vertices. The second variable is called $R_{p_{\mathrm{T}}}$ and is defined as the scalar sum of the p_{T} of the tracks that are associated with the jet and originate from the hard scatter vertex divided by the fully calibrated jet p_{T}, which includes pile-up subtraction. Pile-up jets are expected to have low values of both variables, while hard scatter jets are expected to have larger values: corrJVT~ 1 and $R_{p_{\mathrm{T}}}$ in the range $0.4 - 0.8$.

The JVT is built by combining the two variables in a 2-dimensional likelihood. Its distribution is shown in Figure 4.5 (left) for $Z(\mu\mu)+$jets events in data and MC simulation.

Three working points have been defined for the Run 2 data-taking conditions and applied to jets with $20 < p_{\mathrm{T}} < 60$ GeV and $|\eta| < 2.4$: *loose*, *medium*, *tight*, which target samples signal efficiencies of 95%, 90% and 80%, for pileup fake rates of 3%, 1.0% and 0.4%, respectively.

The measured efficiency as a function of p_{T} for the default working point (*medium*) is reported in Figure 4.5(right) for a $Z(\mu\mu)+$jets selection in data and MC simulation.

Jet cleaning

Jets at high p_{T} from the hard scatter vertex must be distinguished from jets not coming from the pp collision: the latter include fake jets originated by beam induced back-

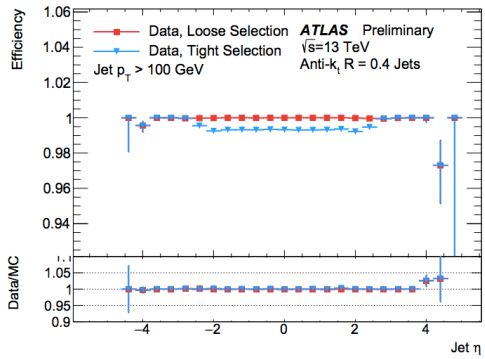

Figure 4.6: Jet quality selection efficiency as a function of η for $p_{\mathrm{T}} > 100$ GeV for the *loose* and *tight* selection criteria. Only statistical uncertainties are shown. The lower portion of the figure shows ratios of efficiencies measured in data and Monte Carlo simulation [72].

grounds, consisting in muons emitted by the beam halo, that traverse the detector and leave energy in the calorimeters. Cosmic ray showers, predominantly muons, can also reach ATLAS and lead to fake jets. These two sources of fake jets are denoted as non-collision background (NCB).

Phenomena of coherent noise or isolated pathological cells in the calorimeters can degrade the reconstruction. This last source of background is substantially removed prior to reconstruction by the data quality inspection [71], but a small fraction of the noise remains undetected.

In order to suppress the fake jets coming from all these backgrounds, a cleaning strategy is set, as described in [72]. It consists in selecting only jets which satisfy several quality criteria. These criteria involve variables that quantify the quality of the signal pulse shape of the LAr calorimeters or measure the fraction of energy deposited in the electromagnetic calorimeters or in the HEC to the total energy of the jet, or the fraction between the scalar sum of the jet tracks coming from the primary vertex to the total jet p_{T}.

Two working points are designed to provide different levels of efficiency in selecting jets from the pp collision (good jets) and rejecting fake jets. The *loose* working point guarantees a selection efficiency for good jets close to 100% in the full η spectrum as shown in Figure 4.6. The *tight* working point is designed to further reject fake jets for analyses sensitive to non-collision backgrounds, such as the mono-jet analysis, while keeping the good jets selection efficiency above 95%.

Candidate jets not satisfying the *loose* (*tight*) criteria are called $BadLoose$ ($BadTight$).

4.2.4 b-tagging

B-jets are jets containing a b-hadron. The presence of displaced vertices and the typically larger shower profiles enable the discrimination of b-jets compared to jets initiated by light quarks or gluons (b-tagging).

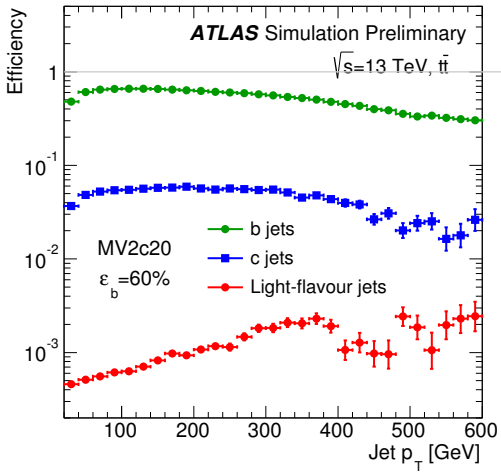

Figure 4.7: The efficiency to tag b, c and light-flavour jets for the `MV2c20` tagger with the 60% operating point. Efficiencies are shown as a function of the jet p_{T} in MC simulations [73].

The b-tagging discriminant uses variables related to the impact parameters of the tracks from the b-hadron decay products, and variables related to the displaced vertices. The most discriminating among these observables are combined using a boosted decision tree (BDT). The `MV2c20` [73] algorithm is defined as the output of such a BDT, where the training is performed assigning b-jets as signal and a mixture of 80% light-flavor jets and 20% c-jets as background. Several working points are defined to target given levels of b-jet selection efficiency.

The efficiency of the 60% working point in selecting b-jets is shown in Figure 4.7 as a function of the jet p_{T}, and compared to the probability of mistakenly tagging a jet containing a c hadron (but not a b hadron) or a light-flavor parton (u-, d-, s-quark or gluon g) jet as a b jet. The `MV2c10` discriminant, introduced in 2016 [74], provides a similar performance in terms of b-jet selection efficiency and slightly improved performance in terms of light-jets rejection.

The b-tagging efficiency and mistag rate are then compared between data and MC simulation and the data-to-simulation ratios are applied as scale factors in simulated events with selected or vetoed b-jets.

4.3 Photons and Electrons

4.3.1 Reconstruction and calibration

Electrons and photons hitting the calorimeters give origin to electromagnetic showers which are essentially undistinguishable. Therefore the electron-photon discrimination comes from the combination of the calorimetric and track information.

The reconstruction of electrons and photons in the region $|\eta| < 2.47$ starts from the

energy deposits in the EM calorimeters. Cells are grouped together in clusters with the *sliding window* algorithm [63]: the energy of the cells is summed within a fixed-size rectangular window in η and ϕ, and the position of the window is adjusted such to contain a local maximal energy deposit.

After clusters are formed, the tracks information is used to classify the clusters as coming from electrons or photons:

- an **electron** is formed by matching a cluster with a well-reconstructed ID track originating from the primary vertex;
- a **converted photon** is reconstructed when a cluster is matched to two tracks which are consistent as originating from a photon conversion or when the cluster is matched to a single track with no hits in the b-layer;
- an **unconverted photon** is reconstructed if a cluster is found without matching tracks.

The cluster energy of electrons and photons is then calibrated using both MC-based and data-driven corrections to improve the energy scale and resolution. The calibration procedure is articulated in several steps, explained in detail in Refs. [75, 76], and are here briefly described.

Detector non-uniformity corrections: data-driven corrections are applied to the data to mitigate effects of non-uniformity of the response of the longitudinal layers of the ECAL between data and simulation and effects due to the non-nominal high-voltage regions.

Layer intercalibration: the scales of the different longitudinal layers of the EM calorimeter are equalized in data with respect to simulation, in order to ensure the correct extrapolation of the response in the various p_{T} ranges used by analyses.

MVA calibration: the electromagnetic cluster energy is calibrated to the original electron and photon energy in simulated MC samples using multivariate techniques. The optimization is performed separately for electrons, converted and unconverted photons.

In-situ corrections: the residual disagreement in the energy scale and resolution between data and simulation are examined and corrected using $Z \to ee$ events. The applicability of these corrections to photons is checked using photons from radiative Z decays and the residual miscalibrations are corrected.

Most of the sources of systematic uncertainty come from the in-situ calibration procedure and include uncertainties on the event selections, calibration procedure and description of the material; given that most uncertainties are taken from the Run 1 measurements, additional uncertainties accounting for the different beam configuration, detector description and statistics of the samples are considered.

Since the full uncertainty model includes more than 70 systematic variations for the energy scale, for analyses not particularly sensitive to the energy scale, a simplified model has been provided, considering all effects as correlated across η bins and summing all effects in quadrature; a similar simplification is provided for the uncertainties on the resolution.

The level of precision achieved in the description of the electromagnetic energy scale and resolution is exemplified in Figure 4.8, which shows the invariant mass distribution from $Z \to ee$ events in data compared to simulation after the application of the full calibration, indicating a precision at the level of few $0.1 - 0.3\%$ on the determination of the energy scale and at the level of $0.2 - 0.5\%$ for the constant term of the energy resolution.

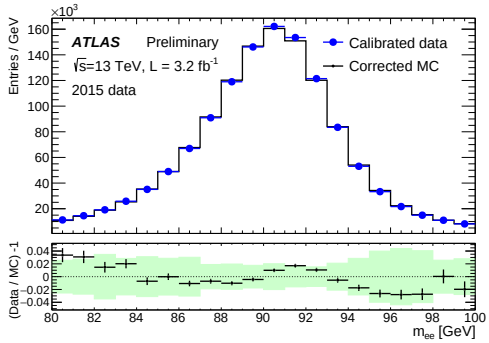

Figure 4.8: Electron pair invariant mass distribution from $Z \to ee$ events in data compared to simulation after the application of the full calibration for the 2015 dataset. The distributions for the data are shown without applying any background subtraction. The simulation is normalized to data. The bottom panels show the residuals for the data/MC ratios together with the total uncertainty (shaded green band) [76].

4.3.2 Photon identification and isolation

Prompt photons are defined as photons not originating from hadron decays and come by several physics processes. The sample of reconstructed prompt photons is affected by a large reducible background, originated by hadronic jets. It is therefore important to define selection criteria to discriminate prompt photons from the hadronic background. The discrimination is provided by quantities that describe the shape and the properties of the associated electromagnetic showers (*identification*) and how isolated a candidate photon is from other particles in the event (*isolation*).

Identification

Photon identification is achieved by imposing requirements on discriminating variables that describe the energy fraction released in the HCAL and the shape of the shower in the ECAL in the various layers. Two levels of identification are employed: the *loose* identification exploits the shower shapes in the second layer of the ECAL and the energy fraction in the HCAL and provides a highly efficient selection; the *tight* identification

Category	Name	Description	Loose	Tight
Hadronic Leakage	R_{had_1}	Ratio of E_{T} in the first sampling of the hadronic calorimeter to E_{T} of the EM cluster (used over the range $\lvert\eta\rvert < 0.8$ or $\lvert\eta\rvert > 1.37$)	✓	✓
	R_{had}	Ratio of E_{T} in all the hadronic calorimeter to E_{T} of the EM cluster (used over the range $0.8 < \lvert\eta\rvert < 1.37$)	✓	✓
EM Middle Layer	R_{η}	Ratio in η of cell energies in 3×7 over 7×7	✓	✓
	w_{η_2}	Later width of the shower	✓	✓
	R_{ϕ}	Ratio in ϕ of cell energies in 3×7 over 7×7		✓
EM Strip Layer	w_{s_3}	Shower width for three strips around the strip with maximum energy deposit		✓
	$w_{s_{\mathrm{tot}}}$	Total lateral shower width		✓
	F_{side}	Energy outside the core of the three central strips but within seven strips divided by energy within the three central strips		✓
	ΔE	Difference between the energy associated with the second maximum in the strip layer and the energy reconstructed in the strip with the minimal value found between the first and second maxima		✓
	E_{ratio}	Ratio of the energy difference associated with the largest and second largest energy deposits over the sum of these energies		✓

Table 4.1: Variables used for *loose* and *tight* photon identification [77].

exploits the information from all layers of the ECAL, including the strips, which provide discrimination from photons originating from pion decays, and applies tighter requirements that the *loose* menu. The description of the discriminating variables are reported in Table 4.1.

Several data-driven techniques are used to measure the photon identification efficiency in data, covering different transverse energy (E_T) regimes, as described in Ref. [78]. The efficiencies are measured separately for converted and unconverted photons and in several η regions. In the energy regime relevant for the mono-photon analysis ($E_T \geq 100$ GeV), the typical identification efficiency for *tight* unconverted (converted) photons is 94% (96%), as shown in Figure 4.9 in the region $|\eta| < 0.6$.

The measured efficiencies in data are compared to those computed in MC simulations: the data-to-simulation ratios (scale factors), which are generally close to unity, are applied to correct the MC for the residual differences. The typical uncertainty on the measured efficiencies range from 1 to 5%.

Isolation

The isolation is a measure of the amount of hadronic activity surrounding the photon candidate; prompt photons are more isolated than photons from hadronic decays. Photon isolation can be characterized by E_T^{iso}, defined as the sum of the transverse energies of the topoclusters around the direction of the photon candidate, after subtracting the energy deposited by the photon candidate and the contribution from the underlying event and the pile-up interactions. In practice, the isolation energy is computed as follows:

$$E_T^{iso} = E_T^{iso,raw} - E_T^{core} - E_T^{leak} - E_T^{PU}, \tag{4.4}$$

where $E_T^{iso,raw}$ represents the transverse energy of the topoclusters which barycenter falls within a cone of angular size $\Delta R = 0.4$ centered around the photon direction, $E_T^{iso,core}$ is the transverse energy contribution of the photon candidate (core) as measured in a window of fixed size in $\Delta\eta \times \Delta\phi$. The imperfect subtraction of the core leads to a remaining photon energy leaking in the isolated cone (E_T^{leak}), which is estimated from single particle MC simulations with no pile-up. The pile-up and underlying event contribution, E_T^{PU}, is estimated event by event, using an energy density technique [79].

The isolation working point used for the mono-photon analysis is

$$E_T^{iso} < 0.022\, E_T + 2.45\,\text{GeV} \tag{4.5}$$

where the E_T-dependent cut provides an efficiency above 90% in the E_T range relevant for the analysis with uncertainties at the level of $1 - 2\%$.

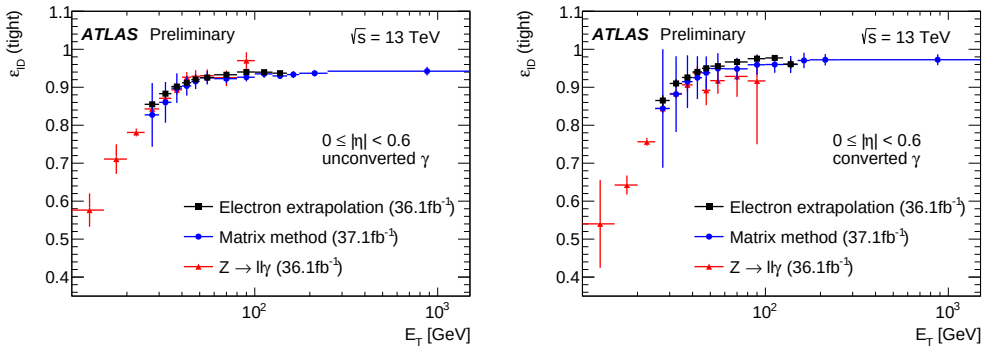

Figure 4.9: Measurements of the identification efficiency for unconverted photons (left) and converted photons (right) as a function of E_T for $|\eta| < 0.6$. The uncertainty bars represent the sum in quadrature of the statistical and systematic uncertainties estimated in each method [80].

4.3.3 Electron identification and isolation

Identification

Identification algorithms are applied to discriminate between signal-like electrons and background-like electrons, such as hadronic jets or converted photons. The identification algorithms employ variables related to the calorimeter shower shapes and several track variables, including track-cluster matching related quantities, track properties and variables measuring bremsstrahlung effects.

The baseline identification algorithm is a likelihood-based method, which simultaneously evaluates several properties of the electron candidates to discriminate between signal-like or background-like with a multivariate analysis. Three levels of identification are provided with increasing background rejections: *loose*, *medium*, *tight*, each optimized in several bins in $|\eta|$ and E_T. Depending on the working point, the signal (background) efficiencies for electron candidates with $E_T = 25$ GeV are in the range from 78 to 92% (0.3 to 0.8%) and increase (decrease) with E_T, as illustrated in Figure 4.10 for the simulation.

The efficiencies in MC simulations are compared to those measured in data with tag-and-probe methods exploiting $Z \to ee$ and $J/\psi \to ee$ decays and the derived data-to-MC ratios as a function of E_T and η are applied as scale factors at analysis level.

Isolation

Electron isolation quantifies the energy of the particles produced around the electron candidate and allows to discriminate prompt electrons from other, non-isolated electron candidates such as electrons originating from photon conversions, electrons from heavy flavor hadron decays and light hadrons misidentified as electrons. Isolation is quantified by two variables: a calorimetric isolation, defined similarly as for photons, but with a smaller cone radius, and a track isolation, defined as the sum of the transverse momenta of all tracks, satisfying quality requirements and originating from the primary vertex,

within a cone around the electron candidate, excluding the electron associated tracks.

Several working points are defined: some of them target a given level of efficiency and use E_T-dependent thresholds, others require fixed thresholds. The working points available for the Run 2 analyses are summarized in Table 4.11.

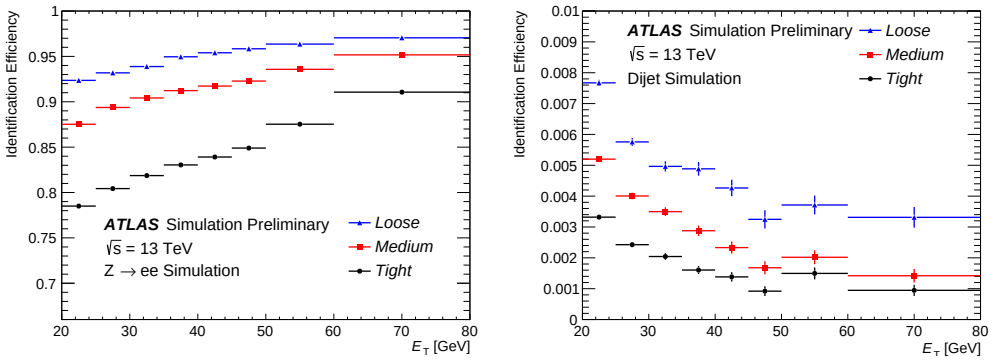

Figure 4.10: Electron identification efficiency for simulated $Z \rightarrow ee$ decays (left) and background rejection for dijet simulated events (right). The efficiencies are measured with respect to reconstructed electrons [81].

	Efficiency		
Operating point	calorimeter isolation	track isolation	total efficiency
LooseTrackOnly	-	99%	99%
Loose	99%	99%	~ 98%
Tight	96%	99%	~ 95%
Gradient	$0.1143\% \times E_T + 92.14\%$	$0.1143\% \times E_T + 92.14\%$	90/99% at 25/60 GeV
GradientLoose	$0.057\% \times E_T + 95.57\%$	$0.057\% \times E_T + 95.57\%$	95/99% at 25/60 GeV

	Cut value	
Operating point	calorimeter isolation	track isolation
FixedCutLoose	0.20	0.15
FixedCutTightTrackOnly	-	0.06
FixedCutTight	0.06	0.06

Figure 4.11: Electron isolation working point definitions: efficiency targeted working points (top) and fixed threshold working points (bottom) [81].

4.4 Muons

Muon reconstruction is performed first independently in the ID and in the MS; the information from the two sub-detectors is then combined to form candidate muons. Several algorithms are used to perform the combination, providing muon candidates in the region $|\eta| < 2.7$ [82].

A calibration of the muon momentum scale is then applied to muon candidates in MC

simulation, to account for differences in the muon momentum scale and resolution between data and simulation. The calibration procedure is described in detail in Ref. [82].

Muon identification is performed by applying quality requirements that select prompt muons (mainly coming from W, Z and Higgs decays) and suppress background muons, coming from in-flight hadron decays. Four working points are provided to address the specific needs of analyses, where the *medium* criteria provide the default selection. The combined reconstruction and identification efficiencies for *medium* muons, as measured using $Z \to \mu\mu$ and $J/\psi \to \mu\mu$ decays, are shown in Figure 4.12 as a function of p_{T} and compared between data and MC simulation.

Similarly to prompt photons and electrons, prompt muons can be further discriminated against muons originating from hadron decays by exploiting the isolation information. Combinations of track-based and calorimeter-based variables that quantify the detector activity around the muon candidate are used to define several working points, including a *loose* working point (used in the mono-photon analysis), which guarantees an isolation efficiency of approximately 99% across η and p_{T}.

4.4.1 Track parameters

Tracks associated to muon and electron candidates are usually required to satisfy criteria of compatibility with the primary vertex of the collision.

For muons (electrons) the recommended requirements for Run 2 analyses are:

$$|d_0/\sigma_{d_0}| < 3\,(5)\,, \quad |\Delta z_0 \sin\theta| < 0.5\,\mathrm{mm}\,, \tag{4.6}$$

where the transverse impact parameter d_0 is the distance of closest approach of the track to the measured beam-line, the longitudinal impact parameter z_0 is the distance along the beam-line between the point where d_0 is measured and the position of the beam-spot, and θ is the polar angle of the track. σ_{d_0} represents the estimated uncertainty on d_0, while Δz_0 is the difference between the track and primary vertex values of z_0.

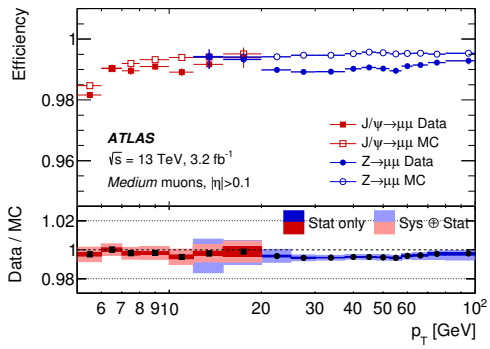

Figure 4.12: Reconstruction efficiency for *medium* muons as a function of the muon p_{T}, in the region $0.1 < |\eta| < 2.5$, as obtained with $Z \to \mu\mu$ and $J/\psi \to \mu\mu$ events. The error bars on the efficiencies indicate the statistical uncertainty. The panel at the bottom shows the ratio of the measured to predicted efficiencies, with statistical and systematic uncertainties. [82].

CHAPTER 5

$E_{\mathrm{T}}^{\mathrm{miss}}$ Reconstruction and Performance

From the Run 1 to the Run 2 of the LHC, the higher energy and the increased luminosity required an effort from the ATLAS collaboration to estimate the performance of the detector under the new conditions.

This chapter deals with the reconstruction and performance of the missing transverse momentum, $E_{\mathrm{T}}^{\mathrm{miss}}$, in Run 2. The discussion is focused on the assessment of the $E_{\mathrm{T}}^{\mathrm{miss}}$ performance in MC simulation and in early collision data, to which the author contributed primarily. This work has been made public in Refs. [1, 2] and has constituted the basis for recommending the Track Soft Term $E_{\mathrm{T}}^{\mathrm{miss}}$ (TST $E_{\mathrm{T}}^{\mathrm{miss}}$) for usage in ATLAS physics analyses.

After an introduction to the concept of missing transverse momentum (Section 5.1), $E_{\mathrm{T}}^{\mathrm{miss}}$ reconstruction is described in Section 5.2. Sections 5.4 and 5.5 deal with the expected $E_{\mathrm{T}}^{\mathrm{miss}}$ performance and performance in early 2015 data, respectively. Selected performance results obtained with the data collected during 2016 are shown in Section 5.6. The systematic uncertainties related to the $E_{\mathrm{T}}^{\mathrm{miss}}$ reconstruction are discussed in Section 5.7.

5.1 $E_{\mathrm{T}}^{\mathrm{miss}}$ definition

In a pp collision, the incoming protons behave as beams of quarks and gluons, with a given distribution in longitudinal momenta but transverse momenta close to zero. Therefore conservation of momentum implies that the vector of the transverse momenta of the collision products should sum to zero. An imbalance in the visible transverse momenta may be indicative of neutral, weakly interacting, stable particles in the final state. Within the SM, these particles are the neutrinos, but many BSM scenarios predict the existence of such particles.

The magnitude of the reconstructed missing transverse momentum is thus an important observable in SM and BSM measurements, serving as experimental proxy for the transverse momentum carried by undetected particles produced in pp collisions.

The reconstruction of $E_{\mathrm{T}}^{\mathrm{miss}}$ is challenging because it involves all detector subsystems and requires an unambiguous representation of the hard interaction of interest. This is made particularly difficult by the presence of signals from pile-up interactions. $E_{\mathrm{T}}^{\mathrm{miss}}$

can also result from particles escaping the acceptance of the detector, particles that are badly reconstructed or fail to be reconstructed altogether. The $E_{\mathrm{T}}^{\mathrm{miss}}$ originating from these effects is called 'fake $E_{\mathrm{T}}^{\mathrm{miss}}$' and can serve as an important measure of the overall event reconstruction performance.

5.2 $E_{\mathrm{T}}^{\mathrm{miss}}$ reconstruction

Reconstructing the $E_{\mathrm{T}}^{\mathrm{miss}}$ means defining an algorithm that sums the transverse momenta of all signals related to a given hard-scattering event. Two contributions are usually identified in the $E_{\mathrm{T}}^{\mathrm{miss}}$ reconstruction algorithms. The first one is from the hard-event signals from fully reconstructed and calibrated physics particles and jets (hard objects). The reconstructed particles are electrons, photons, tau-jets, and muons. The second contribution is from the soft-event signals, and can be reconstructed from charged tracks or calorimeter clusters coming from the hard-scatter vertex but not included in the reconstruction of the hard objects.

$$E_{x(y)}^{\mathrm{miss}} = -\sum_{i\in\{\mathrm{hard\,objects}\}} p_{x(y),i} - \sum_{j\in\{\mathrm{soft\,signals}\}} p_{x(y),i} \tag{5.1}$$

The outputs of the $E_{\mathrm{T}}^{\mathrm{miss}}$ reconstruction are primarily the components $E_{x(y)}^{\mathrm{miss}}$, from which the other related observables are defined: the vector $\mathbf{E}_{\mathrm{T}}^{\mathrm{miss}}$, its magnitude, $E_{\mathrm{T}}^{\mathrm{miss}}$, and the azimuthal angle ϕ^{miss}.

$$\mathbf{E}_{\mathrm{T}}^{\mathrm{miss}} = (E_x^{\mathrm{miss}}, E_y^{\mathrm{miss}}) \tag{5.2}$$

$$E_{\mathrm{T}}^{\mathrm{miss}} = |\mathbf{E}_{\mathrm{T}}^{\mathrm{miss}}| = \sqrt{(E_x^{\mathrm{miss}})^2 + (E_y^{\mathrm{miss}})^2} \tag{5.3}$$

$$\phi^{\mathrm{miss}} = \arctan(E_y^{\mathrm{miss}}/E_x^{\mathrm{miss}}) \tag{5.4}$$

Another quantity built from the $E_{\mathrm{T}}^{\mathrm{miss}}$ reconstruction and used to study the $E_{\mathrm{T}}^{\mathrm{miss}}$ performance is $\sum E_{\mathrm{T}}$, which is constructed from the scalar sum of the transverse momenta of the objects contributing to the $E_{\mathrm{T}}^{\mathrm{miss}}$ reconstruction:

$$\sum E_{\mathrm{T}} = -\sum_{i\in\{\mathrm{hard\,objects}\}} p_{\mathrm{T}i} - \sum_{j\in\{\mathrm{soft\,signals}\}} p_{\mathrm{T}j}, \tag{5.5}$$

and quantifies the total event activity.

As already stated, the $E_{\mathrm{T}}^{\mathrm{miss}}$ reconstruction proceeds through summing the transverse

momenta of hard and soft contributions. The sum is implemented as follows:

$$\begin{aligned}\mathbf{E}_{\mathrm{T}}^{\mathrm{miss}} = &\underbrace{-\sum_{\substack{selected\\electrons}} \mathbf{p}_{\mathrm{T}}{}^{e}}_{\mathbf{E}_{\mathrm{T}}^{\mathrm{miss},e}} \underbrace{-\sum_{\substack{accepted\\photons}} \mathbf{p}_{\mathrm{T}}{}^{\gamma}}_{\mathbf{E}_{\mathrm{T}}^{\mathrm{miss},\gamma}} \underbrace{-\sum_{\substack{accepted\\\tau_{had}}} \mathbf{p}_{\mathrm{T}}{}^{\tau_{\mathrm{had}}}}_{\mathbf{E}_{\mathrm{T}}^{\mathrm{miss},\tau_{\mathrm{had}}}} \\ &\underbrace{-\sum_{\substack{selected\\muons}} \mathbf{p}_{\mathrm{T}}{}^{\mu}}_{\mathbf{E}_{\mathrm{T}}^{\mathrm{miss},\mu}} \underbrace{-\sum_{\substack{accepted\\jets}} \mathbf{p}_{\mathrm{T}}{}^{\mathrm{jet}}}_{\mathbf{E}_{\mathrm{T}}^{\mathrm{miss,jet}}} \underbrace{-\sum_{\substack{unused\\tracks/clusters}} \mathbf{p}_{\mathrm{T}}}_{\mathbf{E}_{\mathrm{T}}^{\mathrm{miss,soft}}} ,\end{aligned} \tag{5.6}$$

where the hard terms are obtained as the negative sum of the momenta for the respective calibrated objects. The selection requirements on the hard objects are discussed in Section 5.2.1.

In a *pp* collision event at the LHC, several reconstructed objects may share signals (i.e. tracks, or clusters); if overlaps are not resolved the contribution of some signals can be double-counted. To avoid this, a procedure to resolve the ambiguities is implemented, as described in Section 5.2.2.

After all contributions from hard objects are summed, the soft term, $\mathbf{E}_{\mathrm{T}}^{\mathrm{miss,soft}}$, is reconstructed from the transverse energy deposited in the detector but not associated with any reconstructed hard object. It may be reconstructed either by calorimeter-based methods, known as the Calorimeter Soft Term (CST), or track-based methods, resulting in the Track Soft Term (TST). The criteria for the definitions of the soft terms are described in Section 5.2.3.

5.2.1 Objects definition

An element of novelty with respect to the Run 1 $E_{\mathrm{T}}^{\mathrm{miss}}$ reconstruction is that the $E_{\mathrm{T}}^{\mathrm{miss}}$ software provides flexibility for the choice of the selection requirements for the hard objects (electrons, muons, tau-jets, photons) entering the $E_{\mathrm{T}}^{\mathrm{miss}}$ calculation. In this way, each analysis can reconstruct the $E_{\mathrm{T}}^{\mathrm{miss}}$ coherently with the object definitions it uses. The criteria to select jets are instead provided centrally.

The criteria chosen for the performance analysis described in this chapter are detailed below.

Electrons: *medium* identification, $p_{\mathrm{T}} > 10$ GeV, $|\eta| < 2.47$, electrons in the transition region $1.37 < |\eta| < 1.52$ are discarded.

Photons: *tight* identification, $E_T > 25$ GeV, $|\eta| < 2.37$, photons in the transition region $1.37 < |\eta| < 1.52$ are discarded.

tau-jets: *medium* identification $p_{\mathrm{T}} > 20$ GeV, $|\eta| < 2.5$, tau-jet candidates in the transition region $1.37 < |\eta| < 1.52$ are discarded.

Muons: *medium* muons, $p_{\mathrm{T}} > 10$ GeV, $|\eta| < 2.7$.

Jets: anti-k_t jets, $R = 0.4$, EM+JES calibration, *medium* JVT, $p_{\mathrm{T}} > 20$ GeV, $|\eta| < 4.5$. The effect of using different p_{T} thresholds on the $E_{\mathrm{T}}^{\mathrm{miss}}$ performance is discussed in Section 5.4.4.

In the following the term 'signal cuts' refers to the set of cuts just listed for a given object category.

5.2.2 Overlap removal

The reconstruction of the $E_{\mathrm{T}}^{\mathrm{miss}}$ terms proceeds with a given order: typically it starts with objects with the highest reconstruction quality, the electrons, followed by photons, then tau-jets, followed by muons and jets. The soft term is computed after all terms from the hard contributions are built.
The order through which the physics objects enter the $E_{\mathrm{T}}^{\mathrm{miss}}$ reconstruction is as follows:

1. electrons passing the signal cuts;
2. photons passing the signal cuts and without overlap with (1);
3. tau-jets passing the signal cuts and without overlap with (1) and (2);
4. muons passing the signal cuts, and passing the $\mu - jet$ overlap removal;
5. jets passing the signal cuts and without overlap with (1),(2),(3) and passing the $\mu - jet$ overlap removal.

The overlap between an object (electron, photon or tau-jet) and a jet is expressed in terms of fraction of common signals contributing to the respective reconstructed energy (at the electromagnetic scale), as measured by the ratio:

$$k_E = \frac{E_{\mathrm{obj}}^{\mathrm{EM}}}{E_{\mathrm{jet}}^{\mathrm{EM}}}. \tag{5.7}$$

In the case of $k_E \leq 50\%$, the jet is included in $E_{\mathrm{T}}^{\mathrm{miss}}$ reconstruction, with its p_{T} scaled by $1 - k_E$. For $k_E > 50\%$, only the tracks associated with the jet, excluding the track(s) associated with the overlapping particle if any, contribute to the soft term.

A special case is the overlap between muons and jets. Jets overlapping with muons may be pile-up jets surviving the JVT cut, and should be removed. A jet resulting from energy loss of the muon in the calorimeters is also not accepted in the $E_{\mathrm{T}}^{\mathrm{miss}}$ reconstruction, to avoid double counting, since the original p_{T} of the muon is already fully reconstructed. Another case is when a photon emitted from final state radiation off the muon is reconstructed as a jet; in this case, the jet should be accepted, as its energy is not recovered in the muon reconstruction otherwise. Several criteria are optimized to remove or retain these kind of jets, as described in detail in Section 3.3.6 of Ref. [83].

5.2.3 Soft Term definitions

Two alternative definitions of the soft term are provided to physics analyses.

Track Soft Term (TST): the track soft term (TST) is built from ID tracks with $p_{\mathrm{T}} > 400$ MeV, which pass criteria of compatibility with the primary vertex, but are not matched to any reconstructed object. Only those tracks associated with the hard scatter vertex are included. ID tracks in the vicinity of the physics objects are excluded, in particular if they are:

- within $\Delta R = 0.05$ of an electron or photon cluster;
- within $\Delta R = 0.2$ of a tau-jet;
- associated to muons;
- associated to jets with the ghost-association [84].

ID tracks from the hard-scatter associated with jets that have been rejected by the overlap removal or associated with jets removed from the JVT cut, are instead included in the soft term.

It is clear that since tracks may be accurately matched to a primary vertex, the TST is relatively insensitive to pile-up effects. One disadvantage is that it does not include contributions from soft neutral particles and from forward regions ($|\eta| > 2.5$). The $E_{\mathrm{T}}^{\mathrm{miss}}$ variant calculated using the track soft term is known as 'TST $E_{\mathrm{T}}^{\mathrm{miss}}$'.

Calorimeter Soft Term (CST): the calorimeter soft term (CST) is reconstructed from the topoclusters which do not belong to any reconstructed hard objects. The $E_{\mathrm{T}}^{\mathrm{miss}}$ as calculated using the calorimeter soft term is known as 'CST $E_{\mathrm{T}}^{\mathrm{miss}}$', and was the standard $E_{\mathrm{T}}^{\mathrm{miss}}$ definition used in most Run 1 analyses. While accounting also for the neutral soft particles, it is not very robust against pile-up, as it will be shown in the following sections.

5.2.4 Track $E_{\mathrm{T}}^{\mathrm{miss}}$

The $E_{\mathrm{T}}^{\mathrm{miss}}$ reconstruction described so far applies to the so-called 'object-based' variants (i.e. TST $E_{\mathrm{T}}^{\mathrm{miss}}$ and CST $E_{\mathrm{T}}^{\mathrm{miss}}$), which use the reconstructed and calibrated physics objects as inputs. A different variable has been studied, which is based almost entirely on track information, called Track $E_{\mathrm{T}}^{\mathrm{miss}}$. Track $E_{\mathrm{T}}^{\mathrm{miss}}$ is reconstructed as the negative sum of the momenta of high-quality tracks associated to the primary vertex of the interaction, except for electrons, for which the calorimeter cluster measurement is used. The soft term is reconstructed similarly as the Track Soft Term.

Track $E_{\mathrm{T}}^{\mathrm{miss}}$ gives a very pile-up-robust $E_{\mathrm{T}}^{\mathrm{miss}}$ estimation, but completely neglects the contribution of neutral particles, which do not form tracks in the ID. Moreover, the η coverage of Track $E_{\mathrm{T}}^{\mathrm{miss}}$ is limited to the tracking volume of $|\eta| < 2.5$, which is smaller than the calorimeter coverage extending to $|\eta| = 4.9$.

5.3 Event selections

Several processes are used to study the $E_{\mathrm{T}}^{\mathrm{miss}}$ performance, chosen for complementary characteristics.

The $Z \to \ell\ell$ process, with $\ell\ell$ being an electron-positron or muon-antimuon pair, is the standard for evaluating the $E_{\mathrm{T}}^{\mathrm{miss}}$ performance owing to its clean detector signature. These events have zero 'genuine' $E_{\mathrm{T}}^{\mathrm{miss}}$. The reconstructed $E_{\mathrm{T}}^{\mathrm{miss}}$ in $Z \to \ell\ell$ events therefore gives information about the intrinsic resolution of the detector, of the algorithms involved and of the object reconstruction efficiencies.

$W \to \ell\nu$ events provide a topology with high-p_{T} neutrinos, in which $E_{\mathrm{T}}^{\mathrm{miss}}$ is expected to be non-zero. These events can give information on the scale of $E_{\mathrm{T}}^{\mathrm{miss}}$.

Top-antitop pair ($t\bar{t}$) events provide a topology with many jets, and so are useful in investigating the robustness of $E_{\mathrm{T}}^{\mathrm{miss}}$ reconstruction in multijet environments.

The event selection criteria used to select the above mentioned classes of events are hereby listed.

- **$\mathbf{Z \to \ell\ell}$ selection**: the selection of this class of events requires there be exactly two selected leptons with $p_{\mathrm{T}} > 25$ GeV. The leptons must be of the same flavour (electron or muon) and of opposite charge. The reconstructed invariant mass of the dilepton system, $m_{\ell\ell}$, is required to be consistent with the mass of the Z boson ($|m_{\ell\ell} - m_Z| < 25$ GeV).

- **$\mathbf{W \to \ell\nu}$ selection**: events are required to contain exactly one good lepton. In order to reduce the multijet background, in which one jet mimics the isolated lepton from the W boson, selections are applied on $E_{\mathrm{T}}^{\mathrm{miss}}$ and m_{T}[1]. The selections are $E_{\mathrm{T}}^{\mathrm{miss}} > 25$ GeV and $m_{\mathrm{T}} > 40$ GeV. In order to maintain a consistent set of events when comparing the $E_{\mathrm{T}}^{\mathrm{miss}}$ definitions, these two requirements are made always using the TST $E_{\mathrm{T}}^{\mathrm{miss}}$.

- **$\mathbf{t\bar{t}}$ selection:** Only semi-leptonic $t\bar{t}$ events in MC simulation are considered, that is, requiring exactly one selected lepton (electron or muon) in the event.

5.4 Expected performance

5.4.1 $E_{\mathrm{T}}^{\mathrm{miss}}$ distributions

In this section, the behavior of the reconstructed $E_{\mathrm{T}}^{\mathrm{miss}}$ is examined in Monte Carlo simulated events with an average $\langle\mu\rangle = 20$.

As mentioned, $Z(\ell\ell)$ + jets events are the primary standard for evaluation of $E_{\mathrm{T}}^{\mathrm{miss}}$ performance owing to the absence of genuine missing transverse momentum. A non-zero

[1] The reconstructed transverse mass of the lepton and the $E_{\mathrm{T}}^{\mathrm{miss}}$ system is defined as

$$m_{\mathrm{T}} = \sqrt{2p_{\mathrm{T}}^{\ell}E_{\mathrm{T}}^{\mathrm{miss}}(1 - \cos\Delta\phi)} \tag{5.8}$$

where $\Delta\phi$ is the azimuthal angle between the lepton momentum and the $E_{\mathrm{T}}^{\mathrm{miss}}$.

average $E_{\mathrm{T}}^{\mathrm{miss}}$ is indicative of a bias in $E_{\mathrm{T}}^{\mathrm{miss}}$, essentially due to the limited detector acceptance and to particles that fail to be reconstructed altogether; the spread around the mean is a measure of the resolution of the $E_{\mathrm{T}}^{\mathrm{miss}}$ reconstruction. $Z(\ell\ell)+$ jets events are therefore a good choice for the study of imperfections in the $E_{\mathrm{T}}^{\mathrm{miss}}$ reconstruction process.

Distributions of $E_{x(y)}^{\mathrm{miss}}$ and $\sum E_{\mathrm{T}}$ Figure 5.1(a) compares the distributions of the missing transverse momentum components along the x axis as reconstructed using the three alternative definitions TST $E_{\mathrm{T}}^{\mathrm{miss}}$, CST $E_{\mathrm{T}}^{\mathrm{miss}}$ and Track $E_{\mathrm{T}}^{\mathrm{miss}}$.
The TST $E_{\mathrm{T}}^{\mathrm{miss}}$ and CST $E_{\mathrm{T}}^{\mathrm{miss}}$ definitions show very similar tails, while the TST $E_{\mathrm{T}}^{\mathrm{miss}}$ has a narrower peak. For Track $E_{\mathrm{T}}^{\mathrm{miss}}$, the tails visible at high $|E_x^{\mathrm{miss}}|$ can be mostly attributed to the lack of sensitivity to neutral particles in jets. There is also a contribution from the reduced η acceptance of the ID as compared to the calorimeter, which plays different roles depending on the event topology.

Figure 5.1(b) shows the distribution of $\sum E_{\mathrm{T}}$, which is a measure of the event activity. The CST $E_{\mathrm{T}}^{\mathrm{miss}}$ shows greater event activity, owing largely to its lack of discrimination against pile-up by primary vertex. The difference between the TST $E_{\mathrm{T}}^{\mathrm{miss}}$ and Track $E_{\mathrm{T}}^{\mathrm{miss}}$ reveals the contribution of neutral particles, to which the calorimeter-based jet term is sensitive, but the track-based method is not.

The performance of $E_{\mathrm{T}}^{\mathrm{miss}}$ reconstruction is similar between $Z(\mu\mu)+$jets and $Z(ee)+$jets events, and so only $Z(\mu\mu)+$ jets samples are shown in this and subsequent figures.

Distributions of $E_{\mathrm{T}}^{\mathrm{miss}}$ versus jet multiplicity Figure 5.2 compares the distributions of total missing transverse momentum as reconstructed using TST, CST $E_{\mathrm{T}}^{\mathrm{miss}}$, and Track $E_{\mathrm{T}}^{\mathrm{miss}}$. Distributions for events containing 0, 1, and 2 or more reconstructed jets are shown separately in order to illustrate the effect on the $E_{\mathrm{T}}^{\mathrm{miss}}$ distribution. An average non-zero value of $E_{\mathrm{T}}^{\mathrm{miss}}$ can be noticed in all distributions, indicating a bias in the $E_{\mathrm{T}}^{\mathrm{miss}}$ reconstruction; the bias is smaller for TST and Track $E_{\mathrm{T}}^{\mathrm{miss}}$ compared to CST $E_{\mathrm{T}}^{\mathrm{miss}}$.

For events with no hard jets, TST $E_{\mathrm{T}}^{\mathrm{miss}}$ and Track $E_{\mathrm{T}}^{\mathrm{miss}}$ are expected to be similar, since their soft terms are defined by the same procedure. The small difference between TST and Track $E_{\mathrm{T}}^{\mathrm{miss}}$ for $E_{\mathrm{T}}^{\mathrm{miss}} \gtrapprox 50$ GeV in Figure 5.2 a can then be primarily attributed to jets mistakenly reconstructed as taus or photons, which are included in the TST $E_{\mathrm{T}}^{\mathrm{miss}}$ but escape the Track $E_{\mathrm{T}}^{\mathrm{miss}}$.

Distributions of soft term versus jet multiplicity The soft term distributions are also shown separately for different jet multiplicities in Figure 5.3. As expected, the soft term for TST $E_{\mathrm{T}}^{\mathrm{miss}}$ and Track $E_{\mathrm{T}}^{\mathrm{miss}}$ has a lower average than the soft term for CST $E_{\mathrm{T}}^{\mathrm{miss}}$ in all cases.

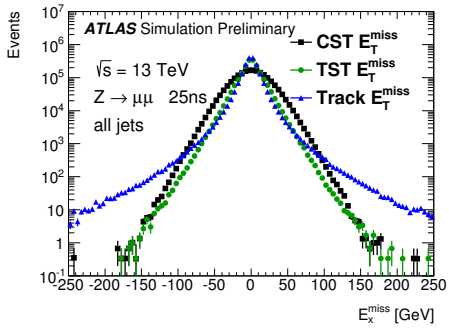

(a) E_x^{miss}

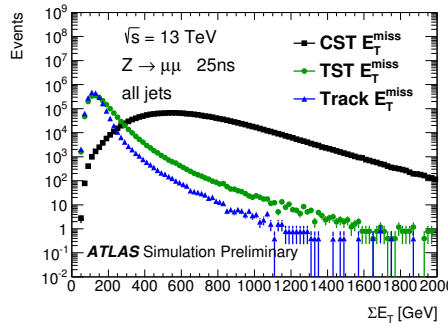

(b) $\sum E_{\text{T}}$

Figure 5.1: Distributions of (a) the x component of the total $E_{\text{T}}^{\text{miss}}$, and (b) the $\sum E_{\text{T}}$. These are shown for the TST $E_{\text{T}}^{\text{miss}}$, CST $E_{\text{T}}^{\text{miss}}$ and Track $E_{\text{T}}^{\text{miss}}$ definitions, using POWHEG+PYTHIA $Z(\mu\mu)$ + jets simulated events.

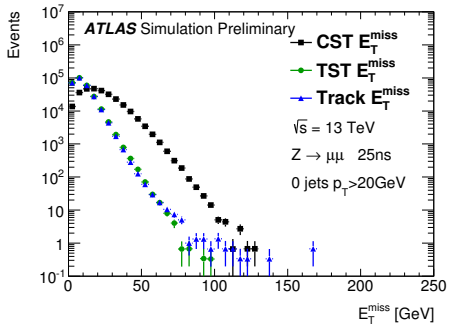

(a) N_{jets} =0

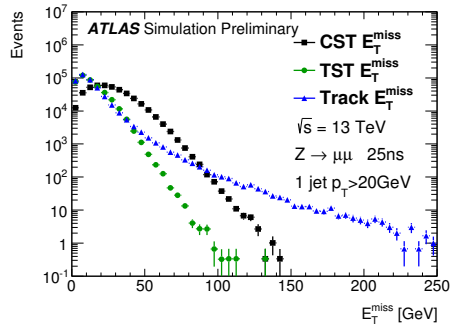

(b) N_{jets} =1

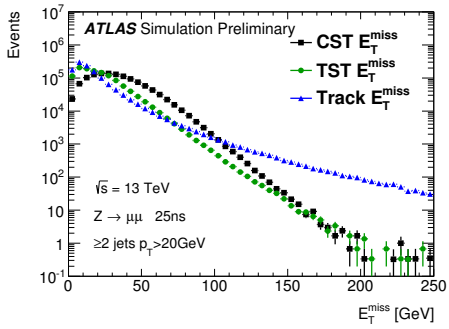

(c) $N_{\text{jets}} \geq$2

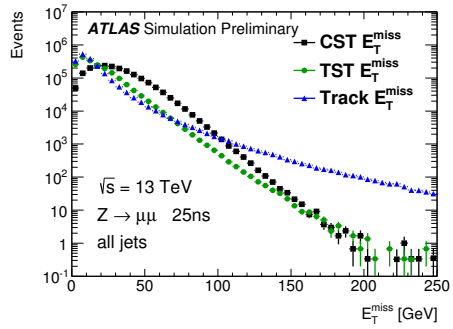

(d) Inclusive N_{jets}

Figure 5.2: Distributions of the total TST $E_{\text{T}}^{\text{miss}}$, CST $E_{\text{T}}^{\text{miss}}$ and Track $E_{\text{T}}^{\text{miss}}$, shown for POWHEG+PYTHIA $Z(\mu\mu)$ + jets simulated events. The distributions are separated based on the number of calibrated jets with $p_{\text{T}} > 20$ GeV. The figures (a), (b) and (c) separately show events with 0, 1, and 2 or more jets, while figure (d) shows events for all N_{jets}.

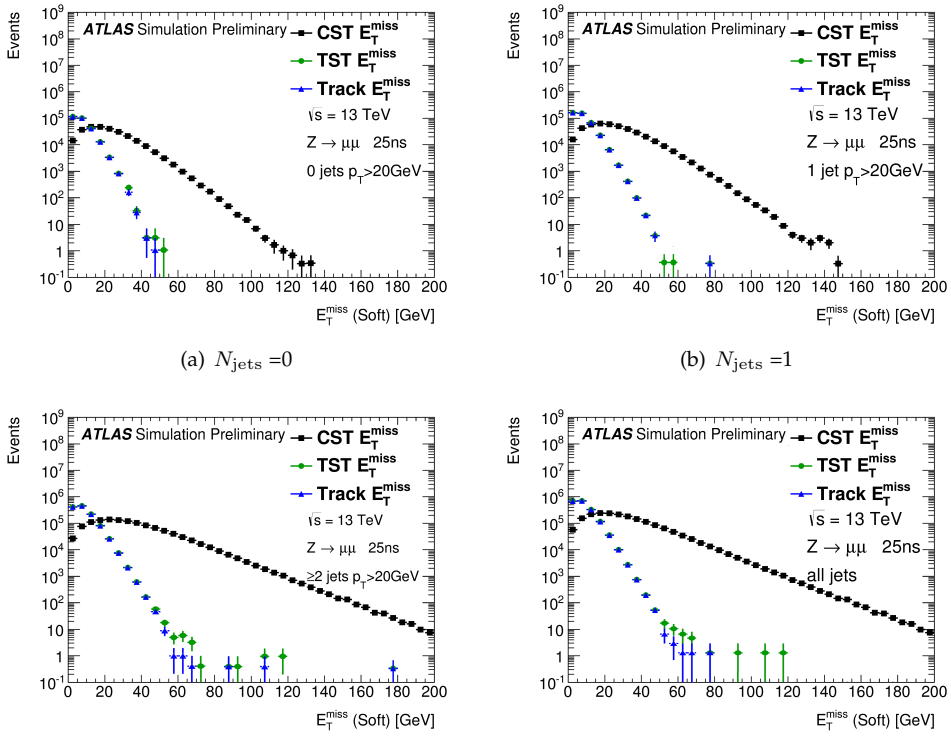

(a) N_{jets} =0

(b) N_{jets} =1

(c) N_{jets} ≥2

(d) Inclusive N_{jets}

Figure 5.3: Distributions of the $E_{\text{T}}^{\text{miss}}$ soft term as reconstructed by the TST, CST and Track $E_{\text{T}}^{\text{miss}}$ methods, shown for POWHEG+PYTHIA $Z(\mu\mu)$ + jets simulated events. The distributions are separated based on the number of calibrated jets with $p_{\text{T}} > 20$ GeV. The figures (a), (b) and (c) separately show events with 0, 1, and 2 or more jets, while figure (d) shows events for all N_{jets}.

5.4.2 Scale and linearity

In $Z(\mu\mu)$ + jets events, the axis defined by the p_{T} of the Z boson is useful to quantify biases in the scale of the $E_{\mathrm{T}}^{\mathrm{miss}}$. The unit vector along this axis is defined as:

$$\mathbf{A_Z} = \frac{\mathbf{p}_{\mathrm{T}}^{\ell^+} + \mathbf{p}_{\mathrm{T}}^{\ell^-}}{|\mathbf{p}_{\mathrm{T}}^{\ell^+} + \mathbf{p}_{\mathrm{T}}^{\ell^-}|} \tag{5.9}$$

where $p_{\mathrm{T}}^{\ell^+}$ and $p_{\mathrm{T}}^{\ell^-}$ are the transverse momenta of the leptons from the Z boson decay. The mean value of the $\mathbf{E}_{\mathrm{T}}^{\mathrm{miss}}$ projected onto $\mathbf{A_Z}$ is a measure of the $E_{\mathrm{T}}^{\mathrm{miss}}$ scale, sensitive to the balance between the leptons and the soft hadronic recoil. For perfect balance of the leptons against the soft hadronic recoil, the projection of $\mathbf{E}_{\mathrm{T}}^{\mathrm{miss}}$ onto $\mathbf{A_Z}$ would be zero.

Figure 5.4 shows the projection of $E_{\mathrm{T}}^{\mathrm{miss}}$ onto $\mathbf{A_Z}$ for $Z(\mu\mu)$ + jets events with zero (a) and any number of jets (b). The projection is negative for all $E_{\mathrm{T}}^{\mathrm{miss}}$ definitions, which for zero-jet events indicates an underestimation of the soft recoil due to detector inefficiencies and coverage limitations. In the zero-jet case, there is reasonable agreement between the three $E_{\mathrm{T}}^{\mathrm{miss}}$ definitions. The track-based methods show a slightly greater underestimation of the soft recoil, owing to their insensitivity to soft neutral particles. If events with $N_{\mathrm{jets}} > 0$ are included, Track $E_{\mathrm{T}}^{\mathrm{miss}}$ displays an increasing projection along the axis of the Z boson. This is attributed to the loss of neutral particles from high-p_{T} jets recoiling against the Z boson. The difference between the CST $E_{\mathrm{T}}^{\mathrm{miss}}$ and the TST $E_{\mathrm{T}}^{\mathrm{miss}}$ for $p_T^Z > 40$ GeV indicates a slightly greater imbalance for the CST $E_{\mathrm{T}}^{\mathrm{miss}}$.

The presence of a neutrino in the $W(\ell\nu)$ + jets final state means that these events come with genuine $E_{\mathrm{T}}^{\mathrm{miss}}$. These events are therefore useful to evaluate the $E_{\mathrm{T}}^{\mathrm{miss}}$ linearity. The relative deviation Δ^{lin} of the reconstructed $E_{\mathrm{T}}^{\mathrm{miss}}$ from the $E_{\mathrm{T}}^{\mathrm{miss,True}}$ can be used at this aim:

$$\Delta^{\mathrm{lin}}(E_{\mathrm{T}}^{\mathrm{miss,True}}) = \langle \frac{E_{\mathrm{T}}^{\mathrm{miss}} - E_{\mathrm{T}}^{\mathrm{miss,True}}}{E_{\mathrm{T}}^{\mathrm{miss,True}}} \rangle. \tag{5.10}$$

If $E_{\mathrm{T}}^{\mathrm{miss}}$ were reconstructed at the correct scale, the relative deviation from linearity would be zero. Figures 5.5 and 5.6 show Δ^{lin} as a function of $E_{\mathrm{T}}^{\mathrm{miss,True}}$ for $W(\mu\nu)$ + jets and $t\bar{t}$ simulated events. Since $E_{\mathrm{T}}^{\mathrm{miss}}$ is by definition positive and has a finite resolution, a positive bias in the linearity at low $E_{\mathrm{T}}^{\mathrm{miss,True}}$ is expected[2]. At higher $E_{\mathrm{T}}^{\mathrm{miss,True}}$, CST $E_{\mathrm{T}}^{\mathrm{miss}}$ and TST $E_{\mathrm{T}}^{\mathrm{miss}}$ reconstruct the correct scale to better than 5% accuracy. Track $E_{\mathrm{T}}^{\mathrm{miss}}$ significantly underestimates the $E_{\mathrm{T}}^{\mathrm{miss}}$ scale, as it omits the contribution of neutral particles within jets.

5.4.3 Resolution

Another important measurement of the performance of the $E_{\mathrm{T}}^{\mathrm{miss}}$ reconstruction is the resolution of the $E_{\mathrm{T}}^{\mathrm{miss}}$, defined as the width of the $E_{\mathrm{T}}^{\mathrm{miss}}$ distribution. In previous studies [85], this was expressed as the width of a Gaussian fit to $E_{x(y)}^{\mathrm{miss}}$. Here, the rootmean-square (RMS) of the distribution is used, in order to better accommodate the non-Gaussian

[2] In addition, the selection of $W(\mu\nu)$ + jets events requires $E_{\mathrm{T}}^{\mathrm{miss}} > 25$ GeV

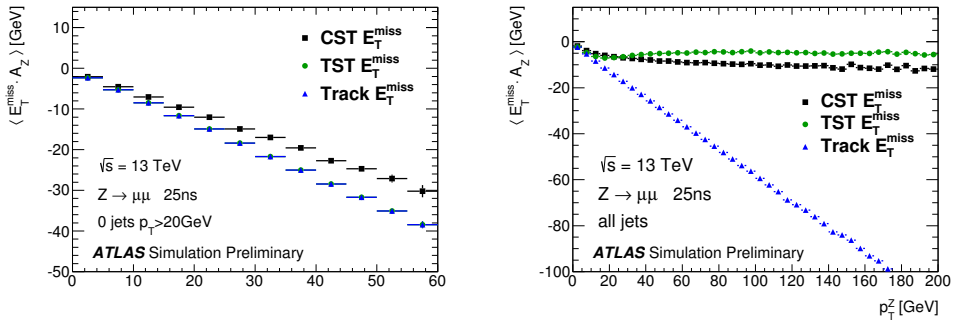

(a) $\langle \mathbf{E}_{\mathrm{T}}^{\mathrm{miss}} \cdot A_Z \rangle$, $N_{\mathrm{jets}} = 0$ (b) $\langle \mathbf{E}_{\mathrm{T}}^{\mathrm{miss}} \cdot A_Z \rangle$, inclusive N_{jets}

Figure 5.4: Comparison of the response for TST $E_{\mathrm{T}}^{\mathrm{miss}}$, CST $E_{\mathrm{T}}^{\mathrm{miss}}$ and Track $E_{\mathrm{T}}^{\mathrm{miss}}$: the mean projection of $E_{\mathrm{T}}^{\mathrm{miss}}$ along the direction of the Z in POWHEG+PYTHIA $Z(\mu\mu)$ + jets events is shown for (a) N_{jets} = 0 and (b) inclusive N_{jets}.

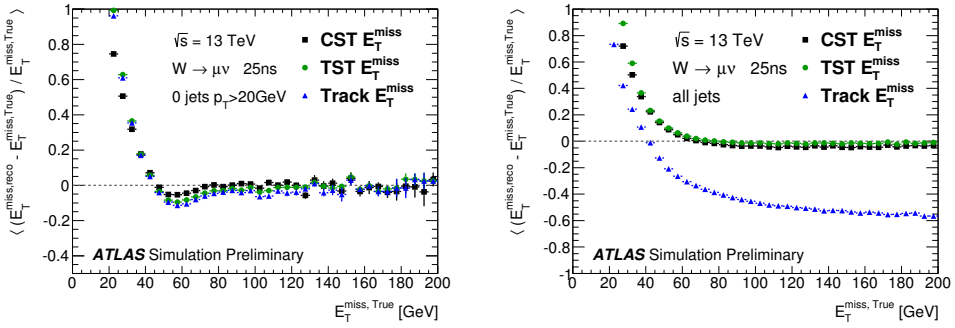

(a) Δ^{lin}, $N_{\mathrm{jets}} = 0$ (b) Δ^{lin}, inclusive N_{jets}

Figure 5.5: Comparison of $\Delta^{\mathrm{lin}}(E_{\mathrm{T}}^{\mathrm{miss,True}})$ for TST $E_{\mathrm{T}}^{\mathrm{miss}}$, CST $E_{\mathrm{T}}^{\mathrm{miss}}$ and Track $E_{\mathrm{T}}^{\mathrm{miss}}$ as a function of $E_{\mathrm{T}}^{\mathrm{miss,True}}$ in POWHEG+PYTHIA $W(\mu\nu)$ + jets events is shown for (a) N_{jets} = 0 and (b) inclusive N_{jets}. For perfect scale agreement between reconstructed and true $E_{\mathrm{T}}^{\mathrm{miss}}$, a zero value of Δ^{lin} would be expected.

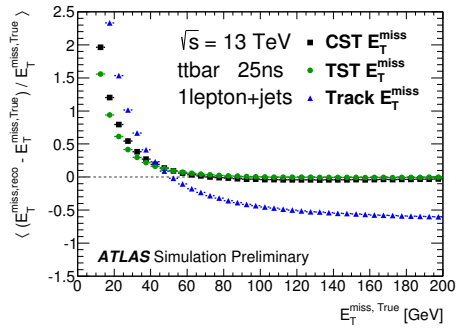

Figure 5.6: Comparison of $\Delta^{\mathrm{lin}}(E_{\mathrm{T}}^{\mathrm{miss,True}})$ for TST $E_{\mathrm{T}}^{\mathrm{miss}}$, CST $E_{\mathrm{T}}^{\mathrm{miss}}$ and Track $E_{\mathrm{T}}^{\mathrm{miss}}$ as a function of $E_{\mathrm{T}}^{\mathrm{miss,True}}$ in $t\bar{t}$ events. For perfect scale agreement between reconstructed and true $E_{\mathrm{T}}^{\mathrm{miss}}$, a zero value of Δ^{lin} would be expected.

tails observed in track-based $E_{\mathrm{T}}^{\mathrm{miss}}$ methods. The resulting comparison between TST $E_{\mathrm{T}}^{\mathrm{miss}}$, CST $E_{\mathrm{T}}^{\mathrm{miss}}$ and Track $E_{\mathrm{T}}^{\mathrm{miss}}$, as a function of the scalar sum of transverse energy in the event using the CST soft term (CST $\sum E_{\mathrm{T}}$) is shown in Figures 5.7 and 5.8. In both $Z(\mu\mu)+$jets and $W(\mu\nu)+$jets events, the CST has a steadily increasing width with increasing event activity. The track-based methods are less sensitive to this variation. This change can be partly attributed to increasing jet resolution, hence its influence on the TST $E_{\mathrm{T}}^{\mathrm{miss}}$ but not on Track $E_{\mathrm{T}}^{\mathrm{miss}}$. At low $\sum E_{\mathrm{T}}$ and in events with no hard jets, TST $E_{\mathrm{T}}^{\mathrm{miss}}$ is dominated by the soft hadronic recoil, and so is very similar to Track $E_{\mathrm{T}}^{\mathrm{miss}}$. As the event activity increases, TST $E_{\mathrm{T}}^{\mathrm{miss}}$ tends towards CST $E_{\mathrm{T}}^{\mathrm{miss}}$, as the contribution of jets comes to dominate.

The resolution in simulated $t\bar{t}$ events is shown in Figure 5.9. This topology demonstrates the effect of a high jet multiplicity: typical events have $N_{\mathrm{jets}} \geq 4$, as compared to 1-2 jets for $W(\mu\nu)+$jets events. Here, the behavior of CST $E_{\mathrm{T}}^{\mathrm{miss}}$ is very similar to its behavior for $Z(\mu\mu)+$jets and $W(\mu\nu)+$jets events, its resolution being slightly degraded by the increased event activity. TST $E_{\mathrm{T}}^{\mathrm{miss}}$ and CST $E_{\mathrm{T}}^{\mathrm{miss}}$ resolutions are very similar, as in this topology the resolution is dominated by the jet term, which they have in common. The resolution of the Track $E_{\mathrm{T}}^{\mathrm{miss}}$ suffers, owing to the increased jet multiplicity, from which neutral particles are lost.

As a more direct measure of the performance of $E_{\mathrm{T}}^{\mathrm{miss}}$ under varying pile-up conditions, the resolution in E_x^{miss}, E_y^{miss} is shown as a function of the number of primary vertices in the event, N_{PV}. The resulting comparison is shown for $Z(\mu\mu)+$jets events in Figure 5.10. $W(\mu\nu)+$jets events exhibit very similar behavior. The resolution of CST $E_{\mathrm{T}}^{\mathrm{miss}}$ increases with an increasing number of primary vertices. This is to be expected, as the additional interactions deposit energy in the calorimeter which the calorimeter-based method cannot distinguish from the deposits of the hard-scatter process. The resolution of Track $E_{\mathrm{T}}^{\mathrm{miss}}$ has very little dependence on the number of primary vertices, since tracks may be effectively associated to the hard-scatter vertex. When hard jets are present in events with low N_{PV}, the track-based method displays a larger resolution than calorimeter-based methods, owing to its neglect of neutral particles. The TST $E_{\mathrm{T}}^{\mathrm{miss}}$ displays a hybrid

behavior, combining the small resolution at low N_{PV} with the flat profile of the track-based method in events with no hard jets.

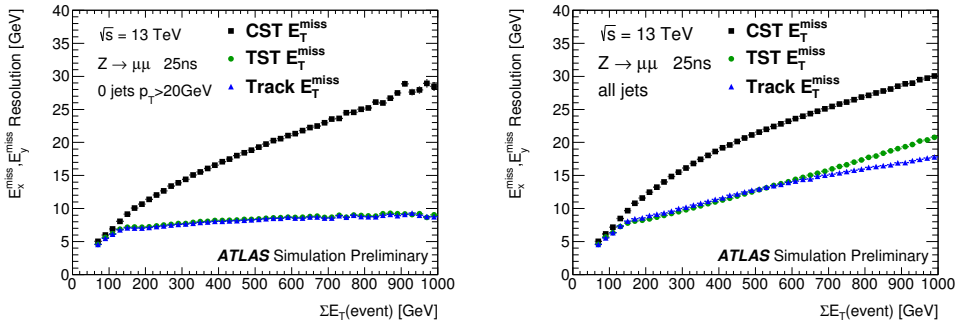

(a) $E_{\mathrm{T}}^{\mathrm{miss}}$ resolution, $N_{\mathrm{jets}} = 0$

(b) $E_{\mathrm{T}}^{\mathrm{miss}}$ resolution, inclusive N_{jets}

Figure 5.7: Comparison of the resolution for TST $E_{\mathrm{T}}^{\mathrm{miss}}$, CST $E_{\mathrm{T}}^{\mathrm{miss}}$ and Track $E_{\mathrm{T}}^{\mathrm{miss}}$; the resolution is quantified as the RMS of E_x^{miss},E_y^{miss} as a function of the CST $\sum E_{\mathrm{T}}$ for (a) N_{jets} = 0 and (b) inclusive N_{jets}. $Z(\mu\mu)$ + jets POWHEG+PYTHIA samples are shown.

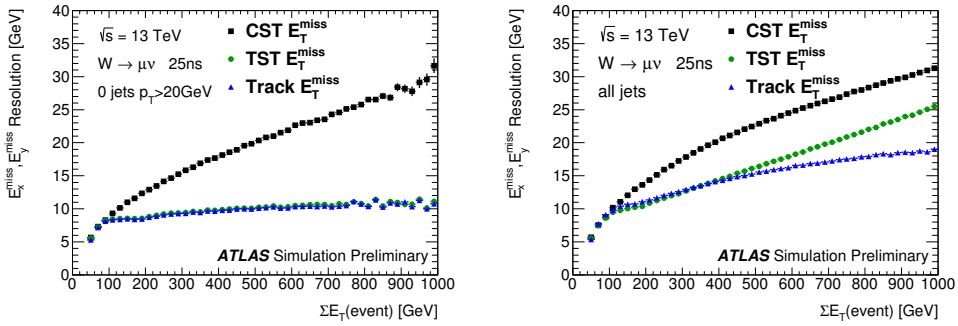

(a) $E_{\mathrm{T}}^{\mathrm{miss}}$ resolution, $N_{\mathrm{jets}} = 0$

(b) $E_{\mathrm{T}}^{\mathrm{miss}}$ resolution, inclusive N_{jets}

Figure 5.8: Comparison of the resolution for TST $E_{\mathrm{T}}^{\mathrm{miss}}$, CST $E_{\mathrm{T}}^{\mathrm{miss}}$ and Track $E_{\mathrm{T}}^{\mathrm{miss}}$; the resolution is quantified as the RMS of E_x^{miss},E_y^{miss} as a function of the CST $\sum E_{\mathrm{T}}$ for (a) N_{jets} = 0 and (b) inclusive N_{jets}. $W(\mu\nu)$ + jets POWHEG+PYTHIA samples are shown.

5.4.4 Effect of jet selection

Jets resulting from pile-up interactions are on the whole softer than those resulting from a hard scatter. A threshold in p_{T} is therefore applied to those jets entering the $E_{\mathrm{T}}^{\mathrm{miss}}$ jet term. Figure 5.11(a) shows the effect on the TST $E_{\mathrm{T}}^{\mathrm{miss}}$ resolution of the value of the threshold applied for events containing an arbitrary number of jets. Higher values of the threshold reduce the effect of pile-up on $E_{\mathrm{T}}^{\mathrm{miss}}$, and so improve the resolution of the reconstruction. However at high values of the jet p_{T} threshold, the $E_{\mathrm{T}}^{\mathrm{miss}}$ becomes biased

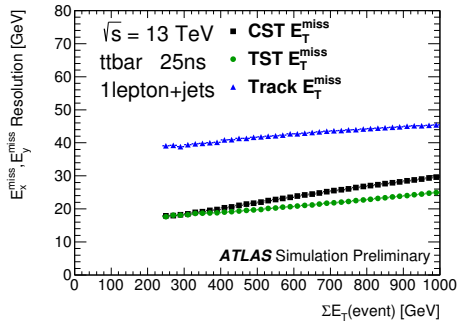

Figure 5.9: Comparison of the resolution for TST $E_{\mathrm{T}}^{\mathrm{miss}}$, CST $E_{\mathrm{T}}^{\mathrm{miss}}$ and Track $E_{\mathrm{T}}^{\mathrm{miss}}$; the resolution is quantified as the RMS of E_x^{miss},E_y^{miss} as a function of the CST $\sum E_{\mathrm{T}}$ in $t\bar{t}$ events.

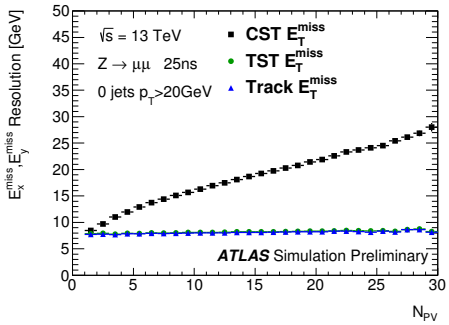

(a) $E_{\mathrm{T}}^{\mathrm{miss}}$ resolution, $N_{\mathrm{jets}} = 0$

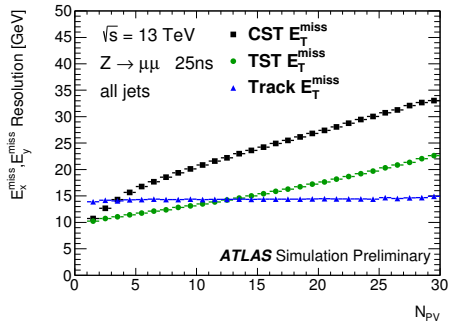

(b) $E_{\mathrm{T}}^{\mathrm{miss}}$ resolution, inclusive N_{jets}

Figure 5.10: Comparison of the resolution for TST $E_{\mathrm{T}}^{\mathrm{miss}}$, CST $E_{\mathrm{T}}^{\mathrm{miss}}$ and Track $E_{\mathrm{T}}^{\mathrm{miss}}$; the resolution is quantified as the RMS of E_x^{miss},E_y^{miss} as a function of the N_{PV} for (a) N_{jets} = 0 and (b) inclusive N_{jets}. $Z(\mu\mu)$ + jets POWHEG+PYTHIA samples are shown.

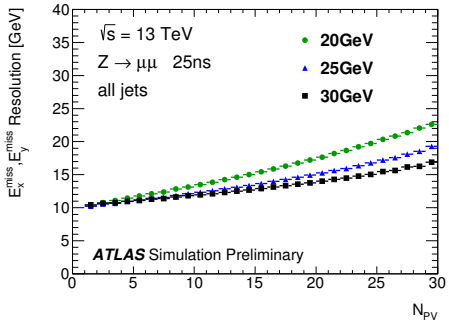

(a) $E_{\mathrm{T}}^{\mathrm{miss}}$ resolution

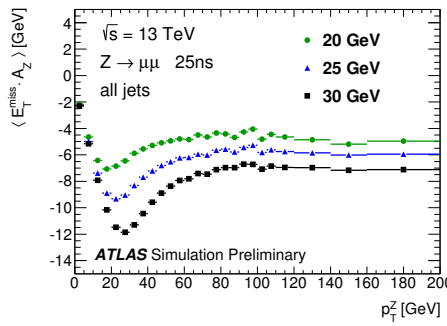

(b) $\langle \mathbf{E}_{\mathrm{T}}^{\mathrm{miss}} \cdot A_Z \rangle$

Figure 5.11: TST $E_{\mathrm{T}}^{\mathrm{miss}}$ performance shown in POWHEG+PYTHIA simulated $Z(\mu\mu)$+jets events for different values of the jet p_{T} threshold, as quantified by (a) the resolution as a function of N_{PV} and (b) the projection of $E_{\mathrm{T}}^{\mathrm{miss}}$ along the direction of the Z boson p_{T}.

against the direction of the Z boson, as hard-scatter jets are falsely removed. This can be seen in Figure 5.11(b), which shows the TST $E_{\mathrm{T}}^{\mathrm{miss}}$ projected along the direction of the Z transverse momentum. Raising the jet p_{T} above 20 GeV brings an improvement in resolution, but at the cost of a significant bias in $E_{\mathrm{T}}^{\mathrm{miss}}$ direction. For this reason, 20 GeV is set as the minimum calibrated p_{T} to select a jet.

5.5 Performance in early 2015 data

In this section, the performance of TST $E_{\mathrm{T}}^{\mathrm{miss}}$ reconstruction in early 2015 data is studied and compared to the expected performance from the MC simulations. Two processes are studied: $Z(\mu\mu)$ + jets and $W(e\nu)$ + jets selections. The integrated luminosity used for these studies corresponds to approximately $6\,\mathrm{pb}^{-1}$; given the relatively large statistical fluctuations in the collected samples and the preliminary nature of these studies, the systematic uncertainties on the MC simulations are not evaluated.

5.5.1 $E_{\mathrm{T}}^{\mathrm{miss}}$ distributions

$Z(\mu\mu)$ + jets events: approximately 4000 events are collected. Figure 5.12 shows the distributions of $E_{\mathrm{T}}^{\mathrm{miss}}$, $\sum E_{\mathrm{T}}$, E_x^{miss}, E_y^{miss} for TST $E_{\mathrm{T}}^{\mathrm{miss}}$. Figure 5.13 shows distributions for the jet, muons and soft terms for TST $E_{\mathrm{T}}^{\mathrm{miss}}$. The agreement in the bulk of the distributions is within 20%. In the high $E_{\mathrm{T}}^{\mathrm{miss}}$ and $\sum E_{\mathrm{T}}$ regions the data deviate somewhat from the background expectation but the statistical precision of the data is limited. The feature at zero in the jet term TST $E_{\mathrm{T}}^{\mathrm{miss}}$ is due to events with no jets.

$W(e\nu)$ + jets events: about 40000 events in data pass the $W(e\nu)$ + jets selection. Figure 5.14 shows the overall TST $E_{\mathrm{T}}^{\mathrm{miss}}$ distribution and the soft term of the TST $E_{\mathrm{T}}^{\mathrm{miss}}$. The agreement between data and MC simulation is worse with respect to the $Z(\mu\mu)$ + jets events in the low $E_{\mathrm{T}}^{\mathrm{miss}}$ region.

5.5.2 Response and resolution for $Z(\mu\mu)$ + jets events

The $E_{\mathrm{T}}^{\mathrm{miss}}$ resolution is evaluated in $Z(\mu\mu)$+jets data and MC events in which no genuine $E_{\mathrm{T}}^{\mathrm{miss}}$ is expected. The resolution is plotted as a function of the $\sum E_{\mathrm{T}}$ in the event. Consistently, the value of the resolution in each bin is estimated from the root-mean square of the combined of E_x^{miss} and E_x^{miss} in bins of $\sum E_{\mathrm{T}}$ (N_{PV}). Reasonable agreement is found between data and MC simulation, considering the low statistics available in data, as shown in Figure 5.15.

Figure 5.16 shows the $E_{\mathrm{T}}^{\mathrm{miss}}$ scale for data and MC simulation. The scale in $Z(\mu\mu)$ + jets events is defined as detailed in Section 5.4.2. Each bin is required to have a minimum of 200 events to be considered in the scale plot. The negative bias of about 5 GeV likely indicates an underestimation of the TST $E_{\mathrm{T}}^{\mathrm{miss}}$ from two sources: the TST $E_{\mathrm{T}}^{\mathrm{miss}}$ does not include contributions from the soft neutral particles and the limited acceptance of

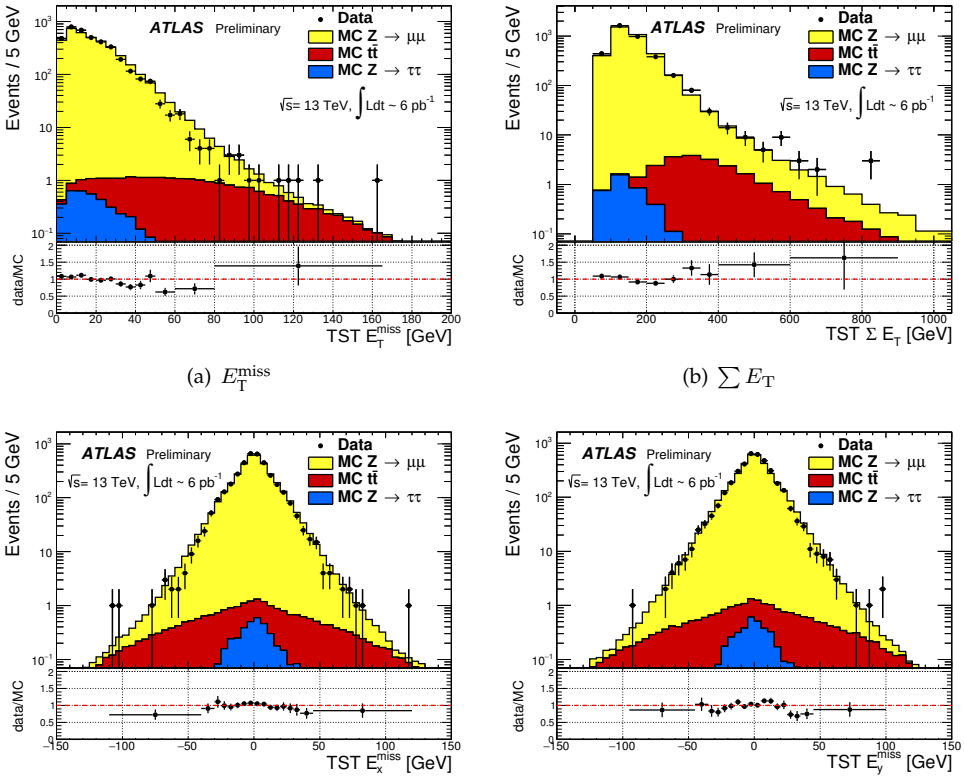

(a) $E_{\mathrm{T}}^{\mathrm{miss}}$ (b) $\sum E_{\mathrm{T}}$

(c) E_x^{miss} (d) E_y^{miss}

Figure 5.12: Distributions of TST $E_{\mathrm{T}}^{\mathrm{miss}}$ (a), $\sum E_{\mathrm{T}}$ (b), E_x^{miss} (c), E_y^{miss} (d) in $Z(\mu\mu)$+jets events. The expectation from MC simulation is superimposed and normalized to data, after each MC sample is weighted with its corresponding cross-section.

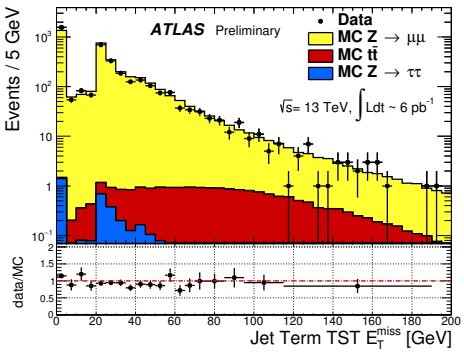

(a) Jet Term

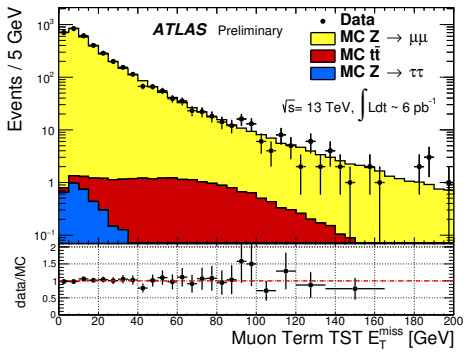

(b) Muon Term

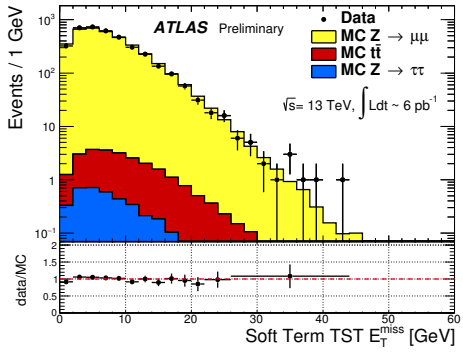

(c) Soft Term

Figure 5.13: Distributions of jet term (a), muon term (b) and soft term (c) for TST $E_{\mathrm{T}}^{\mathrm{miss}}$ in $Z(\mu\mu)+$ jets events. The expectation from MC simulation is superimposed and normalized to data, after each MC sample is weighted with its corresponding cross-section.

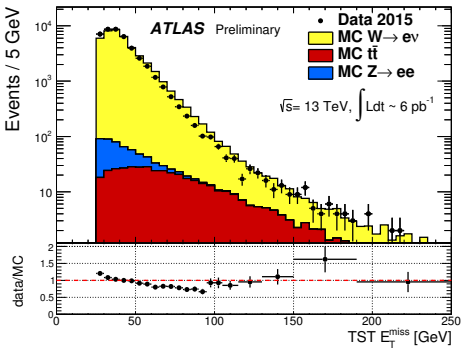

(a) $E_{\mathrm{T}}^{\mathrm{miss}}$

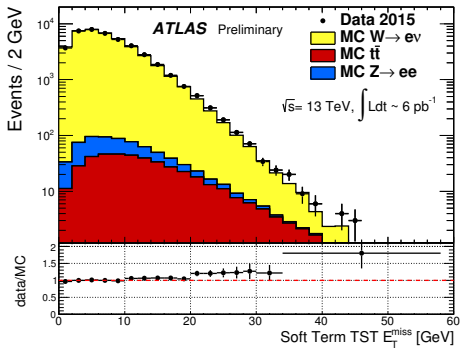

(b) Soft term

Figure 5.14: Distributions of TST $E_{\mathrm{T}}^{\mathrm{miss}}$ (a) and soft term (b) in $W(e\nu)+$jets events. The expectation from MC simulation is superimposed and normalized to data, after each MC sample is weighted with its corresponding cross-section.

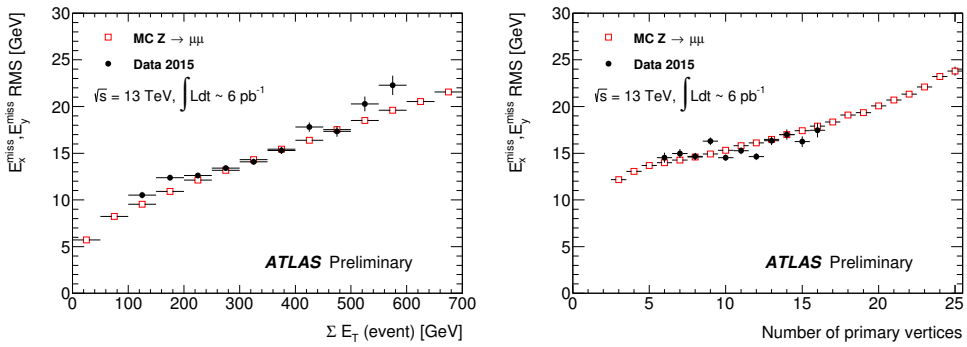

(a) $E_{\mathrm{T}}^{\mathrm{miss}}$ resolution vs $\sum E_{\mathrm{T}}$ (b) $E_{\mathrm{T}}^{\mathrm{miss}}$ resolution vs N_{PV}

Figure 5.15: Distributions of TST E_x^{miss}, E_y^{miss} resolution as a function of $\sum E_{\mathrm{T}}$ and of the number of primary vertices in $Z(\mu\mu)$+jets events. The data (black circles) and MC simulation (red squares) are overlaid.

the ID. The agreement is good between the data and MC simulation, except for some fluctuations for high p_T^Z events, due to low statistics.

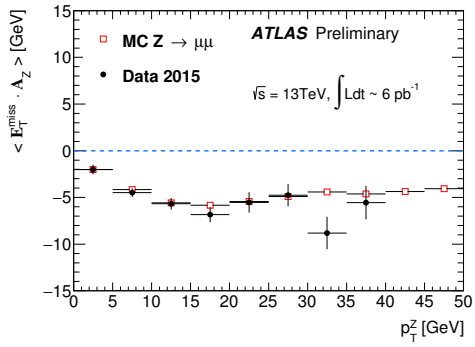

Figure 5.16: Distributions of TST $E_{\mathrm{T}}^{\mathrm{miss}}$ scale as a function of p_T^Z. The data (black circles) and MC simulation (red squares) are overlaid.

5.6 Performance in 2016 data

A few results on the performance of the TST $E_{\mathrm{T}}^{\mathrm{miss}}$ on a larger data sample are presented in this section. The data used for these results corresponds to 8.5 fb^{-1} and was collected by ATLAS during 2016, when the average pile-up was $\langle\mu\rangle = 25$.

Figure 5.17 shows the distributions of the $E_{\mathrm{T}}^{\mathrm{miss}}$ (a) and the soft term (b) in $Z(ee)$ + jets events in data, compared to the MC simulations, which also include diboson and top processes. All the MC samples are normalized to their cross-section. The agreement between the data and the simulation is remarkable. The $E_{\mathrm{T}}^{\mathrm{miss}}$ resolution for 0-jet events shown in (c) confirms the observations of Section 5.4.3, with an almost flat behavior as a function of pile-up and the value of the resolution below 10 GeV. There is good agreement between the data and the MC simulation.

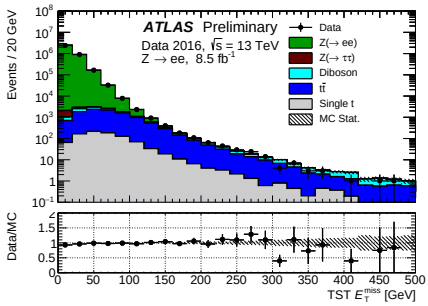

(a) TST $E_{\mathrm{T}}^{\mathrm{miss}}$

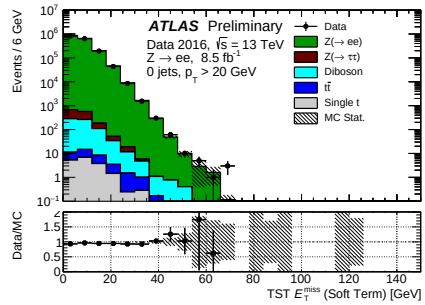

(b) TST soft term

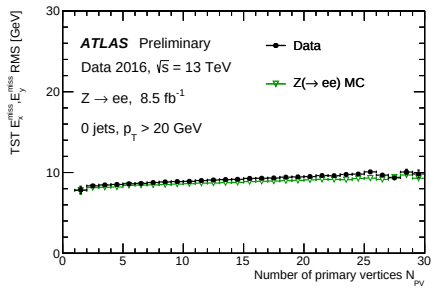

(c) TST $E_{\mathrm{T}}^{\mathrm{miss}}$ resolution

Figure 5.17: TST $E_{\mathrm{T}}^{\mathrm{miss}}$ (a) and TST soft term (b) distributions for a selection of $Z(ee)$ + jets events in the 2016 ATLAS dataset. The expectation is superimposed using POWHEG+PYTHIA MC simulated events for the relevant signal physics processes including some background processes, and normalizing the expectation based on the cross-sections. The shaded band represents the MC statistical uncertainty. TST $E_{\mathrm{T}}^{\mathrm{miss}}$ resolution (c) as a function of the number of primary vertices for a selection of $Z(ee)$+jets events with 0 jets, compared between data and $Z(ee)$+jets expectation [86].

5.7 Track Soft Term systematic uncertainties

Scale and resolution uncertainties on the hard objects are propagated in the $E_{\mathrm{T}}^{\mathrm{miss}}$ computation and automatically taken into account. Therefore, the only component of systematic uncertainty on the $E_{\mathrm{T}}^{\mathrm{miss}}$ which needs to be evaluated is the uncertainty on the scale and resolution of the soft term. In this section the method to compute the systematic uncertainties assigned to the track-based soft term is discussed, together with the derived uncertainties based on MC simulations studies.

5.7.1 Methodology

The method to compute the uncertainty on the soft term is based on the balance between hard and soft contributions in $Z(\mu\mu)+$ jets events.

In a $Z(\mu\mu)+$ jets final state, one would expect that hard and soft contributions perfectly balance: $\mathbf{p}_{\mathrm{T}}^{\mathrm{hard}} = -\mathbf{p}_{\mathrm{T}}^{\mathrm{soft}}$, where $\mathbf{p}_{\mathrm{T}}^{\mathrm{hard}}$ is defined as the sum of the $\mathbf{p}_{\mathrm{T}}$ of all reconstructed particles. While this expectation does not hold due to the experimental inefficiencies, it nevertheless raises the expectation that, for events without jets, $\mathbf{p}_{\mathrm{T}}^{\mathrm{soft}}$ points in the direction of the hadronic recoil, i.e. opposite to $\mathbf{p}_{\mathrm{T}}^{\mathrm{hard}}$ in the transverse momentum plane. The deviation from this expectation is measured in terms of the parallel and perpendicular projections of $\mathbf{E}_{\mathrm{T}}^{\mathrm{miss,soft}}$ onto the direction of $\mathbf{p}_{\mathrm{T}}^{\mathrm{hard}}$; these are defined as $E_{||}^{\mathrm{miss,soft}}$ and $E_{\perp}^{\mathrm{miss,soft}}$ respectively.

The average $\langle E_{||}^{\mathrm{miss,soft}} \rangle$ in a given bin of phase space defined by $p_{\mathrm{T}}^{\mathrm{hard}}$ measures the response of soft term. The effect of the soft term resolution on the $E_{\mathrm{T}}^{\mathrm{miss}}$ is measured by two components: the fluctuations in response ($\sigma^2(E_{||}^{\mathrm{miss,soft}})$) and the fluctuations in the angular deflection around the $\mathbf{p}_{\mathrm{T}}^{\mathrm{hard}}$ axis, measured by $\sigma^2(E_{\perp}^{\mathrm{miss,soft}})$.

5.7.2 Results based on MC simulations

The uncertainties are evaluated from the differences in $\langle E_{||}^{\mathrm{miss,soft}} \rangle$, $\sigma^2(E_{||}^{\mathrm{miss,soft}})$, $\sigma^2(E_{\perp}^{\mathrm{miss,soft}})$ between different MC samples. The procedure consists in extracting the distributions of the above mentioned quantities in bins of $\mathbf{p}_{\mathrm{T}}^{\mathrm{hard}}$, convolving them with Gaussian smearing functions, and then fitting the distributions. The fitted width reflects the uncertainty in the resolution, while the mean reflects the uncertainty in the scale. Three generators are examined: POWHEG + PYTHIA 8, SHERPA and HERWIG; in addition to these variations, systematic uncertainties are assigned to other aspects of the Run 2 data taking conditions:

- alternative azimuthal detector material distribution;
- alternative bunch spacing of 50 ns, as compared to the nominal sample with 25 ns;
- ATLFAST2 simulation, as opposed to full GEANT-based simulation (only for analyses using ATLFAST2).

These additional uncertainties are added to the difference of generators under the assumption that these variations are independent, and summing their contribution in quadrature. The effect of the derived uncertainties is illustrated in Figure 5.18: in (a) the $\langle E_{||}^{\mathrm{miss,soft}} \rangle$, in (b) the $\sigma^2(E_{||}^{\mathrm{miss,soft}})$ and in (c) the $\sigma^2(E_{\perp}^{\mathrm{miss,soft}})$.

The combined effect of the three uncertainties on the total $E_{\mathrm{T}}^{\mathrm{miss}}$ distributions is illustrated in Figure 5.19. The resolution smearing of the soft term results in a variation of roughly 2% which is constant with $E_{\mathrm{T}}^{\mathrm{miss}}$. The increasing spread at high $E_{\mathrm{T}}^{\mathrm{miss}}$ is owing to the scale variation in the soft term.

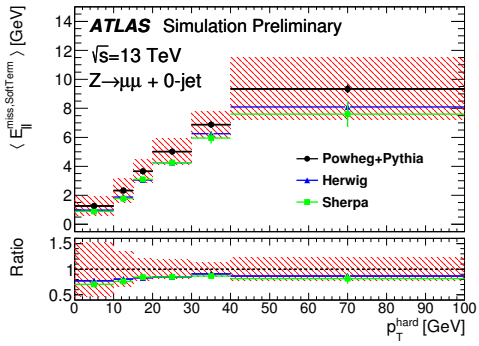

(a) $\langle E_{||}^{\mathrm{miss,soft}} \rangle$

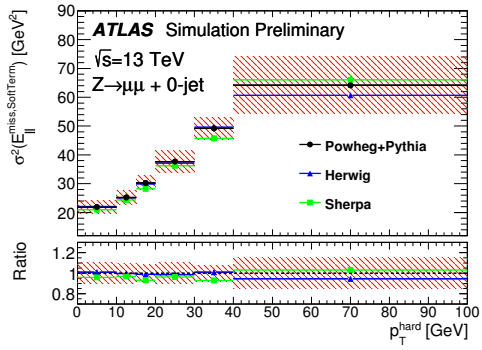

(b) $\sigma^2(E_{||}^{\mathrm{miss,soft}})$

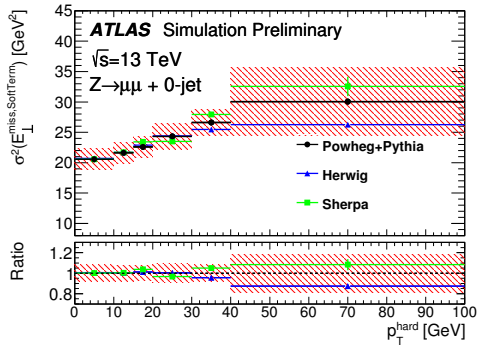

(c) $\sigma^2(E_{\perp}^{\mathrm{miss,soft}})$

Figure 5.18: RMS and mean of the $E_{\mathrm{T}}^{\mathrm{miss,soft}}$ projected into components longitudinal and transverse to $\mathbf{p}_{\mathrm{T}}^{\mathrm{hard}}$ in $Z(\mu\mu)$ + jets 0-jet events. Points are shown for POWHEG+PYTHIA (nominal), HERWIG and SHERPA generators. The shaded band shows the effect of the TST systematic uncertainties with contributions from the difference of generators, the change in detector geometry and the variation in bunch spacing.

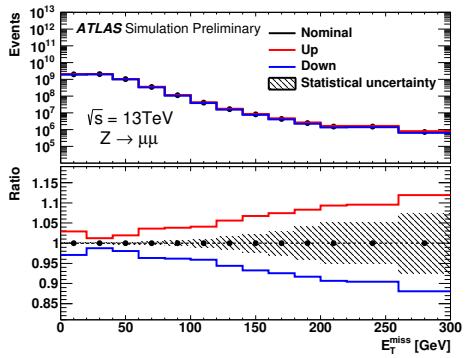

Figure 5.19: Total TST $E_{\mathrm{T}}^{\mathrm{miss}}$, and its variations, resulting from the combined TST systematic uncertainties. The hatched band shows the statistical uncertainty in the ratio.

CHAPTER 6

Particle Dark Matter Models

Specific models of DM production are needed for several scopes in mono-X analyses. Monte Carlo simulations of the signals on an event-by-event basis are essential to optimize the discovery potential of the searches; if a deviation was found from the SM expectations, a comparison of the observed excess to simulated signal events would help to characterize the excess. Benchmark models are usually considered more interesting if the associated relic abundance match the observed value and, at this aim, a detailed description of the model is needed to solve the Boltzmann equation. Specific signal hypothesis are also essential to compare the sensitivity of collider searches to that of direct detection and indirect detection experiments.

In this chapter the benchmarks models used in the mono-X searches and their connection with the DM problem are discussed, with a particular focus on those used in the mono-photon and mono-jet searches.

6.1 Introduction: effective field theories and simplified models

Since observations so far do not provide strong constraints on the nature of DM from the point of view of particle physics, Effective Field Theory (EFT) approaches have been studied as primary benchmark models in previous mono-X searches at the LHC and at the Tevatron. These EFTs assume that DM production occurs through contact interaction involving a quark-antiquark pair or two gluons and two DM particles. In this case, the $E_{\mathrm{T}}^{\mathrm{miss}}$ distribution of the signal is only determined by the nature and mass of the particle and the Lorentz structure of the interaction and only the overall production rate is a free parameter to be constrained or measured [87]. The contact interaction approximation holds when the momentum transfer in the collision is small compared to the typical suppression scale of the EFT. If this is the case, EFT models are quite simple and provide a way to compare the results with non-collider DM searches. When this is not the case, models involving the explicit production of a mediating particle can be used to describe DM interactions in a realistic way (see e.g. [88, 89]).

Simplified models are simple ultra-violet (UV) complete theoretical models which predict a DM candidate and an additional particle, mediating the interaction between DM

and SM particles. They are called 'simplified' because they involve a small number of additional parameters compared to the SM. These models do not arise from a simplification of particular complete theories, but are the result of additional renormalizable terms to the SM Lagrangian. The classification of these models is usually based on the properties of spin and parity of the mediator.

The complete discussion of the models used as benchmarks in the mono-X searches in the LHC experiments in Run 2 can be found in Reference [87]. In this chapter three models are introduced given their relevance in the mono-jet and mono-photon searches: an $s-$channel axial-vector (vector) mediator simplified model, which has been the primary benchmark in many DM searches since the beginning of Run 2; an EFT model which involves photons directly in the interaction with DM particles, and for which the mono-photon search has a unique sensitivity; and a $t-$channel colored scalar mediator model, the characterization and simulation of which has been an integral part of the author's work.

6.2 $s-$ channel axial-vector mediator

6.2.1 Model

A simple extension of the SM is given by adding a $U(1)$ symmetry under which the DM particle is colored. Quarks q and DM particles χ (a Dirac fermion) are assumed to interact via the exchange of an $s-$channel mediator Z' with vector or axial-vector interaction of the form:

$$\mathcal{L}_{axial-vector} = \sum_{q=u,d,c,s,b,t} g_q Z'_\mu \bar{q}\gamma^5\gamma^\mu q + g_\chi Z'_\mu \bar{\chi}\gamma^5\gamma^\mu \chi\,, \tag{6.1}$$

$$\mathcal{L}_{vector} = \sum_{q=u,d,c,s,b,t} g_q Z'_\mu \bar{q}\gamma^\mu q + g_\chi Z'_\mu \bar{\chi}\,,\gamma^\mu \chi \tag{6.2}$$

where g_χ is the coupling between the DM particle and the mediator, while g_q is the universal coupling between quarks and mediator. Leptons are explicitly assumed not to couple with the mediator, in order to avoid the constraints on the model parameter phase-space given by Drell-Yan data.

The leading order diagram for a mono-jet final state is shown in Figure 6.1.

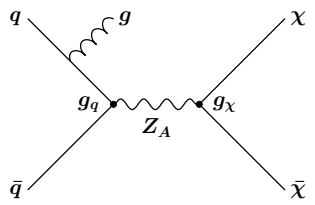

Figure 6.1: Leading order mono-jet process for the $s-$ channel axial-vector model.

Assuming that the mediator does not couple to any other visible or invisible states, the width of the mediator is set by the requirement that only the decays strictly necessary for the self-consistency of the model are possible (*minimal* width). The minimal width for the axial-vector and vector models takes the form:

$$\Gamma(m_{Z_A})_{\text{min}} = \frac{g_\chi^2 m_{Z_A}}{12\pi}\beta_\chi^3\theta(m_{Z_A}-2m_\chi) + \sum_q \frac{3g_q^2 m_{Z_A}}{12\pi}\beta_q^3\theta(m_{Z_A}-2m_q)\ , \tag{6.3}$$

$$\Gamma(m_{Z_V})_{\text{min}} = \frac{g_\chi^2 m_{Z_V}}{12\pi}\left(1+\frac{2m_\chi^2}{M_{Z_V}^2}\right)\beta_\chi\theta(m_{Z_V}-2m_\chi) + \sum_q \frac{3g_q^2 m_{Z_V}}{12\pi}\beta_q^3\theta(m_{Z_V}-2m_q)\ , \tag{6.4}$$

where $\theta(x)$ denotes the Heaviside function and $\beta_f = \sqrt{1-\frac{4m_f^2}{M^2_{Z_A/Z_V}}}$ is the velocity of the fermion f in the mediator rest frame.
The minimal set of parameters for these two models is then given by four parameters:

$$g_q,\ g_\chi\, m_\chi, m_{Z_A/Z_V}\ . \tag{6.5}$$

6.2.2 Kinematics in the invisible decay channel

The kinematics of this model are rather simple and the main characteristics are thereby mentioned.

- On-shell region: when $m_{Z_A/Z_V} > 2m_\chi$ the mediator is on-shell. The DM system recoils against the initial-state-radiation jet, which leads to a mono-jet signature. Experimentally the variable of interest is the $E_{\text{T}}^{\text{miss}}$, which has a falling spectrum, with a higher average $E_{\text{T}}^{\text{miss}}$ for higher mediator masses. For a given mediator mass, the $E_{\text{T}}^{\text{miss}}$ distribution is almost constant for varying m_χ, as illustrated in Figure 6.2(a); the cross-section decreases as the m_χ approaches m_{Z_A/Z_V}.

- Threshold: when $m_{Z_A/Z_V} \sim 2m_\chi$, the mediator production is resonantly enhanced and both the cross-section and the kinematic distributions change more rapidly as a function of the two masses.

- Off-shell region: when $m_{Z_A/Z_V} < 2m_\chi$ DM particles are produced via an off-shell mediator. The $E_{\text{T}}^{\text{miss}}$ spectrum hardens with increasing m_χ, accompanied by the gradual decrease of the cross section, as illustrated in Figure 6.2(a).

- Couplings dependence: lower couplings lead to lower production cross sections. Coupling values in the range 0.1-1.45, with $g_q = g_\chi$, correspond to a rough estimate of the lower sensitivity of mono-jet analyses and a maximum coupling value such that $\Gamma_{min} < m_{Z_A/Z_V}$. The shapes of the $E_{\text{T}}^{\text{miss}}$ and key variables do not depend on the couplings in these ranges, as illustrated in Figure 6.2(b).

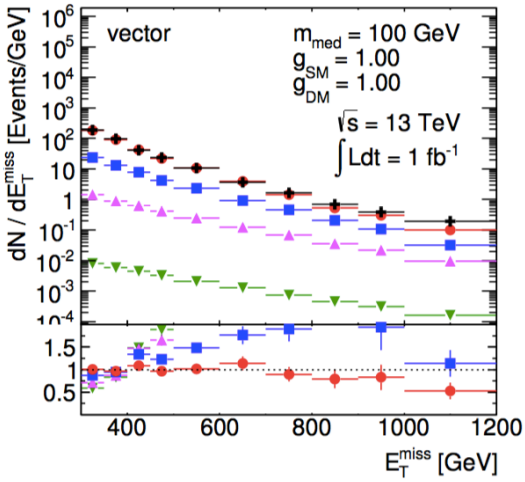

m_{DM} [GeV]	Γ/m_{med}	$\sigma \times A_{300}$ [fb]	$\sigma \times A_{500}$ [fb]
10	0.424	1.9e+04	1.8e+03
30	0.423	1.8e+04	1.7e+03
100	0.398	2.9e+03	4.1e+02
300	0.398	2.2e+02	5.2e+01
1000	0.398	1.6e+00	5.4e-01

(a) m_χ dependence

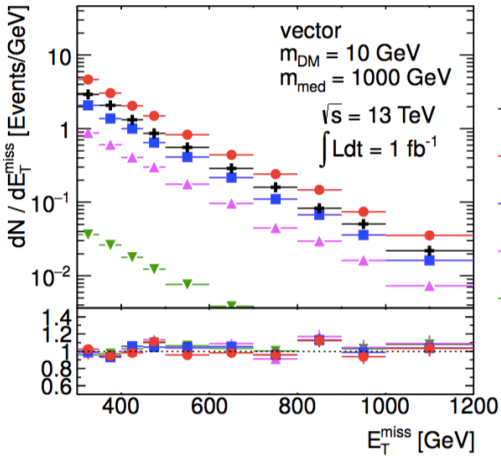

g_{SM}	g_{DM}	Γ/m_{med}	$\sigma \times A_{300}$ [fb]	$\sigma \times A_{500}$ [fb]
1.00	1.00	0.504	4.8e+02	1.2e+02
1.45	1.45	1.059	7.5e+02	1.8e+02
0.25	1.00	0.056	3.5e+02	9.0e+01
0.50	0.50	0.126	1.5e+02	3.8e+01
0.10	0.10	0.005	6.3e+00	1.6e+00

(b) couplings dependence

Figure 6.2: $E_{\mathrm{T}}^{\mathrm{miss}}$ distributions for different DM masses (a) and different couplings (b) for the vector mediator model. Ratios of the normalized distributions with respect to the first one are shown. A_{300} and A_{500} in the table denote the acceptance of the $E_{\mathrm{T}}^{\mathrm{miss}} > 300$ GeV and $E_{\mathrm{T}}^{\mathrm{miss}} > 500$ GeV cuts, respectively [87].

- Interaction dependence: comparing $E_{\mathrm{T}}^{\mathrm{miss}}$ distributions for vector and axial-vector interactions does not highlight significant differences for fixed massed and couplings. For on-shell mediators the cross sections of vector and axial-vector are similar; with increasing DM mass, when getting closer to the on-shell/off-shell transition, the relative difference between the cross sections increases, with the vector ones having larger cross sections.

The considerations on the kinematics and cross-section trends reported above for the mono-jet case are applicable to signatures where a photon, a W or a Z boson is radiated from the initial state partons instead of a gluon. The leading order Feynman diagram for the mono-photon case is shown in Figure 6.3. In general, in the case of the mono-photon and mono-V cross-sections are smaller than mono-jet, due to the higher probability to radiate a gluon compared to an electroweak boson.

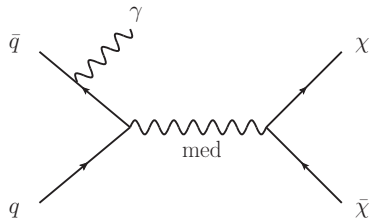

Figure 6.3: Leading order mono-photon process for the $s-$ channel axial-vector model.

6.3 Electroweak EFT model

This model predicts an electroweak boson accompanied by DM particles in the final state; as opposed to the $s-$ channel model, discussed in the previous section, the final-state boson does not come from initial-state radiation, but is directly involved in the interaction of the DM particles. To describe this interaction, an EFT dimension-7 operator is considered, given that a UV-complete model is not yet available for this kind of vertex. The Lagrangian for this model is parameterized by k_1 and k_2, which control the coupling to the $U(1)$ and $SU(2)$ gauge sectors of the SM, respectively. The interaction Lagrangian is [90, 91]:

$$\mathcal{L} = \frac{k_1}{\Lambda^3}\chi\bar{\chi}A_{\mu\nu}A^{\mu\nu} + \frac{k_2}{\Lambda^3}\chi\bar{\chi}F_{\mu\nu}F^{\mu\nu}\,, \tag{6.6}$$

where Λ is the EFT suppression scale and $A_{\mu\nu}$ and $F_{\mu\nu}$ are the field strength tensors of the $U(1)$ and $SU(2)$ sectors.

For the mono-photon final state, DM production proceeds via $q\bar{q} \to \gamma \to \gamma\chi\bar{\chi}$, without requiring initial-state radiation. The process is shown in Fig. 6.4.

The minimal set of parameters for this model is given by the four parameters

$$k_1,\, k_2,\, \Lambda,\, m_\chi. \tag{6.7}$$

The first three parameters only influence the cross-section. The dependence on m_χ modifies the $E_{\mathrm{T}}^{\mathrm{miss}}$ and photon p_{T} spectra only, with harder spectra obtained for higher values

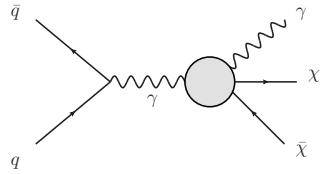

Figure 6.4: Leading order mono-photon process for the electroweak EFT model.

of m_χ, as shown in Figure 6.5.

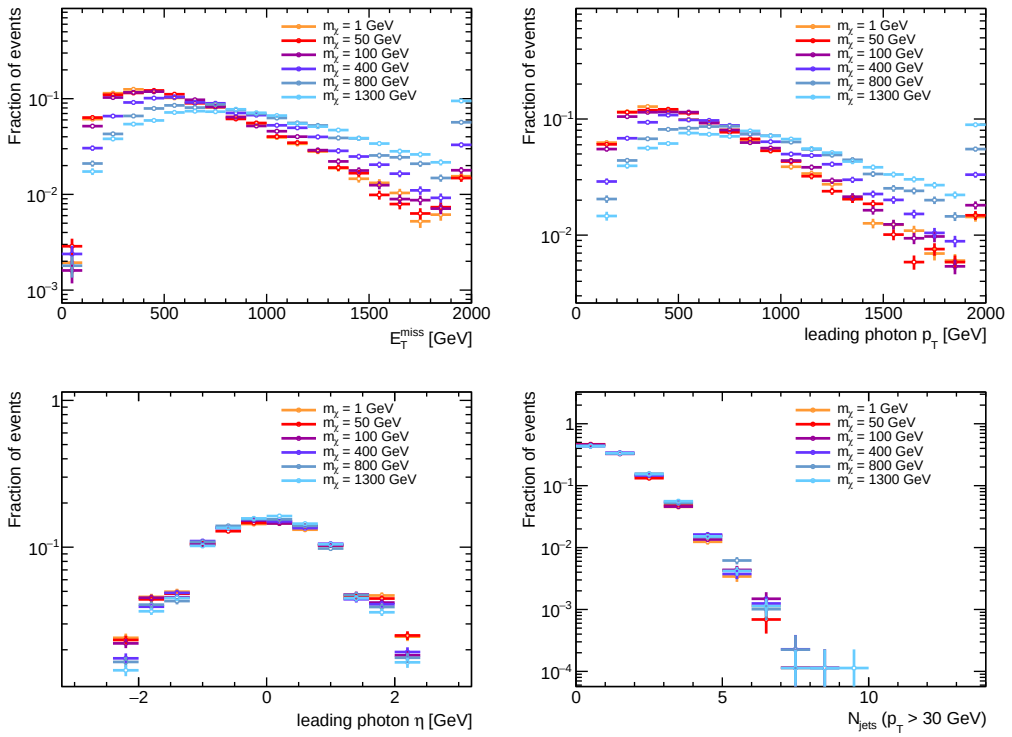

Figure 6.5: $E_{\mathrm{T}}^{\mathrm{miss}}$, leading photon p_{T}, leading photon η and jet multiplicity distributions for samples in the Electroweak EFT model with increasing m_χ. The other free parameters have been fixed to $k_1 = k_2 = 1$ and $\Lambda = 3.0$ TeV. Spectra are normalized to unity.

6.4 $t-$ channel colored scalar mediator

Section 6.2 addressed the case where the DM particles are produced via the exchange of an $s-$channel mediator. $t-$channel interactions are possible when SM and DM particles are coupled directly via the exchange of a colored mediator and this kind of interaction leads to a distinct phenomenology compared to the $s-$ channel model.

This section discusses in detail the generation procedure and the phenomenology of this

model for the mono-jet final state. While the model has been discussed previously in the literature (e.g. [92, 93, 94]), an interface with a parton shower was not available and the studies reported in this work constitute the first complete implementation of the model in a mono-jet final state at a collider experiment.

Previous characterization studies on the $t-$ channel model in the context of the LHC experiments [87] did not clearly establish whether this model presents a distinct phenomenology compared to that of the squark pair production in the MSSM theory. This question is addressed in the current discussion.

The model and its parameters are introduced in Section 6.4.1, the most relevant aspects of the generation procedure are discussed in Section 6.4.2, followed by the characterization in terms of kinematic distributions in Section 6.4.3. Section 6.4.4 discusses the connection of this model with the relic density constraints. More technical aspects of the validation procedure are reported in Appendix A.

6.4.1 Model

The $t-$channel model discussed here is a variation of the model by Bell et al. [93] and that by Papucci et al. [92]. It assumes that three colored spin-0 mediators $\eta_{(i)}$ couple to the SM quarks and to the DM particles, which are assumed Dirac spinors, with interaction Lagrangian:

$$\mathcal{L}_{\text{int}} = g_{q\chi} \sum_{i=1,2,3} \left(\eta_{(i),L} \bar{Q}_{(i),L}\right) \chi \,, \tag{6.8}$$

where g is the DM-quark coupling, and the sum is over the three quark doublets.

Each mediator is assumed to decay to the associated DM-quark pair with a branching fraction of 100% and minimal width of the form [87]:

$$\begin{aligned} \Gamma(\eta_{(i)} \to \bar{u}_{(i)}\chi) = \frac{g_{(i)}^2}{16\pi M_{\eta_{(i)}}^3} \left(M_{\eta_{(i)}}^2 - m_{u_{(i)}}^2 - m_\chi^2\right) \times \\ \times \sqrt{\left(M_{\eta_{(i)}}^2 - \left(m_{u_{(i)}} + m_\chi\right)^2\right)\left(M_{\eta_{(i)}}^2 - \left(m_{u_{(i)}} - m_\chi\right)^2\right)} \,, \end{aligned} \tag{6.9}$$

where, to ensure that the DM particle is stable and the mediator width is always defined, $m_\chi^2 + m_q^2 < M_\eta^2$ [1] and $4m_\chi^2/M_\eta^2 < \left(1 - m_q^2/M_\eta^2 + m_\chi^2/M_\eta^2\right)^2$ are required.

As the LHC is insensitive to the chirality of the quarks we assume for simplicity that the spin-0 mediator couples as an $SU(2)$ doublet to the left-handed quarks only. We also make the simplifying assumption that only the first two generations of mediator doublets $\eta_{(i)}$ are coupled and have degenerate masses and equal couplings. With these assumptions, the free parameters of the model are three:

$$m_\chi,\, M_\eta,\, g \,. \tag{6.10}$$

[1] We stress that the WIMP particle is assumed to be stable, i.e. $M_\eta > m_\chi$.

This model is referred to as $t-$channel model (as already done in [87] and e.g. in [92]) because it notably allows for t-channel interactions unlike other simplified and EFT models considered in previous mono-jet searches.

6.4.2 Generation procedure

The leading-order processes involved in the process with two DM particles and a single jet are shown in Figure 6.6(a), while (b) shows the relevant diagrams for the processes where two DM particles and two jets are produced. Also the second kind of processes are relevant in a mono-jet final state, since the ATLAS mono-jet selection puts a veto only on the fifth jet. It can be noticed that diagrams involving the exchange of mediators via $s-$ channel are present. In order to correctly simulate processes of this kind, which contain massive resonances which can go on-shell, we adopt a generation procedure which closely follows that described in [92] and therein motivated. The procedure requires that the generation of a given phase-space point is split according to the number of on-shell mediators. This is motivated by two reasons:

- if one generates only the contribution given by `pp > dm dm + (0,1,2)j`, this would not include any extra initial state radiation jets for the case of the mediator pair production. This is a problem when the difference in mass M_η-m_χ becomes small, since such contributions become important;
- the $t-$channel model admits the simultaneous presence of final-state partons with significantly different hard scales. In the scenario where `pp > j + med med, med > j dm` and $M_\eta \approx m_\chi$, the jet from hard scattering and the jet from the mediator decay may require a different matching treatment. Making a sample generation according to the number of on-shell mediators ensures that processes of this type are modeled correctly in the MC.

Samples are simulated at LO with MADGRAPH 5 v2.3.3 [95] and interfaced to PYTHIA 8.186[96]. The generation of each phase-space point is split into three subsamples:

- sample 1: the mediator is pair-produced in association with 0, 1, or 2 jets in MADGRAPH and then decayed by PYTHIA;
- sample 2: the mediator is produced in association with a DM particle plus 0, 1, or 2 jets in MADGRAPH with the decay of the mediator again performed by PYTHIA
- sample 3: the DM particles are pair-produced in association with 0, 1, or 2 jets.

For both samples 2 and 3, all internal $s-$ channel mediators are required to be off-shell in order to avoid phase space double-counting. This procedure is well defined when the mediator width is sufficiently small; otherwise a reweighting of the samples is needed to account for possible double counting across samples. The reweighting is described in detail in A.1.

The matching between MADGRAPH and PYTHIA is performed within the CKKW-L scheme [97]. The syntax of the matching process is tailored such that the merging is possible even for a final state where PYTHIA itself produces the decay products; this method allows to invoke the matching on the 'non-decayed' event. The parton matching scale is set to $M_\eta/8$ for split sample 1 and to 30 GeV for split samples 2 and 3. The validation of this choice is described in A.2.

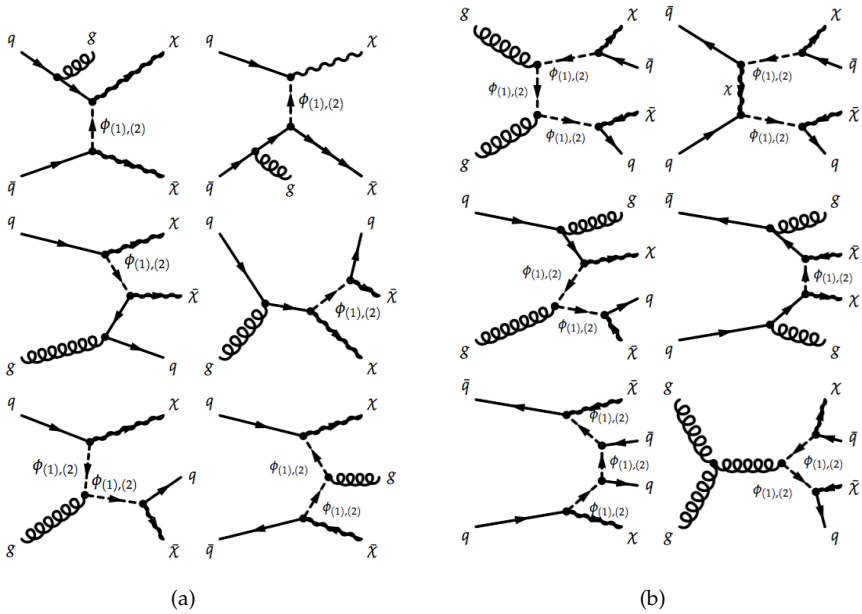

Figure 6.6: Leading order single-jet (a) and two-jet (b) processes from the $t-$ channel model, from [87]. Note that the mediator is indicated with the letter ϕ.

6.4.3 Kinematics

The model is characterized by a complex phenomenology, given the large number of diagrams involved. The kinematic characteristics of the full model can be understood in terms of the kinematics of the three classes of diagrams (samples 1,2,3) and their relative importance is ruled by the coupling g. The masses of the mediator and DM particle and their difference are also important to characterize the trends of the kinematic distributions and the cross-sections; in particular two mass regimes can be identified with different characteristics: the regime when the mediator is largely on-shell ($M_\eta \gg m_\chi$) and the compressed regime ($M_\eta \sim m_\chi$).

Split samples

In the on-shell regime, the kinematics of samples 1 and 2 are characterized by the presence of a Jacobian peak in the $E_{\mathrm{T}}^{\mathrm{miss}}$ and leading jet p_{T} distributions. This peak arises from

on-shell production of the mediator, approximately at rest, and is located at approximately $M_\eta/2$. When the mediator mass is sufficiently large, this leads to hard spectra and high jet multiplicities. When mediators in the internal lines cannot go on-shell, as in sample 3, the t-channel diagrams dominate and the kinematics are instead characterized by softer spectra and lower jet multiplicities. Key distributions of the three split samples and the combined sample are exemplified for a signal point in the on-shell regime in Figure 6.7.

In the compressed regime, the Jacobian peak of samples 1 and 2 is shifted to lower values and samples 1 and 2 present softer spectra compared to the on-shell regime. The kinematics of sample 3 are instead rather independent on the mass hierarchy between the DM particle and the mediator. These characteristics are illustrated in Figure 6.8.

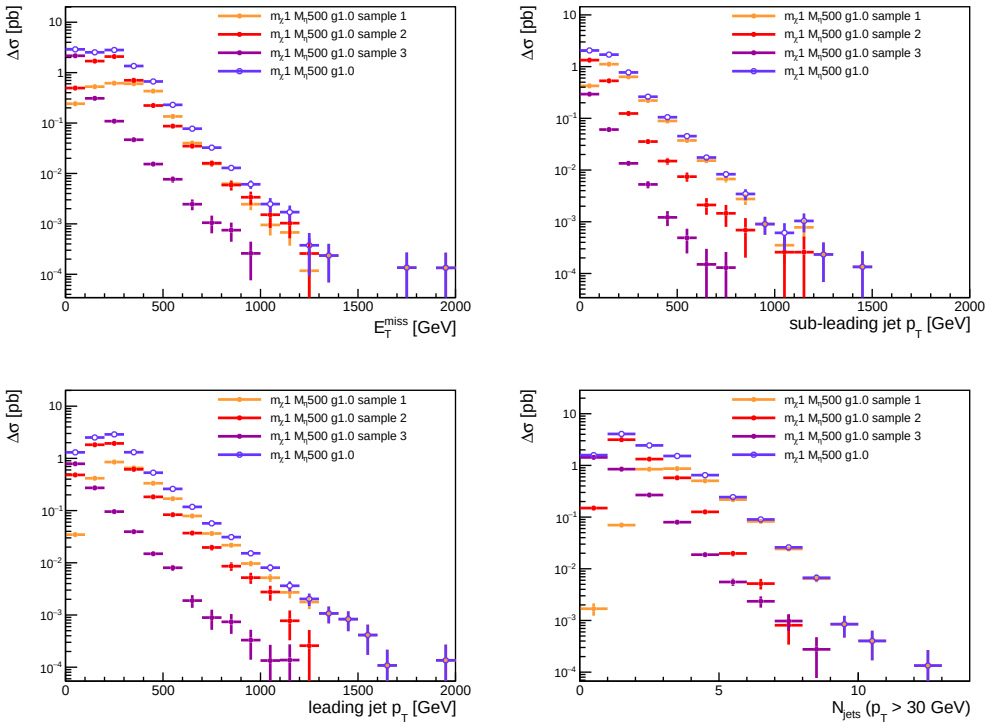

Figure 6.7: $E_{\mathrm{T}}^{\mathrm{miss}}$, leading jet p_{T}, sub-leading jet p_{T}, and jet multiplicity distributions for m_χ = 1 GeV, M_η = 500 GeV, $g = 1$. Distributions are shown separately for the split samples (closed markers, colors indicated in the legend), and for the combined sample (open markers). Spectra are normalized to their cross-section.

Mass dependence

When considering the combined samples, a pronounced dependence on the mediator mass can be seen in the kinematics, as demonstrated in Figure 6.9. This is mainly ruled

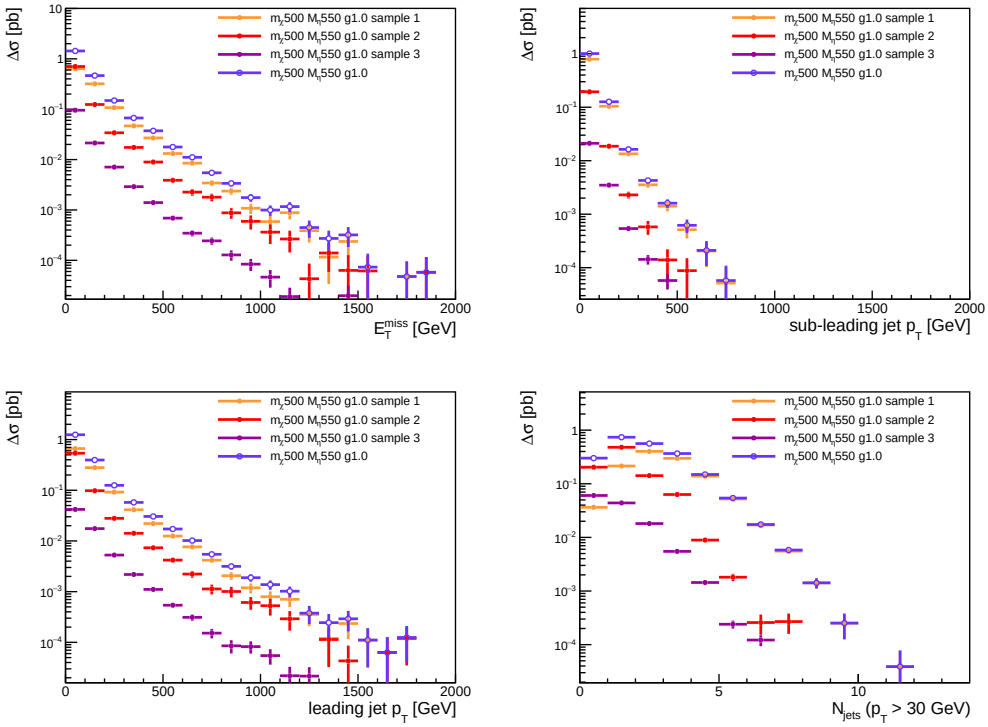

Figure 6.8: $E_{\mathrm{T}}^{\mathrm{miss}}$, leading jet p_{T}, sub-leading jet p_{T}, and jet multiplicity distributions for m_{χ} = 500 GeV, M_{η} = 550 GeV, $g = 1$. Distributions are shown separately for the split samples (closed markers, colors indicated in the legend), and for the combined sample (open markers). Spectra are normalized to their cross-section.

by the shift of the Jacobian peak to higher values with increasing mediator mass.

The dependence of the kinematics on the DM mass is instead mild, as shown in Figure 6.10. The shift of the $E_{\mathrm{T}}^{\mathrm{miss}}$ spectrum to lower values, when m_{χ} is large, is due to the smaller phase space available for the mediator decay.

Figure 6.11 shows the dependence of the cross-section on the mass parameters: at fixed m_{χ}, the cross-section decreases rather steeply with increasing M_{η}. At fixed M_{η}, the cross-section decreases with increasing m_{χ}: the dependence is mild when the mediator is largely on-shell, it becomes steeper in the compressed regime.

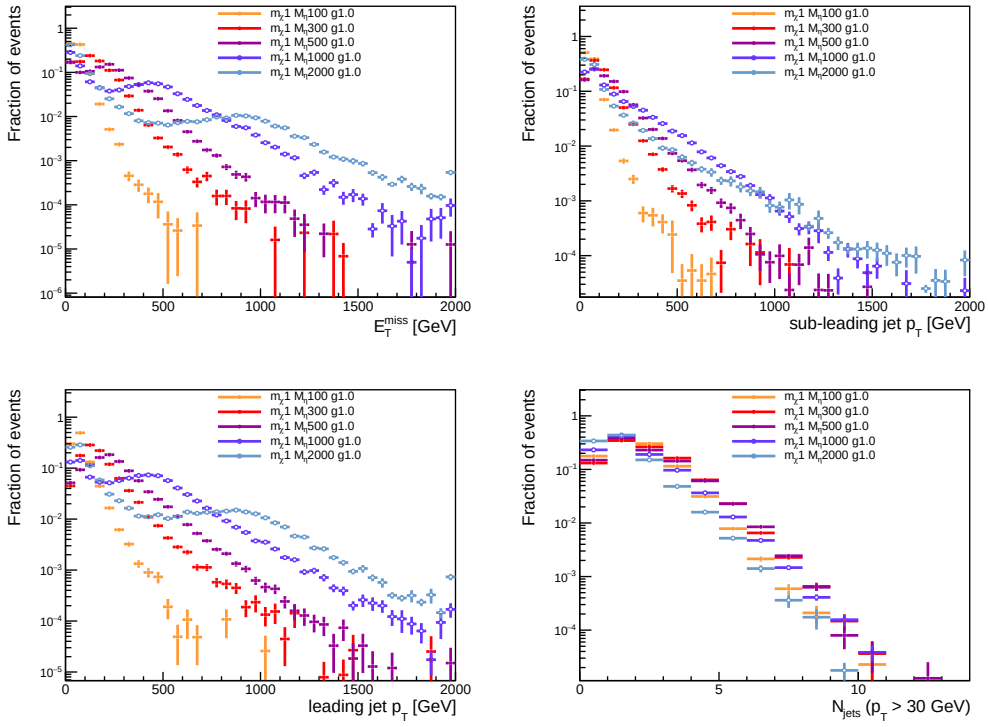

Figure 6.9: $E_{\mathrm{T}}^{\mathrm{miss}}$, leading jet p_{T}, sub-leading jet p_{T}, and jet multiplicity distributions of the combined sample for m_{χ} = 1 GeV, $g = 1$ and several values of M_{η}. Spectra are normalized to unity.

Coupling dependence

Higher values of the coupling leads to higher cross-sections. Also the kinematics of the model present a pronounced coupling dependence, as opposed to the $s-$channel model. This happens because in the case of the t − channel model, the coupling strength rules the relative importance of the various sub-samples: in particular when the coupling is low, the cross-section for sample 1 is much higher than for the other sub-samples and the kinematics are subsequently dominated by this contribution. When the coupling is instead larger, the cross-section for sample 3 becomes important and all samples play

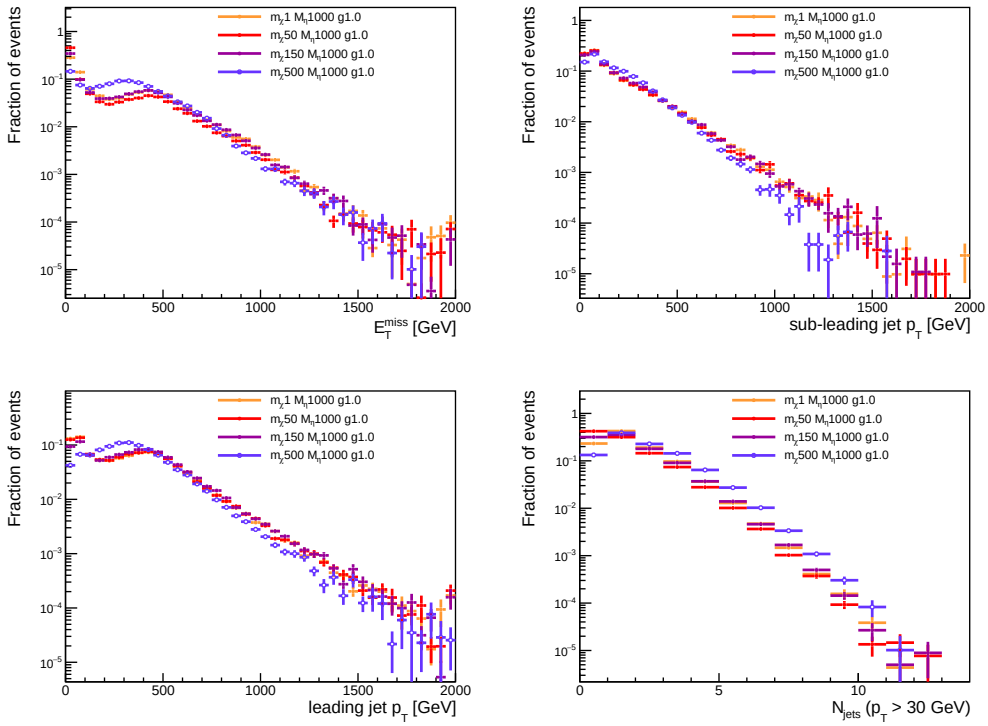

Figure 6.10: $E_{\mathrm{T}}^{\mathrm{miss}}$, leading jet p_{T}, sub-leading jet p_{T}, and jet multiplicity distributions of the combined sample for M_η = 1000 GeV, $g = 1$, and several values of m_χ. Spectra are normalized to unity.

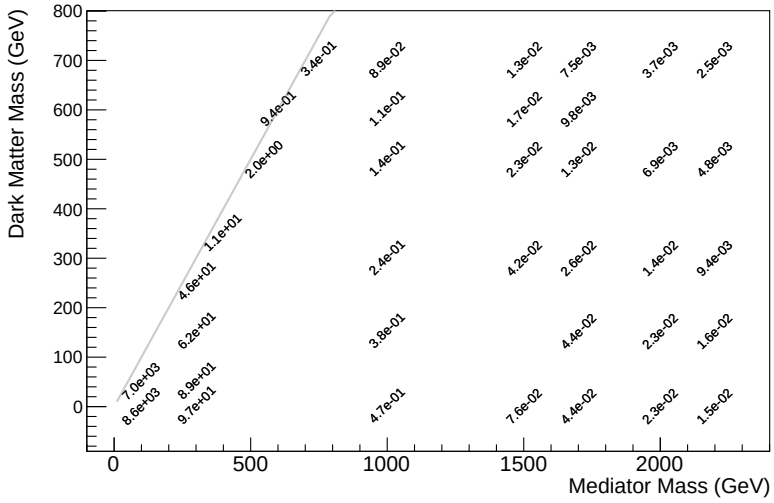

Figure 6.11: Cross-sections, expressed in pb, for several $t-$ channel signal points in the $m_\chi - M_\eta$ plane at fixed coupling $g = 1$.

a role in determining the kinematic distributions. This is demonstrated for the on-shell regime in Figure 6.12 for two choices of couplings: $g = 0.25$ and $g = 1.0$.

In the compressed regime, instead, sample 3 is sub-dominant for all couplings, therefore the dependence on the coupling is less pronounced as illustrated in Figure 6.13

The coupling dependence is also an important consideration for the characterization of the $t-$ channel model in comparison with the simplified model that describes the production of light squarks in the context of SUSY searches. The two models have similar Lagrangians, with the most important difference being the coupling, which is fixed and proportional to the weak coupling in the SUSY case, and is instead a free parameter in the $t-$ channel model. We find that the kinematics and the cross-sections predicted by the SUSY model are recovered for low values of the g coupling in the $t-$ channel model, while the $t-$ channel model predicts a distinct phenomenology for higher values of g. This is illustrated for example in Figure 6.14, where, at fixed M_η and m_χ, the kinematic distributions of the $t-$ channel model for several values of g are compared to those obtained in this SUSY scenario.

Further details regarding the comparison between the two models are reported in A.3.

6.4.4 Relic density constraints

The computation of the relic density, $\Omega_\chi h^2$, predicted by the $t-$ channel model is performed with MadDM 2.0.6 [98] in order to ascertain whether or not the model is sufficient to explain the dark matter abundance observed in the universe today. The model settings used for the computation are chosen consistently with those chosen for the generation of the samples.

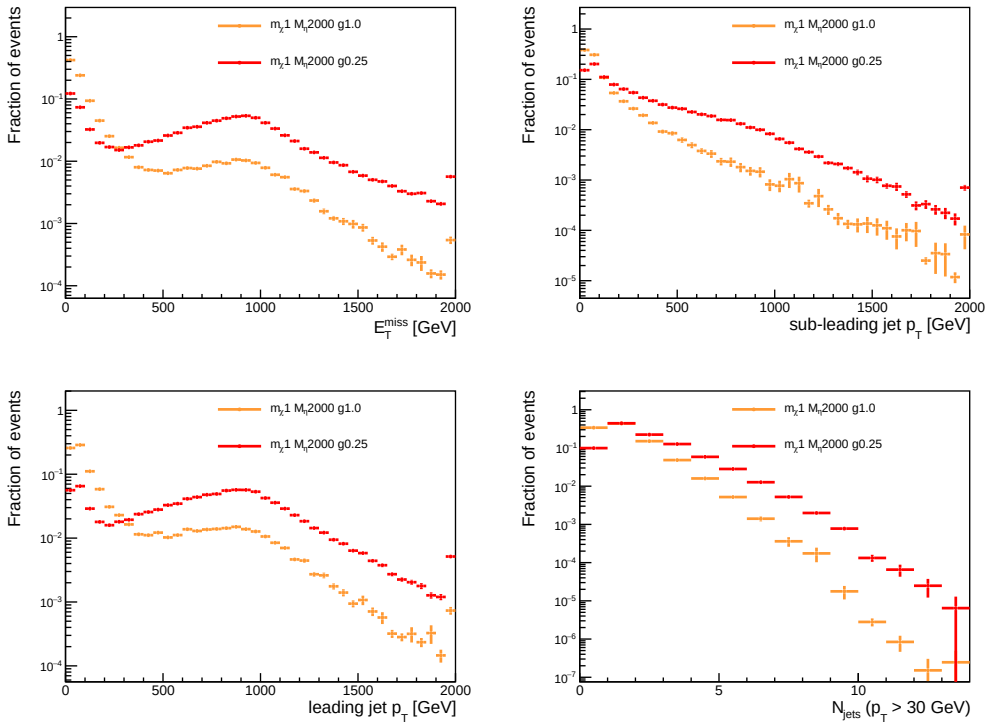

Figure 6.12: $E_{\mathrm{T}}^{\mathrm{miss}}$, leading jet p_{T}, sub-leading jet p_{T}, and jet multiplicity distributions for m_χ = 1 GeV, M_η = 2000 GeVand two values of the coupling: $g = 0.25$, $g = 1.0$. Spectra are normalized to unity.

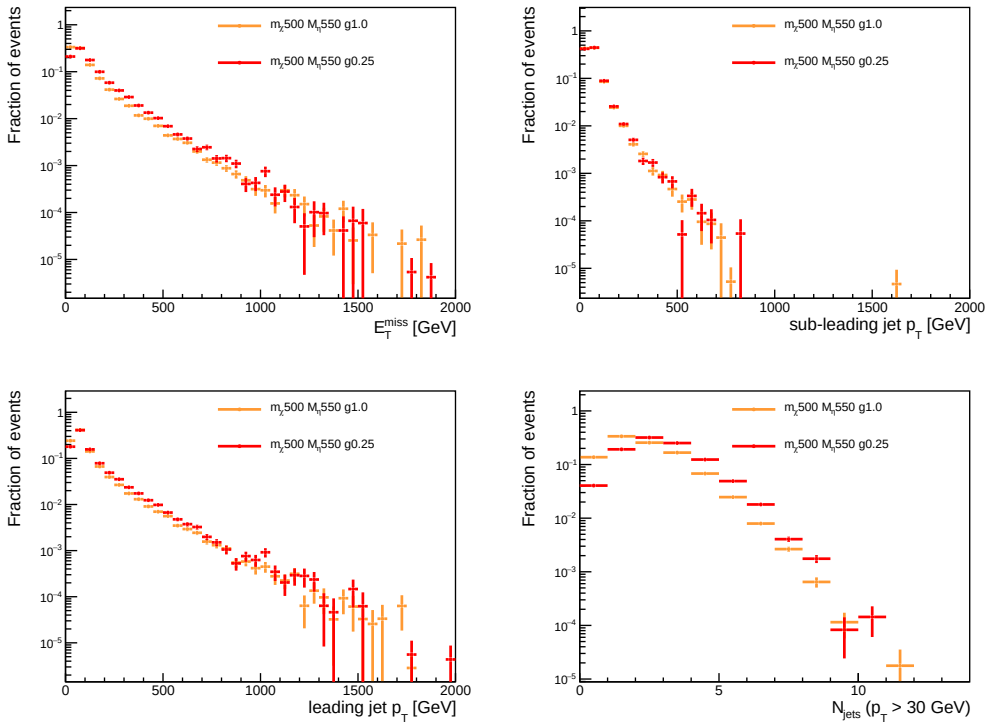

Figure 6.13: $E_{\mathrm{T}}^{\mathrm{miss}}$, leading jet p_{T}, sub-leading jet p_{T}, and jet multiplicity distributions for m_{χ} = 500 GeV, M_{η} = 550 GeVand two values of the coupling: $g = 0.25$, $g = 1.0$. Spectra are normalized to unity.

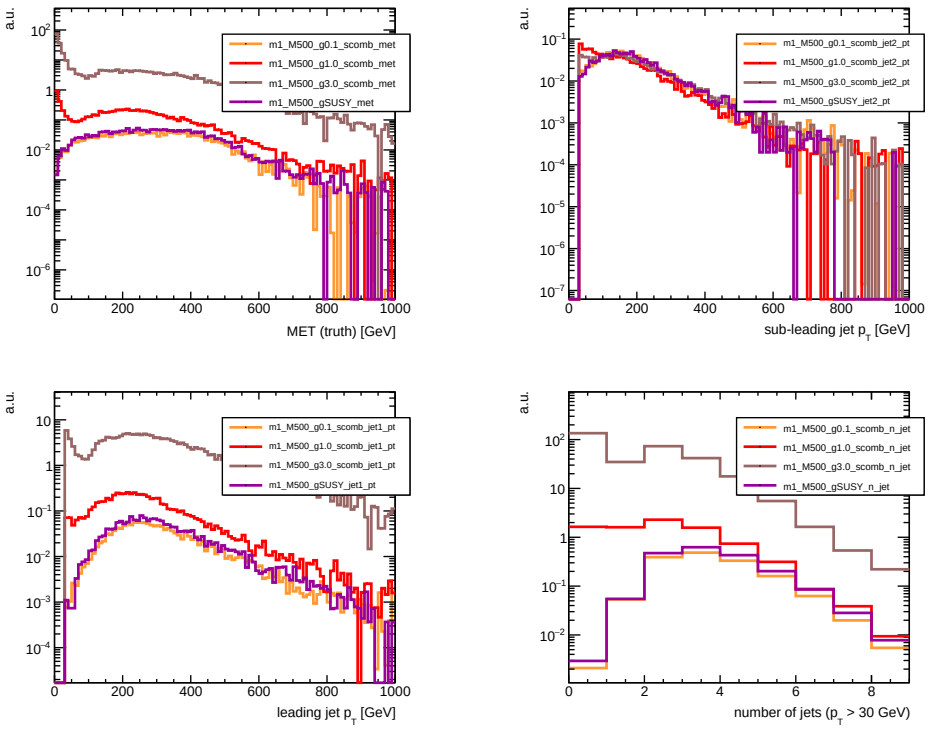

Figure 6.14: $E_{\mathrm{T}}^{\mathrm{miss}}$, leading jet p_{T}, sub-leading jet p_{T}, and jet multiplicity distributions for m_{χ} = 1 GeV, M_{η} = 500 GeV. The distributions for the $t-$channel model with several couplings ($g = 0.1$ in orange, $g = 1.0$ in red, $g = 3.0$ in grey) are compared to the distributions for the MSSM model (purple). Spectra are normalized to their cross-section.

A scan of the dark matter and mediators masses is performed for various coupling choices as shown in Figure 6.15: for each point of the scan the predicted relic density is compared to the value $\Omega_\chi h^2 = 0.12$ as observed by Planck [19]. Regions of the parameter space where the predicted relic density is lower than the observed value are indicated in green, while regions where the t − channel interaction predict an over-abundance of dark matter are indicated in grey. As the coupling grows, increasingly large regions of parameter space become viable.

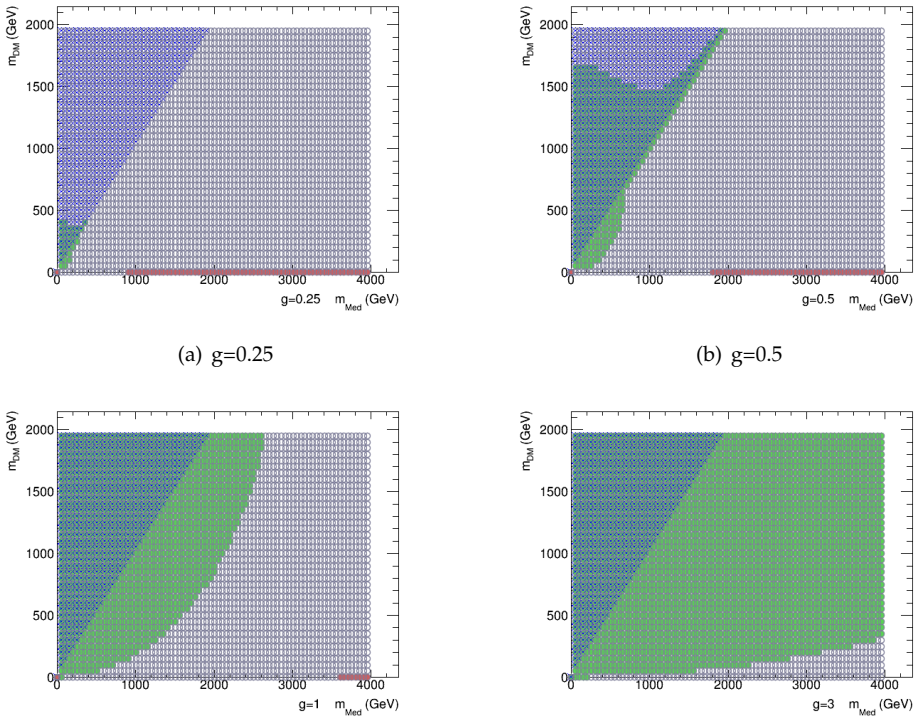

(a) g=0.25

(b) g=0.5

(c) g=1.0

(d) g=3.0

Figure 6.15: Scan over mediator and dark matter masses for different values of the coupling g. Green points indicate where the predicted $\Omega_\chi h^2 < 0.12$; red points indicate the cases in which the computation performed by MadDM failed; blue points indicate where the mediator width is zero.

6.4.5 Parameters scan

The coupling regime that we consider interesting ranges between the values 0.25 and 1: couplings strengths lower than 0.25, while in principle interesting, lead to kinematic distributions that are too similar to those coming from light squark-pair production in the MSSM. Higher values of the coupling, while interesting in terms of relic density, lead to increasingly larger mediator widths, thus implying additional subtleties in the splitting and recombination procedure of the samples.

For the mass parameters, we consider the case where $M_\eta > m_\chi$: when the mediator is largely on-shell, the large independence of the cross-section and kinematics from the dark matter mass does not require a fine granularity; the compressed regime instead requires a finer granularity, since the cross-section of samples 1 and 2 quickly decreases when approaching the diagonal ($M_\eta = m_\chi$). Figure 6.16 illustrates the signal grid employed in the mono-jet analysis for the coupling value $g = 1$: the regions with finer granularity are those where the sensitivity of the analysis is expected to decrease.

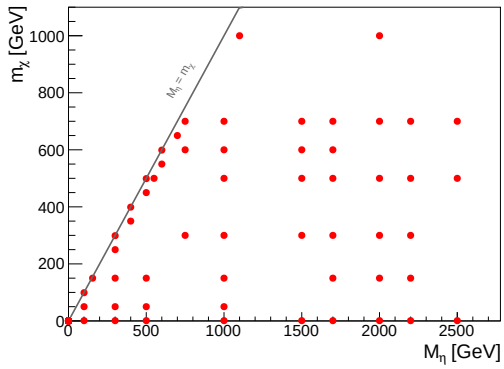

Figure 6.16: Grid of the points generated for the $t-$channel model for coupling $g = 1$. The line at $M_\eta = m_\chi$ indicates the kinematic limit of the phase-space of the model.

CHAPTER 7

Mono-Photon Search with 2015 Data

Collider reactions characterized by the presence of a large missing transverse momentum ($E_{\mathrm{T}}^{\mathrm{miss}}$) recoiling against a visible object X are called 'mono-X' or '$E_{\mathrm{T}}^{\mathrm{miss}}$ + X' and are sensitive channels to physics beyond the Standard Model predicting new invisible particles in the final state. Searches in the mono-X channels usually do not target specific signals, but rather look for statistically significant deviations from the predicted background due to Standard Model processes in well-defined phase-spaces, driven by the experimental signature of interest.

A common aspect to analyses with large $E_{\mathrm{T}}^{\mathrm{miss}}$ in the final state is the dominant and irreducible source of background from the production of Z decaying to neutrinos, which yields exactly the same signature as the signal. The precise estimation of this background is the key challenge of these analyses. The most straightforward way to predict this background is to rely on the MC simulation. However, predictions from MC usually come with large experimental, modeling and theoretical uncertainties. For a more refined estimation, it is common practice to correct the normalization of the MC prediction for the data-to-simulation ratio calculated in regions where no signal is expected (control regions). In practice, the MC simulation is fitted to the data in several of these control regions simultaneously, thereby determining the absolute value of the MC prediction (normalization) and constraining the systematic uncertainties on such prediction (nuisance parameters). Making use of control regions, which are kinematically similar to the region of interest (or signal region), allows for a reduction of the impact of the systematic uncertainties with reduced extrapolation from the control regions to the region of interest.

In the mono-photon analysis, the problem of estimating the irreducible $Z(\nu\nu)\gamma$ background is tackled by defining control regions enriched in $Z(\ell\ell)\gamma$ events, where the selection of the events is based on a modified computation of the $E_{\mathrm{T}}^{\mathrm{miss}}$ in which the p_{T} of the leptons is vectorially added to the standard $E_{\mathrm{T}}^{\mathrm{miss}}$ calculation; in such regions, the kinematics of the $Z(\ell\ell)\gamma$ process mimic those of the $Z(\nu\nu)\gamma$ process. In Chapter 8 an evolution of this approach will be discussed in the context of the mono-jet search.

The present chapter is dedicated to the discussion of the analysis of mono-photon final states with the data collected by ATLAS during 2015 at a center-of-mass energy of 13 TeV [3]. After a brief introduction to the mono-photon signature (Section 7.1), Sec-

tion 7.2 discusses the data and the MC simulation samples used for the analysis; Sections 7.3 and 7.4 cover the definition of the physics objects and the event selection, respectively. The background estimation is examined in Section 7.5. Section 7.7.1 is dedicated to the test of the background estimation strategy in a validation region. The results of the background estimation in the signal region are described in Section 7.7.2; the systematic uncertainties are reviewed in Section 7.6. Finally the interpretation of the results in terms of model-independent limits and in the context of the DM models examined in Chapter 6 is dealt with in Section 7.8.

7.1 Mono-photon signature

The mono-photon signature consists of events characterized by a large missing transverse momentum recoiling against a high-p_{T} photon, no additional leptons and at most one jet. As opposed to other mono-X signatures, the mono-photon final state is characterized by a low level of background coming from SM processes. Multijet processes, top quark and W + jets and Z + jets processes, which are abundant backgrounds for many searches at the LHC, are strongly reduced by the large $E_{\mathrm{T}}^{\mathrm{miss}}$ selection, by the requirement of a highly energetic photon and by the veto on extra jets. Besides the irreducible $Z(\nu\nu)\gamma$ background, an important source of background consists in events with a W boson decaying leptonically, produced in association with a photon, where the lepton is missed.

7.2 Data and Simulation samples

This analysis is performed on the data from proton-proton collision at $\sqrt{s} = 13$ TeV recorded by ATLAS at the LHC during 2015. The data sample used corresponds to a total integrated luminosity of 3.2 fb^{-1}, collected with a bunch spacing of 25 ns.

Sections 7.2.1 and 7.2.2 report the details of the samples used for this analysis along with the generators and the most important parameters adopted for the generation of the events.

7.2.1 Signals

Dark Matter samples The Dark Matter models considered for this search have been described in Chapter 6. The values of the free parameters and of the event generation settings were chosen following the recommendations of the ATLAS/CMS DM forum [87].

Samples of DM production in simplified models are generated via an s-channel mediator with axial-vector interactions. The abbreviation for this model is indicated with 'dmA'. The g_q coupling is set to be universal in quark flavour and equal to 0.25, g_χ is set to 1.0, and Γ_{med} is computed as the minimum width allowed given the couplings and masses. The PDF set used is NNPDF30_lo_as_0130 [99]. MG5_aMC@NLO v2.2.3 [95] is used to generate the events, in conjunction with PYTHIA 8.186 [100] with the NNPDF2.3LO PDF set [101, 102] and the A14 set of tuned parameters (tune) [103]. A photon with at

least 130 GeV of transverse momentum is required in MG5_aMC@NLO. For a fixed m_χ, higher m_{med} leads to harder p_{T}^{γ} and $E_{\text{T}}^{\text{miss}}$ spectra. For a very heavy mediator (≥ 10 TeV), EFT conditions are recovered.

For DM samples from an EFT model involving dimension-7 operators (referred to as 'EW EFT model') with a contact interaction of type $\gamma\gamma\chi\bar{\chi}$, the parameters which only influence the cross section are set to $k_1 = k_2 = 1.0$ and $\Lambda = 3.0$TeV. A scan over a range of values of m_χ is performed. The settings of the generators, PDFs, underlying-event tune and generator-level requirements are the same as for the simplified model DM sample generation described above.

ADD samples Also samples from the ADD model of LED [104] have been used for the analysis optimization. This model aims to solve the hierarchy problem by hypothesizing the existence of n additional spatial dimensions of size R, leading to a new fundamental scale M_{D} related to the Planck mass, M_{Planck}, through $M_{\text{Planck}}^2 \approx M_{\text{D}}^{2+n} R^n$. If these dimensions are compactified, a series of massive graviton (G) modes results. Stable gravitons would be invisible to the ATLAS detector, but if the graviton couples to photons and is produced in association with a photon, the detector signature is a $\gamma + E_{\text{T}}^{\text{miss}}$ event. Signal samples for ADD models are simulated with PYTHIA, using the NNPDF2.3LO PDF with the A14 tune. A requirement of $p_{\text{T}} > 100\ GeV$ is applied to the leading-order (LO) matrix elements for the $2 \to 2$ process to increase the efficiency of event generation. Simulations are run for two values of the scale parameter M_{D} (2.0 and 3.0 TeV) and with the number of extra dimensions, n, varied from two to six.

7.2.2 Background samples

The SM processes which can lead to a mono-photon final state are the following:

- $Z(\nu\nu)\gamma$: this is the only irreducible SM background;
- $W(\tau\nu)\gamma$: the τ can either decay leptonically and be missed or decay hadronically and be reconstructed as a jet;
- $W(e\nu)\gamma$: the e is not reconstructed, or is reconstructed as a γ;
- $W(\mu\nu)\gamma$: the μ is not reconstructed;
- $Z(\ell\ell)\gamma$: both taus, electrons or muons are missed;
- $Z(\nu\nu) +$ jets: a jet fakes a γ;
- $W(e\nu) +$ jets: the e or a jet fakes a γ;
- $W(\mu\nu)+$jets and $W(\tau\nu)+$jets: the μ/τ is not reconstructed or the τ is reconstructed as a jet and a jet fakes a γ;
- $t\bar{t}$, single-t and diboson: similar to the $W +$ jets backgrounds;

- γ + jets and multi-jet: a high fake $E_{\mathrm{T}}^{\mathrm{miss}}$ is produced by a miscalibration or misreconstruction of a jet or a γ and a jet fakes a γ in the case of multi-jet.

For $Z\gamma$ and $W\gamma$ backgrounds, events containing a charged lepton and neutrino or a lepton pair together with a photon and possible associated jets are simulated using the SHERPA 2.1.1 generator [105]. The matrix elements including all diagrams with three electroweak couplings are calculated with up to three partons at LO and merged with SHERPA parton shower [106] using the ME+PS@LO prescription [107]. The CT10 PDF set [108] is used in conjunction with a dedicated parton shower tuning developed by the SHERPA authors. For $Z(\ell\ell)\gamma$ events a requirement on the dilepton invariant mass of $m_{\ell\ell} > 10$ GeV is applied at generator level.

For the γ + jets process, events containing a photon with associated jets are simulated using SHERPA 2.1.1, generated in several bins of photon p_{T} from $35\,\mathrm{GeV}$ up to larger than $1\,\mathrm{TeV}$. The matrix elements are calculated at LO with up to three partons (lowest p_{T} slice) or four partons and merged with SHERPA parton shower using the ME+PS@LO prescription.

The CT10 PDF set is used in conjunction with the dedicated parton shower tuning.

For W/Z + jets backgrounds, events containing W or Z bosons with associated jets are also simulated using SHERPA 2.1.1. The matrix elements are calculated for up to two partons at NLO and four partons at LO using the Comix [109] and OpenLoops [110] matrix element generators and merged with SHERPA parton shower using the ME+PS@NLO prescription [111]. As in the case of the γ + jets samples, the CT10 PDF set is used together with the dedicated parton shower tuning. The W/Z+jets predictions are normalized to NNLO cross sections [112]. These samples are also generated in several p_{T} bins.

Multi-jet processes are simulated using the PYTHIA 8.186 generator. The A14 tune is used together with the NNPDF2.3LO PDF set. The EvtGen v1.2.0 program [113] is used to simulate the bottom and charm hadron decays.

Diboson processes with four charged leptons, three charged leptons and one neutrino or two charged leptons and two neutrinos are simulated using the SHERPA 2.1.1 generator. The matrix elements contain all diagrams with four electroweak vertices. They are calculated for up to one parton (for either four charged leptons or two charged leptons and two neutrinos) or zero partons (for three charged leptons and one neutrino) at NLO, and up to three partons at LO using the Comix and OpenLoops matrix element generators and merged with SHERPA parton shower using the ME+PS@NLO prescription. The CT10 PDF set is used in conjunction with the dedicated parton shower tuning. The generator cross sections are used in this case, which are at NLO.

For the generation of $t\bar{t}$ and single top quarks in the Wt and s-channel, the POWHEG-BOX v2 [114, 115] generator is used, with the CT10 PDF set used in the matrix element calculations. For all top processes, top-quark spin correlations are preserved. For t-channel production, top quarks are decayed using MadSpin [116]. The parton shower, fragmentation, and the underlying event are simulated using PYTHIA 6.428 [117] with the CTEQ6L1 [118] PDF sets and the corresponding Perugia 2012 tune [119]. The top

mass is set to 172.5 GeV. The EvtGen v1.2.0 program is used for properties of the bottom and charm hadron decays.

Multiple pp interactions in the same or neighboring bunch crossings superimposed on the hard physics process (referred to as pile-up) are simulated with the soft QCD processes of PYTHIA 8.186 using the A2 tune [120] and the MSTW2008LO PDF set [121]. The events are weighted to accurately reproduce the average number of interactions per bunch crossing in data.

All simulated samples are processed with a full ATLAS detector simulation [122] based on GEANT4 [123] and reconstructed using the same software as that used for collision data.

7.3 Physics objects definition

Among the collections of physics objects available, each analysis chooses the object definitions that are most suitable for the scope of the analysis. Typically *baseline* objects are defined with looser identification criteria and are used for pre-selection cuts, while *signal* objects are defined with tighter criteria and are usually used for the main kinematical cuts of the analysis.

The reconstruction of the physics objects has been described in detail in Chapters 4 and 5. Calibrations and scale factors are applied to the physics objects to account for the differences between data and MC in the calibration, reconstruction, identification and isolation efficiency.

The definitions and criteria used for this analysis are described below.

Photons

- **Baseline photons:** *loose* identification, $p_{\mathrm{T}} > 10$ GeV[1], $|\eta| < 2.37$, excluding the crack region $1.37 < |\eta| < 1.52$.
- **Signal photons:** same as the baseline photons, but with *tight* identification, and isolation criterion given by: $E_T^{iso} < 0.022\, p_{\mathrm{T}}^{\gamma}$ + 2.45 GeV.

Electrons

- **Baseline electrons:** *medium* identification, $p_{\mathrm{T}} > 7$ GeV and $|\eta| < 2.47$. Also standard requirements on the significance of the impact parameter are applied, as explained in Section 4.3.3.
- **Signal electrons:** same as baseline electrons and in addition the *loose* isolation is required.

Muons

[1]Throughout the chapter, the notation p_{T} will be used instead of E_T to indicate the p_{T} of the photon, as measured from the energy deposits in the EM calorimeter.

- **Baseline muons:** *medium* identification, $p_{\mathrm{T}} > 6$ GeV and $|\eta| < 2.7$, $|d_0|/\sigma_{d_0} < 3.0$ and $|z_0| \sin\theta < 0.5$ mm.
- **Signal muons:** same as baseline muons and in addition *loose* isolation working point.

Jets reconstructed using the anti-k_t algorithm with $R = 0.4$ and calibrated at the EM+JES scale. Hadronic decays of the tau-leptons are treated as jets in the analysis.

- **Baseline jets:** $p_{\mathrm{T}} > 20$ GeV, $|\eta| < 4.5$.
- **Signal jets:** $p_{\mathrm{T}} > 30$ GeV, $|\eta| < 4.5$. In addition, to remove jets originating from pile-up, JVT > 0.64 is applied to jets with $|\eta| < 2.4$ and $30\,\mathrm{GeV} < p_{\mathrm{T}} < 50\,\mathrm{GeV}$.

Missing transverse momentum

The baseline objects described above are used as input for the $E_{\mathrm{T}}^{\mathrm{miss}}$ reconstruction to allow a $E_{\mathrm{T}}^{\mathrm{miss}}$ definition as coherent as possible to the objects defined in the analysis; similarly, hadronic decays of τ leptons are treated as jets.

The 'Soft Term' computation used is that of the TST, as explained in Section 5.2.3.

In addition to the standard computation for the $E_{\mathrm{T}}^{\mathrm{miss}}$, two additional definitions of $E_{\mathrm{T}}^{\mathrm{miss}}$ are used, where the p_{T} of the signal electrons or of the signal muons are added to the standard $E_{\mathrm{T}}^{\mathrm{miss}}$ calculation:

$E_{\mathbf{T}}^{\mathbf{miss}}(\textbf{no-}\mu)$: computed as $E_{\mathrm{T}}^{\mathrm{miss}}$ but adding the p_{T} of signal muons vectorially;

$E_{\mathbf{T}}^{\mathbf{miss}}(\textbf{no-}e)$: computed as $E_{\mathrm{T}}^{\mathrm{miss}}$ but adding the p_{T} of signal electrons vectorially;

Despite the different computations, these variants are denoted with the same notation ($E_{\mathrm{T}}^{\mathrm{miss}}$) throughout the chapter.

Overlap removal To resolve ambiguities which occur in the object reconstruction and identification, an overlap removal procedure which follows the recommendations of [124] is performed. The overlap removal is performed on the baseline objects and in the following order:

- if an electron shares its inner detector track with a muon, the electron is removed and the muon is kept, in order to remove electron candidates coming from radiation off the muon, followed by photon conversion.
- If a photon and an electron are found within $\Delta R < 0.4$ the object is interpreted as an electron and the photon is discarded. This permits to reduce the electron-to-photon fake rate;
- if a photon and a muon are found within $\Delta R < 0.4$ the object is interpreted as a muon and the overlapping photon is discarded, as it is likely that it comes from radiation off the muon;
- if a jet and an electron are found within $\Delta R < 0.2$ the object is interpreted as an electron and the jet is discarded, to avoid double-counting;

- if instead a jet and an electron are found within $0.2 < \Delta R < 0.4$ the object is interpreted as a jet and the electron is discarded, as it is likely that the electron comes from the decay of an in-jet hadron;
- if a jet and a muon are found within $\Delta R < 0.4$, then the muon is discarded, since it probably comes from decay of an in-jet hadron; however, if the number of tracks with $p_{\mathrm{T}} > 0.5\,\mathrm{GeV}$ associated with the jet is less 3, the jet is discarded, because it is likely to be seeded by muon radiation;
- finally, if a photon and a jet are found within $\Delta R < 0.4$, the object is interpreted as a photon and the overlapping jet is discarded to avoid double counting.

7.4 Event selection

7.4.1 Pre-selection

The preselection cuts are designed to select interesting events and reject the ones where a detector issue has occurred. Most of these requirements are common to many ATLAS physics analyses.

- **Data quality**: only data recorded in periods with stable beam conditions and optimal functional conditions of the detector are used for physics analyses. *Good Runs Lists* are provided for each period of data taking and are organized in lists of runs, the quality of which has been assessed by the Data Quality groups of the various sub-detectors.
- **Trigger**: events are selected if the HLT trigger finds a photon candidate with $p_{\mathrm{T}} > 120$ GeV and loose isolation. This trigger item is indicated as `HLT_g120_loose`.
- **Good vertex**: only events with a reconstructed primary vertex with at least two associated tracks are kept.
- **Jet cleaning**: events with any $BadLoose$ jet, not overlapping with neither leptons nor photons, with $p_{\mathrm{T}} > 20$ GeV are rejected.
- **Event cleaning**: other corrupted events which are not excluded by the criteria of the Good Runs Lists are rejected, such as events with a noise burst in the Liquid Argon calorimeter and events with a variety of problems in the Tile calorimeter. Events written on disk more than once, due to problems at DAQ or derivation level, are sometimes present. The duplicates are removed.

7.4.2 Trigger efficiency

In contrast with the analysis performed in Run 1, a photon trigger is employed instead of a $E_{\mathrm{T}}^{\mathrm{miss}}$ trigger; the photon trigger has a sharper turn-on, with a full efficiency already at 150 GeV. Furthermore, the single photon trigger can be used throughout all analysis control regions.

The efficiency of HLT_g120_loose trigger has been studied in first data and measured as a function of the calibrated p_{T} of the offline leading photon, satisfying the *tight* identification criterion and with $|\eta| < 2.37$ excluding the calorimeter crack region. The events are selected based on the pre-selection criteria mentioned above, except that the photon trigger is replaced by the HLT trigger on $E_{\mathrm{T}}^{\mathrm{miss}}$ with threshold at 100 GeV (HLT_xe_100). The turn on curve is shown in Figure 7.1 for data and MC simulation. The MC simulation includes all the most important background processes, normalized according to their cross section, as described in Section 7.5.1. The measured efficiency in data and MC is shown with the statistical uncertainty in Table 7.1 for two different cuts on the p_{T} of the leading photon corresponding to the thresholds in the validation region (125 GeV, see Sec. 7.4.5) and in the signal region (150 GeV, see Sec. 7.4.3).

For $p_{\mathrm{T}}^{\gamma} > 150$ GeV the trigger is fully efficient in data and in simulation; for $p_{\mathrm{T}}^{\gamma} > 125$ GeV the measured efficiencies in data and simulation differ by 1%.

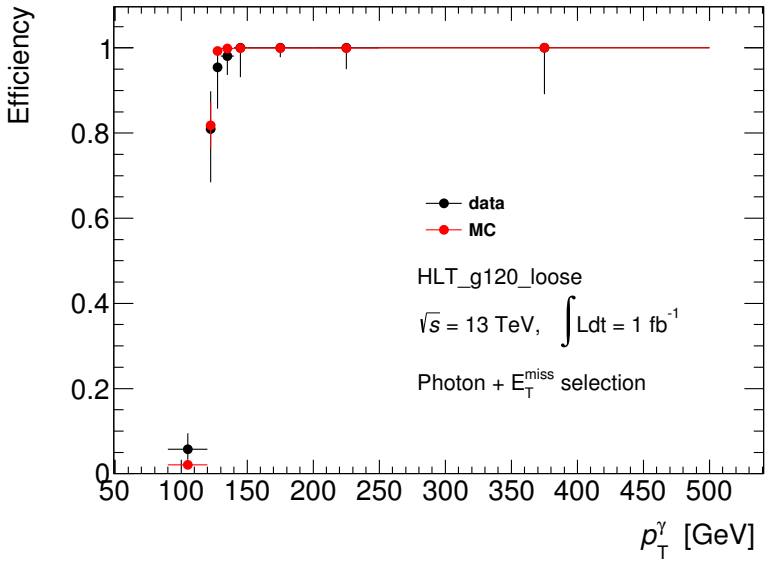

Figure 7.1: Trigger efficiency in data and MC for HLT_g120_loose trigger shown as a function of the offline leading photon p_{T}.

	$p_{\mathrm{T}}^{\gamma} > 125$ GeV	$p_{\mathrm{T}}^{\gamma} > 150$ GeV
Efficiency in data	0.991 + 0.005 - 0.010	0.997 + 0.003 - 0.008
Efficiency in MC	0.9991 + 0.0001 - 0.0001	0.99996 + 0.00004 - 0.00004

Table 7.1: Trigger Efficiencies for HLT_g120_loose in data and MC for different cuts on the leading photon p_{T}.

7.4.3 Signal region

The set of pre-selection and selection requirements define a *region*: events in a given region have common features but may come from different processes. The most important region for the analysis is the signal region, SR, populated by events with one energetic photon and large $E_{\mathrm{T}}^{\mathrm{miss}}$. The SR selection criteria are optimized in order to have a high significance of the expected signal over the predicted background.

Events in the SR are selected by requiring:

- $E_{\mathrm{T}}^{\mathrm{miss}} > 150\,\mathrm{GeV}$;
- at least 1 baseline photon;
- the leading photon must be a signal photon and have $p_{\mathrm{T}} > 150\,\mathrm{GeV}$;
- the leading photon must not overlap with $E_{\mathrm{T}}^{\mathrm{miss}}$: $\Delta\phi(\gamma, E_{\mathrm{T}}^{\mathrm{miss}}) > 0.4$;
- jet veto: events with at most one signal jet are retained; if there is a jet, this jet must have $\Delta\phi(E_{\mathrm{T}}^{\mathrm{miss}}, \mathrm{jet}) > 0.4$;
- lepton veto: events with any baseline electron or muon are discarded.

Optimization of the signal region definition

The choice of the selection cuts used for the SR starts from the selections used for the Run 1 analysis [125], but some requirements are revisited for this analysis. In these studies, the background expectations are extracted from MC simulations.

The cut on the leading photon has been increased from 125 GeV (in Run 1) to 150 GeV, in order to select a symmetric configuration between the $\mathbf{E}_{\mathrm{T}}^{\mathrm{miss}}$ and the photon $\mathbf{p}_{\mathrm{T}}$; the linear correlation between $E_{\mathrm{T}}^{\mathrm{miss}}$ and photon p_{T} is a characteristic of the signal samples investigated in the analysis.

The η acceptance of the leading photon has been extended from 1.37 to 2.37; this is motivated by the higher significance of the signal over the background with the looser cut, as shown for a selection of signal samples in Figure 7.2. The figure of merit used for this study is the asymptotic significance:

$$Z = \sqrt{2 \cdot \left((N_{\mathrm{sig}} + N_{\mathrm{bkg}}) \log\left(1 + N_{\mathrm{sig}}/N_{\mathrm{bkg}}\right) - N_{\mathrm{sig}} \right)} \tag{7.1}$$

7.4.4 Control regions

The control regions are chosen in such a way to be kinematically very close to the SR, but orthogonal to it; they are built by reverting one or more selection requirement of the SR; a given CR is optimized to be dominated by a given process. Four control regions (CRs) are defined: one enriched in $W\gamma$, two in $Z\gamma$ and one in γ + jets backgrounds.

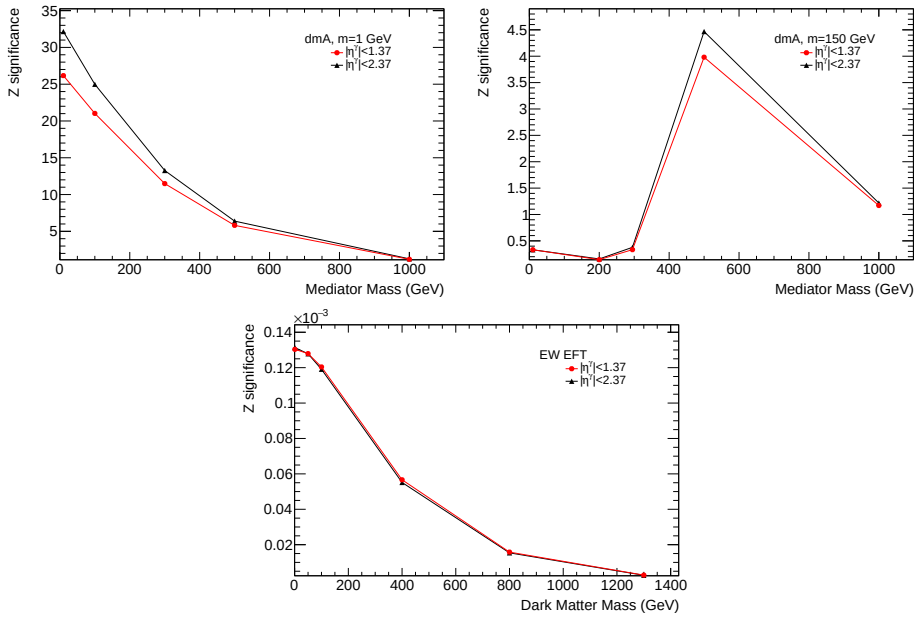

Figure 7.2: Significance Z for the dmA and EW EFT models when extending the threshold on the $|\eta^{\gamma}|$ requirement from 1.37 to 2.37 in the SR.

- **Single-Muon Control Region**, CR$\gamma\mu$: the same selection of the SR is applied, except for the muon veto: it is required that exactly one signal muon is present in the event. For this control region the $E_{\mathrm{T}}^{\mathrm{miss}}$ calculation is from the $E_{\mathrm{T}}^{\mathrm{miss}}$(no-$\mu$) variant. This region is mainly enriched in $W(\mu\nu)\gamma$ events.

- **Two-Muon (Two-Electron) Control Region**, CR$\gamma\mu\mu$ (CRγee): the same selection of the SR is applied, except for the lepton veto: it is required that exactly two signal muons (electrons) are present in the event and no baseline electron (muon). The $E_{\mathrm{T}}^{\mathrm{miss}}$ calculation is from the $E_{\mathrm{T}}^{\mathrm{miss}}$(no-$\mu$) ($E_{\mathrm{T}}^{\mathrm{miss}}$(no-$e$)) variant. The Two-muon (Two-Electron) invariant mass is required to be greater than 20 GeV to be coherent with the generator level cut of the $Z\gamma$ and $W\gamma$ background samples. This second kind of control regions is enriched mainly in $Z(\mu\mu)\gamma$ and $Z(ee)\gamma$ events, respectively.

  Figure 7.3 shows a comparison between $E_{\mathrm{T}}^{\mathrm{miss}}$ distributions in the MC: that of $Z(\nu\nu)\gamma$ in the SR, that of $Z(\mu\mu)\gamma$ in the CR$\gamma\mu\mu$ and $Z(ee)\gamma$ in the CRγee. It can be seen, that within the statistical fluctuations these variables have the same distribution.

- **Photon-Jet Control Region**, CRγj: the same selection of the SR is applied except for a lower $E_{\mathrm{T}}^{\mathrm{miss}}$ range: $85\,\mathrm{GeV} < E_{\mathrm{T}}^{\mathrm{miss}} < 110\,\mathrm{GeV}$ to enrich this region of γ + jets background.

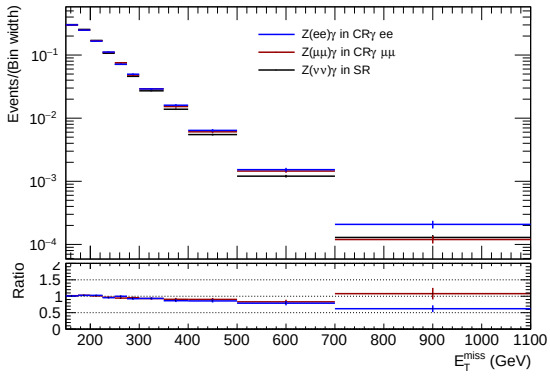

Figure 7.3: Comparison of $E_{\mathrm{T}}^{\mathrm{miss}}$ distributions with or without lepton p_{T} added, according to the region: $Z(\nu\nu)\gamma$ in the SR, $Z(\mu\mu)\gamma$ in the CR$\gamma\mu\mu$ and $Z(ee)\gamma$ in the CRγee.

7.4.5 Validation region

A validation region (VR) is defined in view of validating the background estimation techniques before unblinding the SR. At this aim, the region is chosen to be as similar as possible to the signal region in the background composition and in the statistical uncertainty, while keeping the signal contamination to a minimum.

For the definition of the VR a smaller dataset is used compared to that used for the full analysis; it corresponds to 1 fb^{-1}of the data collected at $\sqrt{s} = 13$ TeV.

The events in this region are selected with the same criteria used for the signal region, except for lower $E_{\mathrm{T}}^{\mathrm{miss}}$ and p_{T}^{γ} cuts, to increase the statistical power of the dataset considered and to dilute the signal contamination, and for a cut on the $\Delta\phi(\gamma, E_{\mathrm{T}}^{\mathrm{miss}})$, to suppress the signal contamination. In particular it is required:

$$E_{\mathrm{T}}^{\mathrm{miss}} > 110\,\mathrm{GeV}, \quad p_{\mathrm{T}}^{\gamma} > 125\,\mathrm{GeV}, \quad \Delta\phi(\gamma, E_{\mathrm{T}}^{\mathrm{miss}}) < 3.0 \tag{7.2}$$

While this definition of the VR partially overlaps with that of the SR, it still provides a better validation as compared to the validation strategy employed in the Run 1 analysis [125], where the VR was orthogonal to the SR but at the cost of changing the $E_{\mathrm{T}}^{\mathrm{miss}}$ regime radically.

Figure 7.4 shows the $\Delta\phi(\gamma, E_{\mathrm{T}}^{\mathrm{miss}})$ distribution of several signal samples; the residual signal contamination after the $\Delta\phi(\gamma, E_{\mathrm{T}}^{\mathrm{miss}}) < 3.0$ requirement varies from 20% to 35% depending on the particular signal model. The effect of the residual signal contamination in the VR is estimated to be negligible by comparing the significance of the signal over the background between the current VR and the SR of the Run 1 analysis. In order to perform the comparison, the MC backgrounds are rescaled to the 8 TeV cross-section and to the integrated luminosity of Run 1. A few representative signal samples (of the EW EFT and ADD models) are tested and their asymptotic significance is shown for several thresholds of the $\Delta\phi(\gamma, E_{\mathrm{T}}^{\mathrm{miss}})$ cut in Table 7.2.

From this table it can be seen that the sensitivity to signal discovery in the VR is lower than that obtained by the Run 1 analysis, which had not found any sign of new physics.

The choice of the VR with the threshold at 3.0 for the $\Delta\phi(\gamma, E_{\mathrm{T}}^{\mathrm{miss}})$ is found to provide a sufficiently low signal contamination ($Z_{\mathrm{VR}}/Z_{\mathrm{SR@8}TeV} < 1$), while keeping the statistical power of the sample to a reasonable level.

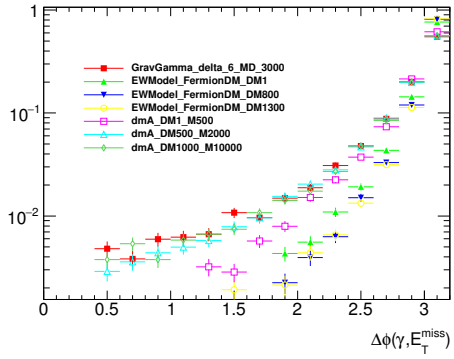

Figure 7.4: Distribution of $\Delta\phi(\gamma, E_{\mathrm{T}}^{\mathrm{miss}})$ for several signal samples.

	Ratio of significances $Z_{\mathrm{VR}}/Z_{\mathrm{SR@8}TeV}$			
$\Delta\phi(\gamma, E_{\mathrm{T}}^{\mathrm{miss}})$	ADD n=2	ADD n=6	EW EFT m_χ=100 GeV	$N_{\mathrm{VR}}^{bkg}/N_{\mathrm{SR}}^{bkg}$
2.85	0.11	0.58	0.20	0.19
2.90	0.13	0.68	0.23	0, 22
2.95	0.16	0.81	0.29	0.25
3.0	0.19	0.97	0.36	0.31
3.05	0.25	1.24	0.48	0.37

Table 7.2: Optimisation of the $\Delta\phi(\gamma, E_{\mathrm{T}}^{\mathrm{miss}})$: the columns show the cut value and the ratio of the asymptotic significance in VR and the one in SR at 8 TeV for a few representative signal samples. The final column shows the ratio between the number of expected events in the VR and nominal SR.

Control regions of the VR

Four control regions are defined similarly as the nominal CRs described in Section 7.4.4, except for the thresholds on $E_{\mathrm{T}}^{\mathrm{miss}}$ and p_{T}^{γ}:

$$E_{\mathrm{T}}^{\mathrm{miss}} > 110\,\mathrm{GeV}, \quad p_{\mathrm{T}}^{\gamma} > 125\,\mathrm{GeV}. \tag{7.3}$$

These control regions are used to estimate the background in the VR, and are named: CR$\gamma\mu$(VR), CR$\gamma\mu\mu$(VR), CRγee(VR), CRγj(VR).

7.5 Background estimation

An overview of the background processes which yield a mono-photon final state was given in Section 7.2.2.

The dominant background process is the $Z(\nu\nu)\gamma$, which is irreducible; secondary contributions come from $W(\ell\nu)\gamma$, where the lepton is outside the detector acceptance or passes the lepton veto, or, in the case of tau decaying hadronically, is reconstructed as a jet. The $Z(\ell\ell)\gamma$ processes enter the signal region in a similar way but such cases are rare because both leptons have to pass the signal region cuts. $\gamma +$ jets events enter the SR if fake $E_{\mathrm{T}}^{\mathrm{miss}}$ above threshold is produced by a miscalibration or misreconstruction of a photon or a jet. For these backgrounds control regions are built reverting one or more cuts used to define the Signal Region, allowing one of these processes to become dominant (see Section 7.4.4). The control regions are fitted simultaneously to the data, using MC predictions rescaled such to match the data yields, as explained in 7.5.1.

The processes which lead to a mono-photon final state due to the presence of electrons or jets misidentified as photons, such as $W/Z +$ jets, $t\bar{t}$ and diboson, are evaluated with two data-driven techniques, which are described in Sections 7.5.2 and 7.5.3, respectively.

Non-collision backgrounds are highly suppressed by applying the jet cleaning and the *tight* identification cut on the leading photon. An additional criterion is employed to further suppress this background, as explained in Section 7.5.4.

Table 7.3 summarizes the techniques used for the estimation of the different sources of background.

Process	Background estimation method
$Z(\nu\nu)\gamma$	simultaneous fit to the data
$W(\ell\nu)\gamma$	simultaneous fit to the data
$Z(\ell\ell)\gamma$	simultaneous fit to the data
$\gamma +$ jets	simultaneous fit to the data
fake photons from electrons	Tag&Probe method, Sec. 7.5.2, data-driven
fake photons from jets	2-dim sideband method, Sec.7.5.3, data-driven
non-collision background	Sec.7.5.4, data-driven

Table 7.3: Background estimation techniques used for the different processes contributing to the signal region.

7.5.1 Simultaneous fitting technique

A simultaneous fit in the CRs and the SR, based on the profile likelihood approach, is used as the baseline technique for the background estimation and for the signal extraction. This technique enables to predict the signal and background yields in both CRs and SR exploiting the data constrain in all these regions at the same time. The use of the simultaneous fit allows a straightforward combination of multiple CRs and permits a coherent treatment of the correlation of the systematic uncertainties across the different

regions.
Technically, the implementation of the likelihood and the statistical treatment of the results is performed by means of the HistFitter package [126].

The likelihood model employed for this analysis is hereby described.
Let:

- r run over the signal or control regions;
- the random variable N_r^{obs} be the observed total yield in the region r;
- $N_r^X = N_r^X(\theta)$ be the expected yield of process X in the region r;
- $\vec{\theta}$ be the vector of nuisance parameters describing systematic uncertainties on the predicted yield of each background in each region;
- μ be the free parameter associated to the normalisation of the considered signal (*signal strength*);
- $\vec{\kappa}$ be the vector of free parameters of the fit, the $\kappa-$ factors, associated to the normalization of the backgrounds, $\vec{\kappa} = \left(\kappa^W, \kappa^Z, \kappa^\gamma\right)$.

Then the likelihood $\mathcal{L}$ is defined as:

$$\mathcal{L}(\mu, \vec{\kappa}, \vec{\theta}) = \prod_r \text{Poisson}\left(N_r^{\text{obs}} \mid \mu N_r^{\text{sig}}(\vec{\theta}) + N_r^{\text{bkg}}(\vec{\kappa}, \vec{\theta})\right) f_{\text{constr}}(\vec{\theta}), \tag{7.4}$$

where

$$\begin{aligned} N_r^{\text{bkg}} = {} & \kappa^Z \times N_r^{Z(\nu\nu)\gamma} \\ & + \kappa^W \times (N_r^{W(\tau\nu)\gamma} + N_r^{W(\mu\nu)\gamma} + N_r^{W(e\nu)\gamma}) \\ & + \kappa^Z \times (N_r^{Z(\tau\tau)\gamma} + N_r^{Z(\mu\mu)\gamma} + N_r^{Z(ee)\gamma}) \\ & + \kappa^\gamma \times N_r^{\gamma\text{+jets}} \\ & + N_r^{\gamma\text{-from-e}} + N_r^{\gamma\text{-from-jet}}. \end{aligned} \tag{7.5}$$

From the above equation, it is clear that the $Z(\nu\nu)\gamma$ and $Z(\ell\ell)\gamma$ processes share the same normalisation factor, while $W(\ell\nu)\gamma$ processes are multiplied by a different one.
The dependence of N_r^X on the nuisance parameters $\vec{\theta}$ (which allow for fluctuations with respect to the nominal prediction of the yield of each process) is omitted in Eq. 7.5 to simplify the notation. The term f_{constr} of Eq. 7.4 represents the product of Gaussian constraints applied to each of the nuisance parameters.
With the exception of $N_r^{\gamma\text{-from-e}}$ and $N_r^{\gamma\text{-from-jet}}$ which are data-driven, the expected prefit yield of a given process in a given region is obtained from the MC simulation and computed as follows:

$$N_r^X = \frac{\sum_j^{\text{sel in } r} w_i^{MC} w_i^{PU} w_i^{eSF} w_i^{\mu SF}}{\sum_n^{\text{gen}} w_n^{MC}}, \times\sigma \times \epsilon_{\text{filter}} \times \mathcal{L} \tag{7.6}$$

where the sum in the numerator runs over the selected events in the region r, while the sum in the denominator runs over the generated events in the MC sample.

- w_i^{MC} is the event weight associated to the generation of the event;
- w_i^{PU} is the event weight associated to the pile-up reweighting procedure [127];
- $w_i^{e/\mu SF}$ is the total event scale factor which accounts for the data/MC difference in the reconstruction, identification and isolation efficiency of the selected (vetoed) electrons and muons in the event (see below for more details);
- σ is the cross-section of the sample;
- ϵ_{filter} is the filter efficiency associated to the MC sample, if a filter at generation level is applied;
- $\mathcal{L}$ is the integrated luminosity.

Lepton scale factors

Lepton scale factors are applied in the lepton-enriched control regions to account for differences between data and simulation in the reconstruction, identification and isolation efficiency of the leptons. They are applied as provided by the combined performance groups.
For the regions with explicit vetoes on the leptons, such as the `SR`, scale factors need to be determined to correct for the differences in the veto efficiency between data and simulation. Thanks to the connection with the efficiency scale factors, average veto scale factors are computed over a simulation sample as follows:

- the total number of events (with and without leptons) is imposed to be conserved before and after applying the lepton efficiency scale factors in a given simulation sample:

$$\begin{aligned} N_{tot} &= N_{0\ell} + N_{\geq 1\ell} \\ &= \langle SF_{veto} \rangle N_{0\ell} + \sum_{i=1}^{N_{\geq 1\ell}} w_i \\ &= \langle SF_{veto} \rangle N_{0\ell} + \langle SF \rangle N_{\geq 1\ell} \end{aligned} \tag{7.7}$$

  where $\ell = e, \mu$, $\langle SF_{veto} \rangle$ is the average veto efficiency scale factor, w_i is the efficiency scale factor weight applied to each event and $\langle SF \rangle$ is its average value in the sample;

- $\langle SF \rangle$ is computed for each sample, separately for electrons and muons, selecting events which pass a relaxed $E_{\text{T}}^{\text{miss}}$ and p_{T}^{γ} cuts and the requirement of at least one baseline lepton,

- the average veto scale factor is determined as:

$$\langle SF_{veto} \rangle = 1 + (1 - \langle SF \rangle) \frac{N_{\geq 1\ell}}{N_{0\ell}} \tag{7.8}$$

  and applied on simulated events, depending on whether the region they fall in has a lepton veto.

Fitting procedures

Two fitting procedures are employed in the analysis:

- **CR-only counting fit**: it is used primarily for the estimation of background and to assess the impact of systematic uncertainties on the background expectation. It uses the likelihood model described in Eq. 7.5, except that the terms in the CRs are not included and the signal component is set to zero ($\mu = 0$);
- **CR+SR counting fit**: it is used for the interpretation of the results in terms of the considered signal models. It uses the full likelihood described in Eq. 7.5.

7.5.2 Electrons faking photons

Electrons and photons have very similar signatures in the EM calorimeters. The converted photons also leave a signal in the tracking system. These effects make the electron/photon separation difficult and a fraction of electrons are mistakenly identified as photons.
In order to derive the contribution of such fake photons to the event yield, a two-step approach is taken:

fake rate estimation: in the first step, the probability of electrons to fake photons (fake rate) is measured. The fake rate is measured through a tag-and-probe method which selects events with one signal electron (tag) and one electron/photon (probe); the tag-and-probe invariant mass is required to be compatible with the Z mass and the fake rate is derived as a function of p_{T} and η of the probe;

fake rate application: in the second step, the background contribution coming from electrons faking photons is derived by using the fake rate to scale control regions in which the requirement of having one signal photon is replaced by the requirement to have a probe electron. These regions are collectively referred to as 'mono-electron CRs'.

The methodology for the fake rate estimation, along with the estimation of this background in all regions of the analysis are illustrated in the following paragraphs.

Methodology

The probability of electrons to fake photons is measured in data through a tag-and-probe procedure, where two exclusive samples of tag-and-probe electrons (*ee* sample) and tag

electrons and probe photons ($e\gamma$ sample) are built and the number of events in such samples are counted in bins of p_{T} and η of the probe electron/photon. The fake rate is then computed as:

$$f(p_{\mathrm{T}}, \eta) = \frac{N^{e\gamma}(p_{\mathrm{T}}, \eta)}{N^{ee}(p_{\mathrm{T}}, \eta)} \tag{7.9}$$

For the definition of the two samples the following selection criteria are used:

- For the electrons:
  - **tag electrons** are identified using the *medium* requirement, must have $p_{\mathrm{T}} > 25$ GeV, $\eta < 2.47$, and pass standard requirements on the transverse and longitudinal impact parameter.
  - **probe electrons** are required to have $p_{\mathrm{T}} > 125$ GeV (for the estimation of the fakes in the validation region and associated CRs) or $p_{\mathrm{T}} > 150$ GeV (for the estimation of the fakes in the SR and associated CRs), be outside the crack region, be identified by the *medium* requirement and be isolated, using the *loose* isolation working point.
- For the photons:
  - The **probe photons** are selected in the same way as the signal photons used in this analysis, starting at $p_{\mathrm{T}} > 125$ GeV (for the estimation of the fakes in the VR and associated CRs) or $p_{\mathrm{T}} > 150$ GeV (for the SR and associated CRs).
- For the tag-and-probe selection:
  - events are accepted if $E_{\mathrm{T}}^{\mathrm{miss}} < 40$ GeV and if they contain at least one tag-and-probe pair (either a probe electron or photon) within 10 GeV from the Z boson mass.

In order to assess the robustness of this method and evaluate the uncertainties on the fake rate, the fake rate computed in data is directly compared to that obtained by applying the tag-and-probe method on simulation samples from $Z(ee)+$ jets MC and to that computed only with the truth information of $Z(ee)+$jets and $W(e\nu)+$jets samples[2]. The latter is referred to as 'true fake rate', f^{true}, and is computed by selecting samples of true electrons and photons respectively:

- $true-e\ sample$: events are selected if there is at least one electron passing the probe requirements at detector level and is also associated at truth level to an isolated electron coming from a Z (or W) boson;
- $true-\gamma\ sample$: events are selected if there is at least one photon passing the probe requirements at detector level and is also associated at truth level to an isolated electron or to final state radiation coming from a Z (or W) boson.

[2]Most of the electron-to-photon background in the SR is expected to come from $W(e\nu)+$ jets events.

In a given MC sample the number of events of these samples are counted ant the real fake rate is then computed as:

$$f^{true}(p_{\mathrm{T}}, \eta) = \frac{N^{true-\gamma}(p_{\mathrm{T}}, \eta)}{N^{true-e}(p_{\mathrm{T}}, \eta)} \tag{7.10}$$

As in the Run 1 analysis, the following sources of systematic uncertainties are considered and added in quadrature for the evaluation of the fake rate:

- the difference between the fake rate measured in data in the nominal mass window of ± 10 GeV around the Z mass and the one measured in a reduced mass window of ± 5 GeV;
- the difference between the tag-and-probe fake rate and the true fake rate on the $Z(ee) +$ jets MC samples;
- the difference between the true fake rate in $Z(ee) +$ jets and $W(e\nu) +$ jets MC samples.

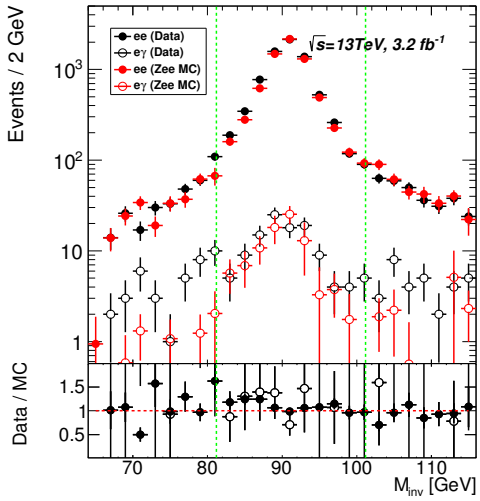

Figure 7.5: Invariant mass distribution of the tag-and-probe pair as measured in the data and in the $Z(ee)$+jets Monte Carlo samples, for electron and photon probes. A mass window of 10 GeVaround the Z mass is used to evaluate the fake rate. Plot by collaborator.

Fake rate estimation

Figure 7.5 shows the invariant mass distributions of the ee and $e\gamma$ pairs in the respective samples, as measured in data, compared to the ones obtained by using simulation samples from $Z(ee) +$ jets MC. While MC is not used to derive the fake rate value, the simulation describes rather well the data, suggesting that the fake rate is quite well modeled and that the QCD contamination of the tag-and-probe sample is minimal.

The fake rates from the tag-and-probe method in data are reported together with their statistic and systematic uncertainties in Tables 7.4 and 7.5 in regions of photon p_{T} and η.

	$\lvert\eta\rvert < 1.37$		
	$125 < p_{\mathrm{T}} < 200$ GeV	$150 < p_{\mathrm{T}} < 200$ GeV	$p_{\mathrm{T}} > 200$ GeV
Total (stat+syst)	$1.2 \pm 0.2 \pm 0.4$	$0.8 \pm 0.2 \pm 1.1$	$1.2 \pm 0.3 \pm 1.0$

Table 7.4: Electron-to-photon fake rates, in %, as measured in data and in Monte Carlo samples for $|\eta| < 1.37$ in bins of p_{T}.

	$\lvert\eta\rvert > 1.52$		
	$125 < p_{\mathrm{T}} < 200$ GeV	$150 < p_{\mathrm{T}} < 200$ GeV	$p_{\mathrm{T}} > 200$ GeV
Total (stat+syst)	$2.6 \pm 0.4 \pm 0.8$	$2.4 \pm 0.6 \pm 0.8$	$2.0 \pm 0.8 \pm 1.5$

Table 7.5: Electron-to-photon fake rates, in %, as measured in data and in Monte Carlo samples for $|\eta| > 1.52$ in bins of p_{T}.

Mono-electron CRs and background estimates

For each SR, CRs and VR of the analysis, a corresponding mono-electron region is built in data: for example the mono-electron region associated to the SR is obtained by replacing the requirement on the signal photon with that of a probe electron and by requiring that no other signal photons are present in the event. The same logic applies to the other control and validation regions; if more than one probe electron is present in a given event, all possibilities of an electron faking a photon are taken into account.

The estimation of the background coming from electron-to-photon fakes is obtained by scaling the number of events in these control regions by the measured fake rate.

Table 7.6 shows the electron-to-photon fake estimates for the VR and for the SR with their associated control regions including the statistical and systematic uncertainties.

Region	Electron-to-photon fake estimate
SR	$21.6 \pm 0.6 \pm 5.9 \pm 17.4$
CR$\gamma\mu$	$1.66 \pm 0.16 \pm 0.47 \pm 1.46$
CR$\gamma\mu\mu$	$0.05 \pm 0.02 \pm 0.01 \pm 0.05$
CRγee	$0.00 \pm 0.00 \pm 0.00 \pm 0.00$
CRγj	$5.76 \pm 0.30 \pm 1.54 \pm 4.85$
VR	$6.0 \pm 0.3 \pm 1.2 \pm 1.6$
CR$\gamma\mu$ (VR)	$1.31 \pm 0.15 \pm 0.24 \pm 0.35$
CR$\gamma\mu\mu$ (VR)	$0.06 \pm 0.03 \pm 0.01 \pm 0.01$
CRγee (VR)	$0.00 \pm 0.00 \pm 0.00 \pm 0.00$
CRγj (VR)	$4.58 \pm 0.28 \pm 0.84 \pm 1.21$

Table 7.6: Electron-to-photon fakes estimated in the SR, VR and associated CRs. The uncertainty is separated in three terms, one due statistical uncertainty in the electron fake rate, one due to the limited statistics of each mono-electron region, the third one due to the systematic uncertainties related to the electron fake rate estimation.

7.5.3 Jets faking photons

Hadronic jets can be reconstructed as photons and processes with large $E_{\mathrm{T}}^{\mathrm{miss}}$ and a high p_{T} jet can lead to a mono-photon signature. Such processes are highly reduced by asking stringent requirements on the photon identification and isolation variables.

The remaining contributions can be estimated with a data-driven technique. In particular, this analysis employs a two-dimentional side-band method, which methodology and results are described in the following paragraphs.

Methodology

The 2-dimensional side-band method is based on the definition of three control regions, obtained by inverting or loosening the isolation and identification requirements on the photon.

As already noted, there are two levels of identification for photons: *loose* and *tight*. Intermediate levels of identification are obtained by requiring that photons pass the *loose* criteria but fail one or more among among the cuts of the *tight* menu (see Table 4.1. These photons are denoted as *tight-n* and are defined as follows:

- for *tight*-3, photons must fail the F_{side}, ΔE, w_{s_3} requirements;
- for *tight*-4, photons must fail the F_{side}, ΔE, w_{s_3}, E_{ratio} requirements;
- for *tight*-5, photons must fail the F_{side}, ΔE, w_{s_3}, E_{ratio}, $w_{s_{tot}}$ requirements;

The isolation requirement can be inverted as follows:

$$E_T^{iso} - 0.022\, p_{\mathrm{T}}^{\gamma} > 3\,\mathrm{GeV}. \tag{7.11}$$

Photons satisfying this criterion are said to be non-isolated.

Based on these definitions, three more regions are defined for a given analysis region (the SR or CRs) and their event counts in data are denoted as:

- N_A: the number of events where the leading photon is *tight* and isolated;
- N_B: the number of events where the leading photon is *tight* and non-isolated;
- M_A: the number of events where the leading photon is *tight*-4 and isolated;
- M_B: the number of events where the leading photon is *tight*-4 and non-isolated.

A sketch of the regions and their event counts is reported in Figure 7.6.

Under the assumption that the leakage of real photons in the inverted regions is negligible and that the correlation between isolation and identification is negligible. the estimated number of jet-to-photon background events (N_{bkg}^{A}) in the analysis region of

interest can be obtained, along with the number of events with true photons (N^A_{sign}), via the following equations:

$$N^A_{bkg} = \frac{N^B M^A}{M_B}\,, \tag{7.12}$$

$$N^A_{sign} = N_A - N^A_{bkg}\,. \tag{7.13}$$

The purity of the sample is defined as:

$$P = \frac{N^A_{sign}}{N^A}\,. \tag{7.14}$$

The signal leakage is quantified by three coefficients, as defined by:

$$c_1 \overset{\text{def}}{=} \frac{N^B_{sign}}{N^A_{sign}}\,, c_2 \overset{\text{def}}{=} \frac{M^A_{sign}}{N^A_{sign}}\,, c_3 \overset{\text{def}}{=} \frac{M^B_{sign}}{N^A_{sign}}\,, \tag{7.15}$$

and illustrated in Figure 7.6.

When correcting for the signal leakage, the estimated number events from true photons becomes:

$$N^A_{sign} = N^A - \left(N^B - N^A_{sign}\cdot c_1\right)\frac{\left(M^A - N^A_{sign}\cdot c_2\right)}{\left(M^B - N^A_{sign}\cdot c_3\right)}\,. \tag{7.16}$$

The correction is similarly propagated to the number of estimated background events.

The signal leakage coefficients are evaluated with $W\gamma$, $Z\gamma$ MC samples and are reported in Table 7.7.

Systematic uncertainties are computed to take into account the variation of the background estimates when modifying the identification and isolation requirements for the definition of the regions of the method. The following variations are considered:

- for the identification, the difference between the estimates using *tight*-3 and *tight*-5 instead of *tight*-4;
- for the isolation, the difference between the estimates obtained using an isolation energy gap of 2 and 4 GeV instead than the nominal 3 GeV. Larger variations were considered, but it was checked that they would not yield significant additional variations to the background estimates.

The method is validated on a pseudo-data sample, composed of a mixture of $W(\mu\nu)\gamma$ and $W(\mu\nu)$ + jets events from MC simulation, with an injected purity $P_{MC} = 84\%$. The estimated purity with the 2d-sideband method without the signal leakage coefficients is $P = 87\% \pm 2\% \pm 6\%$, compatible within uncertainty with P_{MC}. Correcting the yields for the signal leakage, the estimated purity with the 2d-sideband method becomes $P = 89\% \pm 2\% \pm 5\%$, again compatible within uncertainty with P_{MC}.

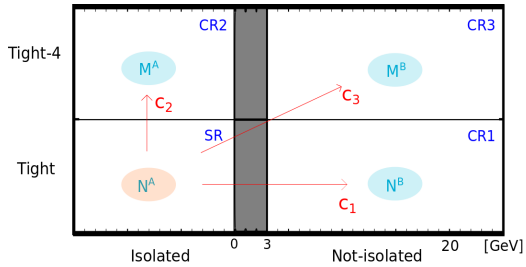

Figure 7.6: Illustration of the 2d-matrix method. Sketch by collaborator.

Signal Leakage Coefficients	
SR	CR$\gamma\mu$
$c_1 = 2.68\% \pm 0.02\%$	$c_1 = 3.67\% \pm 0.04\%$
$c_2 = 2.11\% \pm 0.02\%$	$c_2 = 2.54\% \pm 0.03\%$
$c_3 = 0.312\% \pm 0.008\%$	$c_3 = 0.87\% \pm 0.02\%$
CR$\gamma\mu\mu$	CRγee
$c_1 = 2.32\% \pm 0.07\%$	$c_1 = 2.40\% \pm 0.07\%$
$c_2 = 2.07\% \pm 0.06\%$	$c_2 = 2.08\% \pm 0.06\%$
$c_3 = 0.66\% \pm 0.03\%$	$c_3 = 0.11\% \pm 0.02\%$

Table 7.7: Signal leakage coefficients with their statistical uncertainty in the SR and lepton-enriched CRs.

Reduced Method

The non-*tight* regions of the CR$\gamma\mu\mu$ and CRγee are expected to have low statistics with the complete 2015 dataset and therefore the data-driven estimation produces large statistical uncertainty. To overcome this problem, the application of a *reduced* method is studied. The idea is to apply the ratio $r = \frac{M^A}{M^B}$ evaluated from the SR and CR$\gamma\mu$ (which have more events) to the CR$\gamma\mu\mu$ and CRγee. The number of events with true photons, corrected for signal leakage, is then:

$$N^A_{sign} = \frac{N^A - N^B r}{1 - c_1 r} \tag{7.17}$$

and the number of background events is:

$$N^A_{bkg} = \frac{\left(c_1 N^A - N^B\right) r}{r c_1 - 1} \tag{7.18}$$

The possibility to apply the *reduced* method has been tested on a MC sample which is expected to fairly describe the composition of signal and fake photons in the different analysis regions. The estimated purities are compared in Figure 7.7 for an expected luminosity of 5 fb^{-1}. The estimates with the reduced method are compatible with those from the complete method and have a reduced statistical uncertainties; the reduced method is thus preferred in CR$\gamma\mu\mu$ and CRγee.

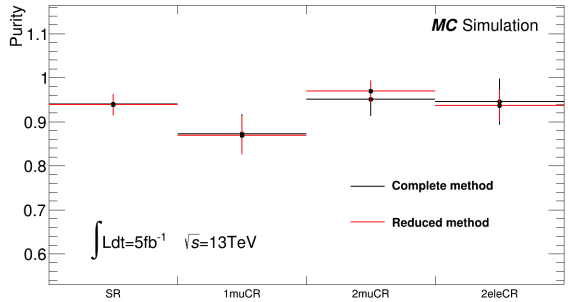

Figure 7.7: Photon purity evaluated with the complete and the reduced methods. For the reduced method, in the SR and in the CR$\gamma\mu$ the r coefficient is obtained from the same regions; in the CR$\gamma\mu\mu$ and CRγee the r coefficient is evaluated as the weighted mean from the SR and the CR$\gamma\mu$. Plot by collaborator.

Background estimates

Both the reduced and complete methods are applied to compute the jet-to-photon background in all analysis regions. An anomalous rate of unconverted photons in the *tight-4&isolated* region has been found to affect the jet-to-photon estimate in the VR, while leaving unaffected the CRs. It has been found to be due to non-collision background and a dedicated study has been performed to suppress this background. After correcting for the beam-induced background, the estimated purities range from 87% to 95% in the various analysis regions. The results for the estimated background events are reported in Table 7.8, along with their statistic and systematic uncertainties.

Region	Jet-to-photon background estimate
VR	$4.50 \pm 1.95 \pm 1.91$
CR$\gamma\mu$ (VR)	$12.2 \pm 3.8 \pm 12.4$
CR$\gamma\mu\mu$ (VR)	$1.3 \pm 0.6 \pm 1.0$
CRγee (VR)	$0.39 \pm 0.30 \pm 0.04$
CRγj (VR)	$15.1 \pm 3.9 \pm 3.4$
SR	$26.6 \pm 5.8 \pm 10.2$
CR$\gamma\mu$	$16.3 \pm 4.1 \pm 10.5$
CR$\gamma\mu\mu$	$1.1 \pm 0.6 \pm 0.5$
CRγee	$2.7 \pm 1.0 \pm 1.1$
CRγj	$9.9 \pm 2.8 \pm 1.5$

Table 7.8: Jet-to-photon fakes estimated in the analysis regions with their statistical and systematic uncertainties.

7.5.4 Non-collision background

The jet cleaning discussed in Section 4.2.3 is a powerful tool to suppress unbalanced fake jets coming from non-collision sources of background (NCB), such as the LHC beam-halo. Unbalanced calorimeter deposits due to the beam-halo can in principle also lead

to topologies with an unbalanced fake photon, and thus to a mono-photon signature.

In particular, events where the photon is identified with relatively loose requirements and a large $E_{\mathrm{T}}^{\mathrm{miss}}$, such as those used for the estimation of the jet-to-photon background, are found to be affected by NCB. *tight*-4 photons present an anomalous peak of isolated photons, as illustrated in Figure 7.8(a). Photons in the peak are concentrated at $|\phi| = 0, 3$ and $|\eta| \sim 2$, as shown in Figure 7.8(b), which are the typical regions where beam-induced energy deposits are concentrated [128]. A dedicated cleaning has been studied to suppress this kind of background, as described in the following.

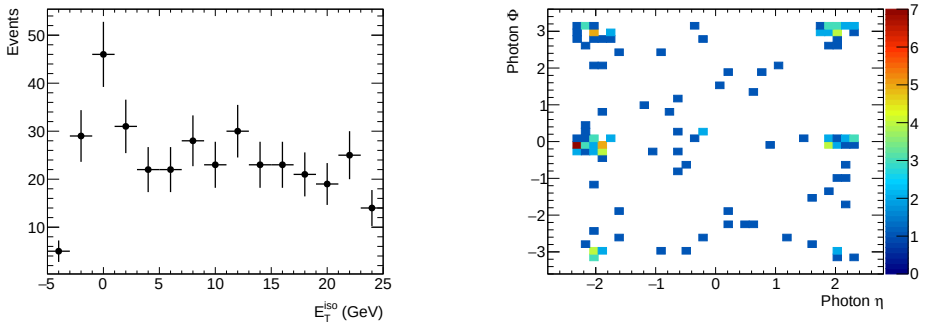

(a) (b)

Figure 7.8: (a) Leading photon isolation distribution for events in the *tight*-4 region of the VR: this region is expected to be populated by jets faking photons with an approximately flat distribution, and the peak at $E_T^{iso} \sim 0$ is not expected. (b) Correlation between the leading photon η and ϕ in the *tight*-4 isolated region of the VR.

Suppression of NCB photons

Several distributions are analyzed in data to characterize photons from non-collision background as opposed to prompt photons from the pp-collisions. At this aim, two selections are defined enriched in NCB and prompt photons, respectively. Both selections include the pre-selection cuts detailed in Section 7.4.1 and the following cuts:

- at least 1 photon, *loose* identification, with $p_{\mathrm{T}} > 125$ GeV, $|\eta| < 2.37$ excluding the calorimeter crack region $1.37 < |\eta| < 1.52$;
- the leading photon must be isolated
- the leading photon must not overlap with $E_{\mathrm{T}}^{\mathrm{miss}}$: $\Delta\phi(\gamma, E_{\mathrm{T}}^{\mathrm{miss}}) > 0.4$;
- no baseline electron and no baseline muon must be reconstructed.

In addition, the following cuts are required:

Prompt photons selection:

- *tight* identification for the leading photon.

NCB-enriched selection:

- *tight*-4 identification for the leading photon;
- $E_{\mathrm{T}}^{\mathrm{miss}} > 125$ GeV;
- $|\Delta\phi(\gamma, E_{\mathrm{T}}^{\mathrm{miss}})| > 3.0$.

Figures 7.9 show several distributions in data separately for these two selections. The η and ϕ distributions for the leading photon in the NCB-enriched selection show the characteristics that are expected from non-collision background, such as the concentration at $|\phi| = 0, 3$ and relatively large pseudo-rapidity ($|\eta| \sim 2$); in contrast, prompt photons are distributed uniformly in ϕ. Other characteristics are the higher probability of NCB photons compared to prompt photons of being classified as unconverted, and the small isolation energy, as illustrated in Figure 7.10.

While the η and ϕ distributions provide a clean discrimination between NCB and prompt photons, requirements on η and ϕ that exclude the regions where NCB is concentrated would produce an unwanted bias in the analysis. Therefore a different discriminant must be deployed.

The clusters associated to NCB photons are not expected to point to the primary vertex of the interaction, and the photon trajectory may be used to discriminate NCB photons from prompt photons. We study the distribution of the z coordinate of the intersection between the extrapolated photon trajectory and the beam axis, here denoted as 'pointed Z', or Z. The distribution of this variable is shown in Figure 7.10 (top) for the NCB-enriched and prompt photons selections. Prompt photons have the pointed Z centered at zero with a symmetric and Gaussian distribution with RMS$= 0.22$ m. In the NCB-enriched region, the distribution of photons presents two asymmetric peaks at pointed $|Z| \sim 5$ m, and tails that extend above to $|Z| = 100$ m. A third smaller population, concentrated at $Z = 0$, is expected to be due to hard-scatter jets misidentified as photons.

Figure 7.10 shows the correlation between the pointed Z and the η of the leading photons (middle) and between the pointed Z and the ϕ of the leading photon (bottom); the correlation between large values of Z and the $\eta - \phi$ regions characteristic of beam-induced-background is evident.

Given that prompt photons concentrate at small values of pointed Z, while NCB photons are concentrated at much higher values, an upper requirement on the pointed $|Z|$ is employed to reject NCB photons. When requiring that $|Z| < 0.25$ m on the leading photon, approximately 96% of the events in the NCB-region are rejected, while 98.6% of the events in the prompt photon selection are retained. Figure 7.12 shows the selection efficiency of the $|Z|$ requirement for several increasing thresholds. An acceptance at the level of 99% is reached for $|Z| < 0.50$ m.

Estimation of residual NCB in the SR

A residual background from NCB photons in the SR, after applying the cut on the photon pointing, may be present due to the requirement on the large $E_{\mathrm{T}}^{\mathrm{miss}}$ and separation

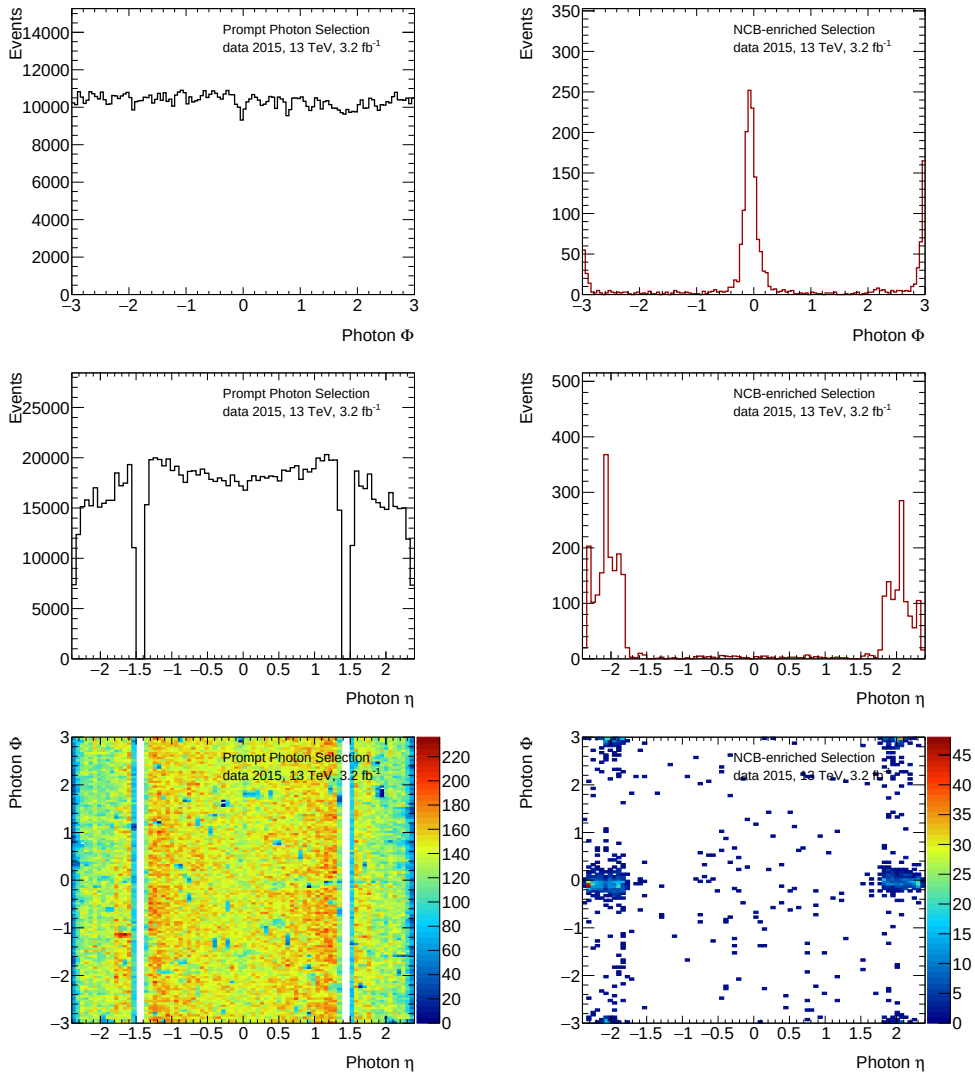

Figure 7.9: Φ (top), η (middle) and Φ versus η (bottom) distributions of the leading photon in the prompt photons selection (left) and in the NCB-enriched selection (right).

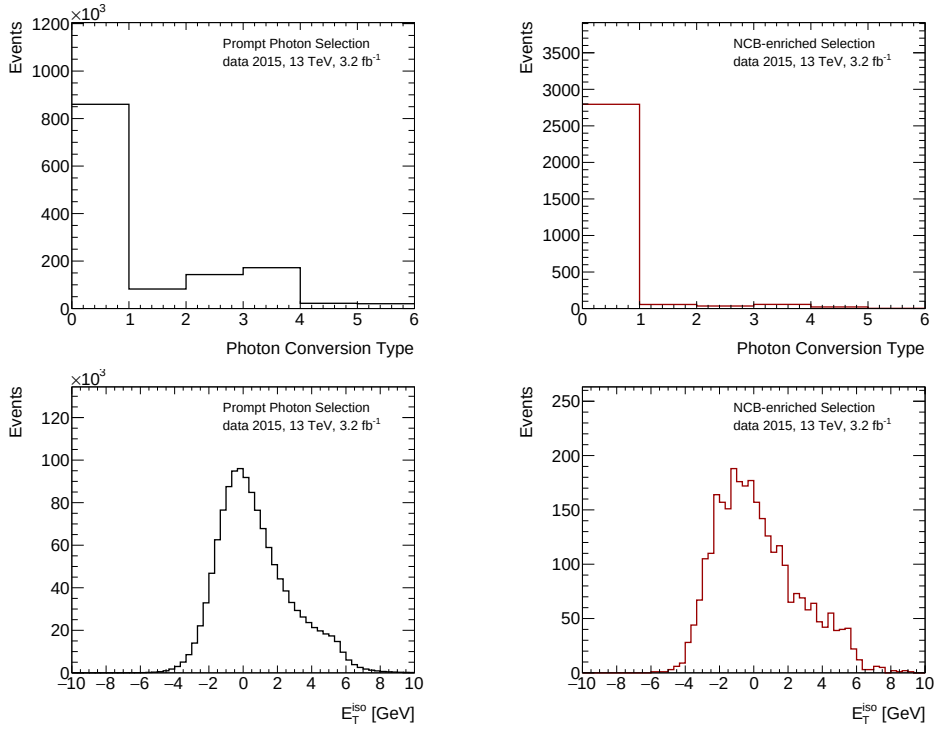

Figure 7.10: Conversion type (top) and isolation (bottom) distributions of the leading photon in the prompt photons selection (left) and in the NCB-enriched selection (right). In the conversion type distribution the first bin indicates unconverted photons, the following bins indicate converted photons with different kinds of associated tracks.

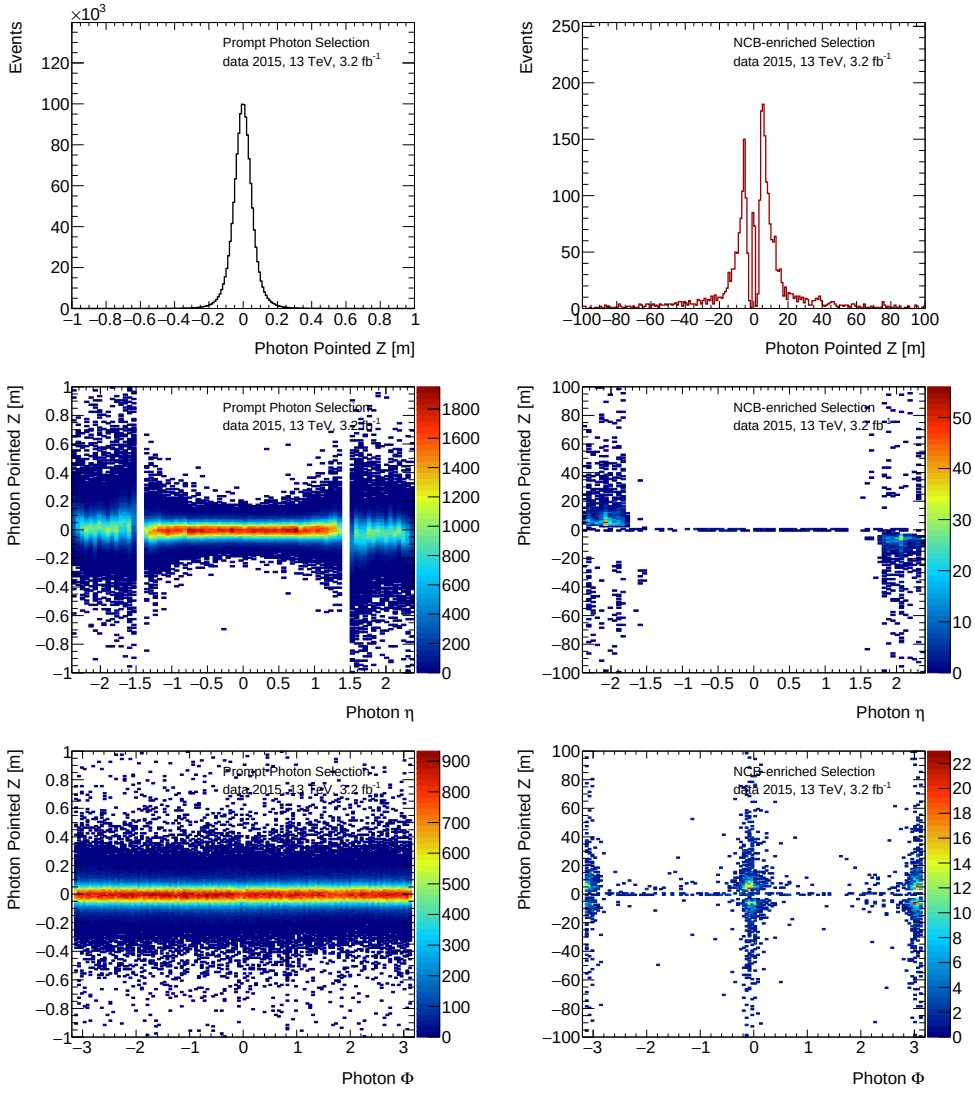

Figure 7.11: Pointed Z (top), pointed Z versus η (middle), pointed Z versus ϕ (bottom) distributions of the leading photon in the prompt photons selection (left) and in the NCB-enriched selection (right).

between the $E_{\mathrm{T}}^{\mathrm{miss}}$ and the leading photon. This residual contribution is estimated by employing an independent identification method compared to the photon pointing. Several identification methods are available in ATLAS to tag NCB events, which make use of the position, direction and timing of the muon segments and match them to the calorimeter activity. We employ the *two-sided* method [128], which has an estimated misidentification probability of the order of 10^{-5}.

A region enriched in NCB is built by reverting the photon pointing requirement on the leading photon in the SR and the number of events counted is referred to as N_{NCB}. In this region the number of events tagged by the *two-sided* method is denoted as N_{NCB}^{tag}. The efficiency of the tagger is then estimated as $\epsilon = N_{NCB}^{\mathrm{tag}}/N_{NCB}$. The number of tagged events in the SR, N_{SR}^{tag}, divided by ϵ is an estimate of the residual contribution of photons from NCB in the SR. The estimated efficiency is $\epsilon = 0.38 + 0.23 - 0.20$. In the SR no event is tagged, $N_{SR}^{\mathrm{tag}} = 0$; therefore this background is estimated to be negligible.

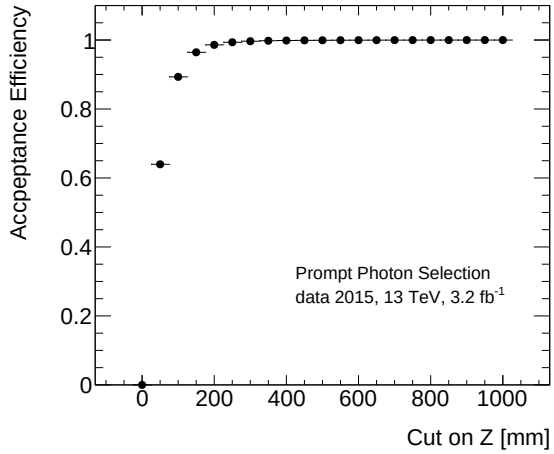

Figure 7.12: Selection efficiency of the $|Z|$ requirement on the leading photon for several increasing thresholds for events in the prompt photons selection.

7.6 Systematic Uncertainties

7.6.1 Sources of uncertainties and statistical treatment

For the backgrounds leading to fake photons, the methods used to evaluate the systematic uncertainties have been explained in Section 7.5.2 and Section 7.5.3.

For the $Z(\nu\nu)\gamma$, $Z(\ell\ell)\gamma$, $W(\ell\nu)\gamma$ and $\gamma+$ jets processes, all variations due to the experimental uncertainties are taken into account. These are related to the knowledge of the energy and momentum scale of the physics objects and of their identification, reconstruction and isolation efficiencies. For each source of uncertainty the corresponding variation on the final yield for each process is obtained by varying the relevant quantity (calibration scale, identification and reconstruction scale factor or efficiency), according to their estimated uncertainty, and by propagating its impact through the analysis chain.

Lepton efficiency uncertainties are propagated to the regions with vetoed leptons through the computation of average veto scale factors (see Section 7.5.1) for each systematic variation.

The uncertainty on the integrated luminosity ($\pm 5\%$) is derived following a methodology similar to that detailed in Ref. [129], from a preliminary calibration of the luminosity scale performed in August 2015.

The uncertainty on the trigger efficiency ($\pm 1\%$ in the VR and null in the SR) is estimated from the difference between data and simulation in the estimated efficiency, as explained in Section 7.4.2.

PDF uncertainties on the background yields are evaluated by reweighting the nominal MC samples, such that they behave as if they had originally been generated with PDFs other than those that were actually used. The reweighting is performed with LHAPDF6 [130]. The uncertainties are computed following the LHC PDF recommendations [131]: separate uncertainties are computed for the MMHT, NNPDF and CT10 families and then combined as follows:

$$\Delta = \frac{1}{2}\left[\max\left(\Delta_{CT10,}{}^{+}, \Delta^{+}_{MMHT}, \Delta^{+}_{NNPDF}\right) - \min\left(\Delta_{CT10,}{}^{-}, \Delta^{-}_{MMHT}, \Delta^{-}_{NNPDF}\right)\right], \tag{7.19}$$

where $\Delta^{+,-}$ are the upper and lower uncertainties on the yield (with their + or - sign) from a given PDF family.

The variation of the yields due to the uncertainties described above are treated as nuisance parameters in the fit. Each nuisance parameter is constrained by a Gaussian centered at zero and of width one. Zero corresponds to the nominal rate in all regions, while $+1(-1)$ corresponds to up (down) $1\,\sigma$ variation. The list of considered sources of uncertainty are listed in Table 7.9 with a brief description and the information about the correlation treatment across different regions of the fit. Each individual source of uncertainty is treated as uncorrelated to the others. If correlations are found in the fit, the final error on the fitted background takes the correlations into account.

For the signal-related systematics, besides the experimental and PDF uncertainties, which are evaluated in the same way described above for the background samples, QCD scale

uncertainties are evaluated by varying the renormalization and factorization scales by factors 2.0 and 0.5 with respect to the nominal values used in the MC generation. The uncertainties due to the choice of underlying-event tune used with PYTHIA 8.186 are computed by generating MC samples with the alternative underlying-event tunes described in [103]. The signal theoretical uncertainties just mentioned are factorized into two components, describing the variation on the acceptance and on the cross-section; only the uncertainties related to the acceptance are used as input in the fit.

Name	Description	Correlation across regions
JetFake_syst	jet-to-photon fake estimation (syst component)	✓
JetFake_stat_REGION	jet-to-photon fake estimation (stat component)	✗
EleFake_syst	e-to-photon fake rate (syst component)	✓
EleFake_stat	e-to-photon fake rate (stat component)	✓
EleFake_statCR_REGION	e-to-photon fake estimate (stat component)	✗
EG_SCALE	scale of photons and electrons	✓
EG_RESO	resolution of photons and electrons	✓
PH_EFF	identification efficiency of photons	✓
PH_ISO	isolation correction of photons	✓
EL_EFF_RECO	reconstruction efficiency of electrons	✓
EL_EFF_ID	identification efficiency of electrons	✓
EL_EFF_ISO	isolation efficiency of electrons	✓
MU_EFF_SYST	reconstruction efficiency of muons (syst component)	✓
MU_EFF_STAT	reconstruction efficiency of muons (stat component)	✓
MU_EFF_SYST_LOWPT	reconstruction efficiency of low-p_{T} muons	✓
MU_ISO_SYST	isolation efficiency of muons (syst component)	✓
MU_ISO_STAT	isolation efficiency of muons (stat component)	✓
MU_ID	resolution of the ID tracks associated to muons	✓
MU_MS	resolution of the MS tracks associated to muons	✓
MU_SCALE	scale of momentum of muons	✓
MET_SCALE	scale of the $E_{\mathrm{T}}^{\mathrm{miss}}$ Track Soft Term	✓
MET_RESO_PARA	resolution of the parallel projection of the Track Soft Term onto $\mathbf{p}_{\mathrm{T}}^{\mathrm{hard}}$	✓
MET_RESO_PERP	resolution of the perpendicular projection of the Track Soft Term onto $\mathbf{p}_{\mathrm{T}}^{\mathrm{hard}}$	✓
JES	jet energy scale	✓
JER	jet energy resolution	✓
LUMI_syst	computation of the integrated luminosity	✓
PH_TRIG_EFF	trigger efficiency	✓
PRW_DATASF	variation of data scale factor for pile-up reweighting	✓
PDF_Comb	combined PDF uncertainties	✓

Table 7.9: List and description of the sources of systematic uncertainty considered for the background estimation.

7.6.2 Impacts of uncertainties

Methodology

The uncertainty on the total background prediction due to each nuisance parameter is evaluated before and after the CR-only fit, as described in Section 7.5.1.

For the post-fit uncertainty, the following procedure is adopted:

- the nominal CR-only fit is performed and the best-fit values of the nuisance parameter of interest is found;

- the CR-only fit is repeated, while fixing the nuisance parameter to its best fit value $+1\sigma$ (or -1σ) and leaving the other parameters free;
- the relative difference between the background yield obtained by the nominal fit and by the second fit is taken as uncertainty.

To evaluate the statistical uncertainty on the background yield, due to the limited statistics of the data in the CRs, the following procedure is adopted:

- the nominal CR-only fit is performed and the best-fit values of the nuisance parameters are found;
- the CR-only fit is repeated, while fixing all nuisance parameters to their best-fit values and leaving the $\kappa-$ factors free;
- the relative difference between the background yield obtained by the nominal fit and by the second fit is taken as statistic uncertainty.

Results

The post-fit uncertainties in the SR are summarized in Table 7.10: the uncertainty on the total background uncertainty, including systematic and statistical contributions, is approximately 11%, dominated by the statistical uncertainty, which amounts to approximately 9%. The systematic uncertainty is dominated by the nuisance parameters related to the data-driven estimates, in particular the electron fake rate. This is mainly driven by the small number of events available for the estimation of the electron-to-photon fake factor. The uncertainty on jet fake rate contributes a relative uncertainty of 2.4% and affects mainly the normalization of $W\gamma$ backgrounds. By comparing the pre-fit (Table 7.11) and post-fit impacts (Table 7.12), it can be noted that after the fit, the effect of many sources of uncertainty, such as the luminosity, cancel out; this effect is explained by the properties of the CR-only fit, where the SR yields of the main backgrounds are obtained at first order as ratios of MC yields in the SR and CRs. For a simplified case of a single process X estimated thanks to a 100% pure control region CR, the post-fit yield in the SR is:

$$N_{SR}^{X,est} = N_{SR}^{X,MC}\kappa = N_{SR}^{X,MC}\frac{N_{CR}^{X,data}}{N_{CR}^{X,MC}} \tag{7.20}$$

If the SR and the CR are kinematically similar, the effect of a systematic variations in $N_{SR}^{X,MC}$ and $N_{CR}^{X,MC}$ will be of a similar size and the variation with respect to the nominal prediction consequently small.

Therefore most of the experimental and theoretical systematics affecting the $W/Z\gamma$ and $\gamma+$ jets background become negligible after the fit; the residual components of these uncertainties are the muon reconstruction and isolation efficiencies which yield a relative uncertainty of 1.5% for the muons and mainly affect the $Z\gamma$ background. An effect of similar size comes from the electron reconstruction and identification efficiencies. The PDF uncertainties have an impact on the $W/Z\gamma$ samples in each region but the effect on

Total background	295
Total background uncertainty	11%
Electron fake rate	5.8%
PDF uncertainties	2.8%
Jet fake rate	2.4%
Muons reconstruction/isolation efficiency	1.5%
Electrons reconstruction/identification/isolation efficiency	1.3%
Jet energy resolution	1.2%
Photon energy scale	0.6%
$E_{\mathrm{T}}^{\mathrm{miss}}$ soft term scale and resolution	0.4%
Photon energy resolution	0.2%
Jet energy scale	0.1%

Table 7.10: Breakdown of the dominant systematic uncertainties on the background estimates. The uncertainties are given relative to the expected total background yield. The individual uncertainties can be correlated and do not necessarily add in quadrature to equal the total background uncertainty.

Systematic	SR	CR$\gamma\mu$	CR$\gamma\mu\mu$	CRγee	CRγj
EG_RESO	(-0.11%, 0.47%)	(-0.01%, 0.06%)	(-0.06%, -0.04%)	(0.12%, 0.48%)	(0.91%, 7.71%)
EG_SCALE	(-2.77%, 2.55%)	(-2.30%, 2.45%)	(-2.53%, 2.48%)	(-2.05%, 2.26%)	(-2.72%, 9.39%)
EL_EFF_ID	(0.51%, -0.59%)	(-0.00%, 0.00%)	(-0.00%, 0.00%)	(-2.74%, 3.22%)	(2.56%, -2.84%)
EL_EFF_ISO	(0.00%, -0.00%)	(-0.00%, 0.00%)	(-0.00%, 0.00%)	(-1.46%, 1.58%)	(-0.04%, 0.04%)
EL_EFF_RECO	(0.19%, -0.20%)	(-0.00%, 0.00%)	(-0.00%, 0.00%)	(-1.13%, 1.21%)	(0.89%, -0.85%)
EleFake_stat	(-1.99%, 2.00%)	(-0.32%, 0.32%)	(-0.04%, 0.04%)	(0.00%, 0.00%)	(-0.72%, 0.72%)
EleFake_statCR_ONEmuCR	(0.00%, 0.00%)	(-0.11%, 0.11%)	(0.00%, 0.00%)	(0.00%, 0.00%)	(0.00%, 0.00%)
EleFake_statCR_PhJetCR	(0.00%, 0.00%)	(0.00%, 0.00%)	(0.00%, 0.00%)	(0.00%, 0.00%)	(-0.14%, 0.14%)
EleFake_statCR_SR	(-0.20%, 0.20%)	(0.00%, 0.00%)	(0.00%, 0.00%)	(0.00%, 0.00%)	(0.00%, 0.00%)
EleFake_statCR_TWOmuCR	(0.00%, 0.00%)	(0.00%, 0.00%)	(-0.08%, 0.08%)	(0.00%, 0.00%)	(0.00%, 0.00%)
EleFake_syst	(-5.88%, 5.87%)	(-1.01%, 1.01%)	(-0.18%, 0.20%)	(0.00%, 0.00%)	(-2.27%, 2.26%)
JER	(0.77%, -0.79%)	(0.93%, -0.95%)	(1.06%, -1.09%)	(0.83%, -0.85%)	(-15.97%, 16.40%)
JES	(2.84%, -3.66%)	(3.48%, -3.77%)	(2.56%, -3.38%)	(1.66%, -2.13%)	(8.99%, -0.51%)
JetFake_statCR_ONEmuCR	(0.00%, 0.00%)	(2.67%, -2.68%)	(0.00%, 0.00%)	(0.00%, 0.00%)	(0.00%, 0.00%)
JetFake_statCR_PhJetCR	(0.00%, 0.00%)	(0.00%, 0.00%)	(0.00%, 0.00%)	(0.00%, 0.00%)	(1.30%, -1.30%)
JetFake_statCR_SR	(1.91%, -1.92%)	(0.00%, 0.00%)	(0.00%, 0.00%)	(0.00%, 0.00%)	(0.00%, 0.00%)
JetFake_statCR_TWOeleCR	(0.00%, 0.00%)	(0.00%, 0.00%)	(0.00%, 0.00%)	(4.70%, -3.83%)	(0.00%, 0.00%)
JetFake_statCR_TWOmuCR	(0.00%, 0.00%)	(0.00%, 0.00%)	(2.07%, -2.28%)	(0.00%, 0.00%)	(0.00%, 0.00%)
JetFake_syst	(3.69%, -3.24%)	(7.77%, -6.78%)	(1.90%, -1.67%)	(5.00%, -4.40%)	(0.73%, -0.64%)
LUMI_SYST	(-4.16%, 4.24%)	(-4.37%, 4.45%)	(-4.74%, 4.83%)	(-4.40%, 4.48%)	(-4.59%, 4.68%)
MET_RESO_PARA	(0.43%, -0.43%)	(0.26%, -0.26%)	(0.16%, -0.16%)	(0.10%, -0.10%)	(2.29%, -2.29%)
MET_RESO_PERP	(0.48%, -0.47%)	(0.20%, -0.19%)	(0.24%, -0.23%)	(0.16%, -0.16%)	(6.10%, -5.96%)
MET_SCALE	(0.14%, -0.47%)	(-0.10%, -0.22%)	(-0.17%, -0.18%)	(-0.07%, -0.15%)	(11.16%, -6.38%)
MU_EFF_STAT	(0.11%, -0.19%)	(-0.30%, -0.02%)	(-0.44%, 0.16%)	(0.12%, -0.11%)	(-0.27%, -0.39%)
MU_EFF_SYST	(0.43%, -0.48%)	(-0.88%, 0.52%)	(-1.57%, 1.22%)	(0.12%, -0.11%)	(-0.08%, -0.57%)
MU_EFF_SYST_LOWPT	(-0.09%, -0.12%)	(-0.18%, -0.13%)	(-0.21%, -0.07%)	(0.12%, -0.12%)	(-0.32%, -0.34%)
MU_ID	(0.03%, -0.11%)	(-0.15%, -0.15%)	(-0.14%, -0.15%)	(0.12%, -0.12%)	(-0.38%, -0.25%)
MU_ISO_STAT	(0.11%, -0.11%)	(-0.23%, -0.09%)	(-0.28%, 0.01%)	(0.12%, -0.12%)	(0.33%, -0.33%)
MU_ISO_SYST	(0.11%, -0.11%)	(-0.53%, 0.20%)	(-0.97%, 0.67%)	(0.12%, -0.11%)	(0.34%, -0.32%)
MU_MS	(-0.11%, -0.11%)	(-0.15%, -0.19%)	(-0.11%, -0.20%)	(-0.11%, -0.12%)	(-0.10%, -0.35%)
MU_SCALE	(0.03%, -0.11%)	(-0.15%, -0.16%)	(-0.12%, -0.14%)	(0.12%, -0.12%)	(-0.22%, -0.31%)
PDF_Comb	(-4.54%, 4.55%)	(-3.94%, 3.95%)	(-1.42%, 1.42%)	(-1.08%, 1.08%)	(-0.96%, 0.96%)
PH_EFF	(1.02%, -1.23%)	(1.02%, -1.33%)	(1.13%, -1.40%)	(1.05%, -1.28%)	(0.92%, -1.58%)
PH_ISO_DD	(0.36%, -0.36%)	(0.50%, -0.50%)	(0.40%, -0.40%)	(0.42%, -0.42%)	(0.99%, -0.98%)
PRW_DATASF	(-0.40%, -0.47%)	(0.70%, -2.64%)	(0.11%, -1.29%)	(0.26%, -1.00%)	(-2.82%, 6.74%)

Table 7.11: Breakdown of the systematic uncertainties on background estimates before the fit in the SR and CRs. The percentages show the size of the uncertainty relative to the total expected background before the fit.

Systematic	SR	ONEmuCR	TWOmuCR	TWOeleCR	PhJetCR
EG_RESO	(-0.21%, -0.09%)	(-0.01%, -0.06%)	(-0.10%, -0.13%)	(0.05%, 0.35%)	(-0.01%, -0.03%)
EG_SCALE	(-0.63%, -0.08%)	(-0.02%, -0.02%)	(-0.11%, 0.05%)	(0.19%, -0.03%)	(-0.02%, -0.01%)
EL_EFF_ID	(1.17%, -1.17%)	(-0.04%, 0.00%)	(1.34%, -1.28%)	(-1.60%, 1.64%)	(-0.04%, -0.04%)
EL_EFF_ISO	(0.40%, -0.42%)	(-0.03%, -0.02%)	(0.67%, -0.64%)	(-0.79%, 0.85%)	(0.00%, 0.00%)
EL_EFF_RECO	(0.41%, -0.46%)	(-0.02%, -0.02%)	(0.50%, -0.48%)	(-0.62%, 0.66%)	(-0.01%, -0.03%)
EleFake_stat	(-1.90%, 1.87%)	(-0.06%, -0.04%)	(-0.04%, 0.05%)	(0.00%, 0.03%)	(-0.02%, -0.01%)
EleFake_statCR_ONEmuCR	(0.00%, -0.03%)	(-0.04%, -0.00%)	(-0.02%, 0.00%)	(-0.02%, -0.01%)	(0.01%, 0.00%)
EleFake_statCR_PhJetCR	(0.01%, -0.03%)	(-0.00%, -0.02%)	(-0.00%, -0.03%)	(-0.00%, -0.03%)	(-0.01%, 0.01%)
EleFake_statCR_SR	(-0.20%, 0.20%)	(0.00%, 0.00%)	(0.00%, 0.00%)	(0.00%, 0.00%)	(0.00%, 0.00%)
EleFake_statCR_TWOmuCR	(0.02%, -0.02%)	(-0.00%, 0.00%)	(-0.02%, 0.03%)	(0.05%, -0.05%)	(-0.00%, 0.00%)
EleFake_syst	(-5.48%, 5.46%)	(-0.01%, -0.06%)	(-0.04%, 0.13%)	(0.10%, -0.05%)	(-0.06%, -0.03%)
JER	(1.23%, -0.81%)	(-0.04%, -0.01%)	(0.05%, -0.02%)	(-0.04%, 0.10%)	(0.01%, -0.02%)
JES	(0.13%, -0.97%)	(-0.01%, -0.02%)	(0.34%, -0.39%)	(-0.39%, 0.60%)	(-0.01%, -0.01%)
JetFake_statCR_ONEmuCR	(-0.63%, 0.62%)	(-0.01%, -0.02%)	(-0.00%, 0.03%)	(0.01%, 0.02%)	(-0.01%, -0.01%)
JetFake_statCR_PhJetCR	(-0.04%, 0.08%)	(-0.03%, -0.02%)	(0.05%, 0.03%)	(0.05%, 0.03%)	(-0.00%, -0.05%)
JetFake_statCR_SR	(1.91%, -1.91%)	(0.00%, 0.00%)	(0.00%, 0.00%)	(0.00%, 0.00%)	(0.00%, 0.00%)
JetFake_statCR_TWOeleCR	(-0.97%, 1.03%)	(-0.06%, 0.01%)	(-1.49%, 1.66%)	(2.42%, -2.39%)	(0.01%, -0.00%)
JetFake_statCR_TWOmuCR	(-0.87%, 0.88%)	(0.01%, -0.04%)	(0.77%, -0.70%)	(-1.14%, 1.17%)	(-0.00%, 0.00%)
JetFake_syst	(0.04%, 0.00%)	(-0.04%, -0.02%)	(-0.89%, 1.13%)	(1.68%, -1.74%)	(-0.00%, -0.03%)
LUMI_SYST	(-0.04%, 0.02%)	(0.01%, -0.01%)	(0.01%, 0.03%)	(0.01%, -0.00%)	(-0.02%, -0.03%)
MET_RESO_PARA	(0.15%, -0.16%)	(-0.04%, -0.01%)	(0.04%, 0.01%)	(-0.01%, 0.05%)	(-0.04%, -0.05%)
MET_RESO_PERP	(-0.04%, 0.08%)	(-0.06%, 0.02%)	(0.09%, -0.01%)	(0.02%, 0.06%)	(-0.01%, -0.00%)
MET_SCALE	(-0.38%, 0.11%)	(-0.04%, 0.02%)	(0.02%, 0.02%)	(0.08%, 0.04%)	(-0.01%, -0.01%)
MU_EFF_STAT	(0.32%, -0.18%)	(-0.04%, -0.00%)	(-0.24%, 0.11%)	(0.27%, -0.15%)	(-0.01%, -0.02%)
MU_EFF_SYST	(1.15%, -1.00%)	(-0.02%, 0.00%)	(-0.64%, 0.58%)	(0.86%, -0.66%)	(-0.01%, -0.02%)
MU_EFF_SYST_LOWPT	(0.03%, -0.02%)	(-0.01%, -0.04%)	(-0.12%, 0.01%)	(0.17%, -0.05%)	(-0.02%, -0.01%)
MU_ID	(0.12%, 0.04%)	(-0.01%, 0.00%)	(-0.09%, -0.00%)	(0.14%, 0.02%)	(-0.02%, -0.02%)
MU_ISO_STAT	(0.19%, -0.04%)	(-0.03%, -0.01%)	(-0.22%, 0.06%)	(0.15%, -0.07%)	(0.02%, -0.02%)
MU_ISO_SYST	(0.53%, -0.35%)	(-0.02%, 0.02%)	(-0.40%, 0.31%)	(0.59%, -0.43%)	(0.00%, -0.02%)
MU_MS	(-0.01%, 0.06%)	(-0.03%, -0.04%)	(-0.01%, -0.04%)	(-0.02%, 0.03%)	(0.00%, -0.01%)
MU_SCALE	(0.11%, 0.04%)	(-0.01%, -0.01%)	(-0.10%, -0.00%)	(0.13%, 0.01%)	(-0.01%, -0.02%)
PDF_Comb	(-2.81%, 2.76%)	(-0.03%, -0.04%)	(-0.10%, 0.14%)	(0.14%, -0.07%)	(-0.04%, 0.01%)
PH_EFF	(0.04%, -0.00%)	(-0.03%, -0.02%)	(0.01%, 0.01%)	(0.01%, 0.03%)	(0.00%, -0.05%)
PH_ISO_DD	(-0.09%, 0.06%)	(-0.03%, -0.04%)	(-0.03%, 0.04%)	(0.01%, 0.00%)	(-0.00%, -0.04%)
PRW_DATASF	(-0.45%, 0.46%)	(-0.01%, -0.02%)	(-0.02%, -0.04%)	(0.14%, 0.17%)	(-0.02%, -0.01%)

Table 7.12: Breakdown of the systematic uncertainties on background estimates after the fit in the SR and CRs. Note that the individual uncertainties can be correlated, and do not necessarily add up quadratically to the total background uncertainty. The percentages show the size of the uncertainty relative to the total expected background.

normalization is largely absorbed into the normalization factors. The uncertainty on the jet energy resolution is approximately 1.2% and the most affected background is $\gamma +$jets.

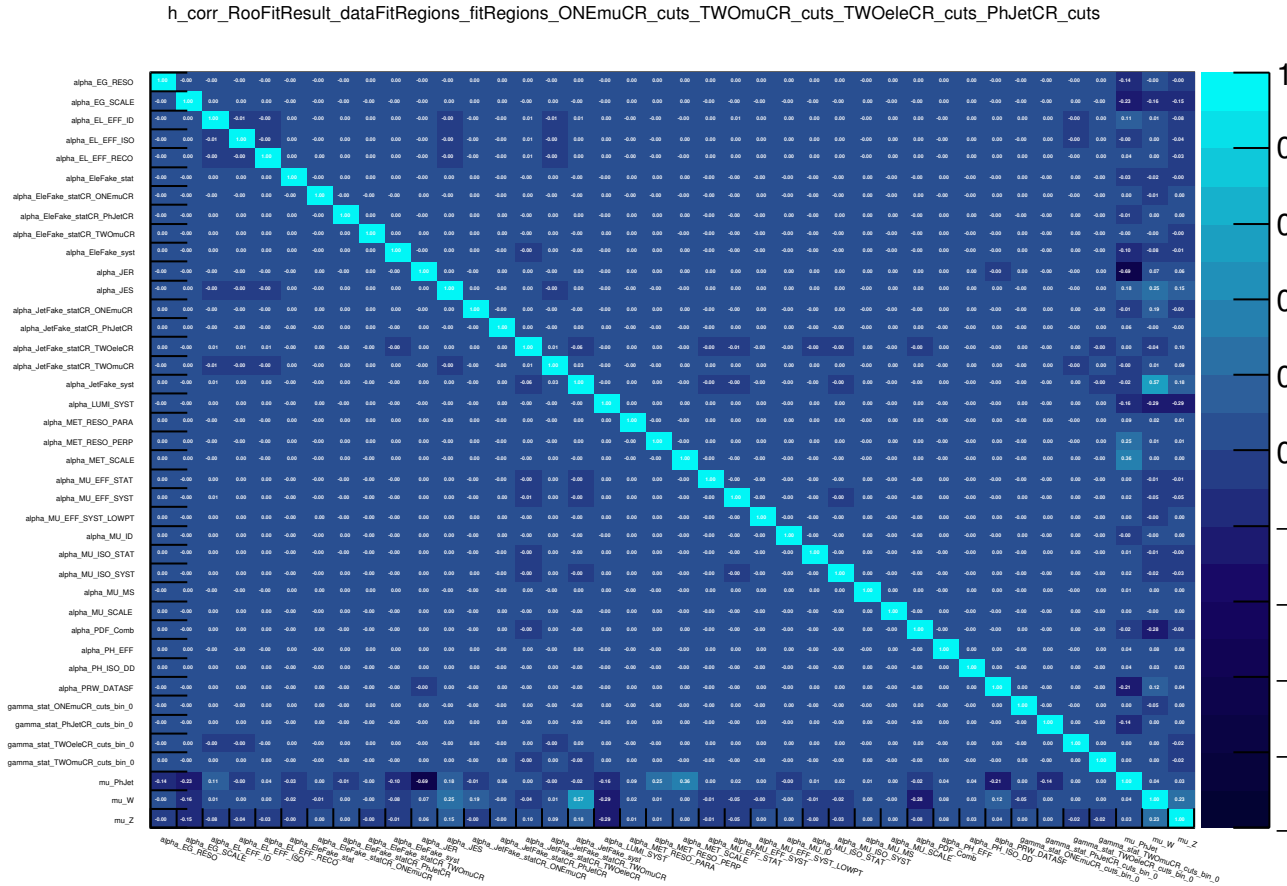

Figure 7.13: Correlation matrix between the nuisance parameters after the CR-only fit to the data.

7.7 Analysis Results

7.7.1 Validation of the background estimation

The CR-only fit, as described in Sec. 7.5.1, is performed to estimate the background yields in the VR and in its CRs. The sources of systematic uncertainties included in the fit have been described in Section 7.6.

Table 7.13 reports the number of observed events in data, as well as the total background (before and after the fit) and all the background components (after the fit) with their uncertainties. The number of observed events in the VR is in good agreement with the number of expected events within the uncertainties. The estimated k-factors after the fit are $\kappa_{Z\gamma} = 1.08 \pm 0.24$, $\kappa_{W\gamma} = 1.24 \pm 0.35$ and $\kappa_{\gamma+\text{jets}} = 0.8 \pm 0.23$.

7.7.2 Results in the SR

After validating the background estimation techniques, the CR-only fit is performed to estimate the background yields in the SR and in its CRs. The impacts of the systematic uncertainties on the predicted background yields have been discussed in Section 7.6.

Table 7.14 reports the number of observed events in data, as well as the total background (before and after the fit) and all the background components (after the fit) with their uncertainties. The number of observed events in the SR is in agreement with the number of expected events within uncertainties.

The estimated k-factors after the fit are $\kappa_{Z\gamma} = 1.19 \pm 0.21$, $\kappa_{W\gamma} = 1.50 \pm 0.26$ and $\kappa_{\gamma+\text{jets}} = 0.98 \pm 0.28$, which are compatible within the uncertainties with those estimated in the VR.

Figures 7.14 and 7.15 show the post-fit $E_{\text{T}}^{\text{miss}}$ distribution of the data and of the background in the CRs, while Figure 7.16 shows the post-fit $E_{\text{T}}^{\text{miss}}$ and p_{T}^{γ} distributions in the SR.

	VR	CR$\gamma\mu$ (VR)	CR$\gamma\mu\mu$ (VR)	CRγee (VR)	CRγj (VR)
Observed Events	79	87	16	12	132
Fitted Background	90 ± 12	87 ± 10	16 ± 3	12 ± 2	132 ± 11
$Z(\nu\nu)\gamma$	32 ± 7	0.10 ± 0.02	0.00 ± 0.00	0.00 ± 0.00	6.4 ± 1.4
$W(\mu\nu)\gamma$	23 ± 6	68 ± 18	0.08 ± 0.03	0.05 ± 0.01	11 ± 3
$Z(\ell\ell)\gamma$	1.0 ± 0.2	5.3 ± 1.1	15 ± 3	11.2 ± 2.4	0.68 ± 0.15
γ + jets	24 ± 6	0.58 ± 0.38	0.00 ± 0.00	0.01 ± 0.01	94 ± 12
Fake γ from electrons	6 ± 2	1.3 ± 0.5	0.06 ± 0.04	0.00 ± 0.00	4.6 ± 1.5
Fake γ from jets	4.5 ± 2.7	12 ± 12	1.29 ± 1.23	0.4 ± 0.4	15 ± 5
Pre-fit background	90 ± 10	74 ± 14	15 ± 2	11 ± 1	153 ± 31

Table 7.13: Observed event yields in 1 fb^{-1}compared to expected yields from SM backgrounds in the VR and in the associated four CRs, as predicted from the simultaneous fit to all single-bin CRs. The background yields before the fit are also shown. The uncertainty includes both the statistical and systematic uncertainties described in Section 7.6. The uncertainties on the individual background components can be correlated and do not necessarily add in quadrature to equal the total background uncertainty.

	SR	CR$\gamma\mu$	CR$\gamma\mu\mu$	CRγee	CRγj
Observed Events	264	145	29	20	214
Fitted Background	295 ± 34	145 ± 12	27 ± 4	23 ± 3	214 ± 15
$Z(\nu\nu)\gamma$	171 ± 29	0.15 ± 0.03	0.00 ± 0.00	0.00 ± 0.00	8.6 ± 1.4
$W(\mu\nu)\gamma$	58 ± 9	119 ± 17	0.14 ± 0.04	0.11 ± 0.03	22 ± 4
$Z(\ell\ell)\gamma$	3.3 ± 0.6	7.9 ± 1.3	26 ± 4	20 ± 3	1.2 ± 0.2
γ + jets	15 ± 4	0.7 ± 0.5	0.00 ± 0.00	0.03 ± 0.03	166 ± 17
Fake γ from electrons	22 ± 18	1.7 ± 1.5	0.05 ± 0.05	0.00 ± 0.00	5.8 ± 5.1
Fake γ from jets	26 ± 12	16 ± 11	1.1 ± 0.8	2.5 ± 1.3	9.9 ± 3.1
Pre-fit background	249 ± 29	105 ± 14	23 ± 2	19 ± 2	209 ± 50

Table 7.14: Observed event yields in 3.2 fb^{-1}compared to expected yields from SM backgrounds in the SR and in the four CRs, as predicted from the simultaneous fit to all single-bin CRs. The background yields before the fit are also shown. The uncertainty includes both the statistical and systematic uncertainties described in Section 7.6. The uncertainties on the individual background components can be correlated and do not necessarily add in quadrature to equal the total background uncertainty.

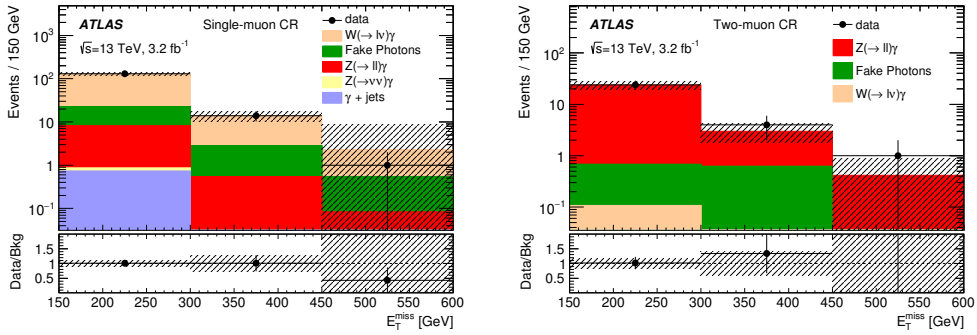

Figure 7.14: Distribution of $E_{\mathrm{T}}^{\mathrm{miss}}$, reconstructed treating muons as non-interacting particles, in the data and for the background in the $\mathtt{CR}\gamma\mu$ (left) and in the $\mathtt{CR}\gamma\mu\mu$ (right). The total background expectation is normalized to the post-fit result in each control region. Overflows are included in the final bin. The error bars on data represent the statistical uncertainties on the event counts; the dashed band on the post-fit prediction represent the statistical and systematic uncertainties on the prediction determined by a bin-by-bin fit. The lower panel shows the ratio of data to expected background event yields.

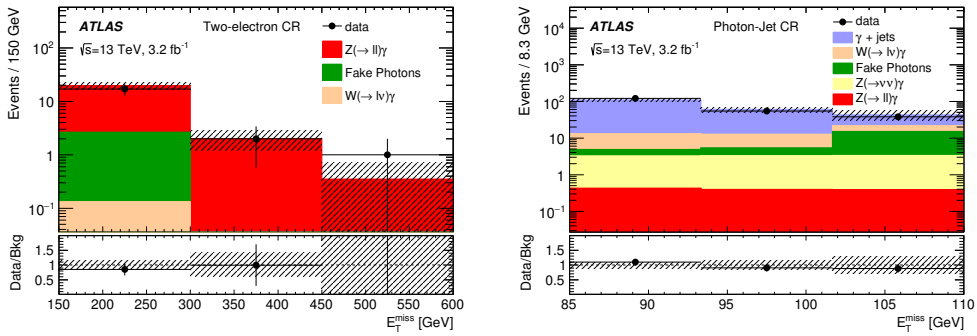

Figure 7.15: Distribution of $E_{\mathrm{T}}^{\mathrm{miss}}$ in the data and for the background in the $\mathtt{CR}\gamma\mathtt{ee}$, where $E_{\mathrm{T}}^{\mathrm{miss}}$ is reconstructed treating electrons as non-interacting particles (left) and in the $\mathtt{CR}\gamma\mathtt{j}$ (right). The total background expectation is normalized to the post-fit result in each control region. Overflows are included in the final bin for the left figure. The error bars on data represent the statistical uncertainties on the event counts; the dashed band on the post-fit prediction represent the statistical and systematic uncertainties on the prediction determined by a bin-by-bin fit. The lower panel shows the ratio of data to expected background event yields.

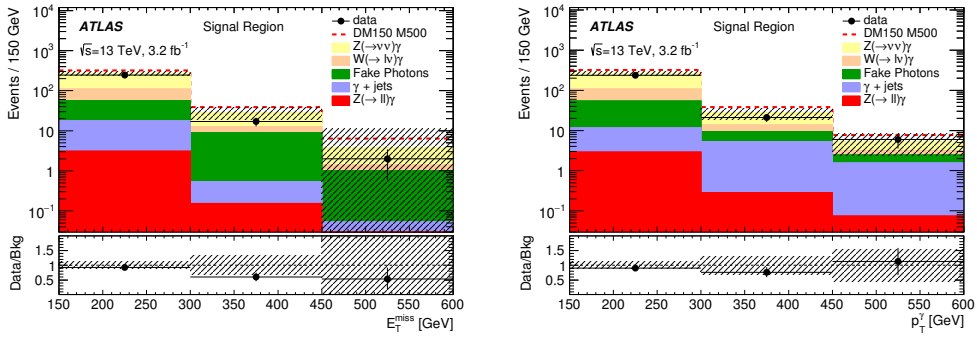

Figure 7.16: Distribution of $E_{\mathrm{T}}^{\mathrm{miss}}$ (left) and p_{T}^{γ} (right) in the SR for data and for the background predicted from the fit in the CRs. Overflows are included in the final bin. The error bars on data represent the statistical uncertainties on the event counts; the dashed band on the post-fit prediction represent the statistical and systematic uncertainties on the prediction determined by a bin-by-bin fit. The expected yield of events from the simplified model with $m_{\chi} = 150\,\mathrm{GeV}$ and $m_{\mathrm{med}} = 500\,\mathrm{GeV}$ is stacked on top of the background prediction. The lower panel shows the ratio of data to expected background event yields.

7.8 Interpretation of the results

The number of events observed in data (264) is consistent with the prediction of 295 ± 34 events from SM backgrounds. The results are therefore interpreted in terms of exclusion limits in models that would produce an excess of mono-photon events. Upper bounds are calculated using a one-sided profile likelihood ratio and the CL_S technique [132, 133], evaluated using the asymptotic approximation [134]. The CR+SR fit configuration is used to extract the limits.

7.8.1 Model-independent limits

The number of selected events coming from a potential new physics process of cross-section σ is

$$N^{new} = L \times \sigma \times A \times \epsilon, \tag{7.21}$$

where L is the integrated luminosity and $A \times \epsilon$ is the product of the acceptance and efficiency of the selection criteria. Without any hypothesis on the model of new physics, a limit on the visible cross-section $\sigma_{vis} = \sigma \times A \times \epsilon$ can be computed, which translates the maximum number of events compatible with the observed data into an upper limit on the cross-section for new physics.

In order to enable reinterpretation of these results outside ATLAS, this limit is translated into a fiducial limit with the procedure described in the following.
A fiducial region is defined at particle level, corresponding to the `SR` selection. The number of events N^{new} can then be rewritten as:

$$\begin{aligned} N^{new} = L \times \sigma \frac{\sum\limits_{i}^{reco} w_i}{\sum\limits_{i}^{gen} w_i} &= L \times \sigma \frac{\sum\limits_{i}^{reco} w_i}{\sum\limits_{j}^{fid} w_j} \frac{\sum\limits_{j}^{fid} w_j}{\sum\limits_{i}^{gen} w_i} \\ &\stackrel{\text{def}}{=} L \times \sigma \times \epsilon^{fid} \times A^{fid} \end{aligned} \tag{7.22}$$

where:

- σ is the cross-section at particle level;
- $\sum\limits_{n}^{Region} w_n$ represents the sum of the event weights in a $Region$, which can be constituted by the generated events at particle level (gen), by the total accepted events at reconstruction level ($reco$) or by the total accepted events at particle level (fid);
- ϵ^{fid} represents the efficiency of the selection at reconstruction level with respect to that at particle level;
- A^{fid} represents the acceptance of the selection at particle level.

By evaluating ϵ^{fid} for a range of models yielding the mono-photon signature it is possible to translate the limits on the σ_{vis} into fiducial limits on the $\sigma^{fid} \stackrel{\text{def}}{=} \sigma \times A^{fid}$, which is

a quantity that can be directly used by theorists and phenomenologists to test a model which yields a mono-photon signature. When evaluating conservatively ϵ^{fid} to be the lowest efficiency found in the DM models studied here, for which the efficiency ranges from 78% to 91%, the observed (expected) upper limits on the fiducial cross section are 17.8 (25.5) fb at 95% confidence level (CL) and 14.6 (21.7) fb at 90% CL. The observed upper limit at 95% CL would be 15.3 fb using the largest efficiency value of 91%.

7.8.2 Dark Matter limits

The results are translated into exclusion limits on WIMP-pair production. Two models are considered: the simplified mediator with axial-vector spin-1 mediator (Section 6.2), and the EFT model with $\gamma\gamma\chi\bar{\chi}$ interaction (Section 6.3).

For the simplified model with an axial-vector mediator, Fig. 7.17 shows the observed and expected contours corresponding to a 95% CL exclusion as a function of m_{med} and m_χ for g_q = 0.25 and g_χ =1. The region of the plane under the limit curves is excluded. The region not allowed due to perturbative unitarity violation is defined by $m_\chi > \sqrt{\pi/2} m_{\text{med}}$ [135]. The line corresponding to the observed DM thermal relic abundance [19] is also indicated in the figure. The search excludes mediator masses of up to 710 GeV for χ masses up to 150 GeV.

The limits on the $m_\chi - m_{\text{med}}$ plane can be translated[3] to limits on the spin-dependent χ–proton scattering cross section versus m_χ and compared to the limits obtained from direct detection searches, as shown in Figure 7.18. The mono-photon search provides stringent limits on the scattering cross section at the order of 10^{-41}cm^2 up to m_χ masses of about 150 GeV.

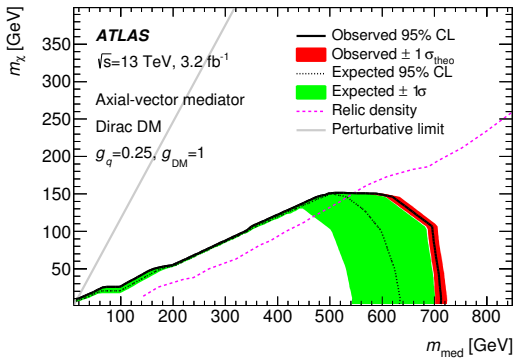

Figure 7.17: The observed and expected 95% CL exclusion limit for a simplified model of dark matter production involving an axial-vector operator, Dirac DM and couplings g_q = 0.25 and g_χ = 1 as a function of the dark matter mass m_χ and the axial-mediator mass m_{med}. The plane under the limit curves is excluded. The region on the left is excluded by the perturbative limit. The relic density curve [19] is also shown.

[3]The procedure for the translation will be discussed in more detail in Section 8.10.2 in the context of the mono-jet analysis.

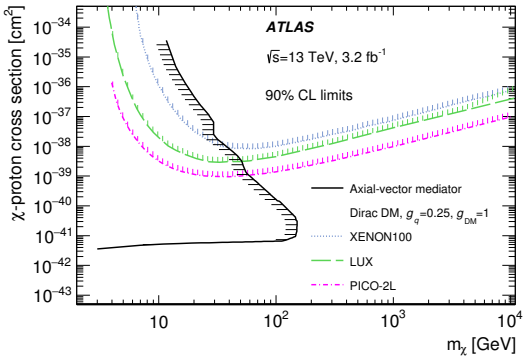

Figure 7.18: The 90% CL exclusion limit on the spin-dependent χ–proton scattering cross section in a simplified model of DM production involving an axial-vector operator, Dirac DM and couplings g_q = 0.25 and g_χ = 1 as a function of the dark matter mass m_χ. Also shown are results from three direct DM search experiments [136, 137, 138].

In the case of the model of $\gamma\gamma\chi\bar{\chi}$ interactions, lower limits are placed on the effective mass scale M^* as a function of m_χ, as shown in Fig. 7.19.

The EFT approximation is not always valid, therefore a truncation procedure is applied [139]. In this procedure, the scale at which the EFT description becomes invalid (M_{cut}) is assumed to be related to M^* through $M_{\text{cut}} = g^* M_*$, where g^* is the EFT coupling. Events having a center-of-mass energy larger than M_{cut} are removed and the limit is recomputed. The effect of the truncation for various representative values of g^* is shown in Fig. 7.19: for the maximal coupling value of 4π, the truncation has almost no effect; for lower coupling values, the exclusion limits are confined to a smaller area of the parameter space, and no limit can be set for a coupling value of unity.

For very low values of M_*, most events would fail the center-of-mass energy truncation requirement, therefore, the truncated limits are not able to exclude very low M_* values. The search excludes model values of M_* up to 570 GeV and effects of truncation for various coupling values are shown in the figure.

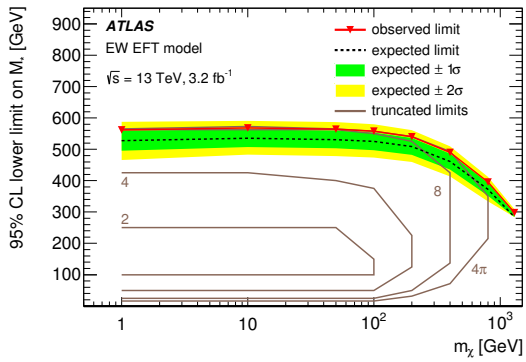

Figure 7.19: The observed and expected 95% CL limits on M_* for the EW EFT model with contact interaction of type $\gamma\gamma\chi\chi$ as a function of dark matter mass m_χ. Results where EFT truncation is applied are also shown, assuming representative coupling values of 2, 4, 8 and 4π.

CHAPTER 8

Mono-Jet Search with 2015 and 2016 Data

The mono-jet signature is characterized by a large missing transverse momentum recoiling against a high-p_{T} jet. It is the most abundant reaction among the mono-X and typically the most sensitive for BSM physics involving the presence of a large $E_{\mathrm{T}}^{\mathrm{miss}}$ and a recoil object from initial state radiation.

The biggest challenge for the analysis of mono-jet final states is the estimation of the dominant irreducible SM background, the $Z(\nu\nu) + \text{jets}$ process. In the previous chapter it was discussed how to measure the irreducible background in the context of the mono-photon analysis: the $Z(\nu\nu)\gamma$ background is measured through the $Z(\ell\ell)\gamma$ channels, where the variable of interest is defined in a way that the $Z(\ell\ell)\gamma$ and $Z(\nu\nu)\gamma$ states have similar kinematics. This allows to reduce the large systematic uncertainties on the background that would come from a pure MC estimate.

In the mono-jet case, a first strategy can be deployed similarly, by defining control regions enriched in leptons to access $Z(\ell\ell) + \text{jets}$ states which mimic the $Z(\nu\nu) + \text{jets}$. An evolution of this approach is provided by using $W(\ell\nu) + \text{jets}$ processes in addition to the $Z(\ell\ell) + \text{jets}$, taking advantage of the higher statistics of the W channels compared to the Z channels.

A further refinement can be obtained by exploiting not only the information on the event counts, but also the information on the shape of the $E_{\mathrm{T}}^{\mathrm{miss}}$ distribution. The $E_{\mathrm{T}}^{\mathrm{miss}}$ distribution provides an observable which has a clear physics meaning, has a large discriminating power and has a clean connection with the p_{T} spectrum of the Z boson, a quantity naturally computed in perturbation theory. Using the shape information requires to generalize the likelihood introduced in Section 7.5.1 to an arbitrary number of bins of the $E_{\mathrm{T}}^{\mathrm{miss}}$ spectrum. If a single normalization parameter is used for the entire spectrum, then a correlation between the low and the high part of the $E_{\mathrm{T}}^{\mathrm{miss}}$ spectrum is established through the shape of the $E_{\mathrm{T}}^{\mathrm{miss}}$ distribution.

These two aspects of the background estimation strategy and the improvement to the analysis sensitivity to which they lead will be discussed with more detail during this chapter.

From the above considerations, it is clear that in order to simultaneously use W and Z control regions to constrain the background in the signal region, it is essential to estimate

the $E_{\mathrm{T}}^{\mathrm{miss}}$ shape uncertainties and to account for possible process correlations of such uncertainties. For the experimental uncertainties, it is straightforward to generalize the computation from a single bin to multiple bins of the $E_{\mathrm{T}}^{\mathrm{miss}}$ spectrum. For the theoretical ones, we instead adopt the approach introduced by Lindert et al. [140], where they provide recommendations for reweighting the $V+$ jets MC samples to perturbative calculations and for assessing the associated theoretical uncertainties in a systematic way.

The samples used for the analysis are detailed in Section 8.2, together with the procedure to reweight the $V+$ jets samples. Section 8.3 describes the objects definition, while Section 8.4 describes the event selection and discusses the shape agreement between data and MC in the control regions. The background estimation techniques and the systematic uncertainties are examined in Sections 8.5 and 8.6, respectively, followed by the discussion on the choice of the background estimation strategy in Section 8.7. The results of the background estimation are presented in Section 8.8, while the interpretation of the results in terms of limits on the DM models are discussed in Section 8.9. Section 8.10 discusses the comparison between the limits set by mono-X and other dark matter searches in ATLAS and CMS with the limits set by direct detection experiments. The future prospects of the analysis are discussed in Section 8.11.

8.1 Mono-jet signature

The mono-jet signature of at least one energetic jet, large $E_{\mathrm{T}}^{\mathrm{miss}}$ and no leptons constitutes a distinctive signature for new physics and has been extensively studied at the LHC [141, 142] in the context of searches of physics beyond the Standard Model. The largest source of background is due to the $Z(\nu\nu)+$jets process, followed by $W(\ell\nu)+$jets processes where the lepton is not reconstructed or the tau decays hadronically and is reconstructed as a jet. Small contributions come from the $t\bar{t}$ and diboson production, where the leptons are missed. The large $E_{\mathrm{T}}^{\mathrm{miss}}$ cut and the requirement that $E_{\mathrm{T}}^{\mathrm{miss}}$ and jets are well separated suppresses the otherwise large multijet contribution. The contribution due to non-collision sources of background, which yield very abundant mono-jet events, is strongly suppressed by a dedicated cleaning of the jets.

8.2 Data and Monte Carlo samples

8.2.1 Data

This analysis is based on the data collected with the ATLAS detector in pp collisions at a center-of-mass energy of 13 TeV during 2015 and 2016, for a total integrated luminosity of $36.1\,\mathrm{fb}^{-1}$. Good luminosity sections are selected using the latest GoodRunsList (GRL) requiring that all sub-detectors were completely functional during the data acquisition.

8.2.2 Monte Carlo simulation

Signals

The models used for the generation of the signal samples have been introduced in Chapter 6.

WIMP s-channel signal samples are simulated in POWHEG-BOX v2 [114, 143, 144] using two implementations of simplified models, introduced in ref. [145]. The DMV model of WIMP-pair production is used for s-channel spin-1 axial-vector or vector mediator exchange at next-to-leading order (NLO), and the DMS_tloop model is used for WIMP-pair production with the s-channel spin-0 pseudoscalar mediator exchange with the full quark-loop calculation at leading order (LO) [146]. Renormalization and factorization scales are set to $H_{\mathrm{T}}/2$ on an event-by-event basis, where $H_{\mathrm{T}} = \sqrt{m^2_{\chi\chi} + p^2_{\mathrm{T},j1}} + p_{\mathrm{T},j1}$ is defined by the invariant mass of the WIMP pair ($m_{\chi\chi}$) and the transverse momentum of the highest-p_{T} parton-level jet ($p_{\mathrm{T},j1}$). The mediator propagator is described by a Breit–Wigner distribution. Events are generated using the NNPDF30 [99] parton distribution functions (PDFs) and interfaced to PYTHIA-8.205 with the A14 set of tuned parameters [147] for parton showering. Couplings of the mediator to WIMP particles and those of the SM quarks are set to $g_\chi = 1$ and $g_q = 1/4$ for the DMV model. A grid of samples is produced for WIMP masses ranging from 1 GeV to 1 TeV and mediator masses between 10 GeV and 10 TeV.

For the $t-$ channel scalar colored mediator samples, the details of the generation procedure have been discussed in Chapter 6 but are here summarized for completeness. Samples are generated with MADGRAPH 5 v2.3.3 [95] at LO using NNPDF23LO PDFs and interfaced to PYTHIA 8.186 with the A14 tune for modeling of parton showering, hadronization and the underlying event. The generation of the different subprocesses is performed following a procedure outlined in Ref. [148]. Since the mediator could be on-shell, for a more consistent treatment the generation is split between DM production with an off-shell mediator and on-shell mediator production followed by decay, and the associated production of up to two partons in the final state is included. Only diagrams involving the first two quark generations are considered and processes with electroweak bosons are suppressed. The matching between MADGRAPH and PYTHIA is performed following the CKKW-L prescription [149]. The parton matching scale is set to $M_\eta/8$ in the case of mediator-pair production, and to 30 GeV otherwise. This particular choice of matching scales optimizes the generation of the samples in the full phase space, and minimizes the impact from scale variations on the shape of the predicted kinematic distributions. The coupling is set to $g = 1$, and a grid of samples is produced for WIMP masses ranging from 1 GeV to 1 TeV and mediator masses between 100GeV and 2.5 TeV.

Background Samples

The main sources of background to this search are:

- $Z(\nu\nu) +$ jets production (irreducible);

- $W(\tau\nu)$ + jets production, with the τ decaying hadronically or into an unidentified charged lepton and a neutrino;
- $W(\mu\nu)$ + jets production, where the muon is not reconstructed or is not identified;
- $W(e\nu)$+jets production, where the electron is not reconstructed or is not identified;
- $Z(\tau\tau)$ + jets production, with the τs decaying hadronically or into an unidentified charged lepton and a neutrino;
- $Z(\mu\mu)$+jets production, where both muons are not reconstructed or not identified;
- $Z(ee)$ + jets production, where both electrons are not reconstructed or not identified;
- diboson production with not-reconstructed or unidentified leptons in the final state;
- $t\bar{t}$ or single $-$ t production with not-reconstructed or unidentified leptons in the final state;
- multijet background, with $E_{\mathrm{T}}^{\mathrm{miss}}$ originating from the misreconstruction of one jet;
- non-collision background (NCB), originating for example from beam-halo interactions with production of a muon which travels parallel to the beam axis and is identified as a jet, or from calorimeter noise (in this case, $E_{\mathrm{T}}^{\mathrm{miss}}$ originates from the kinematic unbalance in the transverse plane).

This section reports the details of the background samples used for the analysis along with the generators and the most important parameters adopted for the generation of the events.

Events containing W or Z bosons with associated jets are simulated using the SHERPA 2.2.1 [105] generator. Matrix elements are calculated for up to 2 partons at NLO and 4 partons at LO using the Comix [109] and OpenLoops [110] matrix element generators and merged with the Sherpa parton shower [106] using the ME+PS@NLO prescription [111]. The `NNPDF30nnlo` PDF set is used in conjunction with dedicated parton shower tuning developed by the Sherpa authors. The W/Z + jets events are normalized to the NNLO cross sections [150]. In the case of $Z(\ell\ell)$ + jets, a cut on $m(\ell^+\ell^-) > 40$ GeV is applied, thus an additional set of samples with 10 GeV $< m(\ell^+\ell^-) <$ 40 GeV are also included.

For the generation of $t\bar{t}$ and single top-quarks in the Wt and s-channel the POWHEG-Box v2 [114, 143, 144] generator with the `CT10` PDF sets in the matrix element calculations is used. Electroweak t-channel single top-quark events are generated using the POWHEG-Box v1 generator. This generator uses the 4-flavour scheme for the NLO matrix elements calculations together with the fixed 4-flavour PDF set CT10f4. For all top processes, top-quark spin correlations are preserved (for t-channel, top quarks are decayed using MadSpin[10a]). The parton shower, fragmentation, and the underlying event are simulated using PYTHIA 6.428 [96] with the `CTEQ6L1` PDF sets and the corresponding Perugia 2012 tune (P2012) [119]. The top mass is set to 172.5 GeV. The EvtGen v1.2.0 program [113] is used for properties of the bottom and charm hadron decays.

Diboson processes with 4 charged leptons, 3 charged leptons + 1 neutrino or 2 charged leptons and 2 neutrinos are simulated using the SHERPA generator (versions 2.2.1 when available and 2.1.1 otherwise). Matrix elements contain all diagrams with four electroweak vertices. They are calculated for up to 1 (4ℓ, 2ℓ+2ν) or 0 partons (3ℓ+1ν) at NLO and up to 3 partons at LO using the Comix and OpenLoops matrix element generators and merged with the SHERPA parton shower using the ME+PS@NLO prescription. In the case of the 2.2.1 samples, the NNPDF3.0nnlo PDF set is used in conjunction with dedicated parton shower tuning developed by the Sherpa authors; the generator cross sections are used in this case (already at NLO). In the case of the 2.1.1 samples, the CT10 PDF set is used in conjunction with dedicated parton shower tuning developed by the SHERPA authors; the generator cross sections are used in this case (already at NLO).

Diboson processes with one of the bosons decaying hadronically and the other leptonically are simulated using the SHERPA 2.2.1 generator. They are calculated for up to 1 additional parton at NLO and up to 3 additional partons at LO using the Comix and OpenLoops matrix element generators and merged with the SHERPA parton shower using the ME+PS@NLO prescription. The NNPDF30nnlo PDF set is used in conjunction with dedicated parton shower tuning developed by the Sherpa authors. The generator cross sections are used in this case (already at NLO).

For the estimation of the NCB processes, MC simulations are not employed; for the multijet processes, a method which employs data and MC simulation is used; given that the method, is implemented outside the scope this thesis, the needed samples are not reported.

8.2.3 Corrections to V + jet processes

The W + jets and Z + jets Sherpa samples are modeled at NLO in QCD (for up to 2 partons, LO for up to 4 partons) and LO in EW. A consistent set of theoretical calculations [140] is available to reweight the V + jets processes to the NLO order, on the QCD side, and to NLO with the addition of 2-loop logarithmic terms (NLL), on the EW side. These calculations provide also a consistent treatment of the systematic uncertainties. The absolute predictions and the associated uncertainties are illustrated in Figure 8.1, separately for the V + jets processes (left) and for their ratios (right).

An overview of the reweighting procedure and its implementation in the analysis are presented in the rest of the section, while the correction factors and the associated systematic uncertainties are discussed in Section 8.6.1.

The following formula, expressed in terms of the differential cross-section for V + jet events as computed from MC simulation (σ^V_{MC}) and from the theory calculation (σ^V_{TH}), describes the procedure for the one-dimensional reweighting of MC samples for V + jet production ($V = Z, W^{\pm}, \gamma$) in a generic variable x (e.g. $x = p^V_{\mathrm{T}}$):

$$\frac{d}{dx}\frac{d}{d\vec{y}}\sigma^V(\vec{\epsilon}_{MC}, \vec{\epsilon}_{TH}) := \frac{d}{dx}\frac{d}{d\vec{y}}\sigma^V_{MC}(\vec{\epsilon}_{MC})\frac{\frac{d}{dx}\sigma^V_{TH}(\vec{\epsilon}_{TH})}{\frac{d}{dx}\sigma^V_{MC}(\vec{\epsilon_{MC}})} \tag{8.1}$$

Where $\vec{y}$ denotes other kinematic variables included in the MC simulation, $\vec{\epsilon}_{MC}$ denotes the set of MC modeling uncertainties from sources independent on the variable x, and

finally, $\vec{\epsilon}_{TH}$ denotes the set of theoretical uncertainties associated with the above correction. It is therefore understood that this procedure is inclusive in all observables except the p_{T} of the boson.

The calculation of $\frac{d}{dx}\sigma_{TH}(\vec{\epsilon}_{TH})$ is first provided at leading order, and then corrected to NLO in QCD and NLO + Sudakov logs in EW (nNLO):

$$\frac{d}{dx}\sigma_{TH}(\vec{\epsilon}_{TH}) = K_{NLO}(x, \vec{\epsilon}_{TH}) \cdot (1 + \kappa_{EW}(x, \vec{\epsilon}_{TH})) \cdot \frac{d}{dx}\sigma_{LO}\,, \tag{8.2}$$

with:

$$\kappa_{EW} = \kappa_{NLOEW} + \kappa_{nNLOSud}\,. \tag{8.3}$$

In order to avoid fluctuations due to the limited MC statistics available for the QCD correction evaluation, a smoothing is applied to the ratio between the theory and MC prediction for the differential cross-section of these processes, as explained with more detail in Section 8.6.1.

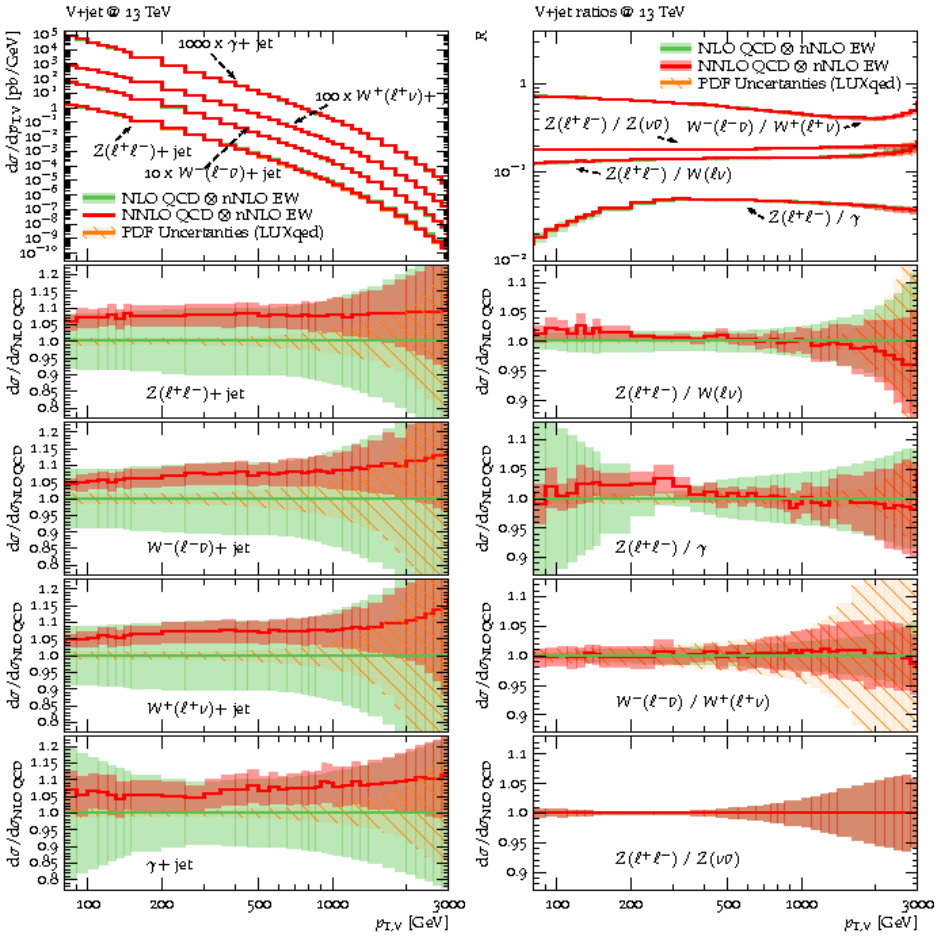

Figure 8.1: Predictions at NLO QCD⊗nNLO EW and NNLO QCD⊗nNLO EW for V + jets spectra (left) and ratios (right) at 13 TeV. The lower frames show the relative impact of NNLO corrections and theory uncertainties normalized to NLO QCD⊗nNLO EW. The green bands at NLO QCD⊗nNLO EW correspond to the combination (in quadrature) of the perturbative QCD, EW and mixed QCD-EW uncertainties, while the NNLO QCD⊗nNLO EW bands (red) display only QCD scale variations. PDF uncertainties are shown as separate hashed orange bands. From [140]. Note that the version of the calculations available for the mono-jet analysis does not include NNLO QCD predictions and PDF uncertainties, as they were not available.

8.3 Physics objects definition

The analysis selection is based on jets, b-jets, muons, electrons, and missing transverse momentum ($E_{\mathrm{T}}^{\mathrm{miss}}$). Photons are used in the $E_{\mathrm{T}}^{\mathrm{miss}}$ calculation and in the overlap removal. The reconstruction of these physics objects has been described in detail in Chapters 4 and 5. Calibrations and scale factors are applied to the physics objects to account for the differences between data and MC in the calibration, reconstruction, identification and isolation efficiency.

The criteria for the definition of the objects employed in this analysis are described in this section. Two categories are introduced for jets, b-jets, photons, electrons and muons: *baseline* objects are used for preselection and vetoes, while *signal* objects are part of the actual analysis selection defining the event topology in the signal and control regions.

Jets reconstructed using the anti-k_t algorithm with $R = 0.4$ and calibrated at the EM+JES scale. Hadronic decays of the tau-leptons are treated as jets in the analysis.

- **Baseline and Signal jets:** $p_{\mathrm{T}} > 30$ GeV and $|\eta| < 2.8$. In addition, to remove jets coming from pile-up it is required that JVT > 0.59 when 30 GeV$< p_{\mathrm{T}} <$ 60 GeV and $|\eta| < 2.4$.
- **B-tagged jets**: `MV2c10` discriminant for jets with $p_{\mathrm{T}} > 30$ GeV and $|\eta| < 2.5$.

Electrons

- **Baseline electrons:** $p_{\mathrm{T}} > 20$ GeV, $|\eta| < 2.47$, *Loose* identification.
- **Signal electrons:** same as baseline electrons and in addition *tight* identification, *FixedCutTight* isolation, standard cuts on the track parameters (see Section 4.4.1).

Muons

- **Baseline muons:** $p_{\mathrm{T}} > 10\,\mathrm{GeV}$, $|\eta| < 2.5$, *medium* identification. Cosmic muons and bad muons are vetoed.
- **Signal muons:** same as baseline muons, and in addition standard cuts on the significance of standard requirements on the track parameters (see Section 4.4.1)

Photons

- **Baseline photons:** $p_{\mathrm{T}} > 20\,\mathrm{GeV}$, $|\eta| < 2.37$, *tight* identification.
- **Signal photons:** same as baseline photons and in addition *FixedCutTight* isolation.

Missing transverse momentum

The baseline objects described above are used as input for the $E_{\mathrm{T}}^{\mathrm{miss}}$ reconstruction; hadronic decays of τ leptons are treated as jets. The 'Soft Term' computation used

is that of the TST, as explained in Section 5.2.3. In addition to the standard computation for the $E_{\mathrm{T}}^{\mathrm{miss}}$, two definitions of $E_{\mathrm{T}}^{\mathrm{miss}}$ are used, where the p_{T} of the signal electrons or of the signal muons are added to the standard $E_{\mathrm{T}}^{\mathrm{miss}}$ calculation.

$E_{\mathbf{T}}^{\mathbf{miss}}(\mathbf{no\text{-}}\mu)$: computed as $E_{\mathrm{T}}^{\mathrm{miss}}$ but adding the p_{T} of signal muons vectorially;

$E_{\mathbf{T}}^{\mathbf{miss}}(\mathbf{no\text{-}}e)$: computed as $E_{\mathrm{T}}^{\mathrm{miss}}$ but adding the p_{T} of signal electrons vectorially;

Overlap removal To resolve ambiguities which occur in the object reconstruction and identification, an overlap removal procedure which follows the recommendations of [124] is performed.

Overlap removal between jets and leptons is applied in two stages. Let us denote with j any baseline jet.

Stage 1

If $\Delta R(j, e/\mu) < 0.2$: The b-tagging used in the overlap removal is adjusted to the working point with 85% efficiency.

- jet is not b-jet: remove the jet and keep the electron or muon;
- jet is b-jet: keep the jet and remove the electron or muon (since the jet is likely coming from a semileptonic b decay).

Stage 2

- $\Delta R(j, e) < 0.4$: remove the electron and keep the jet;
- $\Delta R(j, \mu) < 0.4$ and jet with ≥ 3 associated ID tracks: remove the muon and keep the jet;
- $\Delta R(j, \mu) < 0.4$ and jet with < 3 tracks: keep the muon and discard the jet.

Overlap removal between photons and jets, electrons or muons is applied as follows:

- $\Delta R(\gamma, e) < 0.4$: remove the photon and keep the electron;
- $\Delta R(\gamma, \mu) < 0.4$: remove the photon and keep the muon;
- $\Delta R(\gamma, j) < 0.4$: keep the photon and remove the jet.

8.4 Event selection

The mono-jet analysis employs a number of control regions (CRs) to estimate the backgrounds in the region of interest (or signal region, SR). These control regions target the leptonic decays of the W and Z bosons and are built by requiring very similar criteria as the SR, except for the lepton selections, which are inverted, and the $E_{\mathrm{T}}^{\mathrm{miss}}$ computation, which is defined as the vectorial sum between $\mathbf{E}_{\mathrm{T}}^{\mathrm{miss}}$ and the $\mathbf{p}_{\mathrm{T}}$ of the selected leptons. Each of these computations aim to capture the p_{T} of the system of particles recoiling against the jets in a given region; for this reason, they are collectively referred to as $p_{\mathrm{T}}^{\mathrm{recoil}}$. Table 8.1 reports the main background component and the definition of $p_{\mathrm{T}}^{\mathrm{recoil}}$ for each analysis region.

The selection of CRs and SR is based on a common set of preselection cuts, which will be listed in the next section, together with the criteria for each individual CR and the SR and the kinematic distributions of the most relevant quantities in these regions.

Region	Enriched in	$p_{\mathrm{T}}^{\mathrm{recoil}}$	Comment
SR	$Z(\nu\nu)+$jets, $W+$jets	$E_{\mathrm{T}}^{\mathrm{miss}}$	
CR1mu0b	$W(\mu\nu)+$jets	$E_{\mathrm{T}}^{\mathrm{miss}}$(no-$\mu$)	proxy for $p_{\mathrm{T}}(W)$
CR1mu1b	$t\bar{t}$	$E_{\mathrm{T}}^{\mathrm{miss}}$(no-$\mu$)	proxy for $p_{\mathrm{T}}(W)$ from semi-leptonic $t\bar{t}$
CR1e	$W(e\nu)+$jets, $W(\tau\nu)+$jets	$E_{\mathrm{T}}^{\mathrm{miss}}$(no-$e$)	proxy for $p_{\mathrm{T}}(W)$
CR2mu	$Z(\mu\mu)+$jets	$E_{\mathrm{T}}^{\mathrm{miss}}$(no-$\mu$)	proxy for $p_{\mathrm{T}}(Z)$

Table 8.1: The quantity ($p_{\mathrm{T}}^{\mathrm{recoil}}$) used for the event selection in the various CRs and SR.

8.4.1 Pre-selection

The triggers employed for the selection of SR events and of most of the CRs are calorimeter based $E_{\mathrm{T}}^{\mathrm{miss}}$-triggers: this means that the muon spectrometer information is not used in the evaluation of $E_{\mathrm{T}}^{\mathrm{miss}}$ at trigger level, i.e. that muons are considered as invisible particles. CRs that do not include muons or genuine $E_{\mathrm{T}}^{\mathrm{miss}}$ utilize special triggers, which are mentioned in the respective subsections. The trigger expression includes the lowest unprescaled $E_{\mathrm{T}}^{\mathrm{miss}}$ trigger for every LHC run included in the dataset:

$$\begin{aligned}&(\texttt{HLT\_xe70} \,\&\&\, 2015\,\text{data})\,\text{OR}\\ &(\texttt{HLT\_xe80\_tc\_lcw\_L1XE50}\,\text{OR}\,\texttt{HLT\_xe90\_mht\_L1XE50}\text{OR}\\ &\texttt{HLT\_xe100\_mht\_L1XE50}\,\text{OR}\,\texttt{HLT\_xe110\_mht\_L1XE50})\&\&2016\,\text{data})\end{aligned} \tag{8.4}$$

where the various trigger items employ thresholds of 70, 80, 90, 100, 110 GeV at the HLT, a threshold of 50 GeV at the L1 and different calculations of the $E_{\mathrm{T}}^{\mathrm{miss}}$. Each trigger is found to be fully efficient in the region selected by the analysis ($E_{\mathrm{T}}^{\mathrm{miss}} > 250\,\mathrm{GeV}$).

In order to suppress contributions from calorimeter noise and non-collision background, events with any $BadLoose$ jet, passing the overlap removal described in the previous section, are discarded. Further rejection of non-collision backgrounds is obtained by discarding events with $BadTight$ leading jet.

The preselection cuts for all regions are listed in Table 8.2.

Category	Selection Criteria
Trigger	$E_{\mathrm{T}}^{\mathrm{miss}}$ trigger (see Eq. 8.4)
GRL	`PHYS_StandardGRL_all_Good_25ns`
Vertex	$\geq$1 vertex with $N_{\mathrm{trk}} \geq 2$
Event Cleaning	SCTGood && TileGood && LArGood && CoreFlags
Jet cleaning	No $BadLoose$ baseline jet
Leading jet	$p_{\mathrm{T}} > 250$ GeV, $\lvert\eta\rvert < 2.4$
	not $BadTight$
Jet multiplicity	$N_{\mathrm{jets}} \leq 4$ (signal jets)
Multijet suppression	$\Delta\phi(E_{\mathrm{T}}^{\mathrm{miss}}, \text{any jet}) > 0.4$

Table 8.2: Preselection cuts for all regions except `CR1e`, which employ different triggers. "SCTGood", "TileGood", "LArGood" and "CoreFlags" indicate the requirement that, in the event, there were no SCT, Tile and LAr calorimeter problems and that there were no lost detector fragments in the detector readout, respectively.

8.4.2 `SR`: Signal region

Events are assigned to the signal region, `SR`, if:

- they pass the pre-selection cuts;
- $E_{\mathrm{T}}^{\mathrm{miss}} > 250\,\mathrm{GeV}$;
- no baseline lepton is reconstructed.

Figures 8.2–8.4 show the expected kinematic distributions, where the background prediction is obtained directly from MC simulation, corresponding to an integrated luminosity of $36.1\,\mathrm{fb}^{-1}$.

8.4.3 `CR1mu0b`: one-muon + 0 b-jet control region

The `CR1mu0b` is enriched in the background process $W(\mu\nu)+$jets, and defined in such a way to be orthogonal to a region enriched in events with $t\bar{t}$ and single $-$ t backgrounds, `CR1mu1b`. Events are assigned to `CR1mu0b` region if:

- they pass the pre-selection cuts;
- $E_{\mathrm{T}}^{\mathrm{miss}}(\text{no-}\mu) > 250\,\mathrm{GeV}$;
- no baseline electron is reconstructed;
- exactly one baseline muon is reconstructed;
- the baseline muon passes also the signal muon selection criteria;

- the transverse mass of the $E_{\mathrm{T}}^{\mathrm{miss}} - \mu$ system[1] satisfies $30\,\mathrm{GeV} < m_{\mathrm{T}} < 100\,\mathrm{GeV}$.
- no selected jet is a b-jet;

Since the $E_{\mathrm{T}}^{\mathrm{miss}}$ includes muons as invisible particles, $E_{\mathrm{T}}^{\mathrm{miss}}(\text{no-}\mu)$ is essentially a proxy for $p_{\mathrm{T}}(W)$.
Figures 8.5–8.7 show kinematic distributions for the events in this region, where the total MC distribution is normalized to the number of observed events in data. There is good shape agreement between the data and the MC expectation in the variables that are used for the event selection. The few exceptions are discussed at the end of the section.
The level of purity achieved in this region is 84%.

8.4.4 `CR1mu1b`: one-muon + 1 b-jet control region

This control region is designed to be enriched in the $t\bar{t}$ and single $-$ t backgrounds. It is constructed starting from the same conditions required for `CR1mu0b`, except that at least one b-jet is required, identified as explained in Section 8.3.
Figures 8.8–8.10 show kinematic distributions for the events in this region, where the total MC distribution is normalized to the number of observed events in data. The level of purity achieved in this region is 75%.

8.4.5 `CR2mu`: two-muon control region

The `CR2mu` is enriched in the background process $Z(\mu\mu)$ + jets. Events are assigned to this region if:

- they pass the pre-selection cuts;
- $E_{\mathrm{T}}^{\mathrm{miss}}(\text{no-}\mu) > 250\,\mathrm{GeV}$;
- no baseline electron is reconstructed;
- exactly two baseline muons are reconstructed;
- both the baseline muons pass also the signal muon selection criteria;
- the invariant mass of the dimuon system satisfies $66 < m_{\mu\mu} < 116\,\mathrm{GeV}$.

Figures 8.11–8.14 show kinematic distributions for the events in this region, where the total MC distribution is normalized to the number of observed events in data. The level of purity achieved in this region is 93%.

8.4.6 `CR1e`: one-electron control region

The `CR1e` is mainly enriched in $W(e\nu)$ + jets events. Events are assigned to this region if:

[1] Note that $E_{\mathrm{T}}^{\mathrm{miss}}$, and not $E_{\mathrm{T}}^{\mathrm{miss}}(\text{no-}\mu)$, is used to define the transverse mass.

- they pass the pre-selection cuts, except for the trigger requirements: the trigger expression for this region includes the lowest unprescaled single-electron triggers for every LHC run included in the dataset.
- $E_{\mathrm{T}}^{\mathrm{miss}}(\text{no-}e) > 250\,\mathrm{GeV}$;
- no baseline muon is reconstructed;
- exactly one signal electron is reconstructed with $p_{\mathrm{T}} > 30\,\mathrm{GeV}$ and $|\eta| > 1.52$ or $|\eta| < 1.37$ (to exclude the crack region);
- the transverse mass of the $E_{\mathrm{T}}^{\mathrm{miss}} - e$ system satisfies: $30\,\mathrm{GeV} < m_{\mathrm{T}} < 100\,\mathrm{GeV}$;
- the event has a high $E_{\mathrm{T}}^{\mathrm{miss}}$ significance to suppress the contamination of the multijet background, $E_{\mathrm{T}}^{\mathrm{miss}}/\sqrt{H_{\mathrm{T}}} > 5\,\mathrm{GeV}^{1/2}$, where $H_{\mathrm{T}} = \sum_{\text{signal jets}} p_{\mathrm{T}}$.

This region is defined in a similar way as `CR1mu0b`, with the difference of the absence of any b-jet requirement, the usage of single electron triggers, the introduction of a veto of electrons in the crack, tight isolation criteria and a $E_{\mathrm{T}}^{\mathrm{miss}}$ significance cut.

Figures 8.15–8.17 show kinematic distributions for the events in this region, where the total MC distribution is normalizedd to the number of observed events in data. The level of purity achieved in this region is 76%.

8.4.7 Data/MC agreement in the CRs

In general, there is good shape agreement between data and MC expectation for the kinematic distributions which are used for the event selection in each region.

One exception is the η of the leading jet, η^{jet}, where an asymmetry at the level of 3% can be seen in all regions. This slight asymmetry also reflects on the η of the leptons, which, in these topologies, is correlated to that of the jet. A reweighting in η^{jet} to correct for the asymmetry has been derived and the results of the analysis evaluated again, with the conclusion that the results of the analysis are insensitive to this mismodeling.

A slight mismodeling can also be observed in the jet multiplicity distribution in all `CR`s. Similarly as above, a reweighting in the n_{jet} has been tested, but the results of the analysis are insensitive to the reweighting.

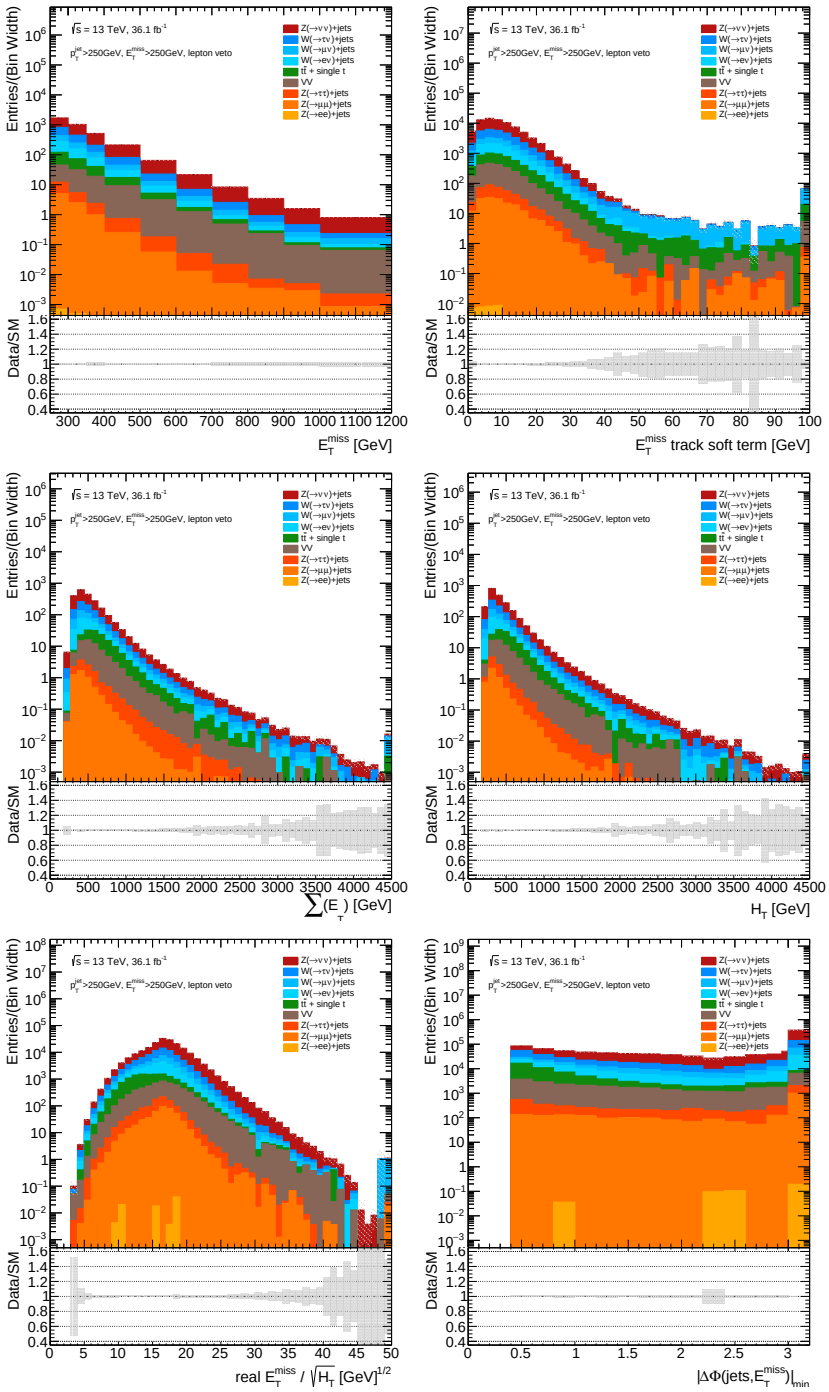

Figure 8.2: Pre-fit Pre-fit kinematic distributions in the SR corresponding to $36.1\,\mathrm{fb}^{-1}$. The error bands in the upper and lower panel include only the uncertainty due to limited MC statistics.

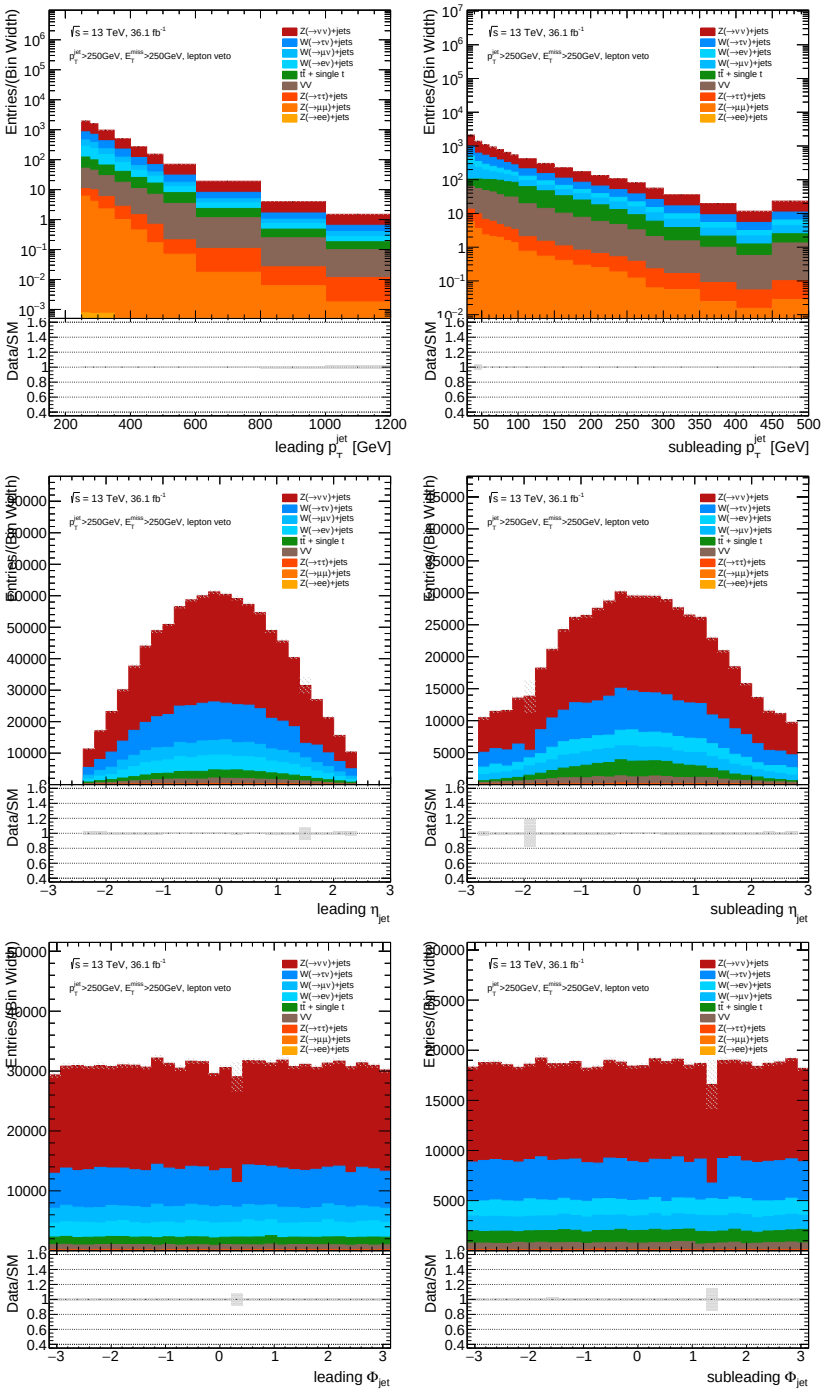

Figure 8.3: Pre-fit Pre-fit kinematic distributions in the SR corresponding to $36.1\,\mathrm{fb}^{-1}$. The error bands in the upper and lower panel include only the uncertainty due to limited MC statistics.

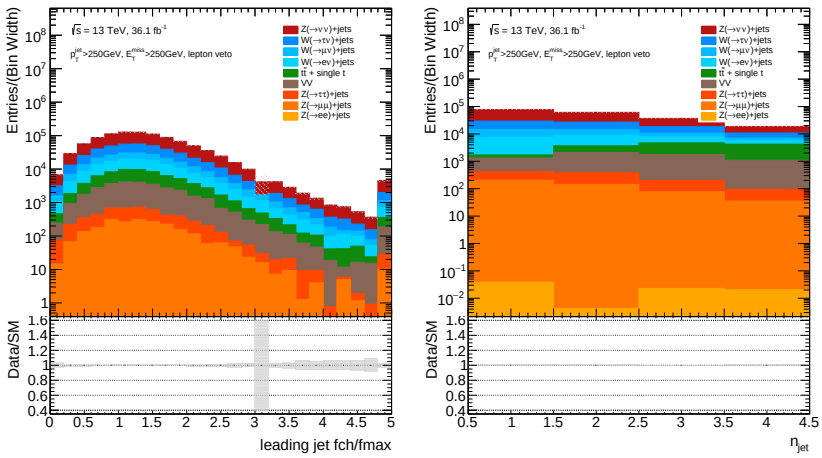

Figure 8.4: Pre-fit Pre-fit kinematic distributions in the SR corresponding to $36.1\,\mathrm{fb}^{-1}$. The error bands in the upper and lower panel include only the uncertainty due to limited MC statistics.

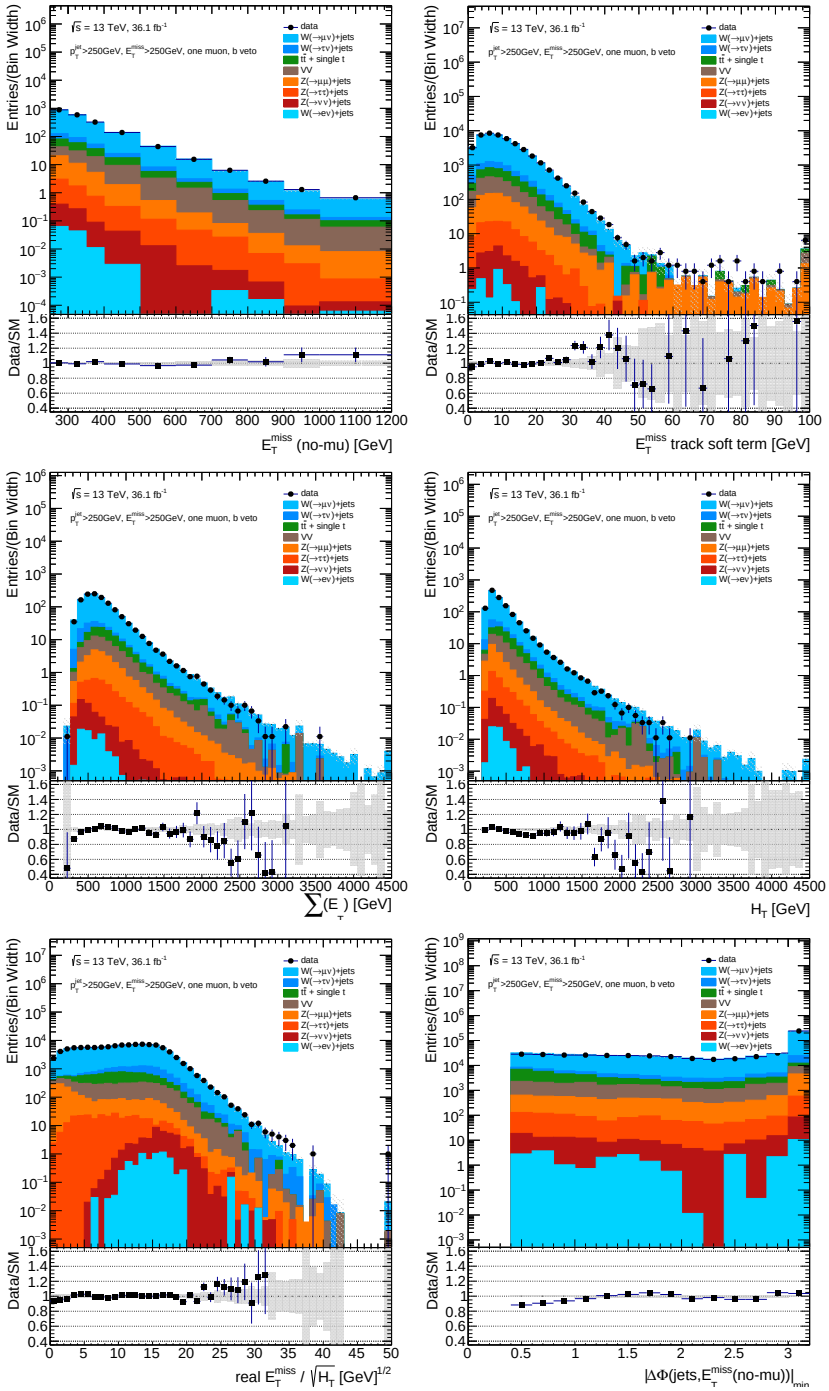

Figure 8.5: Pre-fit kinematic distributions in the `CR1mu0b`. $V+$jets spectra are weighted to higher order corrections (see Section 8.2.3). The sum of the MC spectra are normalized to the total number of observed events in data. The error bands in the upper and lower panel include only the uncertainty due to limited MC statistics.

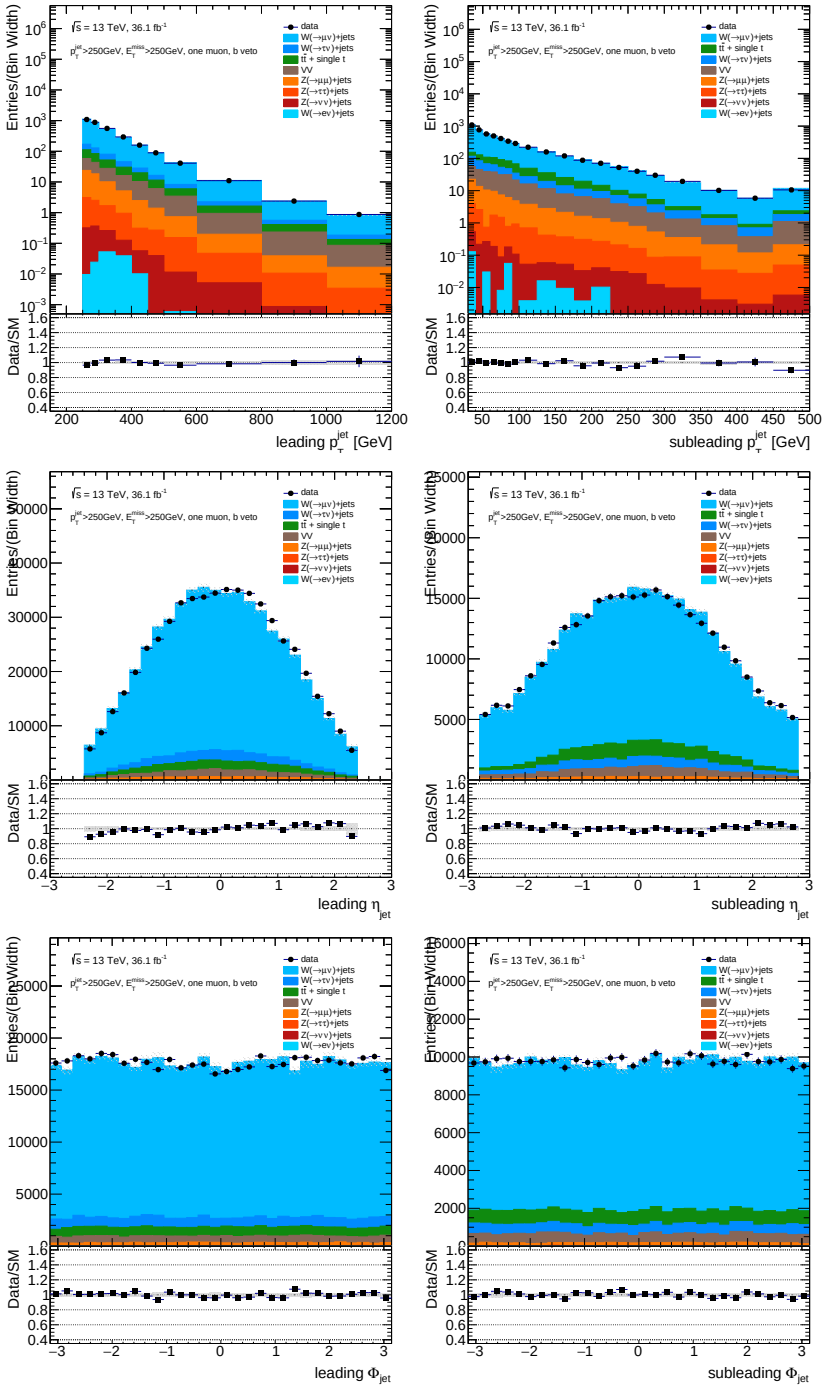

Figure 8.6: Pre-fit kinematic distributions in the `CR1mu0b`. $V+$jets spectra are weighted to higher order corrections (see Section 8.2.3). The sum of the MC spectra are normalized to the total number of observed events in data. The error bands in the upper and lower panel include only the uncertainty due to limited MC statistics.

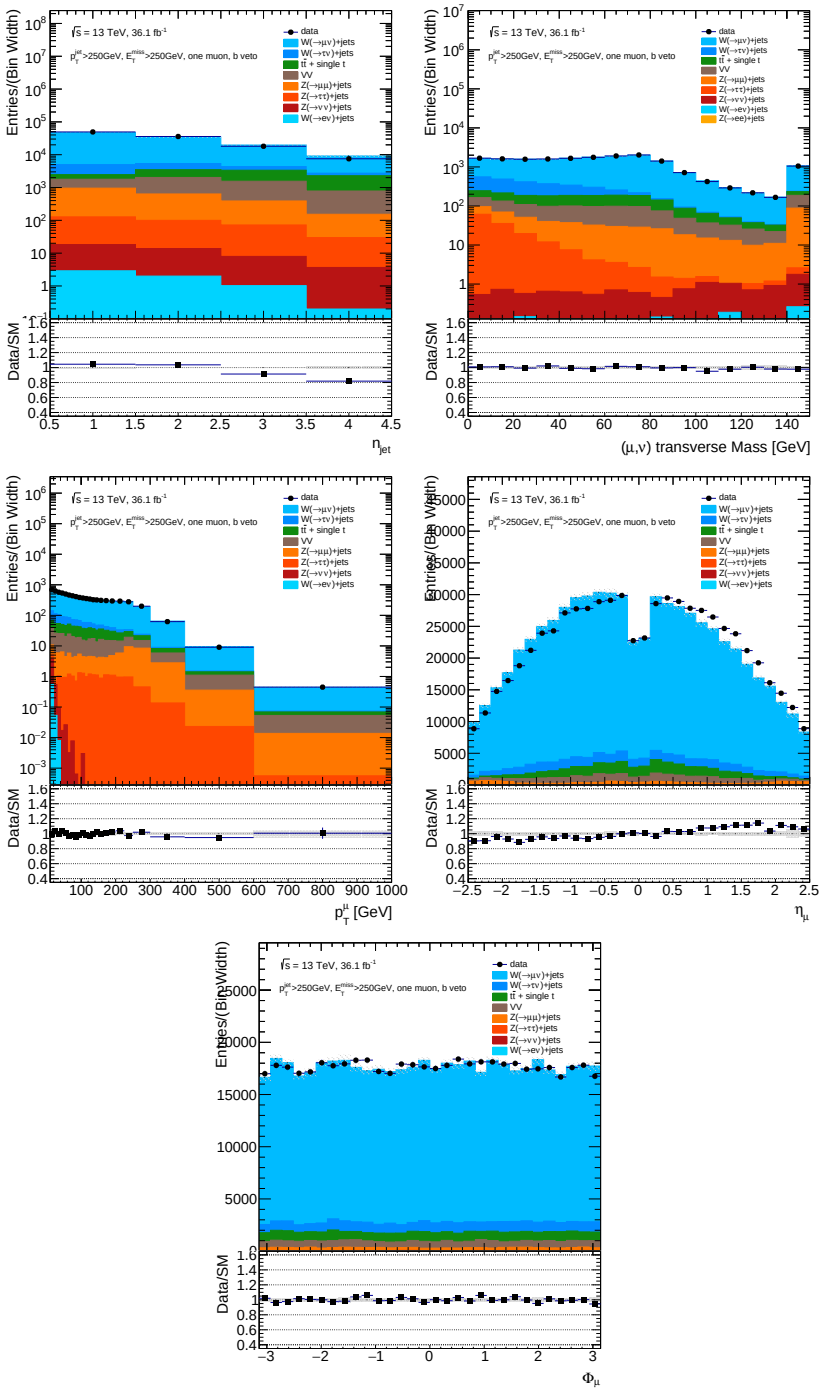

Figure 8.7: Pre-fit kinematic distributions in the `CR1mu0b`. $V+$jets spectra are weighted to higher order corrections (see Section 8.2.3). The sum of the MC spectra are normalized to the total number of observed events in data. The error bands in the upper and lower panel include only the uncertainty due to limited MC statistics.

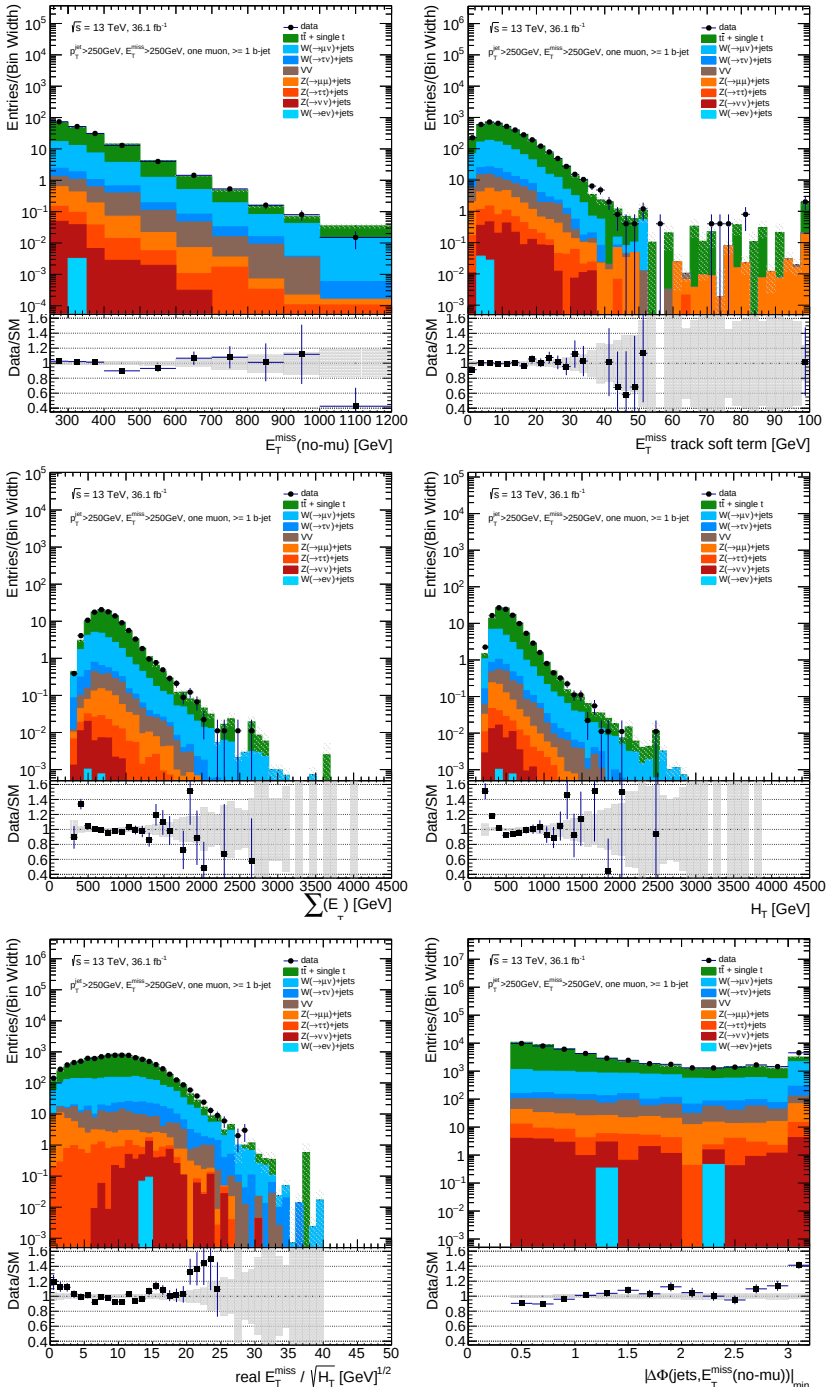

Figure 8.8: Pre-fit kinematic distributions in the `CR1mu1b`. $V+$jets spectra are weighted to higher order corrections (see Section 8.2.3). The sum of the MC spectra are normalized to the total number of observed events in data. The error bands in the upper and lower panel include only the uncertainty due to limited MC statistics.

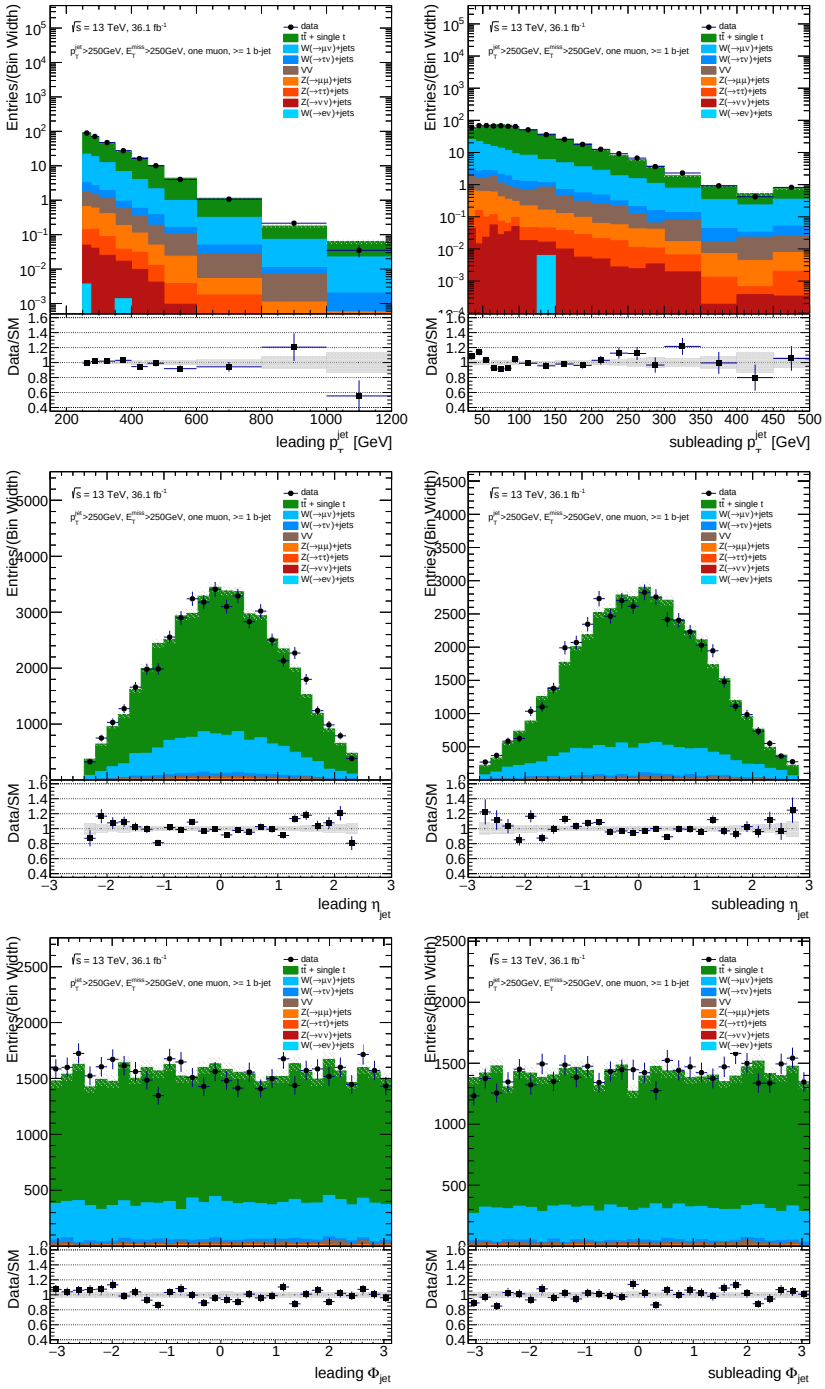

Figure 8.9: Pre-fit kinematic distributions in the `CR1mu1b`. $V+$jets spectra are weighted to higher order corrections (see Section 8.2.3). The sum of the MC spectra are normalized to the total number of observed events in data. The error bands in the upper and lower panel include only the uncertainty due to limited MC statistics.

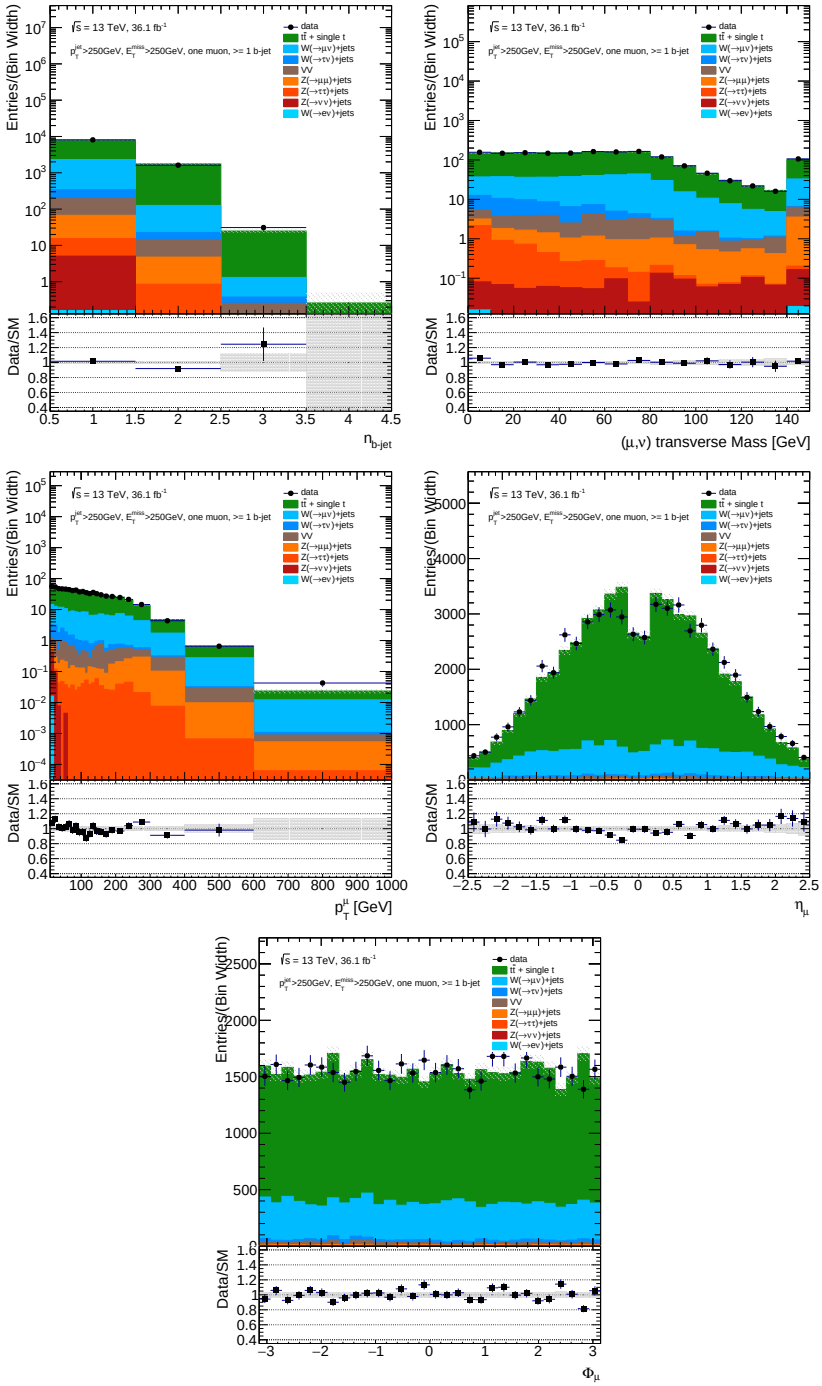

Figure 8.10: Pre-fit kinematic distributions in the `CR1mu1b`. V + jets spectra are weighted to higher order corrections (see Section 8.2.3). The sum of the MC spectra are normalized to the total number of observed events in data. The error bands in the upper and lower panel include only the uncertainty due to limited MC statistics.

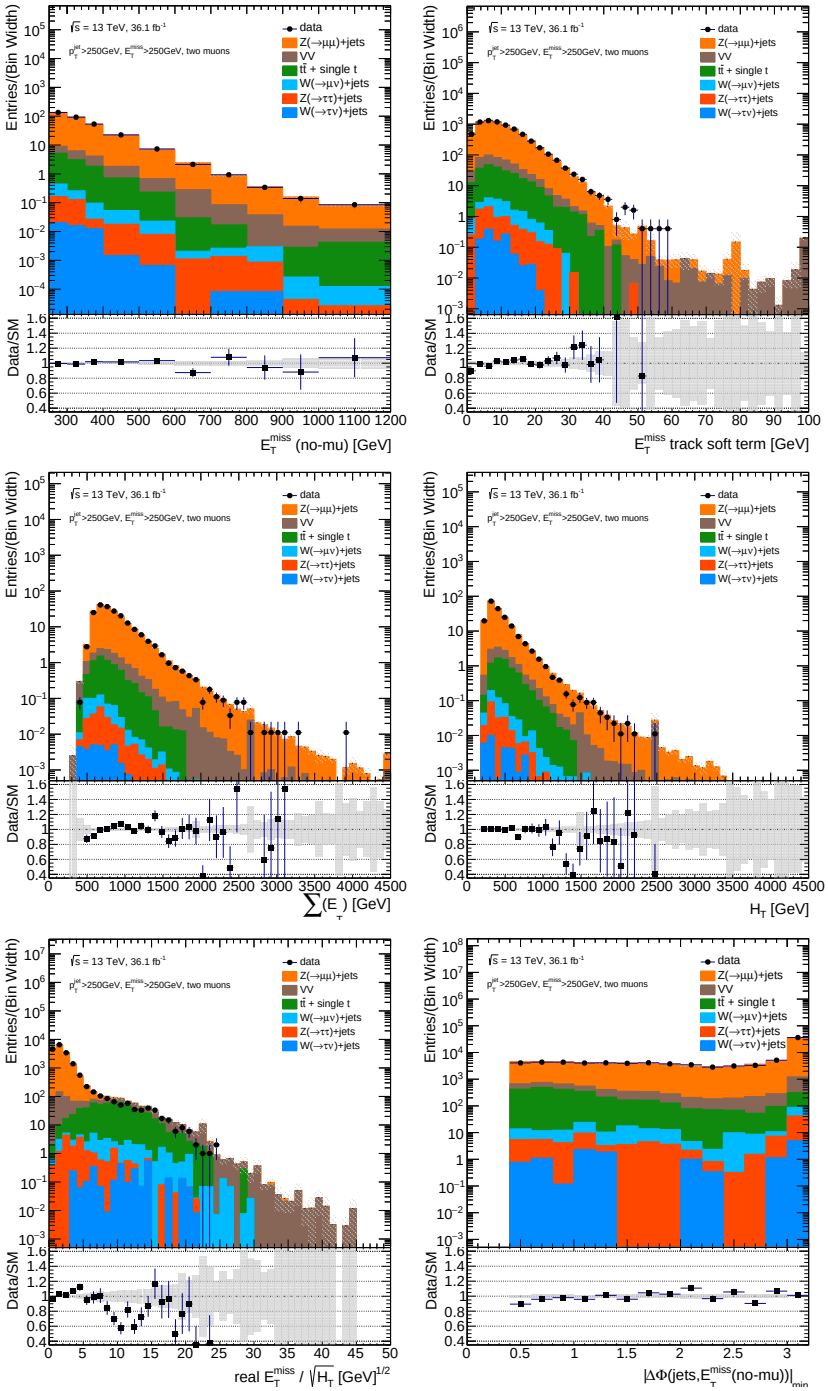

Figure 8.11: Pre-fit kinematic distributions in the `CR2mu`. V + jets spectra are weighted to higher order corrections (see Section 8.2.3). The sum of the MC spectra are normalized to the total number of observed events in data. The error bands in the upper and lower panel include only the uncertainty due to limited MC statistics.

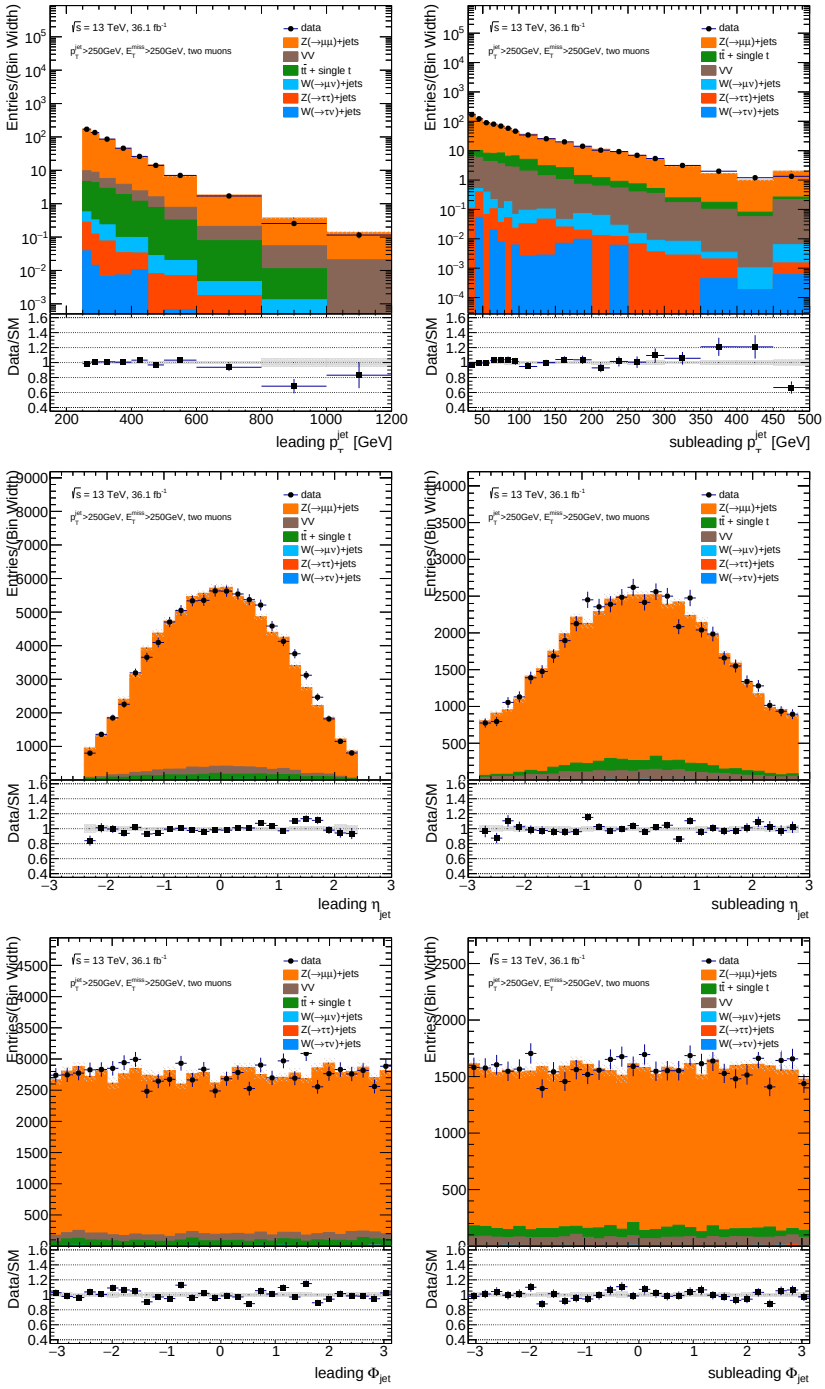

Figure 8.12: Pre-fit kinematic distributions in the `CR2mu`. V + jets spectra are weighted to higher order corrections (see Section 8.2.3). The sum of the MC spectra are normalized to the total number of observed events in data. The error bands in the upper and lower panel include only the uncertainty due to limited MC statistics.

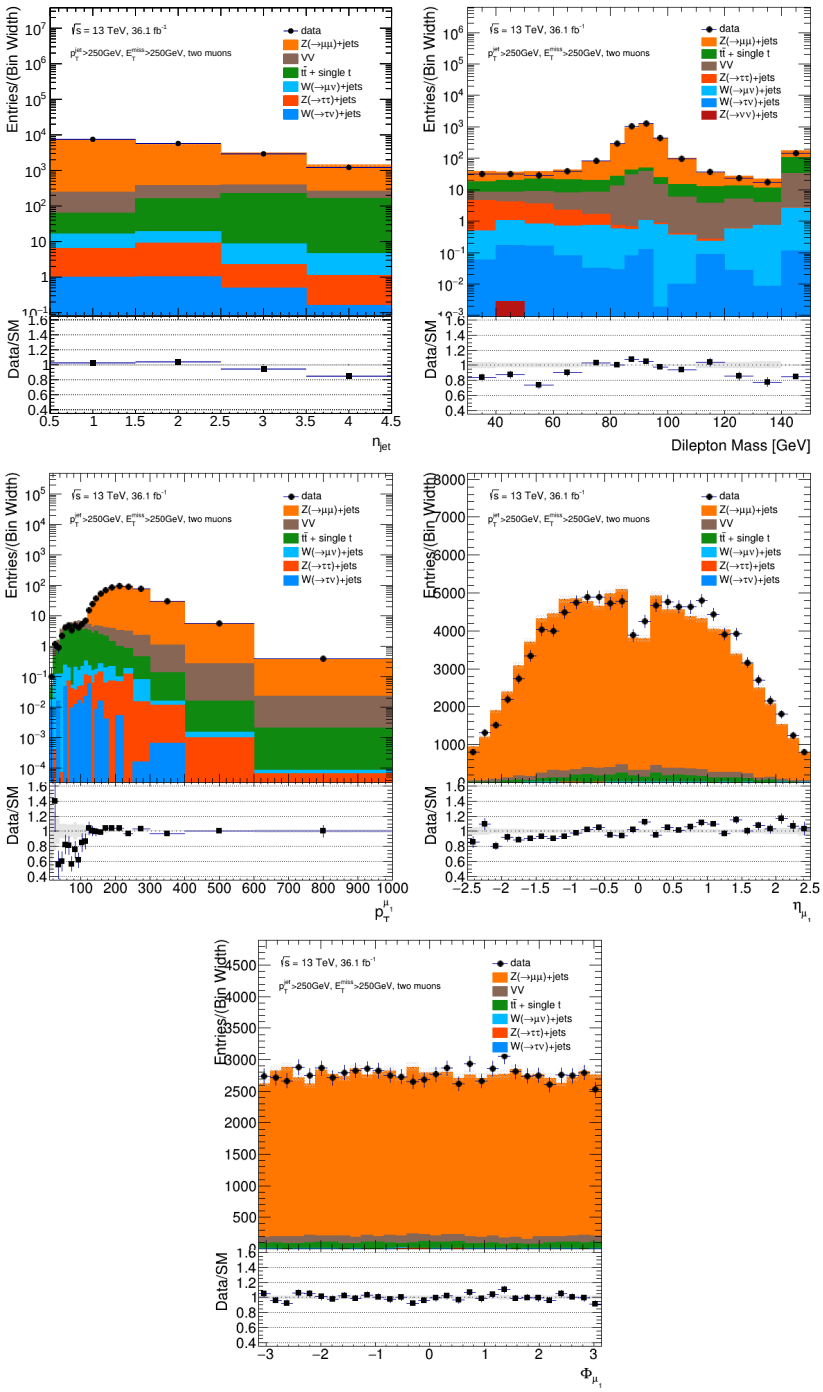

Figure 8.13: Pre-fit kinematic distributions in the CR2mu. V + jets spectra are weighted to higher order corrections (see Section 8.2.3). The sum of the MC spectra are normalized to the total number of observed events in data. The error bands in the upper and lower panel include only the uncertainty due to limited MC statistics. Note that for the distribution of the dimuon invariant mass, the full distribution is shown, but only events with $66 < m_{\mu\mu} < 116\,\text{GeV}$ are retained in CR2mu.

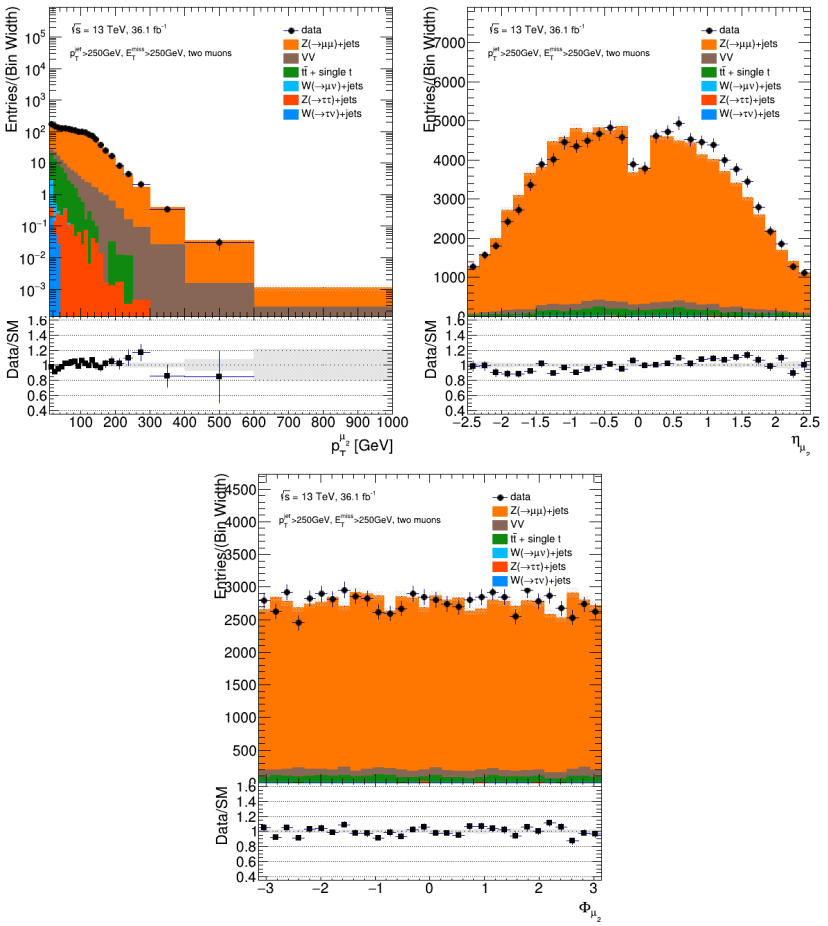

Figure 8.14: Pre-fit kinematic distributions in the `CR2mu`. V + jets spectra are weighted to higher order corrections (see Section 8.2.3). The sum of the MC spectra are normalized to the total number of observed events in data. The error bands in the upper and lower panel include only the uncertainty due to limited MC statistics.

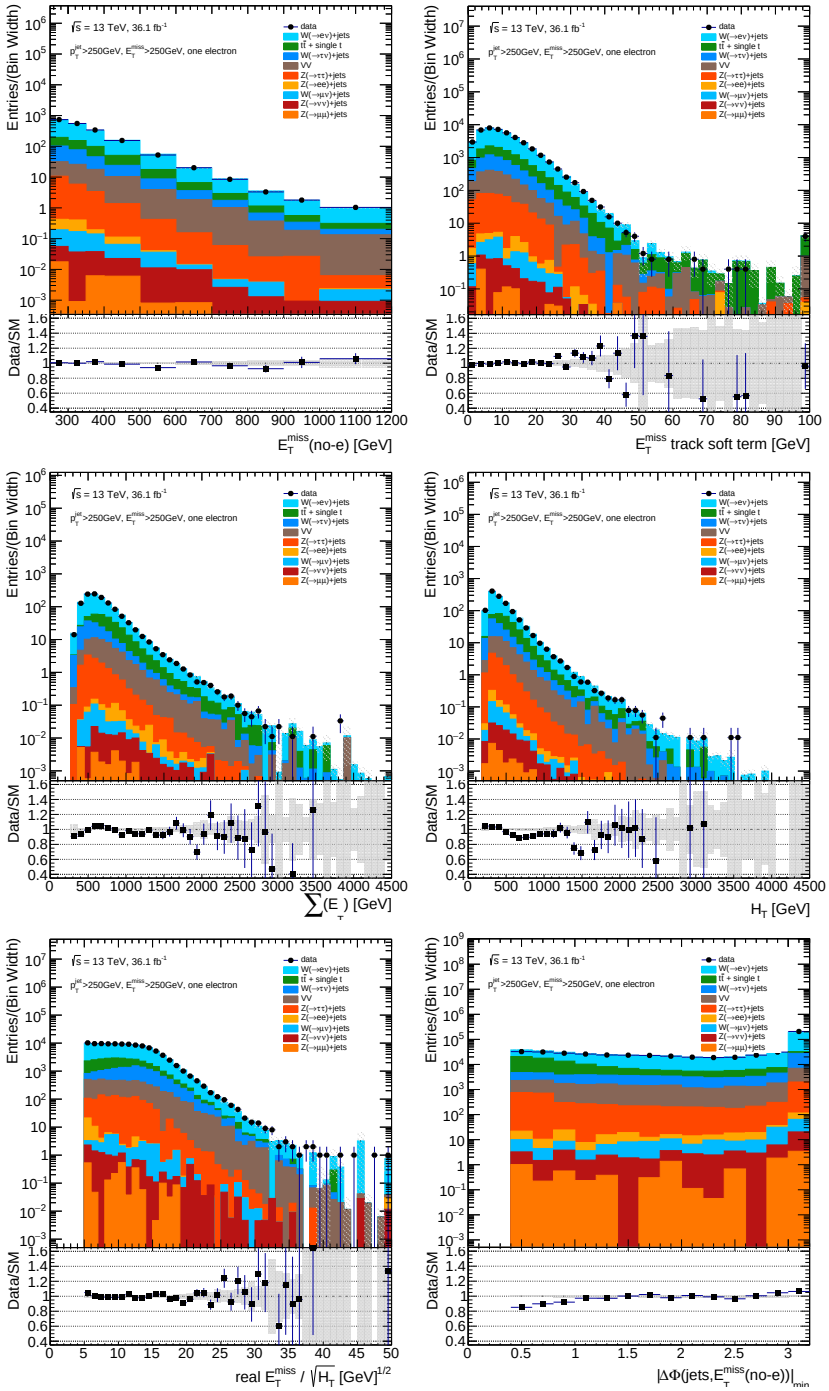

Figure 8.15: Pre-fit kinematic distributions in the `CR1e`. V + jets spectra are weighted to higher order corrections (see Section 8.2.3). The sum of the MC spectra are normalized to the total number of observed events in data. The error bands in the upper and lower panel include only the uncertainty due to limited MC statistics.

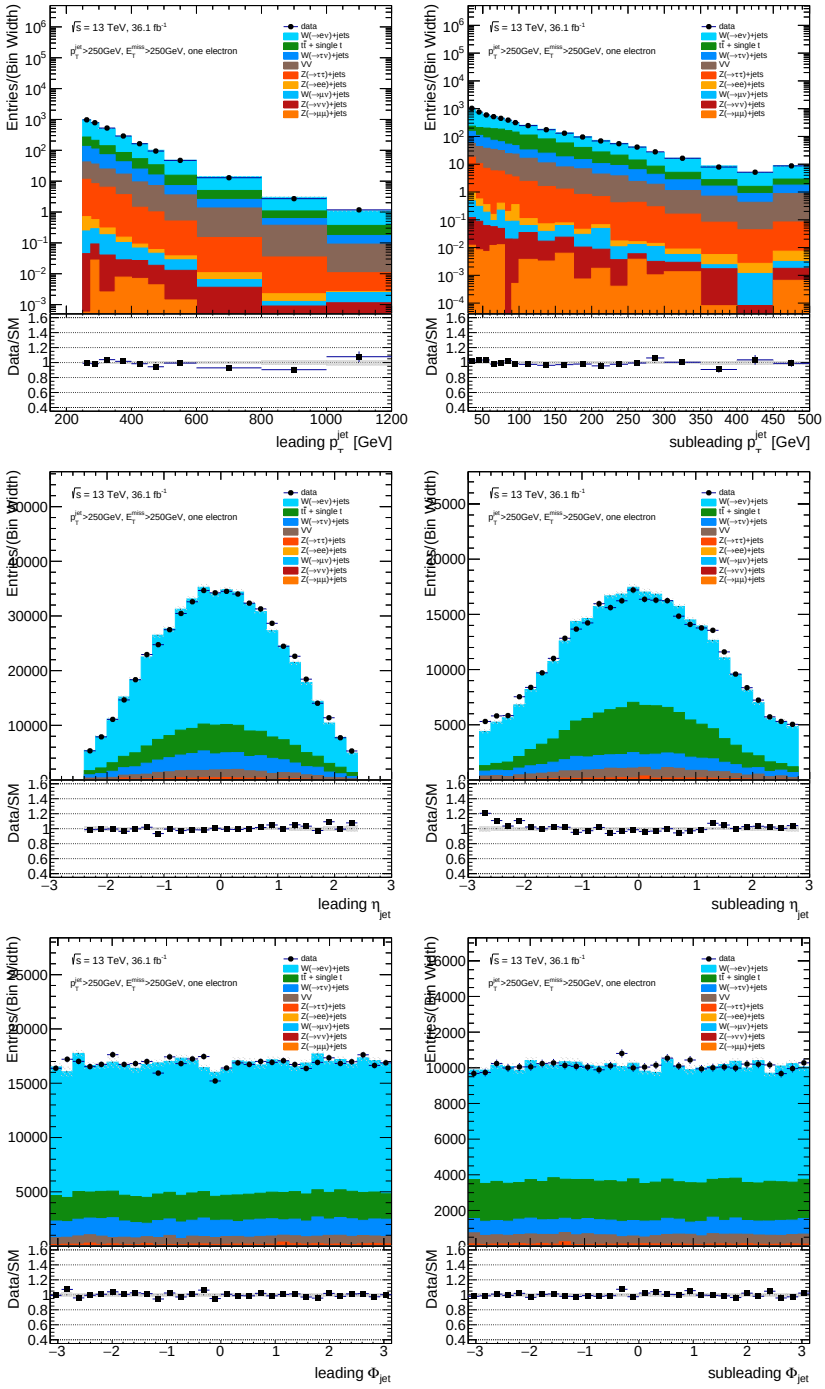

Figure 8.16: Pre-fit kinematic distributions in the `CR1e`. V + jets spectra are weighted to higher order corrections (see Section 8.2.3). The sum of the MC spectra are normalized to the total number of observed events in data. The error bands in the upper and lower panel include only the uncertainty due to limited MC statistics.

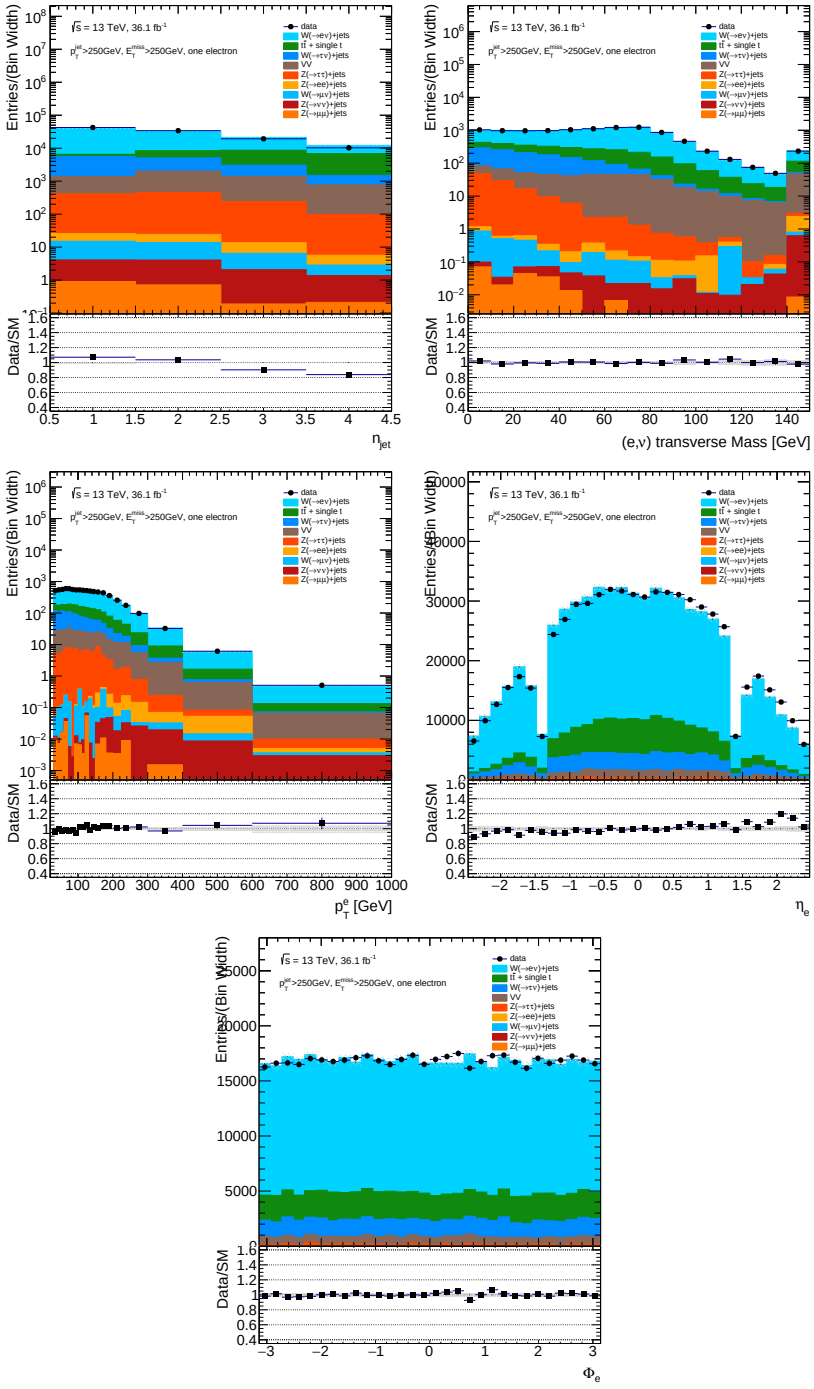

Figure 8.17: Pre-fit kinematic distributions in the CR1e. V + jets spectra are weighted to higher order corrections (see Section 8.2.3). The sum of the MC spectra are normalized to the total number of observed events in data. The error bands in the upper and lower panel include only the uncertainty due to limited MC statistics.

8.5 Background estimation techniques

8.5.1 Overview

An overview of the background processes which yield a mono-jet final state was given in Section 8.1. All dominant backgrounds are evaluated using data control regions.

The dominant background process is the $Z(\nu\nu) + \text{jets}$, which is irreducible; its percentage with respect to the total background ranges from 50% at low $E_{\text{T}}^{\text{miss}}$ up to 70% in the TeV regime. Secondary contributions come from $W(\ell\nu) + \text{jets}$, where the lepton is outside the detector acceptance or passes the lepton veto, or, in the case of tau decaying hadronically, is reconstructed as a jet. $W(\tau\nu) + \text{jets}$ accounts for approximately 20% at low $E_{\text{T}}^{\text{miss}}$, decreasing to 10% at high $E_{\text{T}}^{\text{miss}}$. $W(e\nu) + \text{jets}$ and $W(\mu\nu) + \text{jets}$ together give a contribution of similar size. The $Z(\ell\ell) + \text{jets}$ processes enter the signal region in a similar way but such cases are rare because both leptons have to pass the `SR` requirements.
For all these backgrounds, $V + \text{jets}$-enriched control regions are built, as explained in Section 8.4, and a data-to-simulation factor which normalizes the MC in the `SR`, is extracted from a simultaneous fit to the data in the `CR`s (see Section 7.5.1).

Another important background is the $t\bar{t}$, and the sub-leading single-top, which together account for approximately 4% of the total background at low $E_{\text{T}}^{\text{miss}}$ and decrease to the sub-percent level above 800 GeV. For the estimation of these backgrounds, a dedicated `CR1mu1b` is defined and a data-to-simulation factor is determined from the simultaneous fit to the data in the `CR`s.

Diboson contributions are at the level of 2% at low $E_{\text{T}}^{\text{miss}}$ and decrease to the sub-percent level already for $E_{\text{T}}^{\text{miss}} > 350$ GeV; this background is estimated directly from the MC simulation.

Multijet processes where one or more jets are misreconstructed, leading to large $E_{\text{T}}^{\text{miss}}$, represent a sub-percent level background at low $E_{\text{T}}^{\text{miss}}$ and are negligible at high $E_{\text{T}}^{\text{miss}}$. This background is estimated with a semi-data-driven technique, described in Section 8.5.4.

Residual non-collision backgrounds in the `SR` are estimated in a data-driven way which relies on the different timing between collision and non-collision jets, as described in Section 8.5.3.

Table 8.3 summarizes the techniques used for the estimation of the different sources of background.

8.5.2 Simultaneous fit

The simultaneous fit technique is based on a binned profiled likelihood approach, and is used both for the background estimation and for the signal extraction.

The observable of interest to discriminate between signal and background is the distribution of $p_{\text{T}}^{\text{recoil}}$, introduced in the Section 8.4. The definition of $p_{\text{T}}^{\text{recoil}}$ is each control region tries to capture the p_{T} of the recoil system in events involving the production of a W or Z boson, thus providing a proxy for the true p_{T} of the boson in each region. A demonstration that this is the case is provided in Figure 8.18, which shows the linear

Process	Background estimation method
$Z(\nu\nu)+$ jets	simultaneous fit to data (Section 8.5.2)
$W(\tau\nu)+$ jets	″″
$W(\mu\nu)+$ jets	″″
$W(e\nu)+$ jets	″″
$Z(\tau\tau)+$ jets	″″
$Z(\mu\mu)+$ jets	″″
$Z(ee)+$ jets	″″
$t\bar{t}$ and single $-$ t	″″
diboson	from MC
multijet	jet smearing (Section 8.5.4), data-driven
non-collision background	NCB tagger (Section 8.5.3), data-driven

Table 8.3: Background estimation techniques used for the different processes contributing to the SR.

correlation between the $p_{\mathrm{T}}^{\mathrm{recoil}}$ and the true $p_{\mathrm{T}}(V)$ for the dominant background in the SR and in each CRs. A correlation close to 1 can be observed for these cases. We note that for the $W(\tau\nu)+$ jets process, the correlation factor is smaller, but similar between the SR, and the regions where it is the second-leading background, CR1e and CR1mu0b (see Figure 8.19).

The binning of $p_{\mathrm{T}}^{\mathrm{recoil}}$ is the same in all regions and defined in Table 8.4: the chosen binning provides a good discrimination of the signal over the background and guarantees that the statistical fluctuations of the MC are kept at a reasonable level.

Exclusive bins (for shape fits)		Inclusive bins (for model-independent fits)	
Name	Selection	Name	Selection
BIN_250	$250\,\mathrm{GeV} < p_{\mathrm{T}}^{\mathrm{recoil}} < 300\,\mathrm{GeV}$	BIN>250	$p_{\mathrm{T}}^{\mathrm{recoil}} > 250\,\mathrm{GeV}$
BIN_300	$300\,\mathrm{GeV} < p_{\mathrm{T}}^{\mathrm{recoil}} < 350\,\mathrm{GeV}$	BIN>300	$p_{\mathrm{T}}^{\mathrm{recoil}} > 300\,\mathrm{GeV}$
BIN_350	$350\,\mathrm{GeV} < p_{\mathrm{T}}^{\mathrm{recoil}} < 400\,\mathrm{GeV}$	BIN>350	$p_{\mathrm{T}}^{\mathrm{recoil}} > 350\,\mathrm{GeV}$
BIN_400	$400\,\mathrm{GeV} < p_{\mathrm{T}}^{\mathrm{recoil}} < 500\,\mathrm{GeV}$	BIN>400	$p_{\mathrm{T}}^{\mathrm{recoil}} > 400\,\mathrm{GeV}$
BIN_500	$500\,\mathrm{GeV} < p_{\mathrm{T}}^{\mathrm{recoil}} < 600\,\mathrm{GeV}$	BIN>500	$p_{\mathrm{T}}^{\mathrm{recoil}} > 500\,\mathrm{GeV}$
BIN_600	$600\,\mathrm{GeV} < p_{\mathrm{T}}^{\mathrm{recoil}} < 700\,\mathrm{GeV}$	BIN>600	$p_{\mathrm{T}}^{\mathrm{recoil}} > 600\,\mathrm{GeV}$
BIN_700	$700\,\mathrm{GeV} < p_{\mathrm{T}}^{\mathrm{recoil}} < 800\,\mathrm{GeV}$	BIN>700	$p_{\mathrm{T}}^{\mathrm{recoil}} > 700\,\mathrm{GeV}$
BIN_800	$800\,\mathrm{GeV} < p_{\mathrm{T}}^{\mathrm{recoil}} < 900\,\mathrm{GeV}$	BIN>800	$p_{\mathrm{T}}^{\mathrm{recoil}} > 800\,\mathrm{GeV}$
BIN_900	$900\,\mathrm{GeV} < p_{\mathrm{T}}^{\mathrm{recoil}} < 1000\,\mathrm{GeV}$	BIN>900	$p_{\mathrm{T}}^{\mathrm{recoil}} > 900\,\mathrm{GeV}$
BIN_1000	$p_{\mathrm{T}}^{\mathrm{recoil}} > 1000\,\mathrm{GeV}$	BIN>1000	$p_{\mathrm{T}}^{\mathrm{recoil}} > 1000\,\mathrm{GeV}$

Table 8.4: Bins of the observable $p_{\mathrm{T}}^{\mathrm{recoil}}$ used in the simultaneous fit.

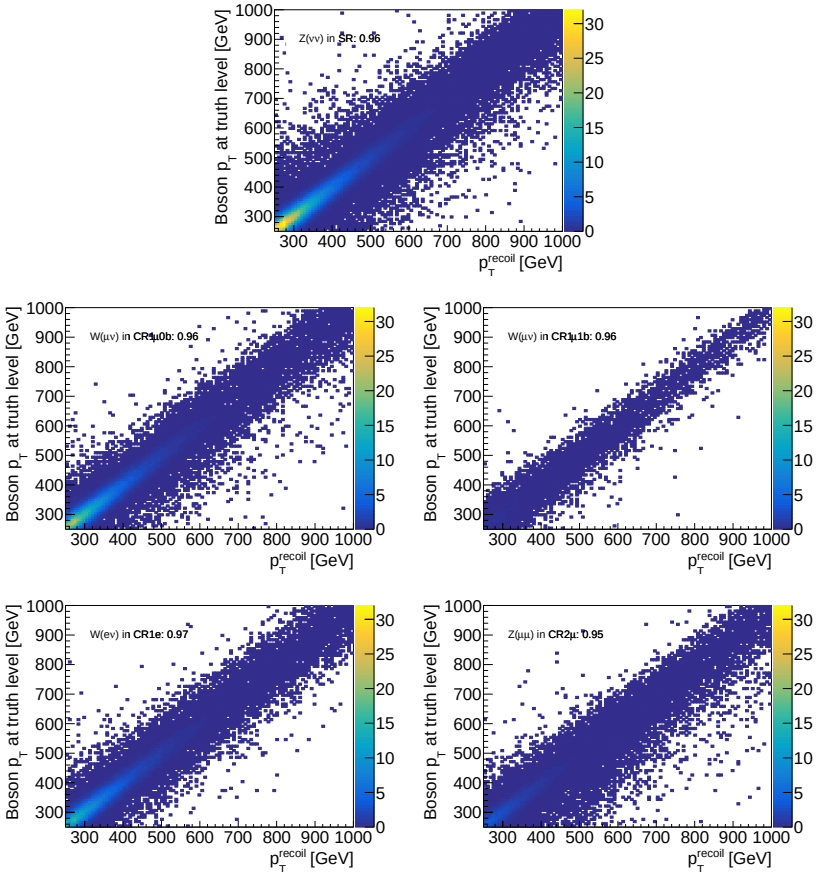

Figure 8.18: Correlation between $p_{\mathrm{T}}^{\mathrm{recoil}}$ and the true $p_{\mathrm{T}}(V)$ for the leading background in a given analysis region. In each plot the correlation factor is also reported.

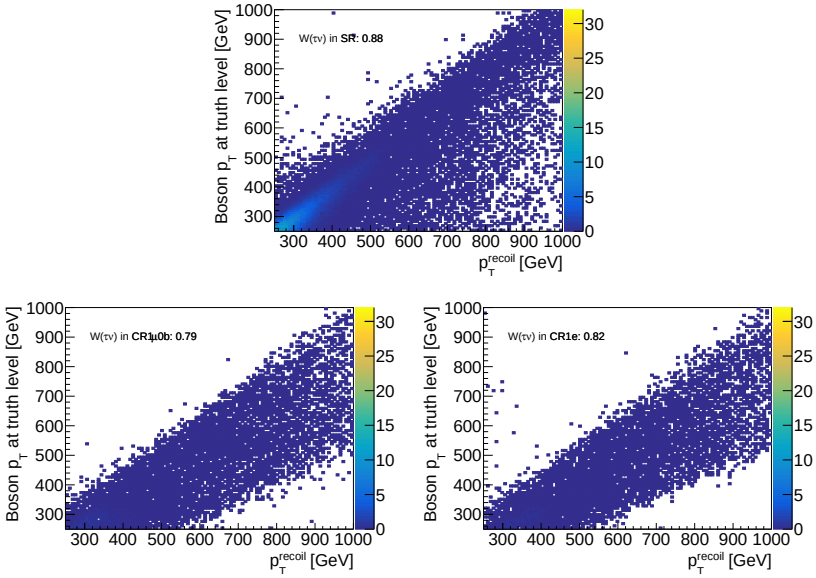

Figure 8.19: Correlation between $p_{\mathrm{T}}^{\mathrm{recoil}}$ and the true $p_{\mathrm{T}}(V)$ for the $W(\tau\nu)+$jets backgrounds in the `SR`, `CR1mu0b`, `CR1e`. In each plot the correlation factor is also reported.

The likelihood model is built similarly as described in Section 7.5.1, with the main difference being the use of a binned likelihood as opposed to a one-bin likelihood.
Let:

- r run over the signal or control regions;
- i run over the $p_{\mathrm{T}}^{\mathrm{recoil}}$ bins;
- the random variable N_{ri}^{obs} be the observed total yield in the i-th $p_{\mathrm{T}}^{\mathrm{recoil}}$ bin of region r;
- $N_{ri}^{X} = N_{ri}^{X}(\theta)$ be the expected yield of process X in the i-th $p_{\mathrm{T}}^{\mathrm{recoil}}$ bin of region r;
- $\vec{\theta}$ be the vector of nuisance parameters describing systematic uncertainties on the predicted yield of each background in each region and $p_{\mathrm{T}}^{\mathrm{recoil}}$ bin;
- μ be the free parameter associated to the normalization of the considered signal (*signal strength*);
- $\vec{\kappa}$ be the vector of free parameters of the fit, the $\kappa-$ factors, associated to the normalization of the backgrounds, $\vec{\kappa} = \left(\kappa^{W/Z}, \kappa^{t}\right)$.

Then, the likelihood $\mathcal{L}$ is defined as

$$\mathcal{L}(\mu, \vec{\kappa}, \vec{\theta}) = \prod_{r}\prod_{i} \mathrm{Poisson}\left(N_{ri}^{\mathrm{obs}} \mid \mu N_{ri}^{\mathrm{sig}}(\vec{\theta}) + N_{ri}^{\mathrm{bkg}}(\vec{\kappa}, \vec{\theta})\right) f_{\mathrm{constr}}(\vec{\theta}), \tag{8.5}$$

where

$$\begin{aligned} N_{ri}^{\mathrm{bkg}} = {} & \kappa^{W/Z}(N_{ri}^{Z(\nu\nu)+\mathrm{jets}} + N_{ri}^{W(\ell\nu)+\mathrm{jets}} + N_{ri}^{Z(\ell\ell)+\mathrm{jets}}) \\ & + \kappa^{t} N_{ri}^{t\bar{t},\mathrm{single}-t} \\ & + N_{ri}^{\mathrm{diboson}} + N_{ri}^{\mathrm{multijet}} + N_{ri}^{\mathrm{NCB}}. \end{aligned} \tag{8.6}$$

The dependence of N_{ri}^{X} on to the systematic uncertainties, which are described as nuisance parameters, is omitted in Eq. 8.6 to simplify the notation. The term f_{constr} of Eq. 8.5 represents the product of the gaussian constraints applied to each of the nuisance parameters.
With the exception of $N_{ri}^{\mathrm{multijet}}$ and N_{ri}^{NCB} which are data-driven, the expected yield of a given process in a given region and bin is obtained from the MC simulation and computed as already reported in Eq. 7.6.
The normalisation factor $\kappa^{W/Z}$ connects the normalisation of the $Z+$jets and the $W+$jets processes: in this way, the information obtained from the control regions enriched in W + jets and Z + jets events is used to constrain the $Z(\nu\nu)$ + jets and $W(\ell\nu)$ + jets backgrounds in the SR. The fact that the normalisation factor is one for all bins enhances the connection between the low and high part of the $p_{\mathrm{T}}^{\mathrm{recoil}}$ spectrum, such that the shape information on the $p_{\mathrm{T}}^{\mathrm{recoil}}$ is used to fit the data. This is particularly important for the bins at high $p_{\mathrm{T}}^{\mathrm{recoil}}$, since it permits to highly reduce the statistical uncertainties. The

importance of using Z and W channels and the shape information is further discussed in Section 8.7.

The normalisation of the $t\bar{t}$ and single-top processes is decoupled from the V + jets processes: a second global normalisation factor κ^t multiplies only these two processes and ensures their connection between the CRs and the SR.

Fitting procedures

Four fitting procedures are used to derive the results:

- **CR-only shape fit** is used primarily for the estimation of background and to assess the impact of systematic uncertainties on the background expectation. It uses the likelihood model of Eq. 8.5, except that the terms in the CRs are not included and the signal component is set to zero ($\mu = 0$). The exclusive $p_{\mathrm{T}}^{\mathrm{recoil}}$ bins defined in Table 8.4 are used;
- **CR+SR shape fit** is used for the interpretation of the results in terms of the considered signal models. It uses the likelihood model of Eq. 8.5 and the exclusive $p_{\mathrm{T}}^{\mathrm{recoil}}$ bins defined in Table 8.4;
- **CR-only counting fit** is used for the background estimation in a given inclusive $p_{\mathrm{T}}^{\mathrm{recoil}}$ bin, as defined in Table 8.4. It uses a simplified likelihood, where only the information from the CRs in a given inclusive $p_{\mathrm{T}}^{\mathrm{recoil}}$ bin is used.
- **CR+SR counting fit** is used for the model-independent limit in a given inclusive $p_{\mathrm{T}}^{\mathrm{recoil}}$ bin, as defined in Table 8.4. It uses the same likelihood model as CR-only counting fit, but including also the SR.

8.5.3 Non-collision background

A high-p_{T} jet recoiling against missing transverse momentum is also the event signature of non–collision background (NCB) jets. Without applying the jet cleaning, the non-collision background dominates the signal region at $\mathcal{O}(100)$ the rate of SM background processes, as shown in Figure 8.20. The *tight* jet cleaning efficiently rejects NCB in the mono-jet SR, suppressing non-collision rates by $\mathcal{O}(10^3)$.

The residual NCB in the SR is estimated using a data-driven method which rely on the characteristic difference in jet time t_{jet} for non–collision jets and jets originating from proton–proton collisions. t_{jet} is calculated from with the energy–weighted average of the time of the energy deposits in the jet, and defined with respect to the event time recorded by the trigger [151]. Jets with $|t_{\mathrm{jet}}| > 5$ ns are predominantly non–collision jets.

The NCB estimation procedure in each bin of $E_{\mathrm{T}}^{\mathrm{miss}}$ is as follows:

- A region enriched in NCB is constructed using the signal region selection but inverting the *tight* cleaning criteria.
- The number of events is counted in the NCB region: $N^{\mathrm{NCB\ region}}$.

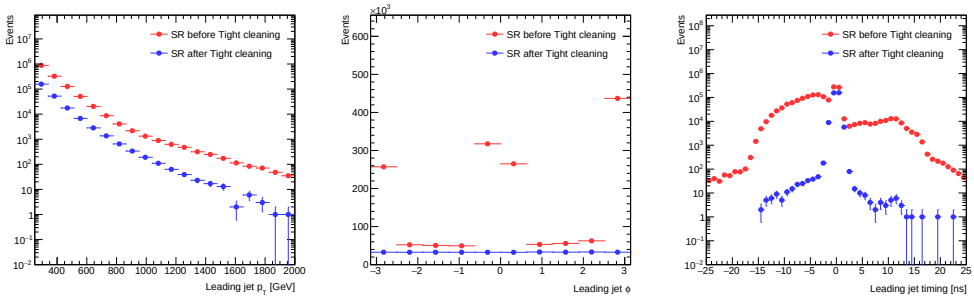

Figure 8.20: Leading jet p_{T}, ϕ, and t_{jet} distributions in the signal region before and after *tight* jet cleaning. The distinctive ϕ structure in the before–cleaning distribution is characteristic of NCB. Plots by collaborator.

- The number of events with leading $t_{\mathrm{jet}} < -5$ ns is counted in the NCB region: $N_{\mathrm{tagged}}^{\text{NCB region}}$.
- The ratio between the number of positively out–of–time jet events and the total number of events in the NCB region is taken as the tagging efficiency: $\epsilon = N_{\mathrm{tagged}}^{\text{NCB region}} / N^{\text{NCB region}}$.
- The number of events with leading $t_{\mathrm{jet}} < -5$ ns is counted in the signal region: $N_{\mathrm{tagged}}^{\mathrm{SR}}$.
- The final NCB estimate is obtained by scaling the number of tagged events in the signal region by the inverse of the tagging efficiency: $N^{\text{NCB in SR}} = N_{\mathrm{tagged}}^{\mathrm{SR}} / \epsilon$.

As the kinematics for positively out–of–time and negatively out–of–time jets are different [128], a crosscheck is performed using leading $t_{\mathrm{jet}} > 5$ ns. The results of this procedure are shown for the inclusive signal region in Table 8.5 and for each bin of $E_{\mathrm{T}}^{\mathrm{miss}}$ in Table 8.6. The predicted NCB is consistent between the two tagging techniques. Given the slight tension between the two tagging techniques, a consrvative uncertainty of 100% is assigned on the estimated yields.

Tagging selection	$N^{\text{NCB region}}$	$N_{\mathrm{tagged}}^{\text{NCB region}}$	$N_{\mathrm{tagged}}^{\mathrm{SR}}$	ϵ	$N^{\text{NCB in SR}}$
$t_{\mathrm{jet}} < -5$ ns	1272810	488371	135	$38.37 \pm 0.06\%$	352 ± 30
$t_{\mathrm{jet}} > 5$ ns	1272810	94043	40	$7.39 \pm 0.02\%$	541 ± 86

Table 8.5: Total amount of non–collision background in the signal region $E_{\mathrm{T}}^{\mathrm{miss}} > 250$ GeV. Errors shown are statistical uncertainties.

8.5.4 Multijet background

The multijet background with large $E_{\mathrm{T}}^{\mathrm{miss}}$ mainly originates from the misreconstruction of the energy of a jet in the calorimeter and to a lesser extent is due to the presence of neu-

$E_{\mathrm{T}}^{\mathrm{miss}}$ bin in SR	$N^{\text{NCB in SR}}$ using $t_{\text{jet}} < -5$ ns	$N^{\text{NCB in SR}}$ using $t_{\text{jet}} > 5$ ns
$250 < E_{\mathrm{T}}^{\mathrm{miss}} < 300$ GeV	242 ± 26	251 ± 55
$300 < E_{\mathrm{T}}^{\mathrm{miss}} < 350$ GeV	71 ± 14	146 ± 42
$350 < E_{\mathrm{T}}^{\mathrm{miss}} < 400$ GeV	29 ± 8	57 ± 28
$400 < E_{\mathrm{T}}^{\mathrm{miss}} < 500$ GeV	18 ± 6	59 ± 34
$500 < E_{\mathrm{T}}^{\mathrm{miss}} < 600$ GeV	4 ± 3	0
$E_{\mathrm{T}}^{\mathrm{miss}} > 600$ GeV	0	0

Table 8.6: Total amount of non–collision background in the specified regions. Errors shown are statistical uncertainties.

trinos in the final state from heavy-flavour hadron decays. This background is strongly suppressed by the requirement on the minimum angular distance between the $E_{\mathrm{T}}^{\mathrm{miss}}$ and the reconstructed p_{T} of the jets. The residual contribution in the SR is determined using the jet smearing method, which is described in detail in Ref. [152].

Dedicated response functions are determined to describe the difference between the true and reconstructed jet p_{T}. These functions are used to smear the jet p_{T} of selected 'seed' events, which are events in data with well-measured jets. Well-measured jets are obtained by minimizing the amount of $E_{\mathrm{T}}^{\mathrm{miss}}$ in the event through a cut on the $E_{\mathrm{T}}^{\mathrm{miss}}$ significance. After smearing these events many times, the obtained sample of events is used to model the distributions of multijet events. Figure 8.21 shows the distributions of key variables for the seed and for the smeared events.

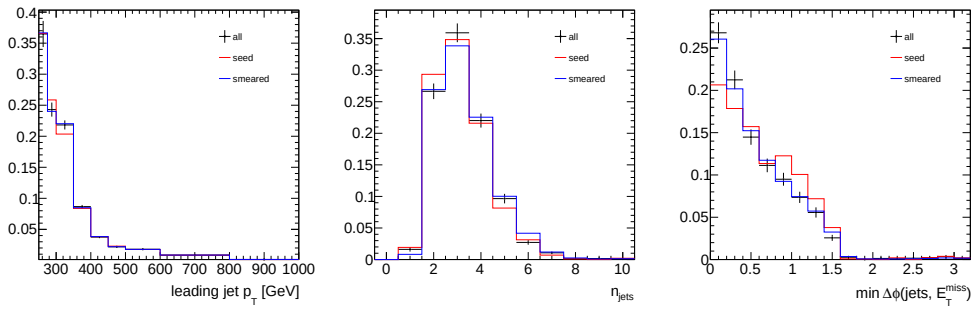

Figure 8.21: Distributions of the leading jet p_{T}, N_{jets} and $\Delta\phi_{\text{min}}(E_{\mathrm{T}}^{\mathrm{miss}}, \text{jet})$ for the seed events before (black) and after (red) the significance cut. Distributions for the smeared events are shown in blue. Plots by collaborator.

The estimated constributions of multijet events in each bin of the SR is then obtained as follows:

- a region enriched in multijet events (CRqcd) is defined by reverting the $\Delta\phi_{\text{min}}(jet, E_{\mathrm{T}}^{\mathrm{miss}}) < 0.4$ cut;
- the number of multijet events (mj) in the CRqcd region is determined as:

$$N_{mj,est}^{\text{CRqcd}} = N_{data}^{\text{CRqcd}} - N_{OtherMC}^{\text{CRqcd}}; \tag{8.7}$$

- if S is the ensemble of the smeared events, the ratio r is defined as:

$$r = \frac{N^S_{|\Delta\phi|>0.4}}{N^S_{|\Delta\phi|<0.4}} \tag{8.8}$$

- the estimated number of events coming from multijet processes in the SR $N^{SR}_{mj,est}$ is then obtained as:

$$N^{SR}_{mj,est} = N^{\mathrm{CRqcd}}_{mj,est} \times r : \tag{8.9}$$

The estimates are summarized in Table 8.7. A conservative 100% uncertainty is assigned on each of the yields.

Region in $E_{\mathrm{T}}^{\mathrm{miss}}$ [GeV]	Signal Region Estimate
250-300	487.4
300-350	165.1
350-400	29.9
400-500	12.6
500-600	5.4
600-700	1.25
700-800	0.66
800-900	0.52
>900	0.22
$\sum$	704

Table 8.7: Multijet estimate in the signal region: the total estimate is 704 events in the region with $E_{\mathrm{T}}^{\mathrm{miss}} > 250$ GeV. The estimates for the exclusive $E_{\mathrm{T}}^{\mathrm{miss}}$-bins are shown here. A conservative uncertainty of 100% is assigned on each estimate.

8.6 Systematic uncertainties

Several sources of experimental and theoretical uncertainties on the knowledge of the background prediction are considered and included in the likelihood model as nuisance parameters. Section 8.6.1 discusses the methods to determine the theoretical uncertainties, while Section 8.6.2 describes the sources of experimental uncertainties. The effect of all these uncertainties on the estimate of the background prior to fitting is summarized in Section 8.6.3.

8.6.1 Theoretical and modeling uncertainties

Theoretical uncertainties on V + jets

As already explained in Section 8.2.3, the V+jets samples are reweighted to perturbative calculations to account for higher corrections. These calculations are provided with a treatment of the systematic uncertainties: QCD and EW uncertainties, as well as those arising from the combination of QCD and EW corrections are consistently calculated for the V + jets processes and are provided on an event-by-event basis and applied as nuisance parameters with Gaussian distributions.

The following sources of uncertainties are provided on the reweighted $p_{\mathrm{T}}(V)$ distribution separately for $Z(\ell\ell)$ + jets, $Z(\nu\nu)$ + jets and $W(\ell\nu)$ + jets channels:

- $\delta_1 K_{NLO}$: accounts for the effect of QCD scales on the normalisation;
- $\delta_2 K_{NLO}$: accounts for the effect of QCD scales on the shape;
- $\delta_3 K_{NLO}$: accounts for non-universality of QCD corrections across Z+jets, W+jets and γ-jet processes;
- $\delta_1 \kappa_{EW}$: accounts for unknown effects beyond EW NNLO;
- $\delta_2 \kappa_{EW}$: accounts for unknown terms in the NLO calculation at high p_{T};
- $\delta_3 \kappa_{EW}$: accounts for the limitations of the Sudakov approximation;
- δK_{mix}: accounts for unknown EW and QCD interference terms not taken into account by treating these as separate corrections.

These nuisance parameters are to be treated as independent from one another, but correlated across boson p_{T} and across processes. Exceptions are the two parameters $\delta_2 \kappa_{EW}$ and $\delta_3 \kappa_{EW}$ for which the universality is not demonstrated and therefore are treated independently for W + jets, Z + jets, but still correlated across boson p_{T}.

Figure 8.22 shows the EW correction factors, obtained as described in Section 8.2.3, for the $Z(\ell\ell)$ + jets, $Z(\nu\nu)$ + jets and $W(\ell\nu)$ + jets processes, together with the associated nuisance parameters. Figure 8.23 shows instead the QCD correction factors for the same processes, together with the QCD associated nuisance parameters. These correction factors are then applied multiplicatively to the MC prediction.

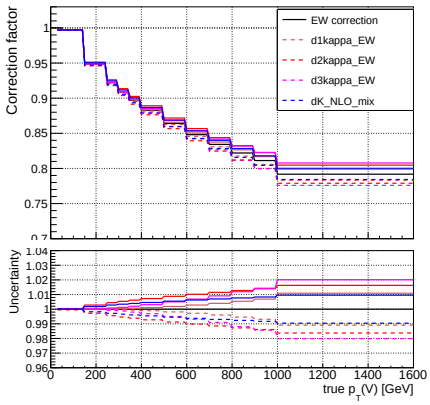

(a) $Z(\ell\ell)$ + jets

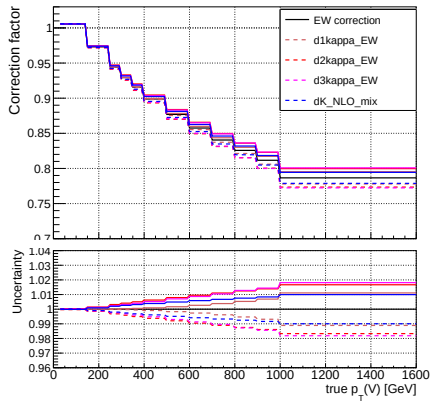

(b) $Z(\nu\nu)$ + jets

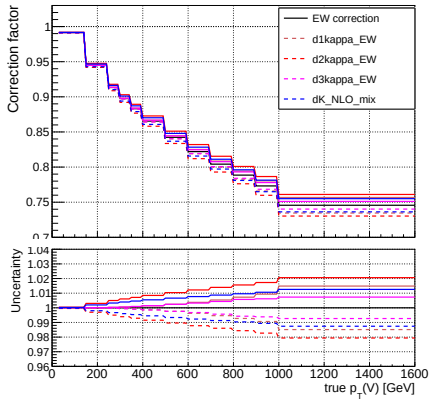

(c) $W(\ell\nu)$ + jets

Figure 8.22: Electroweak correction for the $Z(\ell\ell)$ + jets, $Z(\nu\nu)$ + jets, $W(\ell\nu)$ + jets processes with the corresponding uncertainties. For each variation, the 'up' effect is shown with a solid line, and the 'down' effect with a dashed line. The correction factor is shown on the top pad, while the ratios between the correction factor for any variation and the nominal one are shown in the bottom pad.

As mentioned in Section 8.2.3, a smoothing procedure is performed to derive the QCD correction factor: it consists of a linear fit of the ratio between the MC prediction (before reweighting) and the theory prediction of the same quantity. A systematic uncertainty is added to cover the uncertainty on the determination of the fitting parameters. Figure 8.24 shows the linear fits for the $Z(\ell\ell)$ + jets, $Z(\nu\nu)$ + jets, $W(\ell\nu)$ + jets processes, together with the uncertainty on the fitting procedure. A conservative 10% uncertainty is applied to the inclusive bin to account for the ignorance related to the behavior of the correction factor above 1 TeV.

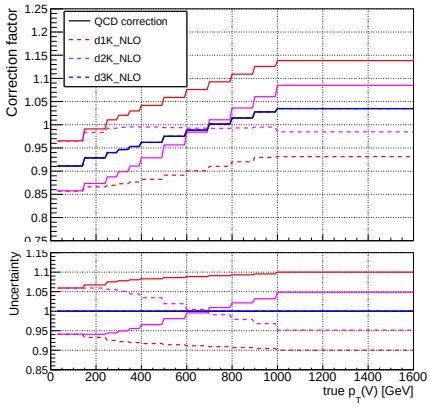

(a) $Z(\ell\ell)$ + jets

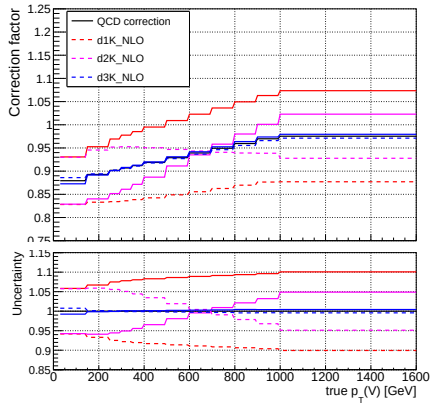

(b) $Z(\nu\nu)$ + jets

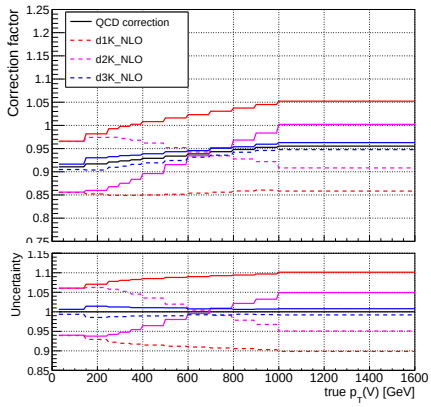

(c) $W(\ell\nu)$ + jets

Figure 8.23: QCD correction factors for the $Z(\ell\ell)$ + jets, $Z(\nu\nu)$ + jets, $W(\ell\nu)$ + jets processes with the corresponding uncertainties. For each variation, the 'up' effect is shown with a solid line, and the 'down' effect with a dashed line. The correction factor is shown on the top pad, while the ratios between the correction factor for any variation and the nominal one are shown in the bottom pad.

PDF uncertainties on V + jets

Uncertainties due to the limited knowledge of parton distribution functions (PDFs) are taken into account on the $p_{\mathrm{T}}^{\mathrm{recoil}}$ at the level of the MC generation and propagated at the reconstruction level by means of event-by-event weights.

Intra–pdf uncertainties are computed taking the standard deviation of the 100 replicas in the `NNPDF30nnlo` set in each $p_{\mathrm{T}}^{\mathrm{recoil}}$ bin. Two alternative pdf sets are used to estimate the inter–pdf uncertainties, `MMHT2014nnlo68cl` and `CT14nnlo`: the uncertainty is computed as the maximal difference of the central value of the alternative pdf set with

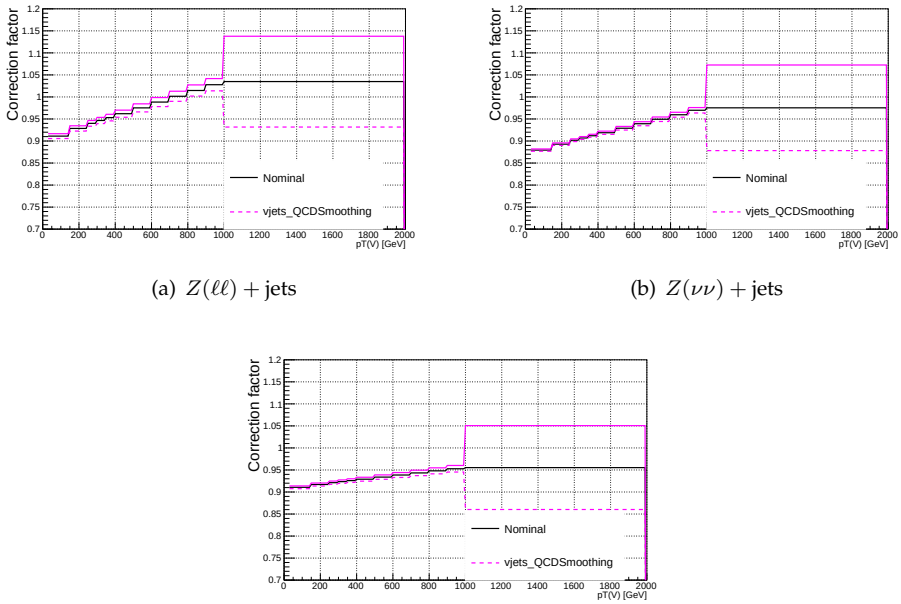

(a) $Z(\ell\ell)+$ jets

(b) $Z(\nu\nu)+$ jets

(c) $W(\ell\nu)+$ jets

Figure 8.24: Smoothed QCD correction (black) with its relative uncertainties (pink) for the $Z(\ell\ell)+$ jets, $Z(\nu\nu)+$ jets, $W(\ell\nu)+$ jets processes.

respect to the nominal. Intra and inter–pdf uncertainties are then added in quadrature. The resulting uncertainties in the analysis region in which each background is dominant are shown in Figure 8.25; with the exception of the $Z(\tau\tau)+$ jets and $W(\tau\nu)+$ jets variations in the high $p_{\mathrm{T}}^{\mathrm{recoil}}$ part of the spectrum, all variations are very similar to each other and range from 2% at low $p_{\mathrm{T}}^{\mathrm{recoil}}$ to $6-8\%$ at high $p_{\mathrm{T}}^{\mathrm{recoil}}$.

These uncertainties are used for all analysis regions with a single nuisance parameter, named 'PDFcomb', and treated as fully correlated across processes and $p_{\mathrm{T}}^{\mathrm{recoil}}$ bins.

Matching uncertainties on $V+$ jets

Uncertainties due to the choice of the CKKW matrix-element-matching scale are evaluated using the parameterisation of Ref. [153], which was derived using samples generated with a different version of SHERPA (v2.1) by varying the matching scale from its nominal value, $20\,\mathrm{GeV}$, to $15\,\mathrm{GeV}$ and $30\,\mathrm{GeV}$. Following what done in Ref. [141], up and down variations of the $p_{\mathrm{T}}^{\mathrm{recoil}}$ distribution are obtained using event-by-event reweighting, based on the number of truth jets as defined in Section 3 of Ref. [153] and depending on the p_{T} slice of the generated samples; the uncertainty is applied to SR yields.

To avoid counting effects due to the fact that the reweighting procedure was obtained with a different version of SHERPA, the relative uncertainty on the yield in each bin of $p_{\mathrm{T}}^{\mathrm{recoil}}$ in the SR is computed by comparing the ratios of yields of each process in the

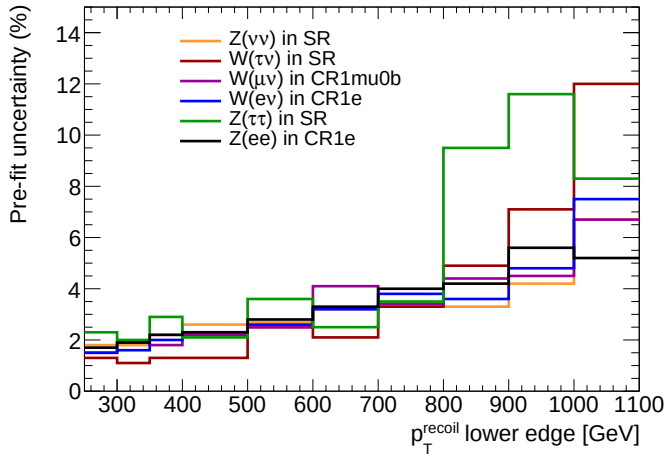

Figure 8.25: Relative PDF systematic uncertainty (in %) on the $W+$jets, $Z+$jets backgrounds as function of the $p_{\mathrm{T}}^{\mathrm{recoil}}$ bins. Uncertainties on a given process are quoted in the region where that process is dominant. The uncertainty quoted on the $Z(ee)+$jets sample is used as a proxy for the $Z(\mu\mu)+$jets.

signal and control regions, obtained with the up and down variations described above, r_{up} and r_{down}, as follows:

$$\text{rel. unc.} = \frac{r_{\mathrm{up}} - r_{\mathrm{down}}}{r_{\mathrm{up}} + r_{\mathrm{down}}}.$$

For $Z(\nu\nu)+$jets, the ratio between $Z(\mu\mu)+$jets in `CR2mu` and $W(\mu\nu)+$jets in `CR1mu0b` is used; consistent results are obtained when different choices are made (e.g. using $W(e\nu)+$jets in `CR1e` as denominator). In the case of $W(\mu\nu)+$jets ($W(e\nu)+$jets), the ratio between `SR` and `CR1mu0b` (`CR1e`) is used. In the case of $W(\tau\nu)+$jets, the ratio between `SR` and `CR1e` is used. In the case of $Z(\mu\mu)+$jets, $Z(ee)+$jets and $Z(\tau\tau)+$jets, the ratio between $Z(\mu\mu)+$jets in `SR` and $Z(\mu\mu)+$jets in `CR2mu` is used for all processes.

The size of this uncertainty ranges between 1.4% and 0.4% in the case of $Z(\nu\nu)+$jets in the `SR`, depending on the $p_{\mathrm{T}}^{\mathrm{recoil}}$ bin. The effect on all other $W+$jets and $Z+$jets processes is less than 0.5%.

The variations on the $p_{\mathrm{T}}^{\mathrm{recoil}}$ spectrum due to this uncertainty is modeled with one nuisance parameter, named 'ckkw', and treated as correlated across processes and $p_{\mathrm{T}}^{\mathrm{recoil}}$ bins.

Diboson backgrounds

The systematic uncertainty for the diboson processes is given by two components: a normalisation uncertainty of 6% [154] on the cross-section and a component derived from the difference between SHERPA and POWHEG-BOX generators. For the latter, the values of the uncertainty are derived from a linear fit of the ratio between the two generators and are summarized in Table 8.8.

The two uncertainty components are then summed up in quadrature. The corresponding nuisance parameter is named 'dibosonSys', and treated as correlated across regions.

Region Name	BIN_250	BIN_300	BIN_350	BIN_400	BIN_500	BIN_600	BIN_700	BIN_800	BIN_900	BIN_1000
SR	3.6	1.6	0.4	3.3	7.3	11.3	15.3	19.3	23	31
CR1e	2.5	1.0	0.4	2.5	5.3	8.2	11.0	13.9	16.7	22.4
CR1mu0b	0.4	0.2	0.0	0.3	0.8	1.2	1.6	2.0	2.4	3.3
CR1mu1b	1.2	2.1	3.1	4.5	6.5	8.4	10.3	12.2	14.2	18.0
CR2mu	0.9	0.6	0.2	0.2	0.8	1.4	2.1	2.7	3.3	4.5

Table 8.8: Relative systematic uncertainty (in %) on the diboson background as function of the $p_{\mathrm{T}}^{\mathrm{recoil}}$ bins in the SR and CRs evaluated from the generators comparison.

Top-quark backgrounds

Theoretical uncertainties on the top-quark processes ($t\bar{t}$, single-top) are computed from the variations given by a different matrix element generator, a different parton shower and different shower radiation model. These are computed using dedicated $t\bar{t}$ samples and applied on both $t\bar{t}$ and single-top, given the large predominance of the former over the latter in the SR.

All systematic uncertainties are obtained from linear fits of the ratio between the nominal and the variated samples, except for the samples with different radiation model, where the semi-difference between the higher and lower variation is considered.

The total uncertainties are evaluated from the sum in quadrature of the several variations and then assigned with the same size to all regions. They are summarized in Table 8.9. The corresponding nuisance parameter is named 'topSys', and treated as correlated across regions.

Region Name	BIN_250	BIN_300	BIN_350	BIN_400	BIN_500	BIN_600	BIN_700	BIN_800	BIN_900	BIN_1000
systematic (%)	24	26	28	31	36	42	47	53	59	72

Table 8.9: Total relative systematic uncertainty (in %) on the top background as a function of $p_{\mathrm{T}}^{\mathrm{recoil}}$ in the signal and control regions

8.6.2 Experimental uncertainties

The complete list of the uncertainties accompanied by a brief description is reported in Table 8.10. Each of the associated nuisance parameters is treated as uncorrelated with the others and fully correlated across the regions and the $p_{\mathrm{T}}^{\mathrm{recoil}}$ bins.

8.6.3 Pre-fit impacts

The above described sources of systematic uncertainties are applied to the individual backgrounds processes and have an impact in the signal and control regions in terms of variations of the expected yields of the total background.

Name	Description
JET_GroupedNP_i (i $\in 1, 2, 3$)	jet energy scale (JES) from in-situ analysis, strongly-reduced 3 NPs scheme
JET_JER_SINGLE_NP	jet energy resolution
JET_EtaIntercalibration_NonClosure	jet eta inter-calibration procedure
MET_SoftTrk_Scale	scale of the $E_{\mathrm{T}}^{\mathrm{miss}}$ track soft term
MET_SoftTrk_ResoPara	resolution of the parallel projection of soft term onto hadronic recoil
MET_SoftTrk_ResoPerp	resolution of the perpendicular projection of soft term onto hadronic recoil
FT_EFF_B	efficiency for tagging b-jets
FT_EFF_C	efficiency for tagging c-jets
FT_EFF_Light	efficiency for tagging light jets
FT_EFF_extrapolation	extrapolation at high p_{T}
FT_EFF_extrapolation_from_charm	extrapolation at high p_{T}
EG_SCALE_ALL	scale of electron/photon energy
EG_RESOLUTION_ALL	resolution of electron/photon energy
EL_EFF_Reco_TOTAL	efficiency of electron reconstruction
EL_EFF_ID_TOTAL	efficiency of electron identification
EL_EFF_Iso_TOTAL	efficiency of electron isolation
EL_EFF_TriggerEff_TOTAL	efficiency of electron trigger
EL_EFF_Trigger_TOTAL	efficiency of electron trigger
MUONS_ID	resolution of the ID tracks associated to muons
MUONS_MS	resolution of the MS tracks associated to muons
MUON_EFF_STAT	efficiency of muon reconstruction (stat component)
MUON_EFF_STAT_LOWPT	efficiency of muon reconstruction (stat at low p_{T})
MUON_EFF_SYS	efficiency of muon reconstruction (stat component)
MUON_EFF_SYS_LOWPT	efficiency of muon reconstruction (syst at low p_{T})
MUONS_SCALE	scale of muon momentum measurement
MUON_BADMUON_STAT	efficiency of bad muons veto (stat component)
MUON_BADMUON_SYS	efficiency of bad muons veto (syst component)
MUON_SAGITTA_RESBIAS	scale of the muon momentum
MUON_SAGITTA_RHO	scale of the muon momentum
MUON_TTVA_STAT	efficiency of track-to-vertex association (stat component)
MUON_TTVA_SYS	efficiency of track-to-vertex association (syst component)
PRW_DATASF	variation of data scale factor for pile-up reweighting
LUMI	integrated luminosity measurement

Table 8.10: List and description of the experimental sources of systematic uncertainty considered in the analysis.

In the SR, the total pre-fit uncertainty ranges from 9.6 to 17.4% going from the low to the high part of the $p_{\mathrm{T}}^{\mathrm{recoil}}$ spectrum, primarily due to theoretical uncertainties on the $V+$jets processes ($8.8-13.6\,\%$), jet energy scale and resolution ($1.9-6.5\,\%$), luminosity ($3.2\,\%$) and uncertainties on the modeling of the $V+$ jets processes ($1.7-6.7\,\%$). Smaller contributions come from the theoretical uncertainties on the top backgrounds ($1.1-1.2\,\%$) and diboson processes ($0.1-2.5\,\%$) and from the uncertainty on the pile-up reweighting procedure ($0.2-1.1\,\%$). The other experimental sources of uncertainties yield negligible variations in the pre-fit background estimates in the SR.

The full breakdown of the uncertainties prior to fitting is reported in Appendix B.1.

8.7 Optimization of the V + jets estimation strategy

The technique to estimate the V + jets backgrounds, as described in Section 8.5, is the result of several optimization studies with respect to the previous version of the ATLAS mono-jet analysis [141], and concentrated on two aspects: the use of a global κ-factor for the entire $p_{\mathrm{T}}^{\mathrm{recoil}}$ spectrum, as opposed of bin-by-bin $\kappa -$ factors, and the use of the same κ-factor for all V + jets processes.

Employing a global κ-factor for the entire $p_{\mathrm{T}}^{\mathrm{recoil}}$ spectrum implies that the predicted spectrum in the SR significantly relies on the MC simulation in the SR. In contrast, when using a κ-factor for each $p_{\mathrm{T}}^{\mathrm{recoil}}$ bin, the MC spectrum in the SR is essentially weighted according to the data-to-simulation ratio in the CRs. This can introduce fluctuations in the prediction, due to the data fluctuations in the CRs. In the previous analysis, this second strategy was employed, motivated by the fact that there was not enough confidence to rely on the shape of the pure MC prediction. A fundamental element of novelty in the analysis described in this work has been the introduction of the theoretical reweighting in the $p_{\mathrm{T}}(V)$ variable (see Section 8.2.3). The reweighting of the MC to higher orders corrections and the use of a consistent treatment of the uncertainties and correlations – an approach that, moreover, had already been employed by the CMS mono-jet search [155] – has given confidence to rely on the shape of $p_{\mathrm{T}}^{\mathrm{recoil}}$ obtained from the reweighted MC.

In the previous ATLAS mono-jet analysis, separate $\kappa -$ factors were applied to the different decays of Z and W, with the consequence that the $\kappa -$ factors absorbed potential differences at the reconstruction level between channels. The role of the $\kappa -$ factors has been revisited in this analysis: with a single κ-factor for all V + jets processes the potential differences between channels at reconstruction level are absorbed in the variation of the nuisance parameters, while the κ-factor accounts for the missing higher orders in the theoretical prediction.

Section 8.7.1 analyzes the improvement in the analysis sensitivity brought by the above discussed aspects, while Section 8.7.2 discusses the validation of the theoretical reweighting procedure.

8.7.1 Optimization of the fitting strategy

The figure of merit used for these studies is the relative uncertainty on the background estimation in the SR after the simultaneous fit. This is a model-independent figure of merit, since to a more precise background prediction corresponds an overall improvement in the signal sensitivity, independently on the particular signal model investigated. CR-only fits are performed, using Asimov datasets, which means that the MC prediction is not fitted directly to the data, but rather on a data sample which equals the total pre-fit background prediction. The likelihood model of reference was described in Section 8.5.2, two elements of which are varied:

- the use of separate $\kappa -$ factors for Z and W processes as opposed to the same κ-factor for all V + jets;

- the use of bin-by-bin $p_{\mathrm{T}}^{\mathrm{recoil}}$ κ − factors as opposed to a global κ − factors for the entire spectrum.

Figure 8.26 compares the uncertainty on the predicted background in the SR for several likelihood configurations. The use of binned κ^{Z} for $Z(\ell\ell)$ + jets and $Z(\nu\nu)$ + jets and binned κ^{W} for $W(\ell\nu)$ + jets (solid blue) provides the lowest precision, since the estimate of the $Z(\nu\nu)$ + jets comes substantially from the CR2mu and CR2e[2], which have a limited statistical power at high $p_{\mathrm{T}}^{\mathrm{recoil}}$.
When using a binned $\kappa^{W/Z}$ for $Z(\nu\nu)$+jets and $W(\ell\nu)$+jets and binned κ^{Z} for $Z(\ell\ell)$+jets (solid orange), as done in the previous mono-jet analysis, the precision is improved from $\gtrsim 500$ GeV, due to the higher statistics of the $W(\ell\nu)$ + jets-enriched regions compared to the $Z(\ell\ell)$ + jets-enriched ones.
When using a binned $\kappa^{W/Z}$ for $W(\ell\nu)$ + jets, $Z(\mu\mu)$ + jets, $Z(\nu\nu)$ + jets (solid red), all V + jets-enriched regions measure the background in the SR, leading to an even better precision.
The differences between these three strategies smooth out, when considering a global κ-factor, since at this point the statistical power of the CRs at high $p_{\mathrm{T}}^{\mathrm{recoil}}$ is not anymore a limiting factor to constrain the high part of the spectrum in the SR, whose precision is instead dominated by the systematic uncertainties.
Given the superior precision obtained with the use of a global κ-factor, this technique has been chosen for the present analysis.

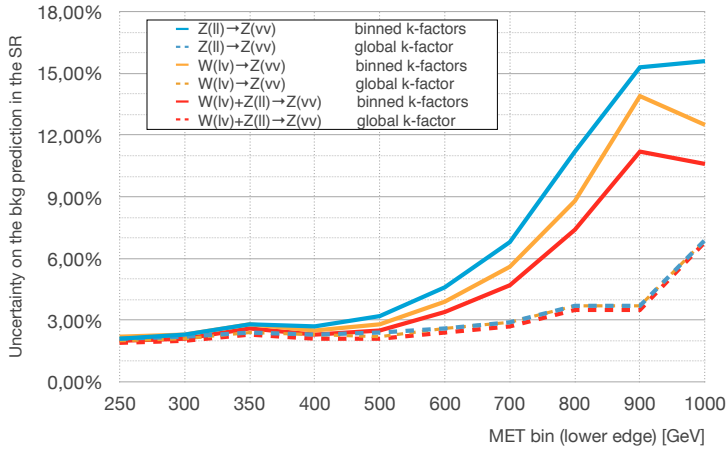

Figure 8.26: The relative estimated uncertainty on the background prediction in each $E_{\mathrm{T}}^{\mathrm{miss}}$ bin of the SR as obtained from several fitting strategies. The fits are performed with Asimov datasets. The fit configurations are described in the text.

[2]For these studies a dielectron control region, defined similarly as the CR2mu region, is employed.

8.7.2 Validation of the theory reweighting procedure

An important check of the sanity of the reweighting is given by the comparison between data and reweighted MC of the $p_{\mathrm{T}}^{\mathrm{recoil}}$ distribution in the control regions. Since in the likelihood model the normalization of the $p_{\mathrm{T}}^{\mathrm{recoil}}$ spectrum of the $V+$jets samples is a free parameter, the absolute agreement between data and MC before the fit is not a necessary condition. The agreement between data and MC is instead required for the ratio of the processes that enter the CR-only fit, i.e. $Z(\ell\ell)+$jets and $W(\ell\nu)+$jets in the respective `CR`s. This is shown in Figure 8.27, where the the ratio between $Z(\mu\mu)+$ jets and $W(\mu\nu)+$ jets shown (left) and the ratio between $W(\mu\nu)+$ jets and $W(e\nu)+$ jets are shown. Good agreement is observed between the data and the simulation after the application of the reweighting.

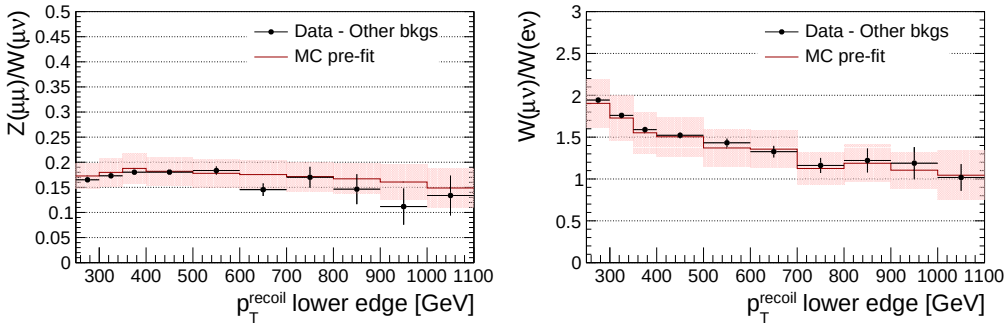

Figure 8.27: Comparison between data and reweighted MC simulation of $Z(\mu\mu)+$ jets in `CR2mu` and $W(\mu\nu)+$ jets in `CR1mu0b` (left) and of $W(\mu\nu)+$ jets in `CR1mu0b` and $W(e\nu)+$ jets in `CR1e` (right) before the simultaneous fit. Uncertainty bands on the MC distributions include statistical and systematic components.

8.8 Results

Once the reweighting procedure has been validated and the fitting strategy optimized, the CR-only shape fit is performed in order to quantify the level of agreement or disagreement of the prediction with the observed data in the SR. Before unblinding the SR, the results in the CRs are examined in Section 8.8.1. The results in the SR are examined in Section 8.8.2, followed by the discussion of the impacts of the systematic uncertainties after the fit (see Section 8.8.3).

The results obtained with the counting experiment fits are reported in Appendix B.2.

8.8.1 Shape fit in the control regions

The CR-only shape fit described in Section 8.5.2 is performed over the four control regions and the results of this fit are discussed.

Figure 8.28 shows all the fitted nuisance parameters, together with the fitted $\kappa-$ factors. The fitted value of $\kappa^{W/Z}$ is 1.26 ± 0.13. This is consistent with the observation that, after the theory reweighting, the absolute normalization in the control regions enriched in $W+$ jets and $Z+$ jets shows an offset that ranges from 20% to 30% with respect to data. The fitted value for κ^{t} is 1.31 ± 0.17. The relatively high fitted value is motivated by the anti-correlation of κ^{t} with the nuisance parameter that describes the theoretical uncertainties on the top-quark processes. As shown in Figure 8.28, the fitted value of this nuisance parameter is pulled to approximately -1σ after the fit, thus explaining the overestimation of the κ^{t}.

The fitted nuisance parameters are generally consistent with 0 and the uncertainty with 1σ. Some degree of constraint after the fit can be observed in the case of the top_Sys and JET_GroupedNP_i: for the former, this is not surprising, given the large values of the input systematic uncertainties (see Section 8.6.1); for the latter, it was checked that the background prediction and uncertainties in the SR do not significantly change using the alternative parametrizations of the strongly-reduced 3 NPs scheme. For the other nuisance parameters, the level of constrain is consistent with that given by the fit to an Asimov dataset, as shown by comparing the top and bottom panel of Figure 8.28.

The estimated background after the fit is reported for every region and compared to the observed number of events in data in Tables 8.11–8.14. The estimates are reported for each $p_{\mathrm{T}}^{\mathrm{recoil}}$ bin and for each background component. Altoghether, the post-fit prediction provides a good description of the observed data. This is also demonstrated in Figures 8.29–8.32, where the post-fit distribution of several key observables is shown and compared to the measured distribution in data.

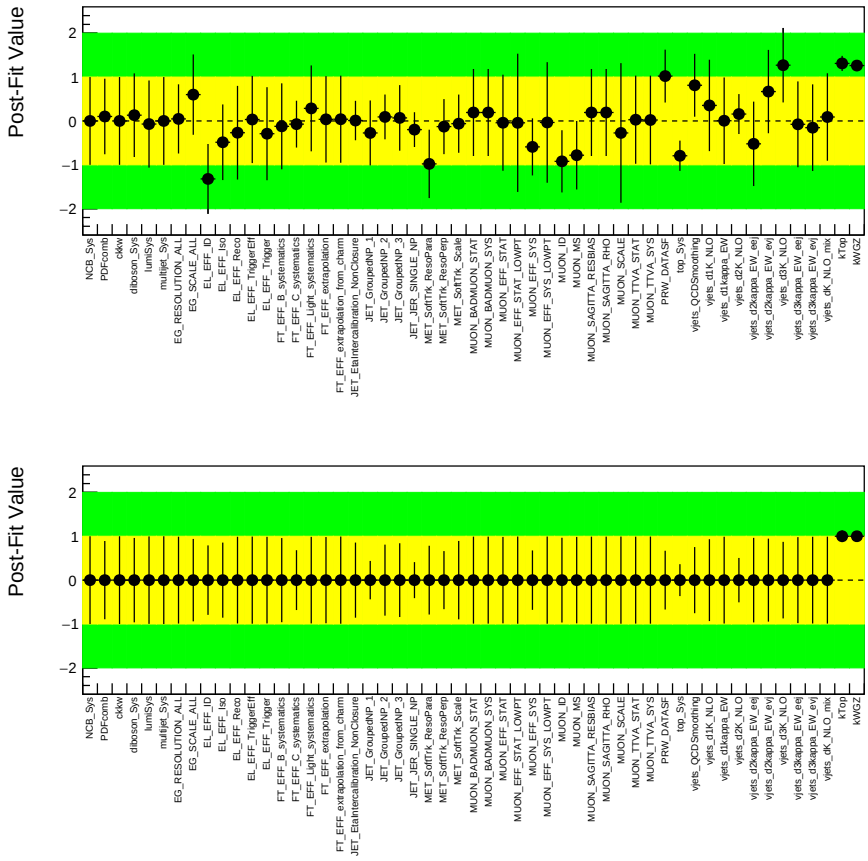

Figure 8.28: Values and uncertainties of the nuisance parameters after the CR-only shape fit to the data (top) and to the Asimov dataset (bottom).

CR1mu0b	BIN_250	BIN_300	BIN_350	BIN_400	BIN_500	BIN_600	BIN_700	BIN_800	BIN_900	BIN_1000
Observed Events	44295	29458	16249	13859	4384	1543	629	258	130	133
Fitted background	44090±230	29590±140	15927±93	13970±80	4477±36	1564±20	603±13	252±6	122±6	128±7
$Z(\nu\nu)+$jets	19±2	11.2±0.4	4±0.3	4.2±0.2	1.6±0.2	0.2±0.1	0.14±0.01	0.05±0.01	0.01±0	0.01±0
$W(\tau\nu)+$jets	2289±70	1647±31	855±21	789±25	270±7	81±5	45±2	19±1	9±1	8±1
$W(\mu\nu)+$jets	38240±270	25390±240	13530±130	11750±110	3763±46	1305±22	482±10	205±5	102±6	106±7
$W(e\nu)+$jets	1±1	3±1	0.8±0.5	0.28±0.03	0±0	0±0	0.03±0	0.02±0	0±0	0.01±0
$Z(\tau\tau)+$jets	129±6	77±4	34±3	29±2	11±1	4.9±0.4	2.8±0.3	0.7±0.2	0.4±0.1	0.09±0.03
$Z(\mu\mu)+$jets	913±23	484±12	234±7	165±4	37±5	15±1	5.3±0.4	3±0.3	1.1±0.1	1.7±0.2
$Z(ee)+$jets	0±0	0±0	0±0	0±0	0±0	0±0	0±0	0±0	0±0	0±0
$t\bar{t}$, single-top	1610±210	1210±160	710±100	626±86	173±27	59±11	27±6	8±2	2±1	3±1
Dibosons	880±60	770±56	558±39	602±42	221±17	98±10	40±4	17±3	8±1	9±1
Multijets	0±0	0±0	0±0	0±0	0±0	0±0	0±0	0±0	0±0	0±0
Non-collision bkgs	0±0	0±0	0±0	0±0	0±0	0±0	0±0	0±0	0±0	0±0
Pre-fit background	34700±3500	23400±2400	12600±1300	11000±1100	3570±360	1250±130	475±51	200±23	92±13	94±16

Table 8.11: Event yields in CR1mu0b before and after the CR-only shape fit, compared to the observed events. For the predictions, both the statistical and systematic uncertainties are included. The uncertainties for the individual background processes can be correlated, and do not necessarily add in quadrature to the total background uncertainty.

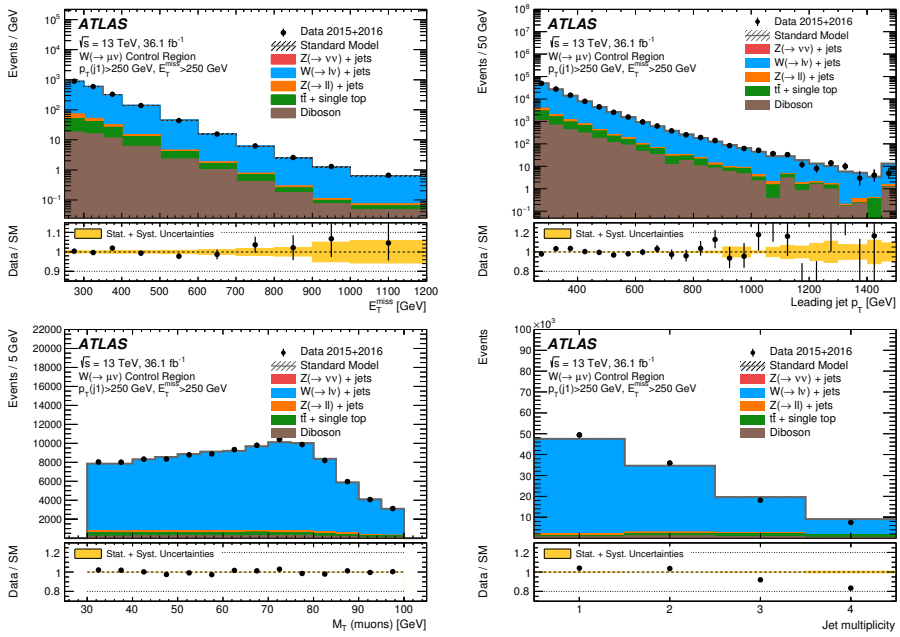

Figure 8.29: The measured $p_{\mathrm{T}}^{\mathrm{recoil}}$, leading jet p_{T}, transverse mass and jet multiplicity distributions in CR1mu0b compared to the background predictions after the fit. The error bands in the ratios include the statistical and systematic uncertainties on the background predictions after the fit. The last bin of the distribution contains overflows. Note that the notations $E_{\mathrm{T}}^{\mathrm{miss}}$ and $p_{\mathrm{T}}^{\mathrm{recoil}}$ are here used interchangeably. The contributions from multijet and non-collision backgrounds are negligible and are not shown.

CR1e	BIN_250	BIN_300	BIN_350	BIN_400	BIN_500	BIN_600	BIN_700	BIN_800	BIN_900	BIN_1000
Observed Events	24280	18048	11079	9947	3353	1251	553	216	110	136
Fitted background	24320±150	18190±100	10931±68	9987±66	3469±31	1216±16	534±9	210±5	102±6	128±9
$Z(\nu\nu)+$jets	0.3±0.2	0.3±0.1	0.2±0.1	0.3±0.1	0.4±0.1	0.14±0.02	0.03±0.01	0.03±0	0.04±0.01	0.04±0.01
$W(\tau\nu)+$jets	1501±30	1139±33	647±22	579±14	211±5	78±3	33±1	14±1	8±1	8±1
$W(\mu\nu)+$jets	0.7±0.1	1±1	3±1	0.8±0.1	0.4±0.2	0±0	0±0	0.15±0.01	0.02±0	0.04±0.02
$W(e\nu)+$jets	19820±230	14490±210	8570±130	7690±110	2678±50	933±18	419±10	167±6	85±3	101±8
$Z(\tau\tau)+$jets	89±8	50±4	43±3	35±2	11±1	2.9±0.3	1.6±0.3	0.6±0.1	0.1±0.1	0.17±0.03
$Z(\mu\mu)+$jets	0.4±0.1	0±0	0.04±0	0.19±0.04	0.06±0.01	0.01±0	0±0	0±0	0±0	0±0
$Z(ee)+$jets	3±3	3±2	0.45±0.45	0.19±0.19	0.2±0.2	0±0	0±0	0±0	0.01±0	0±0
$t\bar{t}$, single-top	2410±210	2030±180	1330±110	1290±110	395±40	122±15	43±8	13±3	6±1	6±3
Dibosons	491±38	473±33	343±24	394±29	173±18	80±8	38±5	14±2	3.41±3.41	13±6
Multijets	0±0	0±0	0±0	0±0	0±0	0±0	0±0	0±0	0±0	0±0
Non-collision bkgs	0±0	0±0	0±0	0±0	0±0	0±0	0±0	0±0	0±0	0±0
Pre-fit background	19700±1900	14900±1500	8960±920	8280±860	2930±320	1030±120	453±53	178±23	89±16	101±23

Table 8.12: Event yields in CR1e before and after the CR-only shape fit, compared to the observed events. For the predictions, both the statistical and systematic uncertainties are included. The uncertainties for the individual background processes can be correlated, and do not necessarily add in quadrature to the total background uncertainty.

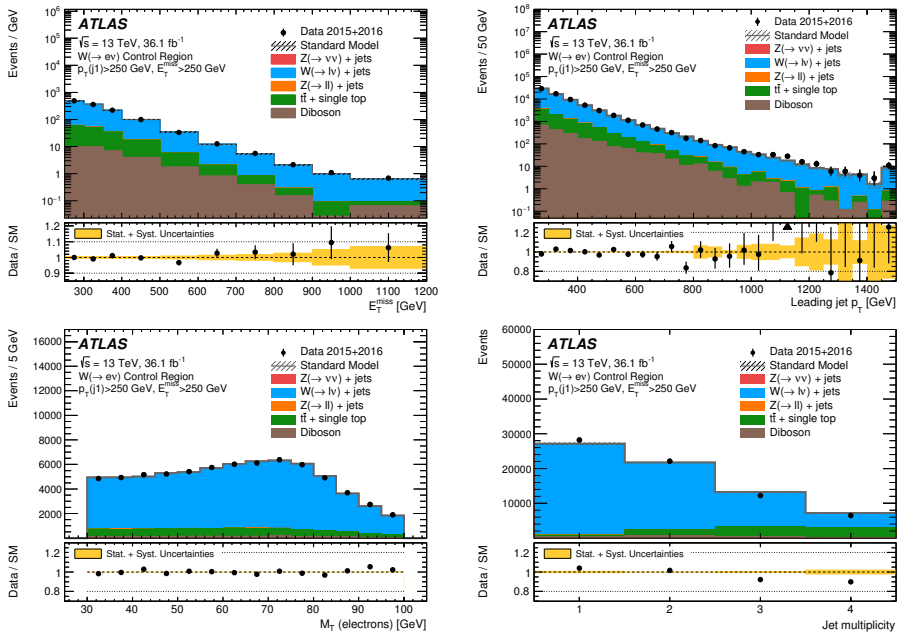

Figure 8.30: The measured $p_{\mathrm{T}}^{\mathrm{recoil}}$, leading jet p_{T}, transverse mass and jet multiplicity distributions in CR1e compared to the background predictions after the fit. The error bands in the ratios include the statistical and systematic uncertainties on the background predictions after the fit. The last bin of the distribution contains overflows. Note that the notations $E_{\mathrm{T}}^{\mathrm{miss}}$ and $p_{\mathrm{T}}^{\mathrm{recoil}}$ are here used interchangeably. The contributions from multijet and non-collision backgrounds are negligible and are not shown.

CR2mu	BIN_250	BIN_300	BIN_350	BIN_400	BIN_500	BIN_600	BIN_700	BIN_800	BIN_900	BIN_1000
Observed Events	6733	4627	2664	2246	731	213	93	34	14	17
Fitted background	6847±71	4693±46	2626±23	2213±21	713±10	248±6	88±3	37±1	17±2	17±1
$Z(\nu\nu)+$jets	0±0	0±0	0±0	0±0	0±0	0±0	0±0	0±0	0±0	0±0
$W(\tau\nu)+$jets	0.9±0.2	0.9±0.3	0.28±0.28	0.1±0.1	0.07±0.01	0±0	0.01±0	0.01±0	0±0	0±0
$W(\mu\nu)+$jets	14±1	6±1	3.1±0.5	3.9±0.5	1.4±0.1	0.1±0.01	0.1±0.1	0.16±0.04	0.03±0.01	0.03±0.01
$W(e\nu)+$jets	0±0	0±0	0±0	0±0	0±0	0±0	0±0	0±0	0±0	0±0
$Z(\tau\tau)+$jets	8±2	8±3	0.9±0.3	1.7±0.1	0.9±0.1	0.11±0.03	0.2±0.1	0.06±0.01	0±0	0.01±0
$Z(\mu\mu)+$jets	6461±71	4436±50	2458±25	2067±23	656±9	222±5	82±3	34±1	15±1	15±1
$Z(ee)+$jets	0±0	0±0	0±0	0±0	0±0	0±0	0±0	0±0	0±0	0±0
$t\bar{t}$, single-top	202±17	118±12	69±6	54±5	18±3	1.3±0.4	0.7±0.2	0±0	0.28±0.04	0.9±0.1
Dibosons	162±11	124±9	95±6	88±6	37±3	25±3	5.5±0.5	2.9±0.2	1.4±0.4	1.2±0.2
Multijets	0±0	0±0	0±0	0±0	0±0	0±0	0±0	0±0	0±0	0±0
Non-collision bkgs	0±0	0±0	0±0	0±0	0±0	0±0	0±0	0±0	0±0	0±0
Pre-fit background	5500±540	3810±400	2130±220	1800±180	575±61	199±20	70±8	29±4	13±2	13±2

Table 8.13: Event yields in CR2mu before and after the CR-only shape fit, compared to the observed events. For the predictions, both the statistical and systematic uncertainties are included. The uncertainties for the individual background processes can be correlated, and do not necessarily add in quadrature to the total background uncertainty.

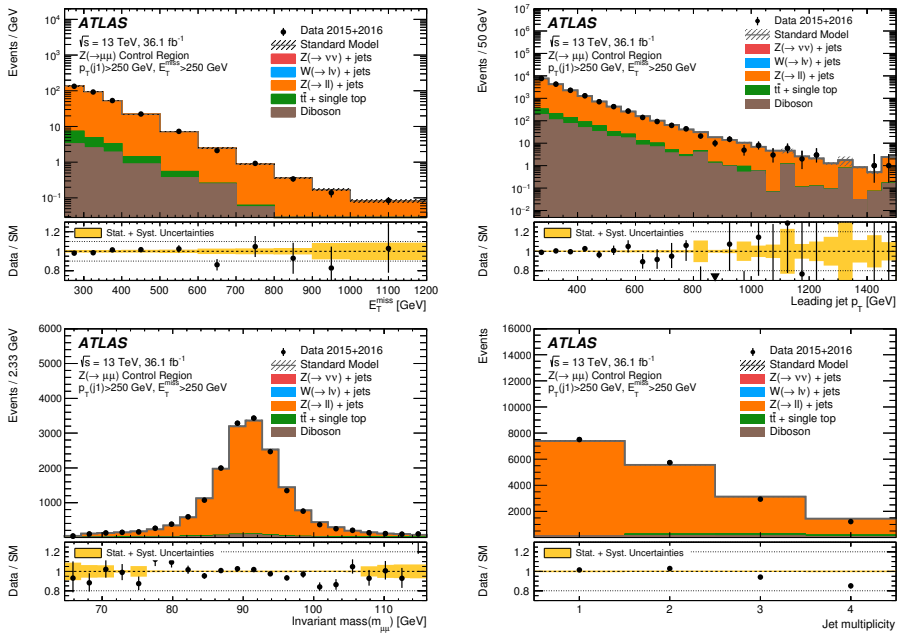

Figure 8.31: The measured $p_{\mathrm{T}}^{\mathrm{recoil}}$, leading jet p_{T}, invariant mass and jet multiplicity distributions in CR2mu compared to the background predictions after the fit. The error bands in the ratios include the statistical and systematic uncertainties on the background predictions after the fit. The last bin of the distribution contains overflows. Note that the notations $E_{\mathrm{T}}^{\mathrm{miss}}$ and $p_{\mathrm{T}}^{\mathrm{recoil}}$ are here used interchangeably. The contributions from multijet and non-collision backgrounds are negligible and are not shown.

CR1mu1b	BIN_250	BIN_300	BIN_350	BIN_400	BIN_500	BIN_600	BIN_700	BIN_800	BIN_900	BIN_1000
Observed Events	3670	2588	1556	1293	398	144	53	16	8	3
Fitted background	3665±49	2543±31	1531±27	1377±23	395±12	128±6	47±4	14±2	8±1	6±1
$Z(\nu\nu)+$jets	2.6±0.4	2±0.4	0.2±0.2	0.3±0.1	0.25±0.03	0.03±0.03	0.01±0	0±0	0.01±0	0±0
$W(\tau\nu)+$jets	67±13	49±7	29±4	35±5	10±1	5±1	2±1	0.7±0.2	0.03±0.01	0.3±0.1
$W(\mu\nu)+$jets	860±160	630±110	373±50	357±54	122±12	55±6	21±3	8±1	6±1	3±1
$W(e\nu)+$jets	0±0	0.2±0.1	0±0	0±0	0±0	0±0	0±0	0±0	0±0	0±0
$Z(\tau\tau)+$jets	6±1	3.6±0.5	2±0.4	1.1±0.3	0.5±0.1	0.04±0.04	0.3±0.3	0.04±0.01	0±0	0.03±0.01
$Z(\mu\mu)+$jets	30±3	20±3	10±1	7±1	1.8±0.2	0.7±0.1	0.2±0.1	0.09±0.09	0.01±0	0.01±0.01
$Z(ee)+$jets	0±0	0±0	0±0	0±0	0±0	0±0	0±0	0±0	0±0	0±0
$t\bar{t}$, single-top	2670±190	1810±120	1102±75	948±68	253±21	64±6	22±4	4±1	2±1	2±1
Dibosons	34±8	26±5	15±4	30±9	8±3	4±1	1.1±0.4	1±1	0.3±0.2	0±0
Multijets	0±0	0±0	0±0	0±0	0±0	0±0	0±0	0±0	0±0	0±0
Non-collision bkgs	0±0	0±0	0±0	0±0	0±0	0±0	0±0	0±0	0±0	0±0
Pre-fit background	3370±700	2390±520	1450±330	1360±340	400±110	127±36	46±15	15±5	7±3	7±3

Table 8.14: Event yields in CR1mu1b before and after the CR-only shape fit, compared to the observed events. For the predictions, both the statistical and systematic uncertainties are included. The uncertainties for the individual background processes can be correlated, and do not necessarily add in quadrature to the total background uncertainty.

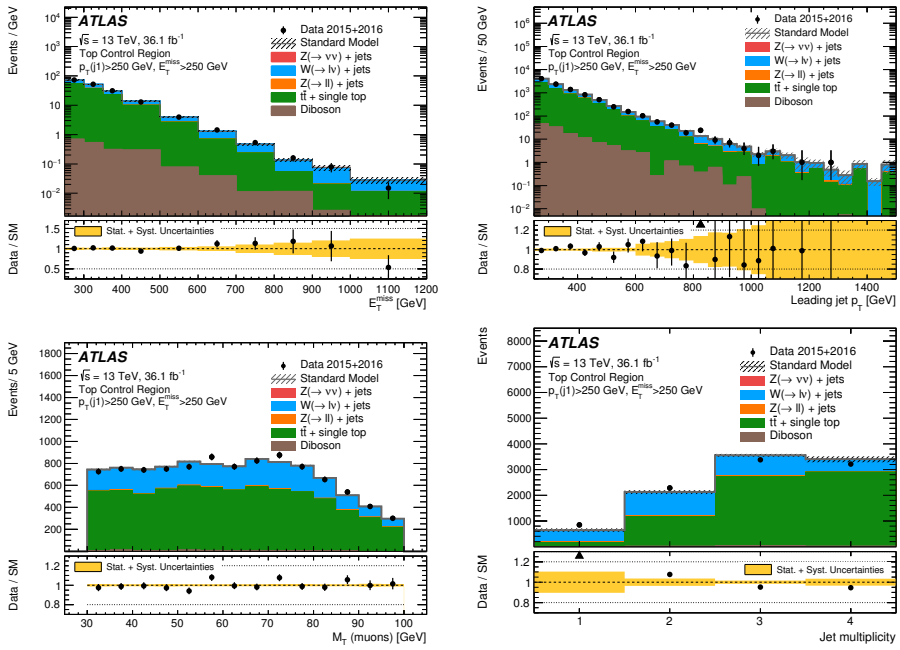

Figure 8.32: The measured $p_{\mathrm{T}}^{\mathrm{recoil}}$, leading jet p_{T}, transverse mass and jet multiplicity distributions in CR1mu1b compared to the background predictions after the fit. The error bands in the ratios include the statistical and systematic uncertainties on the background predictions after the fit. The last bin of the distribution contains overflows. Note that the notations $E_{\mathrm{T}}^{\mathrm{miss}}$ and $p_{\mathrm{T}}^{\mathrm{recoil}}$ are here used interchangeably. The contributions from multijet and non-collision backgrounds are negligible and are not shown.

8.8.2 Results in the SR

The predicted background yields after the CR-only shape fit and the observed number of events in the SR are reported in Table 8.15 for the various $p_{\mathrm{T}}^{\mathrm{recoil}}$ bins, along with the background composition. Figure 8.33 shows several post-fit kinematic distributions in the SR compared to the background predictions. The $p_{\mathrm{T}}^{\mathrm{recoil}}$ distribution includes the impact of different signal scenarios.

The SM predictions on $p_{\mathrm{T}}^{\mathrm{recoil}}$ are determined with a total uncertainty as low as $\pm 2.1\%$ in the first bin of the $p_{\mathrm{T}}^{\mathrm{recoil}}$ distribution, up to 7.1% in the last bin. The compatibility of the predicted background with the observed data is quantified by performing a p-value test of the $\mu = 0$ hypothesis (p_0, calculated following Ref. [134]). The results of the tests show significances within 2.1σ, when considering the signal samples used in the analysis.

8.8.3 Impact of the systematic uncertainties in the SR

As demonstrated in Table 8.15, after the CR-only shape fit the uncertainty on the background prediction is highly reduced: in the lowest $p_{\mathrm{T}}^{\mathrm{recoil}}$ bin it decreases from 10% (pre-fit) to 2% (post-fit), in the highest $p_{\mathrm{T}}^{\mathrm{recoil}}$ bin it goes from 17% to 7%. The improved precision is due to the cancellation of the systematic uncertainties provided by the fit to the control regions, which was already discussed in Section 7.6.2 in the context of the monophoton analysis. The same methodology explained there is here used for discussing the impacts of the systematic uncertainties on the background prediction after the fit.

Among the experimental systematics, the highest sources of uncertainty are the parameters associated to the efficiency of reconstruction and identification of electrons and muons, each of which contribute for $1 - 4\%$ going from low to high $p_{\mathrm{T}}^{\mathrm{recoil}}$. Slightly smaller contributions, of the order of $1-3\%$, come from the uncertainty on the b-tagging efficiency. Other non negligible contributions are due to the uncertainties on the jet energy scale and on the correlated $E_{\mathrm{T}}^{\mathrm{miss}}$ soft term scale and resolution, yielding variations of $1 - 3\%$ depending on the $p_{\mathrm{T}}^{\mathrm{recoil}}$ regime.

The theoretical uncertainties on the V + jets are largely cancelled after performing the fit: the modeling uncertainties on the V + jets (PDF and matching) account together for approximately $1 - 1.5\%$, those associated to the perturbative calculations for $1.5\% - 7\%$, the theoretical uncertainties on the $t\bar{t}$ for $0.5 - 2\%$, those associated to diboson processes for $0.5 - 1\%$. The luminosity uncertainty is negligble after the fit, while the uncertainty on the pile-up reweighting procedure yields variations of $1 - 3\%$ going from low to high $p_{\mathrm{T}}^{\mathrm{recoil}}$. The full breakdown of the uncertainties is reported in Appendix B.1.

A complementary overview of the effect of the systematics is given by examining their effect on the precision of the predicted background directly, as there may be sources of uncertainty which lead to a significant change in the background yields but only slightly affect the total size of the uncertainty or viceversa. Figure 8.34 reports the effect of the systematic uncertainties on the predicted background uncertainty in the SR. The uncertainties are grouped into different categories according to the source of the systematic uncertainty and presented as a function of the $p_{\mathrm{T}}^{\mathrm{recoil}}$ bin.

SR	BIN_250	BIN_300	BIN_350	BIN_400	BIN_500	BIN_600	BIN_700	BIN_800	BIN_900	BIN_1000
Observed Events	111203	67475	35285	27843	8583	2975	1142	512	223	245
Fitted background	111100±2300	67100±1400	33820±940	27640±610	8360±190	2825±78	1094±33	463±19	213±9	226±16
$Z(\nu\nu)+$jets	56600±1400	37600±970	19940±510	17070±460	5450±140	1933±57	773±26	337±12	153±7	162±12
$W(\tau\nu)+$jets	25990±590	13680±310	6060±490	4900±110	1303±35	397±11	149±5	55±5	29±2	24±2
$W(\mu\nu)+$jets	10420±270	6120±200	2940±120	2021±82	534±22	173±9	79±8	21±5	11±1	18±2
$W(e\nu)+$jets	10710±270	5510±140	2656±97	1789±59	532±23	147±9	25±4	18±1	8±1	7±1
$Z(\tau\tau)+$jets	475±20	185±6	95±4	68±4	16±1	5.1±0.3	2.5±0.3	0.3±0.1	0.31±0.04	0.5±0.1
$Z(\mu\mu)+$jets	329±12	167±8	71±4	36±2	6.9±0.5	2±0.2	0.8±0.2	0.4±0.1	0.5±0.1	0.2±0.1
$Z(ee)+$jets	0.06±0.02	0.03±0	0±0	0.02±0.02	0±0	0±0	0±0	0±0	0±0	0±0
$t\bar{t}$, single-top	4100±380	2230±200	1140±110	848±86	203±23	43±6	15±3	4±1	1.3±0.4	1±1
Dibosons	1700±130	1327±90	858±57	874±64	306±29	124±16	49±8	26±5	10±2	13±4
Multijets	490±480	170±160	30±30	13±13	5±5	1±1	1±1	1±1	0.1±0.1	0.1±0.1
Non-collision bkgs	240±240	71±71	29±29	18±18	4±4	0±0	0±0	0±0	0±0	0±0
Pre-fit background	86300±8300	52400±5300	26000±2600	21500±2200	6550±660	2190±220	847±93	352±38	161±20	161±28

Table 8.15: Event yields in SR before and after the CR-only shape fit, compared to the observed events. For the predictions, both the statistical and systematic uncertainties are included. The uncertainties for the individual background processes can be correlated, and do not necessarily add in quadrature to the total background uncertainty.

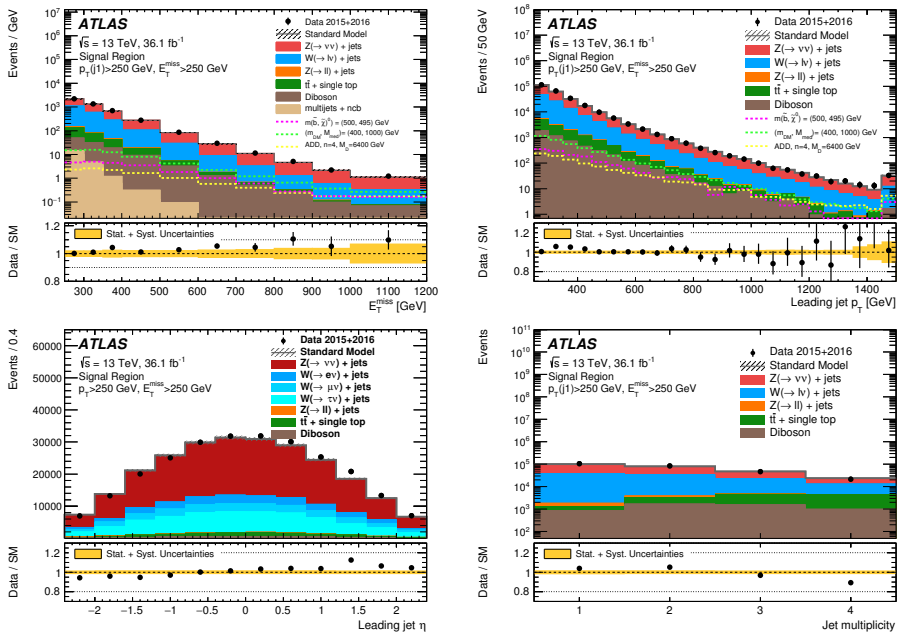

Figure 8.33: The observed $p_{\mathrm{T}}^{\mathrm{recoil}}$, leading jet p_{T}, leading jet $|\eta|$ and jet multiplicity distributions in the SR, compared to the background prediction after the fit. The error bands in the ratios include the statistical and systematic uncertainties on the background predictions. The last bin of the distribution contains overflows.

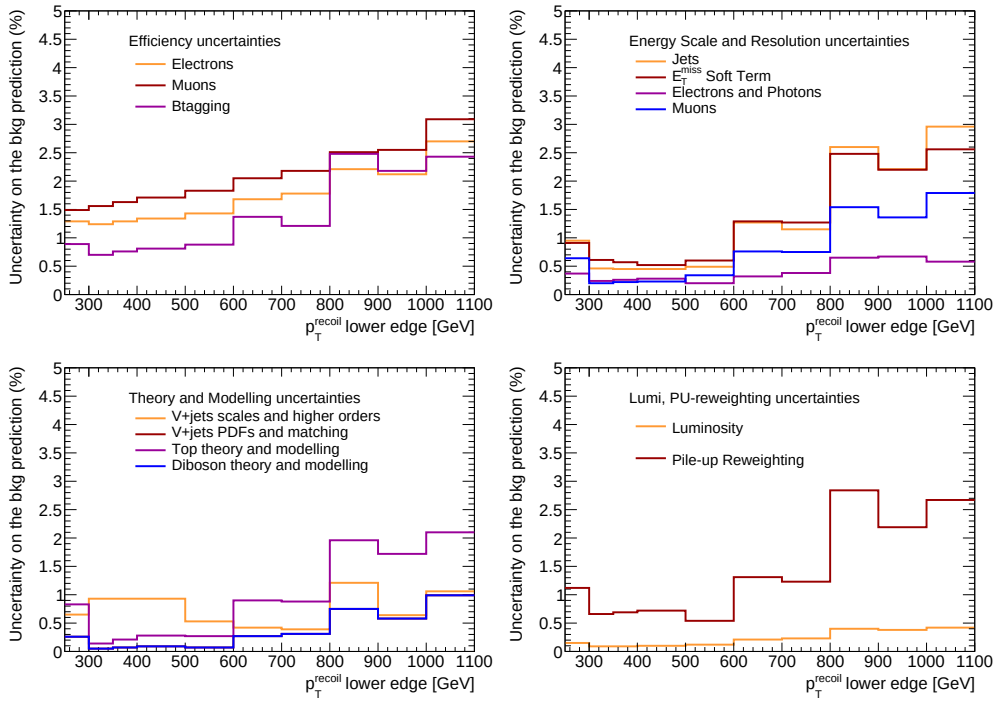

Figure 8.34: Impacts of the various sources of uncertainty on the background precision after the fit in the SR. Results are shown as a function of the p_T^{recoil} bins and grouped into different categories: uncertainties on the efficiency of reconstruction and identification of the physics objects (top left), on their energy scales and resolutions (top right), theoretical and modeling uncertainties (bottom left), luminosity and pile-up reweighting (bottom right). Each line can represent the impact of several parameters, in which case the correlations between them are taken into account.

8.9 Interpretation of the results

Since no significant deviations from the SM predictions can be observed, the results are interpreted in terms of exclusion limits for models that would produce an excess of mono-jet events. Upper bounds are calculated using a one-sided profile likelihood ratio and the CL_S technique [132, 133], evaluated using the asymptotic approximation [134].

8.9.1 Model-independent limits

Without any hypothesis on the signal model of new physics, observed and expected limits on the visible cross-section, defined as the product of the production cross-section, acceptance and efficiency $\sigma \times A \times \epsilon$ can be extracted, taking into consideration the systematic uncertainties on the backgrounds and the uncertainty on the integrated luminosity for the signal. The results are obtained with the counting experiment fits, including both the CRs and the SR, and are presented in Table 8.16. Values of $\sigma \times A \times \epsilon$ above 531 fb (for BIN>250) and above 1.6 fb (for BIN>1000) are excluded at 95% CL.

Selection	$\langle\sigma\rangle^{95}_{\rm obs}$ [fb]	$S^{95}_{\rm obs}$	$S^{95}_{\rm exp}$
BIN>250	531	19135	11700^{+4400}_{-3300}
BIN>300	330	11903	7000^{+2600}_{-2600}
BIN>350	188	6771	4000^{+1400}_{-1100}
BIN>400	93	3344	2100^{+770}_{-590}
BIN>500	43	1546	770^{+280}_{-220}
BIN>600	19	696	360^{+130}_{-100}
BIN>700	7.7	276	204^{+74}_{-57}
BIN>800	4.9	178	126^{+47}_{-35}
BIN>900	2.2	79	76^{+29}_{-21}
BIN>1000	1.6	59	56^{+21}_{-16}

Table 8.16: Observed and expected 95% CL upper limits on the number of signal events, $S^{95}_{\rm obs}$ and $S^{95}_{\rm exp}$, and on the visible cross section, defined as the product of cross section, acceptance and efficiency, $\langle\sigma\rangle^{95}_{\rm obs}$, for the several inclusive $p_{\rm T}^{\rm recoil}$ selections.

8.9.2 Dark Matter limits

The results are translated into exclusion limits on WIMP-pair production. Different simplified models are considered with the exchange of colored scalar mediators in the $t-$ channel model (Section 6.4) and axial-vector and vector mediator in the $s-$ channel (Section 6.2).

For these results, the simultaneous shape fit in the signal regions and in the control regions is performed and used to set observed and expected 95% CL exclusion limits on the parameters of each model. Uncertainties in the signal acceptance times efficiency, the

background predictions, and the luminosity are considered, and correlations between systematic uncertainties in signal and background predictions are taken into account. The fit accounts for the signal contamination of the control regions. Limits are presented as exclusion contours in the parameter space defined by the mass of the WIMP and the mass of the mediator, for fixed couplings.

$t-$ channel colored scalar mediator model

For the $t-$ channel model, typical values of $A \times \epsilon$ in the range from 35% to 0.7% are obtained for `BIN>250` and `BIN>1000` selections, respectively, for a mediator mass of 1 TeV and $m_\eta \gg m_\chi$.

Figure 8.35 presents the observed and expected 95% CL exclusion contours in the M_η–m_χ parameter plane for fixed coupling $g = 1$. Mediator masses up to about 1.67 TeV are excluded at 95% CL for light WIMP particles. Close to the $M_\eta = m_\chi$ kinematic limit for on-shell production of the mediator, masses up to 620 GeV are excluded. The analysis loses sensitivity going to high values of M_η, given the decreased cross-sections.

In the M_η–m_χ plane it is possible to visualize the phase-space that is allowed by the relic density constraints, when assuming that the only mechanism for DM production in the early Universe is the interaction predicted by the $t-$ channel model. The masses corresponding to a predicted relic density as observed by Planck [19] are indicated in the figure as a line that crosses the excluded region at $m_\chi \sim 350$ GeV and $M_\eta \sim 1400$ GeV. The region towards lower WIMP masses or higher mediator masses corresponds to DM overproduction. On the opposite side of the curve, other mechanisms need to exist in order to explain the observed dark-matter relic density.

$s-$ channel vector and axial-vector mediator models

In the case of the exchange of an **axial-vector mediator**, and for WIMP-pair production with $m_{Z_A} > 2m_\chi$, typical $A \times \epsilon$ values for the signal models with a 1 TeV mediator range from 25% to 0.4% for IM1 and IM10 selections, respectively. Very similar values are obtained in the case of the vector mediator, whereas $A \times \epsilon$ values in the range between 32% and 1% are computed for the pseudo-scalar mediator model with $m_{Z_P} = 1$ TeV and $m_\chi = 10$ GeV.

Figure 8.36 (left) shows the observed and expected 95% CL exclusion contours in the $m_{Z_A} - m_\chi$ parameter plane for the simplified model with an axial-vector mediator and couplings $g_q = 1/4$ and $g_\chi = 1$. In addition, observed limits are shown using $\pm 1\sigma$ theoretical uncertainties in the signal cross sections. In the on-shell regime, the models with mediator masses up to 1.55 TeV are excluded for $m_\chi = 1$ GeV. This analysis loses sensitivity to the models in the off-shell regime, where cross sections are suppressed due to the virtual production of the mediator.

Perturbative unitarity is violated in the parameter region defined by $m_\chi > \sqrt{\pi/2}\, m_{Z_A}$ [156]. Similarly as in the case of the $t-$channel model, it is possible to visualize the phase-space region allowed by the relic density constraints in the $m_{Z_A} - m_\chi$ parameter space, when assuming that the only mechanism for DM production is the one predicted by the

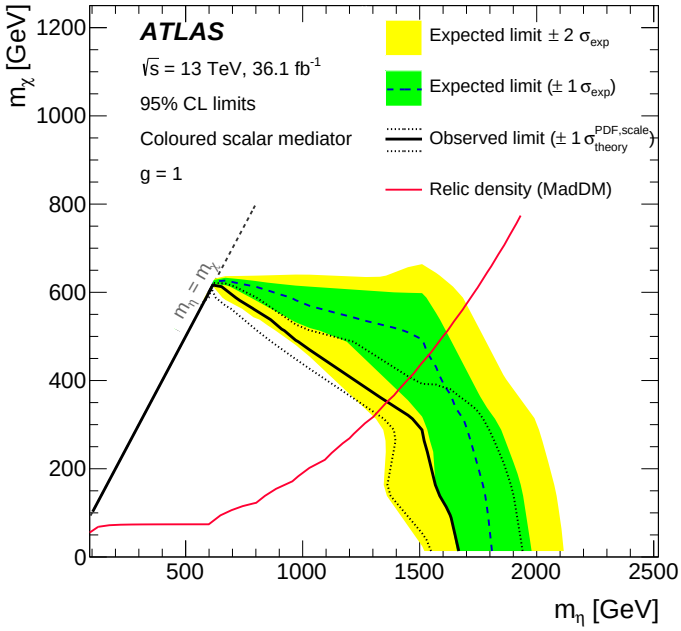

Figure 8.35: Exclusion contours at 95% CL in the M_η–m_χ parameter plane for the colored scalar mediator model, with minimal width and coupling set to $g = 1$. The solid (dashed) curve shows the observed (expected) limit, while the bands indicate the $\pm 1\sigma$ theory uncertainties in the observed limit and $\pm 1\sigma$ and $\pm 2\sigma$ ranges of the expected limit in the absence of a signal. The red curve corresponds to the expected relic density, as computed with MADDM [98]. The kinematic limit for the mediator on-shell production $M_\eta = m_\chi$, is indicated by the dotted line.

axial-vector mediator model. The masses corresponding to a predicted relic density as determined by Planck [19] are indicated in the Figure as a line that crosses the excluded region at $m_{Z_A} \sim 1200$ GeV and $m_\chi \sim 440$ GeV.

The limits from the axial-vector model can be translated into limits on the **vector model**, taking into account the cross-section differences between models, while compatible particle-level acceptances are found between the two. Figure 8.36 (right) shows the 95% CL exclusion contours in the m_{Z_V}–m_χ parameter plane for this simplified model with a vector mediator and couplings $g_q = 1/4$ and $g_\chi = 1$. For very light WIMPs, mediator masses below about 1.55 TeV are excluded. As in the case of the axial-vector mediator model, in the regime $m_{Z_V} < 2m_\chi$, the sensitivity for exclusion is reduced to the region $m_{Z_V} < 400$ GeV and $m_\chi < 200$ GeV.

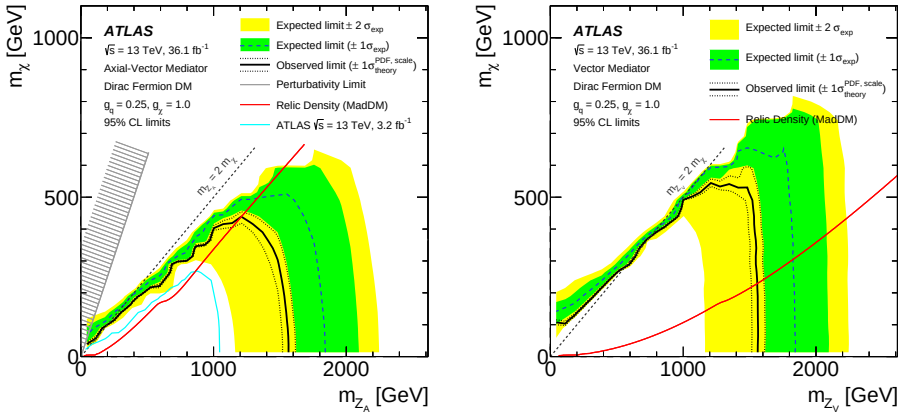

(a) Axial-vector mediator

(b) Vector mediator

Figure 8.36: Axial-vector (left) and vector (right) 95% CL exclusion contours in the $m_{Z_A} - m_\chi$ and $m_{Z_V} - m_\chi$ parameter planes. The solid (dashed) curves show the observed (expected) limits, while the bands indicate the $\pm 1\sigma$ theory uncertainties in the observed limit and $\pm 1\sigma$ and $\pm 2\sigma$ ranges of the expected limit in the absence of a signal. The red curve corresponds to the expected relic density, as computed with MADDM [98]. In the left lot the region excluded due to perturbativity, defined by $m_\chi > \sqrt{\pi/2}\, m_{Z_A}$, is indicated by the hatched area. The dotted line indicates the kinematic limit for on-shell production $m_{Z_A} = 2 \times m_\chi$. The cyan line indicates previous results at 13 TeV [141] using 3.2 fb^{-1}.

8.10 Comparison with other Dark Matter searches

When assuming a specific hypothesis on the interaction between DM and SM particles, it is possible to directly compare the sensitivity of different DM searches: collider, direct detection and indirect detection experiments. Each of these experimental techniques come with their assumptions, which need to be taken into account when performing such comparisons.

In this section we consider the $s-$ channel spin-1 mediator models (vector and axial-vector) and, in this context, we investigate the complementarity between the limits set by the mono-X searches with those set by other ATLAS searches (Section 8.10.1) and those set by direct detection experiments (Section 8.10.2). In Section 8.10.3 the results of the present mono-jet search are compared to those obtained by the mono-jet analysis performed by the CMS experiment.

8.10.1 Mono-X, di-jet, di-lepton searches

The spin-1 models have been examined in the context of final states with DM particles and a jet or a photon. The same interaction described by Eq. 6.1 can lead to fully hadronic final states, when the mediator decays back to jets, thus implying constraints from di-jet searches.

Di-jet final states are dominated by $2 \to 2$ QCD processes that produce a falling spectrum in the invariant mass (m_{jj}) distribution. The presence of a resonant state decaying to two jets, such as the mediator in the axial-vector model, can produce an excess in this distribution, localized near the mass of the resonance. Current di-jet searches [157] do not directly probe these signals at the reconstruction level, but rather provide fiducial limits on the $\sigma \times A \times \mathrm{BR}$ of hypothetical signals modeled as Gaussian peaks in the particle-level m_{jj} distribution. Such limits can be then reinterpreted in the context of the BSM scenario of interest starting from the cross-section at particle level in the defined fiducial region, following the procedure described in A.1 of [158].

The mediator masses that standard di-jet searches can access are limited by the high threshold of the lowest unprescaled single jet triggers on which they rely. In order to probe lower resonance masses, further strategies are developed, such as di-jet searches with an accompanying jet or photon from initial state radiation (di-jet+ISR, [159]) and di-jet searches at the level of trigger-objects (TLA [160]). In the first case, the presence of the ISR object boosts the di-jet system and allows to trigger on much lower thresholds than those of unprescaled single jet triggers. In the second case, only a reduced information is recorded when triggering the events, thus allowing to reduce the large prescale factors applied to low p_{T} single jet triggers. These two types of searches directly use simulated signal samples in the axial-vector and vector models, without need of an unfolding and reinterpretation procedure.

The limits set by mono-X searches and the di-jet searches described above are shown in Figure 8.37 for the case of the axial-vector with coupling strengths $g_\chi = 1.0$ and $g_q = 0.25$. As already shown in the previous section for the mono-jet case and in Section 7.19 for the

mono-photon case, mono-X limits are sensitive to the region where $m_{med} > 2m_{\chi}$ [3], with the mono-jet limits reaching larger values of m_{med} and m_{χ}. Di-jet limits are mostly insensitive to m_{χ}. They cover large regions in m_{med}, starting from approximately 200 GeV up to 2.6 TeV. Mono-X searches remain sensitive to low values of m_{med} and m_{χ}, where di-jet searches are not.

The choice of the coupling strengths can change the interplay in sensitivity between the searches. For example, when assuming lower values g_q, di-jet searches quickly lose their sensitivity, while mono-X searches remain competitive. When extending the interaction Lagrangian of this model to include couplings to charged leptons g_ℓ, as explained in [161], di-lepton searches start to play a role. In Figure 8.39 two coupling scenarios are investigated: the case of axial-vector mediator with couplings $g_\chi = 1.0$ and equal couplings to visible states $g_q = g_\ell = 0.1$, showing the typical impact of di-lepton constraints, and the case of vector mediator with $g_\chi = 1.0$, $g_q = 0.1$ and $g_\ell = 0.01$, which is representative of the case where the coupling to leptons is obtained only at loop-level [161].

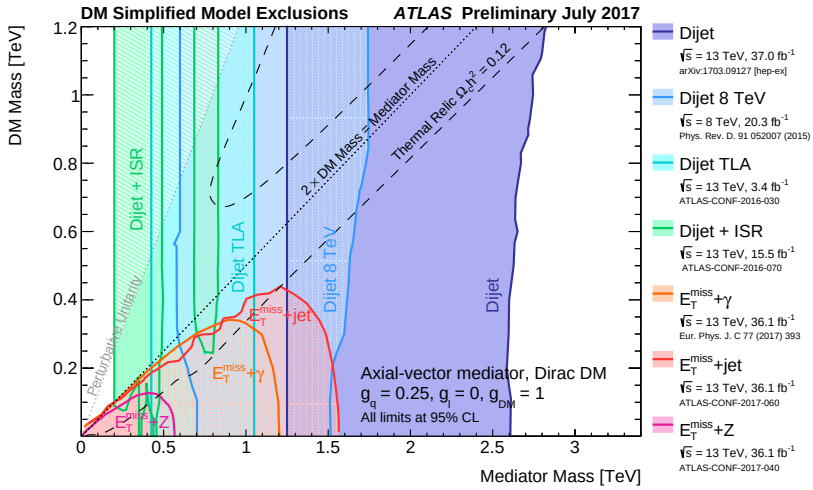

Figure 8.37: Regions in the $m_{\chi} - -m_{med}$ plane excluded at 95% CL by a selection of ATLAS dark matter searches, for the axial-vector mediator model, with coupling strengths $g_\chi = 1.0$, $g_q = 0.25$, $g_\ell = 0$, corresponding to the 'A1' scenario described in [161]. Small fluctuations in the di-jet contours are a product of the di-jet reinterpretation scheme. Dashed curves labeled 'thermal relic' indicate combinations of m_{χ} and m_{med} that are consistent with a dark matter density of $\Omega_c h^2 = 0.112$ and a standard thermal history, as computed in MadDM [98, 161]. A dotted curve indicates the kinematic threshold where the mediator can decay on-shell into dark matter. Plot by collaborator.

[3] In this section, the notation m_{med} can indicate m_{Z_A} or m_{Z_V}, depending on the context.

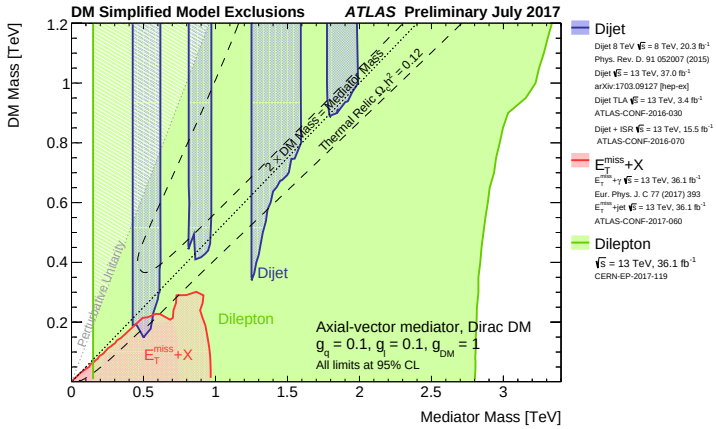

(a)

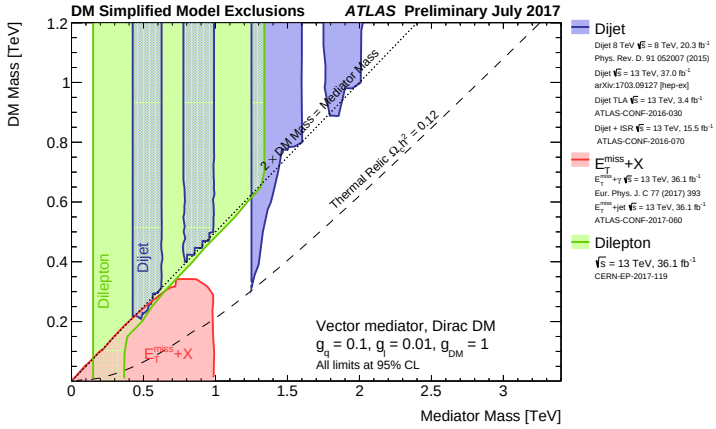

(b)

Figure 8.38: Regions in the $m_\chi - m_{med}$ plane excluded at 95% CL by a selection of ATLAS DM searches, for the scenarios 'A2' (a) and 'V2' (b) described in [161]. The mono-X (or $E_{\mathrm{T}}^{\mathrm{miss}}$ +X) exclusion regions are obtained by rescaling the published exclusion contours, using acceptance and cross-section information from samples simulated at truth-level. The single di-jet and mono-X exclusion region represents the union of exclusions from all analyses of that type. Plots by collaborator.

8.10.2 Mono-jets and direct detection

The models developed for the search of DM at colliders provide a way to compare the results from collider searches, such as the mono-jet, with results from direct detection experiments. This is done by calculating σ^{SD} and σ^{SI}, introduced in Section 2.5, in the context of the simplified model of interest. For the case of the spin-1 mediators considered here, the axial-vector (vector) interaction (cf. Eqs. **??**) underlies the SD (SI) interaction. The respective cross-sections are computed following Ref. [162]:

$$\sigma^{SI} = 6.9 \times 10^{-41}\mathrm{cm}^2 \cdot \left(\frac{g_q g_\chi}{0.25}\right)^2 \left(\frac{1\mathrm{TeV}}{M_{med}}\right)^4 \left(\frac{\mu_{n\chi}}{1\mathrm{GeV}}\right)^2 \quad (SD) \tag{8.10}$$

$$\sigma^{SD} = 2.4 \times 10^{-42}\mathrm{cm}^2 \cdot \left(\frac{g_q g_\chi}{0.25}\right)^2 \left(\frac{1\mathrm{TeV}}{M_{med}}\right)^4 \left(\frac{\mu_{n\chi}}{1\mathrm{GeV}}\right)^2 \quad (SI) \tag{8.11}$$

where $\mu_{n\chi} = m_n m_\chi/(m_n + m_\chi)$ is the reduced mass of the WIMP-nucleon system.

The results obtained from the translation of the axial-vector and vector mono-jet limits presented in Section 8.9.2 are shown in Figures 8.39 and compared to the best limits from direct detection experiments. ATLAS limits are more stringent for m_χ below 200 GeV, for the SD case; for the SI component they provide important bounds for $m_\chi \lessapprox 10$ GeV. It should be stressed that, while the limits provided by ATLAS are valid for this particular interaction and for the chosen couplings, direct detection limits do not assume a specific model for the WIMP-nucleon interaction. In turn, direct detection experiments have to make other assumptions, such as the velocity distribution of the WIMPs in the galaxy and that the measured DM saturates the cosmological density, which do not need to be done by collider experiments.

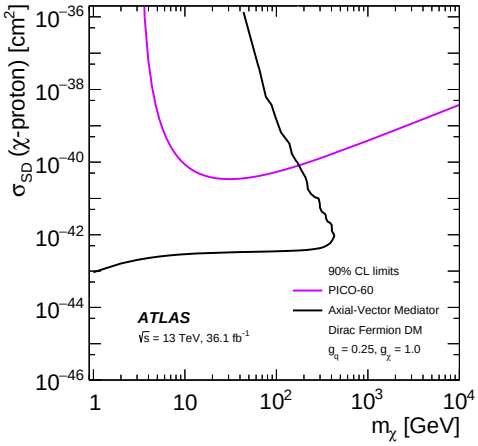

(a) Limits on $\sigma_{SD}(\chi - p)$

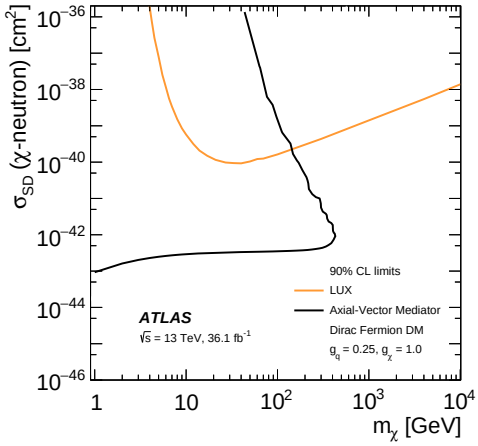

(b) Limits on $\sigma_{SD}(\chi - n)$

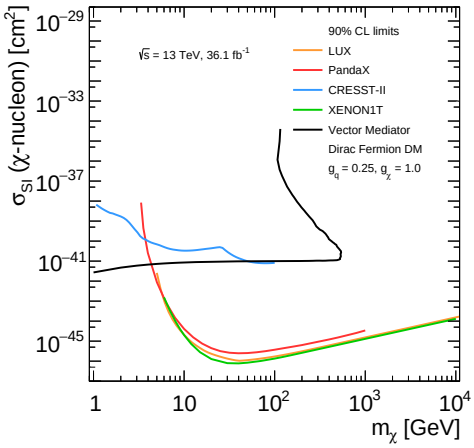

(c) Limits on $\sigma_{SI}(\chi - nucleon)$

Figure 8.39: A comparison of the ATLAS mono-jet limits (black line) to the constraints from direct detection experiments (colored lines) on the SD (top plots) and SI (bottom plot) cross sections, in the context of the simplified model with axial-vector (top) or vector (bottom) mediator and couplings $g_q = 0.25$, $g_\chi = 1.0$. Limits are shown at 90% CL.

8.10.3 Mono-jets at ATLAS and CMS

The latest mono-jet analysis performed by ATLAS has been described in detail in the present chapter and the elements of difference with respect to the previous ATLAS analysis performed on the data collected during 2015 [141] have been highlighted in Section 8.7. The improvement to the analysis sensitivity obtained by the latest mono-jet analysis is exemplified in Table 8.17, for an hypothesized $m_\chi = 1$ GeV in the axial-vector model.

The CMS collaboration has also performed mono-jet analyses at 13 TeV [155, 142] which share a similar analysis strategy as ATLAS. As an element of difference, the CMS analysis makes a more inclusive jet selection, where the p_{T} of the leading jet is required to be higher than 100 GeV and there is no veto on additional jets. Another difference is that two exclusive categories are defined based on the presence of a small-R jet or a large-R jet and used simultaneously in the fit. The binning in $p_{\mathrm{T}}^{\mathrm{recoil}}$ of the CMS analysis is finer. The CMS analysis uses two additional control regions, the `CR2e` and the `CR1`γ, where the jet recoils against two electrons and one photon, respectively. The CMS analysis finally uses bin-by-bin $\kappa-$ factors as opposed to the global κ-factor used by ATLAS.

Like the ATLAS analysis, no significant deviations from the SM predictions have been observed and the results are interpreted in terms of a number of different models, including the $s-$channel axial-vector model. Table 8.18 illustrates an example of expected and observed limits obtained by the two collaborations with the data collected during 2015 and 2016 by the two experiments; the expected sensitivity of the two analyses is similar, with the CMS limit being 5% better than the ATLAS limit. Both CMS and ATLAS have a worse observed limit than the expected, within 1σ and 2σ, respectively, as can be seen in Figure 8.40.

ATLAS, axial-vector model, limit on m_{Z_A} for $m_\chi = 1$ GeV			
	3.2 fb^{-1} [141]	36.1 fb^{-1} 2015-like proj.	36.1 fb^{-1} [5]
Expected	1.2 TeV	1.65 TeV	1.85 TeV
Observed	1.05 TeV	–	1.55 TeV

Table 8.17: Expected and observed exclusion limits on m_{Z_A} obtained by ATLAS for the $s-$channel model with $m_\chi = 1$ GeV. The central column corresponds to the expected limit that would have been obtained by using the same analysis strategy as in [141].

axial-vector model, limit on m_{Z_A} for $m_\chi = 1$ GeV		
	ATLAS 36.1 fb^{-1} [5]	CMS 35.9 fb^{-1} [142]
Expected	1.85 TeV	1.95 TeV
Observed	1.55 TeV	1.75 TeV

Table 8.18: Expected and observed exclusion limits on m_{Z_A} obtained by ATLAS and CMS for the $s-$ channel model with $m_\chi = 1$ GeV.

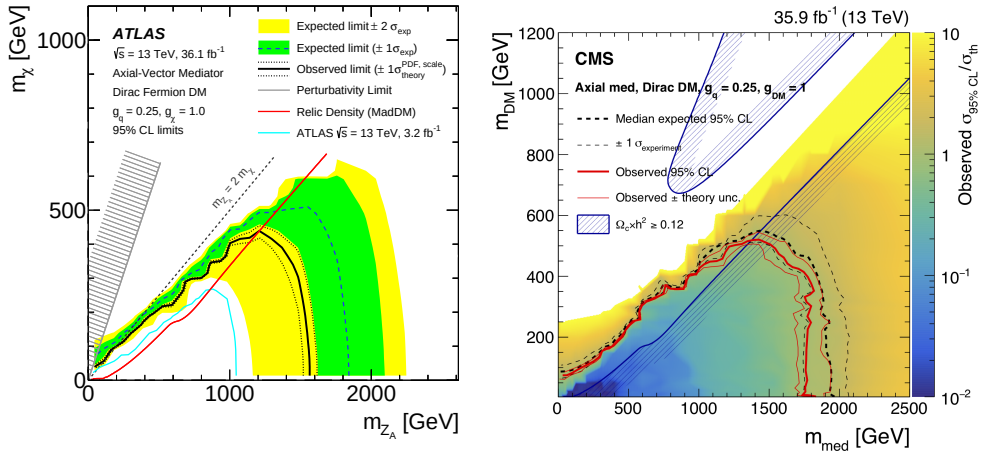

(a) ATLAS (b) CMS

Figure 8.40: Expected and observed limits on the s − channel axial-vector model in the m_χ–m_{Z_A} plane obtained by ATLAS (a) and CMS [142] (b).

8.11 Future prospects

From the discussion of this chapter, it is clear that the ATLAS mono-jet analysis has reached an unprecedented level of precision, where the uncertainty on the background prediction is essentially dominated by the systematic uncertainty. The larger datasets which will become available in the future runs of the LHC will allow to pursue improvements to the sensitivity of the analysis by following several different directions.

One first possible direction is the use of γ + jets final states in the simultaneous fit, by introducing a dedicated CR1γ. The CR1γ can be defined with the same logic as the other V + jets-enriched CRs: a high-p_{T} photon is required to recoil against the high-p_{T} jet, and the p_{T} of the system given by the photon and the $E_{\mathrm{T}}^{\mathrm{miss}}$ serves as observable of intereset ($p_{\mathrm{T}}^{\mathrm{recoil}}$). The larger statistics of the γ + jets sample, compared to the Z + jets and W + jets samples, can help to constrain the V + jets background predictions, especially at large $p_{\mathrm{T}}^{\mathrm{recoil}}$.
The level of improvement which can be obtained on the background estimation precision by using the CR1γ is illustrated in Figure 8.41. When translated in terms of expected limit on the signal strength μ, the improvement is approximately 4% for a $m_{Z_A} = 2$ TeV and $m_\chi = 1$ GeV in the axial-vector model.
The improvement is expected to be larger, once it will become possible to bin the $p_{\mathrm{T}}^{\mathrm{recoil}}$ distribution more finely.
A larger amount of data will enrich the statistics of the higher $p_{\mathrm{T}}^{\mathrm{recoil}}$ bins, allowing for an increased discrimination power between signal and background, especially in the high part of the $p_{\mathrm{T}}^{\mathrm{recoil}}$ spectrum, where lies the sensitivity to the regions at higher mediator and DM masses, which are not yet excluded. With this in mind, it will be important to make sure that the statistics of the MC samples remain adequate.

The larger amount of data that will become available in the future will enable to access larger regions of the parameter space where the DM can lie. By the end of the LHC Run 2, approximately 120 fb^{-1} of data will be collected. The integrated luminosity forseen for the Run 2 and Run 3 together equals about 300 fb^{-1}. The high-luminosity phase of the LHC is expected to deliver a dataset ten times larger.
By conservatively assuming that the analysis strategy will not change and that the level of systematic uncertainties will be the same as in the current version of the analysis, by the end of the Run 2 the reach of the mono-jet analysis in terms of excluded m_{Z_A} will be about 2 TeV for $m_\chi = 1$ GeV. Values of m_χ up to 600 GeV will be excluded for m_{Z_A} up to 1.5 TeV.
A few more examples of projected exclusion limits at different integrated luminosities are shown in Figure 8.42 for a few scenarios in the axial-vector and the scalar colored mediator models.

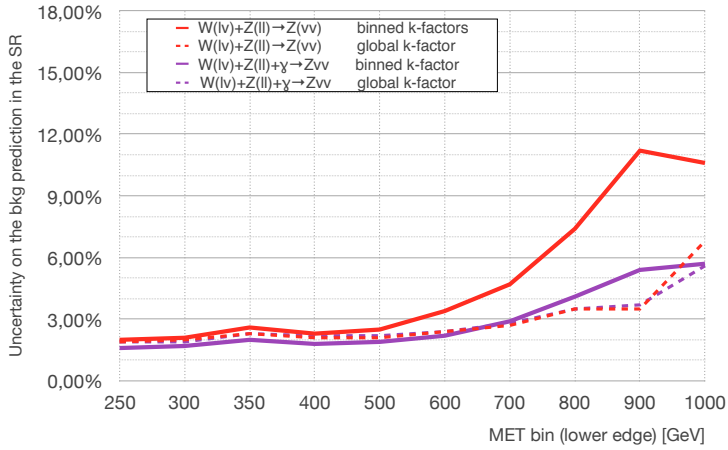

Figure 8.41: The relative estimated uncertainty on the background prediction in each $E_{\mathrm{T}}^{\mathrm{miss}}$ bin of the SR as obtained by the nominal fitting strategy (dashed red) and by including also the CR1γ (dashed purple). Also shown are the curves corresponding to bin-by-bin κ − factors for both strategies (solid red and solid purple, respectively). The fits are performed with Asimov datasets.

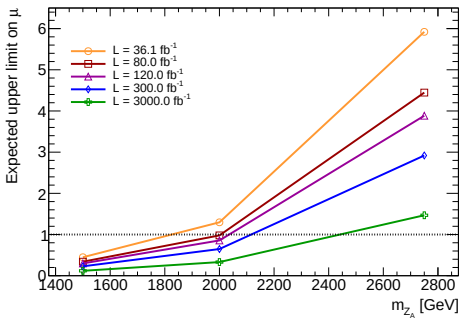

(a) Axial-vector mediator, $m_\chi = 1$ GeV

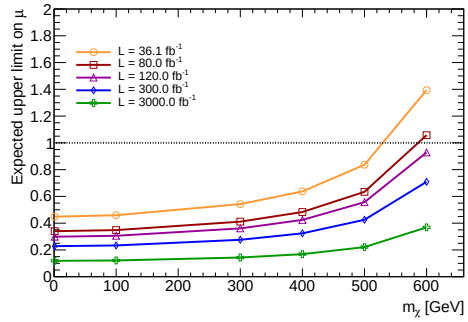

(b) Axial-vector mediator, $m_{Z_A} = 1500$ GeV

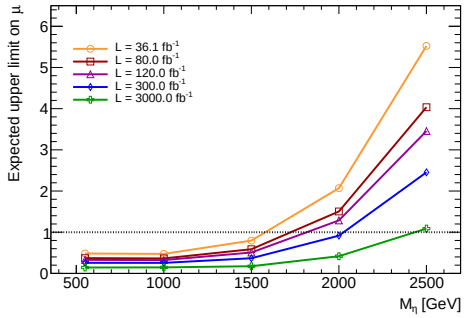

(c) Colored scalar mediator, $m_\chi = 500$ GeV

Figure 8.42: Sensitivity projections for several integrated luminosities in a few DM models scenarios.

Conclusions

This work addressed the problem of searching for dark matter particles at the LHC in a comprehensive way, starting from the study of the performance of the missing transverse momentum, through the investigation of models to describe the production of DM particles in final states with large $E_{\mathrm{T}}^{\mathrm{miss}}$ and a high-p_{T} object, landing to the searches for deviations from the Standard Model predictions in the mono-photon and the mono-jet channels with the data collected by ATLAS during the Run 2 of the LHC.

The $E_{\mathrm{T}}^{\mathrm{miss}}$ is a fundamental quantity for the search of DM particles as WIMPs, since the presence of WIMPs in a pp collision event would be signaled by an imbalance in the total transverse momentum of the collision products. The performance of the $E_{\mathrm{T}}^{\mathrm{miss}}$ reconstruction in the Run 2 has been studied and the computation of the $E_{\mathrm{T}}^{\mathrm{miss}}$ optimized, in particular with regards to the calculation of the soft part of the event, the soft term. It has been demonstrated that, among the variants studied for the Run 2 data-taking conditions, the best compromise between resolution, linearity and stability to pile-up is provided by the TST $E_{\mathrm{T}}^{\mathrm{miss}}$, for which the soft term is computed from track information.

Several DM models predicting mono-X final states have been considered and their phenomenology investigated, with particular focus on simplified models. The $s-$ channel spin-1 mediator model predicts mono-X topologies with a falling $E_{\mathrm{T}}^{\mathrm{miss}}$ spectrum, with a higher average value for higher mediator masses; the coupling strengths rule the production cross-sections, which is the highest for the mono-jet case.
The $t-$channel scalar colored mediator model, investigated in the context of the mono-jet final state, presents a more complex phenomenology, with a $E_{\mathrm{T}}^{\mathrm{miss}}$ spectrum that depends not only on the mass of the mediator, but also on the mass difference between the dark matter and the mediator and on the coupling strength of the interaction. This model has been fully simulated and used in an ATLAS physics analysis for the first time.

Deviations from the SM predictions have been looked for in two mono-X topologies, the mono-photon and the mono-jet. A combination of data-driven and simulation-based techniques have been deployed for the estimation of the backgrounds. The biggest challenge in both searches has been the estimation of the irreducible background. In the mono-photon analysis performed with the 2015 data, the $Z(\nu\nu)\gamma$ background has been

measured through $Z(\ell\ell)\gamma$ states and the achieved precision on the total background estimate is 11%. In the subsequent mono-photon analysis including the 2016 data, this value has approximately halved.

In the case of the mono-jet analysis performed on the 2015 and 2016 data, regions enriched in $W(\ell\nu)+$jets and $Z(\ell\ell)+$jets have been used simultaneously for the estimation of the $Z(\nu\nu)+$jets, with the advantage of a larger sample compared to $Z(\ell\ell)+$jets only. The use of state-of-the-art perturbative calculations and theoretical uncertainties available for the $V+$jets have allowed to treat consistently the $W+$jets and $Z+$jets. The achieved precision on the background estimation ranges from 2% in the intermediate $E_{\mathrm{T}}^{\mathrm{miss}}$ regime, to 7% in the TeV regime and is approximately halved compared to the previous ATLAS mono-jet analysis.

No significant excesses have been found in neither of the searches and the results have been interpreted in the context of the DM models considered. For the case of the effective field theory and $t-$channel production, the limits set by the mono-photon and mono-jet searches, respectively, are the best limits to date: for the former, values of M^* up to 790 GeV are excluded for low WIMP masses, while for the latter the maximum excluded value of M_η is 1.7 TeV and the maximum excluded value of m_χ is 620 GeV.
The phase-space of the $s-$channel model has been further restricted, with the mono-jet limits being the best mono-X limits: the lower limit on the mediator mass is 1.6 TeV for low WIMP masses, in the case of the axial-vector model. This result translates into an upper limit on the scattering cross-section between WIMP and proton equal to 10^{-44} cm^{-2} for low WIMP masses.

By the end of the Run 2, approximately three times larger data samples than considered in this work will be available: an improved understanding of the physics objects, a better theoretical knowledge of the background and signal processes, and the enlarged statistics, will enable to further probe the phase-space where the dark matter can lie.

Appendices

APPENDIX A

Validation of the $t-$ channel samples

This appendix reports technical aspects of the validation procedure for the generation of the $t-$ channel model.

A.1 Parameters and settings for the generation

The MADGRAPH process_cards which are used for the split generation procedure are schematically summarized in table A.1. The syntax `$med` has the effect of removing the phase space over which MADGRAPH regards the mediator as on-shell. This phase space region is expressed by the condition:

$$M_\eta \pm \Gamma \times \texttt{BWcutoff}\,, \tag{A.1}$$

where Γ is the width of the mediator as calculated with equation 6.9 and `BWcutoff` is the Breit-Wigner cutoff parameter.

The default value of `BWcutoff` is 15, which is a suitable choice whenever the width of the mediator is small enough to justify a narrow width approximation. However, when $g \sim \mathcal{O}(1)$ and the width of the mediator is subsequently large, a `BWcutoff` of 15 results in a veto region which leaves little phase space for sample 3. This is dealt with by lowering the value of `BWcutoff` such that $\Gamma \times$ `BWcutoff` does not exceed $\mathcal{O}(50\text{ GeV})$.

When `BWcutoff` is lowered, the duplication of events may occur among the different sub-samples. This is dealt with by rescaling split samples 1 and 2 by weights w^2 and w respectively, where:

$$w = \frac{\int_{M_\eta - \Gamma * \texttt{BWcutoff}}^{M_\eta + \Gamma * \texttt{BWcutoff}} BW(x)dx}{\int_{-\infty}^{\infty} BW(x)dx} \tag{A.2}$$

with $BW(x)$ the Breit-Wigner distribution of the mediator.

In accordance with the methodology described in [92], the Higgs and electroweak bosons are omitted from the hard scatter processes of split samples 1 through 3. This is done primarily for computational convenience as the added diagrams do not yield significant correction for the mass and coupling points of interest.

Sample 1
`define med = etad etadbar etau etaubar etas etasbar etac etacbar`
`define dm = chi chi~`
`generate p p > med med / a h z w+ w- NP=2 QCD=2 @1`
`add process p p > j med med / a h z w+ w- NP=2 QCD=3 @2`
`add process p p > j j med med / a h z w+ w- NP=4 QCD=4 @3`
Sample 2
`define med = etad etadbar etau etaubar etas etasbar etac etacbar`
`define dm = chi chi~`
`generate p p > dm med / a h z w+ w- $med NP=1 QCD=1 @1`
`add process p p > j dm med / a h z w+ w- $med NP=1 QCD=2 @2`
`add process p p > j j dm med / a h z w+ w- $med NP=3 QCD=3 @3`
Sample 3
`define med = etad etadbar etau etaubar etas etasbar etac etacbar`
`generate p p > chi chi~ / a h z w+ w- $med @1`
`add process p p > j chi chi~ / a h z w+ w- $med @2`
`add process p p > j j chi chi~ / a h z w+ w- $med NP=4 QCD=2 @3`

Table A.1: Summary of the MADGRAPH run_card processes for split samples 1, 2 and 3 of the $t-$ channel scalar mediator simplified model. Note that the ellipses in the `med` definition for split samples 1 and 2 indicate the inclusion of only those mediators for which the associated decay to a DM-quark pair is kinematically accessible.

The reference for the full set of parameters that are used for the generation can be found in the *Job options* used for the generation of the samples within the ATLAS MC production. Here we stress few additional parameters that have been optimized:

- *ktDurham* is set to $M_\eta/8$ for sample 1 and to 30 GeV for samples 2 and 3;
- *pt jet* is set to 10 GeV, as opposed to the default value of 20 GeV;
- *Merging:mayRemoveDecayProducts* is set to *ON* for samples 1 and 2, and to *OFF* for sample 3
- *Merging:process* is tailored for the various samples:
  1. pp>{etad,9000006}{etad ,-9000006}{etau,9000007}{etau ,-9000007} {etas,9000008}{etas ,-9000008}{etac,9000009}{etac ,-9000009}
  2. pp>{etad,9000006}{etad ,-9000006}{etau,9000007}{etau ,-9000007} {etas,9000008}{etas ,-9000008}{etac,9000009}{etac ,-9000009} {chi,1000022}{chi ,-1000022}
  3. pp>{chi,1000022}{chi ,-1000022}

A.2 Validation of the matching scale

As stated in the previous section, the parton matching scale is set to $M_\eta/8$ for split sample 1 and to 30 GeV for split samples 2 and 3. This choice is validated for the mono-jet

final state in the following way: the matching scale is varied by a factor 2 or 0.5 for each sub-sample separately and the differences between the nominal choice and these choice are evaluated and found to be small.

Table A.2 shows the variations in terms of cross-section and acceptance of the mono-jet selection for each sub-sample and for a set of representative signal points. It can be seen that for most points, the variations are well below 20%. Figures A.1–A.6 show the key kinematic distributions for a few representative signal points and for each sub-sample separately, after the mono-jet selection. It can be noticed that the distributions are largely independent on the matching scale choice.

m_χ (GeV)	M_η (GeV)	g	Split	σ Low Var(%)	σ Up Var (%)	Acc Low Var(%)	Acc Up Var(%)
1	550	0,25	1	3,5	-0,4	-1,4	-2,7
1	550	0,25	2	-6,2	-1,6	-2,9	0,2
1	550	0,25	3	0,9	-13,6	-4,1	-1,8
1	550	1	1	-4,8	1,8	0,8	-1,5
1	550	1	2	-4,9	-1,0	2,3	1,2
1	550	1	3	17,6	-13,4	-4,6	5,3
1	1000	0,25	1	1,3	2,0	-1,0	-4,7
1	1000	0,25	2	-2,8	-0,3	0,8	-1,5
1	1000	0,25	3	1,4	-16,6	1,2	3,3
1	1000	1	1	-4,3	3,0	2,5	0,1
1	1000	1	2	-7,3	-0,3	1,6	-1,8
1	1000	1	3	-1,6	-8,2	-2,3	0,5
500	550	0,25	1	4,5	2,7	4,8	-0,4
500	550	0,25	2	-12,1	-15,0	9,7	3,0
500	550	0,25	3	23,2	-42,6	-10,8	2,8
500	550	1	1	1,5	0,6	-7,4	-5,4
500	1000	1	2	-6,4	1,0	3,0	-3,8
500	1000	1	3	5,5	-0,8	3,5	3,7
500	1000	0,25	1	5,4	2,9	-3,1	-4,4
500	1000	0,25	2	-7,9	0,9	-2,7	0,1
500	1000	0,25	3	4,6	-2,2	-3,0	-1,9
500	1000	1	1	-2,1	2,0	0,3	-2,8
500	1000	0,25	2	-7,9	0,9	-2,7	0,1
500	1000	0,25	3	4,6	-2,2	-3,0	-1,9
1000	2000	0,25	1	0,0	1,3	1,2	-0,4
1000	2000	0,25	2	-6,4	0,5	2,2	-2,3
1000	2000	0,25	3	5,8	-1,9	-1,8	0,4
1000	2000	1	1	-2,4	1,5	0,4	0,9
1000	2000	1	2	-9,4	-2,0	1,7	-1,5
1000	2000	1	3	3,2	-2,9	2,3	3,8

Table A.2: Variations of cross-section and acceptance for a few signal points for each sub-sample separately when the matching scale is varied by a factor 0.5 and 2.

A.3 Comparison with a SUSY simplified model

This study was conducted to quantify the overlap between the $t-$channel model and the simplified model used in the SUSY 0-lepton search to describe the production of light squarks each decaying to a light squark and a neutralino; the two models are characterized by a similar interaction Lagrangian. More explicitly the similarities and differences between the two simplified models are:

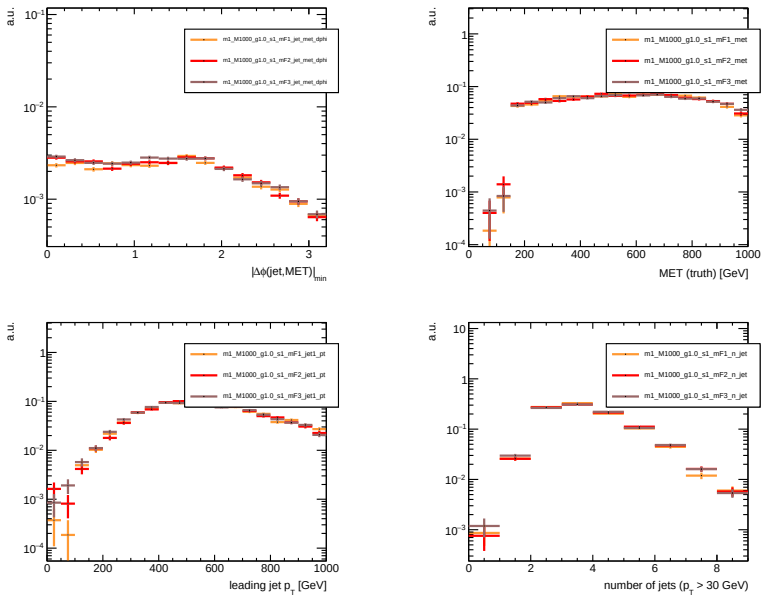

Figure A.1: Key kinematic distributions normalized to unit area after the mono-jet selection for m_χ = 1 GeV, M_η = 1000 GeV, g=1 and sample 1; the nominal scale is indicated in red, the down scale variation in orange and the up scale variation in brown.

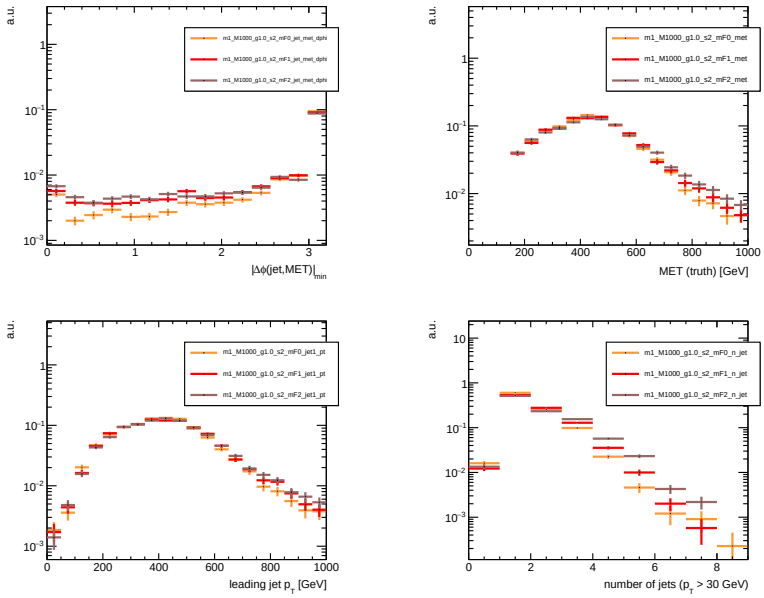

Figure A.2: Key kinematic distributions normalized to unit area after the mono-jet selection for m_χ = 1 GeV, M_η = 1000 GeV, g=1 and sample 2; the nominal scale is indicated in red, the down scale variation in orange and the up scale variation in brown.

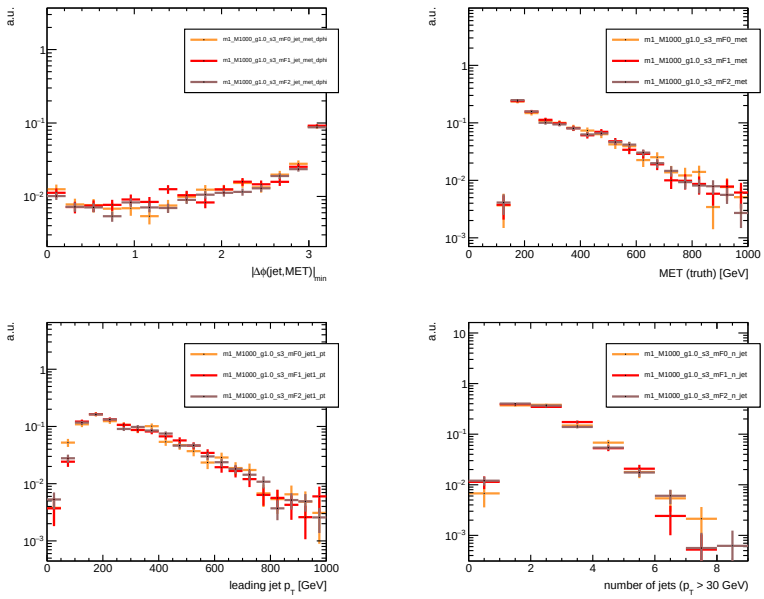

Figure A.3: Key kinematic distributions normalized to unit area after the mono-jet selection for m_χ = 1 GeV, M_η = 1000 GeV, g=1 and sample 3; the nominal scale is indicated in red, the down scale variation in orange and the up scale variation in brown.

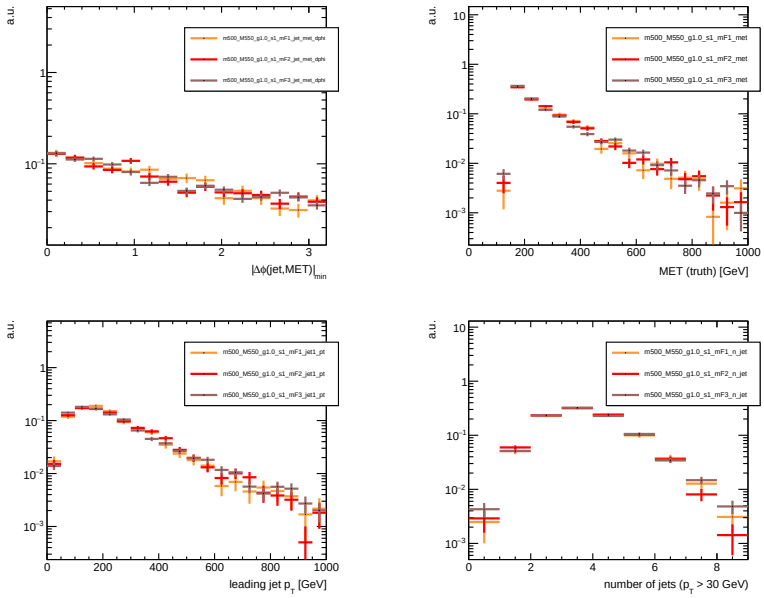

Figure A.4: Key kinematic distributions normalized to unit area after the mono-jet selection for m_χ = 500 GeV, M_η = 550 GeV, g=1 and sample 1; the nominal scale is indicated in red, the down scale variation in orange and the up scale variation in brown.

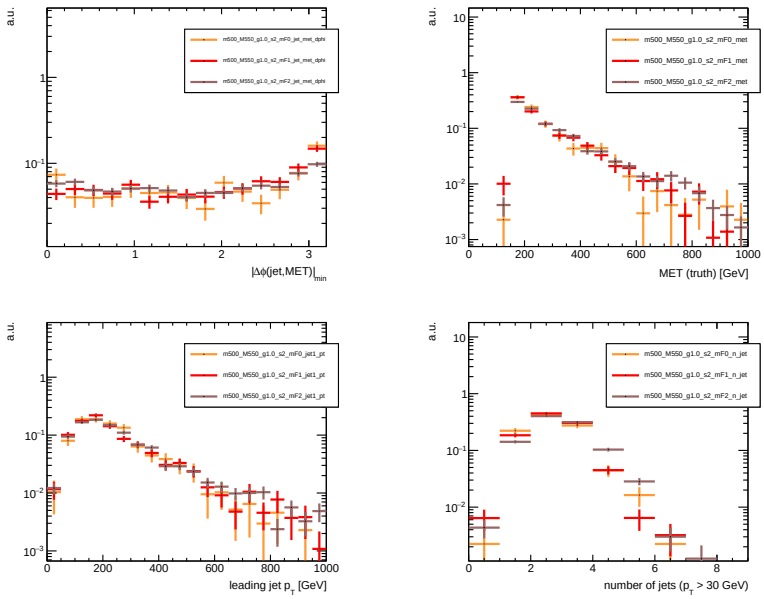

Figure A.5: Key kinematic distributions normalized to unit area after the mono-jet selection for m_χ = 500 GeV, M_η = 550 GeV, g=1 and sample 2; the nominal scale is indicated in red, the down scale variation in orange and the up scale variation in brown.

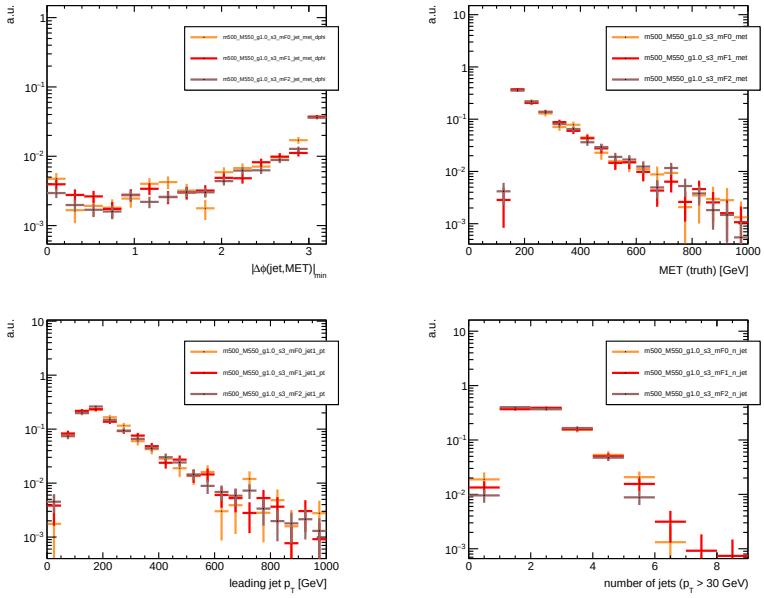

Figure A.6: Key kinematic distributions normalized to unit area after the mono-jet selection for m_χ = 500 GeV, M_η = 550 GeV, g=1 and sample 3; the nominal scale is indicated in red, the down scale variation in orange and the up scale variation in brown.

- the coupling g is a free parameter in the $t-$channel model, while it is fixed in the SUSY model;
- the χ particle of the $t-$channel model is a Dirac spinor, while in the SUSY case it is a Majorana particle; in both cases it is the LSP particle of the model;
- the η_i particles of the $t-$channel model correspond to the squarks in the SUSY model; in both cases the mediator/squark decays with a 100% branching fraction to quark of the same flavor and the LSP.
- in our implementation of the $t-$channel model only left-handed (LH) mediators and quarks are coupled, while in the SUSY model both right-handed (RH) and LH particles are considered

For simplicity we will refer to the mass parameters of the SUSY model with the same names as the $t-$channel model.

Validation of the SUSY samples

Preliminarily a validation of the private generation setup to generate the SUSY signals is performed. The generation setup for private production employs the official ATLAS job options for the signal generation in the SUSY 0-lepton search[1].

Table A.3 shows the comparison for a few signal points between the cross sections of the officially produced samples and those obtained from the private production. Given the different number of events between the two productions and the different versions of the ATLAS MC Production, the agreement of the cross-section is good. Figures A.7 and A.8 show a comparison in terms of kinematic distributions between official and private production.

m_χ (GeV) M_η (GeV)	σ (pb) official	m_χ (GeV) M_η (GeV)	σ (pb) private
100 500	3,74E+00	100 500	4,08E+00
100 1000	4,01E-02	100 1000	4,18E-02
450 500	3,74E+00	450 500	4,07E+00
500 1000	4,01E-02	450 1000	4,16E-02

Table A.3: Comparison of cross sections between official samples and privately produced samples for the SUSY model.

[1] `https://svnweb.cern.ch/trac/atlasoff/browser/Generators/MC15JobOptions/trunk/common/madgraph/MadGraphControl_SimplifiedModel_SS_direct.py?rev=688143+`

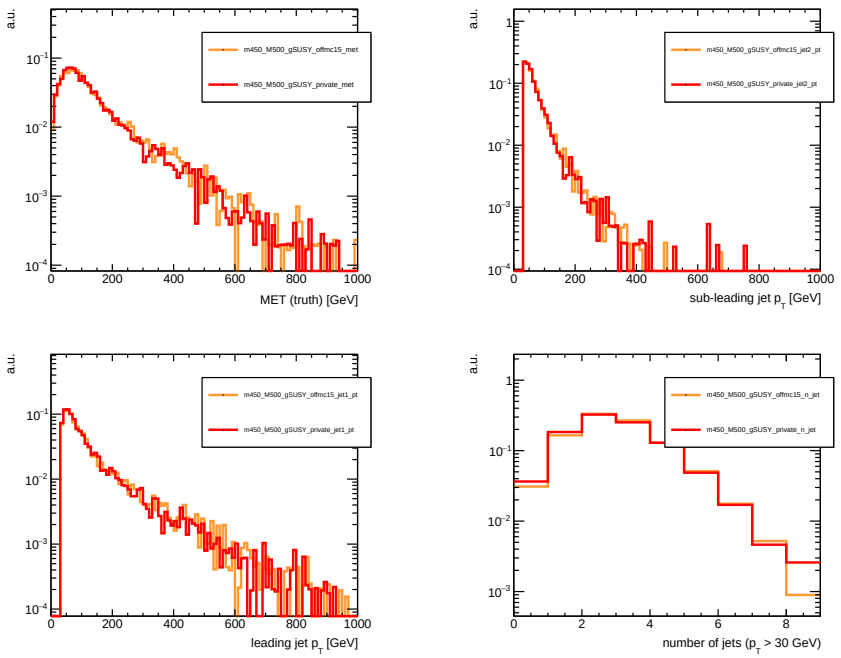

Figure A.7: $E_{\mathrm{T}}^{\mathrm{miss}}$, leading jet p_{T}, sub-leading jet p_{T}, and jet multiplicity distributions for m_{χ} = 450 GeV, M_{η} = 500 GeVfor the official samples (orange) and the private samples (red). Spectra are normalized to unit area.

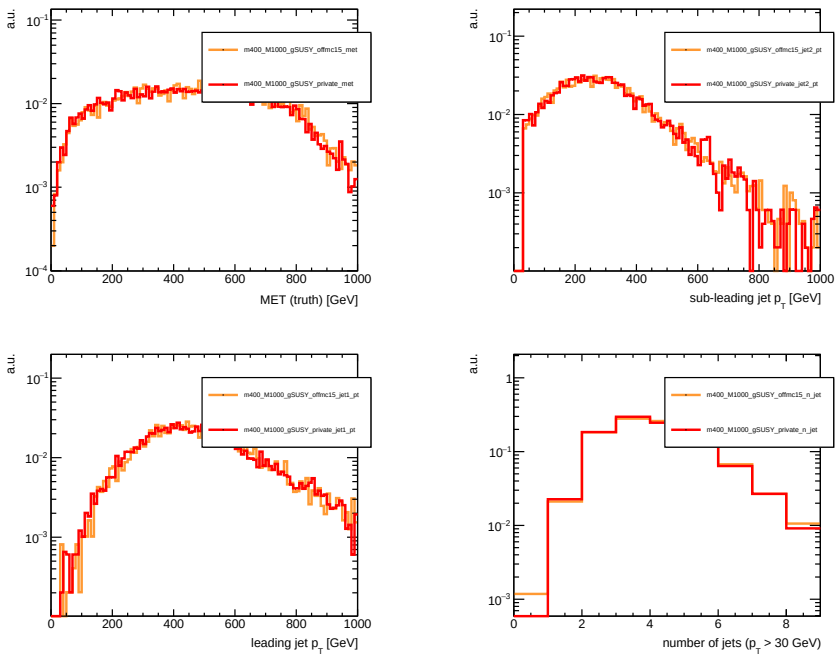

Figure A.8: $E_{\mathrm{T}}^{\mathrm{miss}}$, leading jet p_{T}, sub-leading jet p_{T}, and jet multiplicity distributions for m_{χ} = 400 GeV, M_{η} = 1000 GeVfor the official samples (orange) and the private samples (red). Spectra are normalized to unit area.

Comparison between the $t-$ channel and the SUSY model

The official process card for the SUSY model was changed uniquely to decouple the RH squarks, with the aim of comparing the two models on similar grounds. The same MADGRAPH run card has been used for both, except for the *BWcutoff* parameter, which in the case of the $t-$channel model is set for samples 2 and 3 as described in Section A.1. The same setups for PYTHIA were used except for the *Merging::Process* parameter, which for the case of the $t-$channel was set as specified in Section A.1. The comparison between the two models is performed in terms of cross sections and in terms of kinematics at the truth level (after showering with PYTHIA).

Table A.4 shows the cross-section obtained with the private production of the SUSY model and those obtained for the split samples with the $t-$ channel model at the MADGRAPH level. Contributions from different jet multiplicities are shown separately and summed. From the comparison it can be seen that the cross-section of the SUSY model is recovered by the $t-$ channel model for sufficiently low couplings. It was checked that indeed the diagrams entering the SUSY model are the same as those entering the split sample 1 of the $t-$ channel model.

When moving to higher couplings, the cross-section for the $t-$ channel model becomes larger and the contributions of the samples 2 and 3 become more important. This coupling dependence and similarity between $t-$ channel model and SUSY model for low values of g is further demonstrated by Figures A.9, A.10, A.11 for several kinematic distributions.

m_χ = 450 GeV M_η = 500 GeV

	Sample name	MADGRAPH Syntax	σ 0-jet (pb)	σ 1-jet (pb)	σ 2-jet (pb)	σ Sum (pb)
SUSY		pp > susylq susylq~	1.4e+00	4.9e-01	1.1e-01	2.0e+00
$t-$channel g=0.1	1	pp > med med	1.4e+00	4.9e-01	1.1e-01	2.0e+00
	2	pp > med dm $ med	9.6e-03	3.9e-03	1.0e-03	1.5e-02
	3	pp > dm dm $ med	1.4e-05	5.4e-06	4.3e-06	2.4e-05
$t-$channel g=1.0	1	pp > med med	1.8e+00	5.5e-01	1.2e-01	2.5e+00
	2	pp > med dm $ med	9.6e-01	3.0e-01	6.3e-02	1.3e+00
	3	pp > dm dm $ med	1.4e-01	2.3e-02	3.7e-03	1.7e-01
$t-$channel g=3.0	1	pp > med med	4.0e+01	6.6e+00	1.8e+00	4.8e+01
	2	pp > med dm $ med	8.7e+00	1.1e+01	2.5e+00	2.3e+01
	3	pp > dm dm $ med	1.1e+01	1.8e+00	5.8e-01	1.4e+01

m_χ = 100 GeV M_η = 200 GeV

	Sample name	MADGRAPH Syntax	σ 0-jet (pb)	σ 1-jet (pb)	σ 2-jet (pb)	σ Sum (pb)
SUSY		pp > susylq susylq~	1.7e+02	9.9e+01	4.0e+01	3.1e+02
$t-$channel g=0.1	1	pp > med med	1.7e+02	9.8e+01	4.0e+01	3.1e+02
	2	pp > med dm $ med	1.0e+00	5.7e+00	3.2e+00	1.0e+01
	3	pp > dm dm $ med	1.5e-03	1.5e-02	4.6e-02	6.3e-02
$t-$channel g=1.0	1	pp > med med	2.1e+02	1.1e+02	4.2e+01	3.6e+02
	2	pp > med dm $ med	1.0e+02	6.2e+01	2.1e+01	1.9e+02
	3	pp > dm dm $ med	1.5e+01	3.7e+00	1.1e+00	2.0e+01
$t-$channel g=3.0	1	pp > med med	3.7e+03	9.8e+02	3.5e+02	5.0e+03
	2	pp > med dm $ med	9.3e+02	1.8e+03	6.2e+02	3.4e+03
	3	pp > dm dm $ med	1.2e+03	2.8e+02	1.9e+02	1.7e+03

m_χ = 1000 GeV M_η = 2000 GeV

	Sample name	MADGRAPH Syntax	σ 0-jet (pb)	σ 1-jet (pb)	σ 2-jet (pb)	σ Sum (pb)
SUSY		pp > susylq susylq~	3.6e-05	2.1e-06	7.1e-08	3.9e-05
$t-$channel g=0.1	1	pp > med med	3.6e-05	2.1e-06	7.1e-08	3.9e-05
	2	pp > med dm $ med	5.4e-06	1.5e-06	7.5e-08	7.0e-06
	3	pp > dm dm $ med	7.3e-08	7.2e-08	1.3e-08	1.6e-07
$t-$channel g=1.0	1	pp > med med	1.0e-04	3.1e-06	9.6e-08	1.0e-04
	2	pp > med dm $ med	5.4e-04	6.5e-05	2.0e-06	6.1e-04
	3	pp > dm dm $ med	7.3e-04	6.1e-05	5.1e-06	8.0e-04
$t-$channel g=3.0	1	pp > med med	6.0e-03	9.8e-05	4.3e-05	6.1e-03
	2	pp > med dm $ med	4.9e-03	4.5e-03	1.4e-04	9.6e-03
	3	pp > dm dm $ med	5.9e-02	1.6e-03	4.9e-04	6.1e-02

Table A.4: Comparison of cross sections at the MADGRAPH level between privately produced samples in the SUSY model and $t-$channel samples obtained with the splitting procedure for a few signal benchmark points.

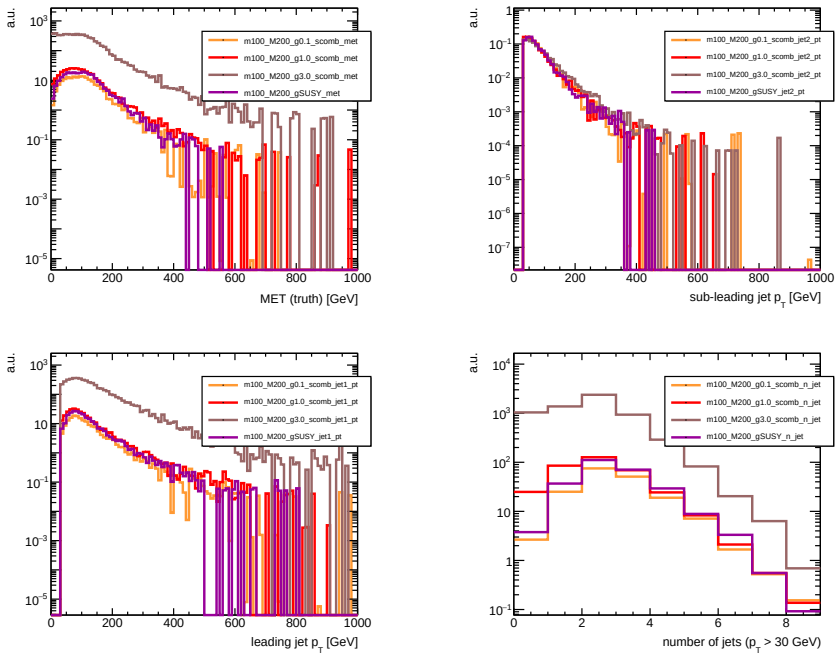

Figure A.9: $E_{\mathrm{T}}^{\mathrm{miss}}$, leading jet p_{T}, sub-leading jet p_{T}, and jet multiplicity distributions for m_{χ} = 100 GeV, M_{η} = 200 GeV. The distributions for the $t-$channel model with several couplings ($g = 0.1$ in orange, $g = 1.0$ in red, $g = 3.0$ in grey) are compared to the distribution for the SUSY model (purple). Spectra are normalized to their cross-section.

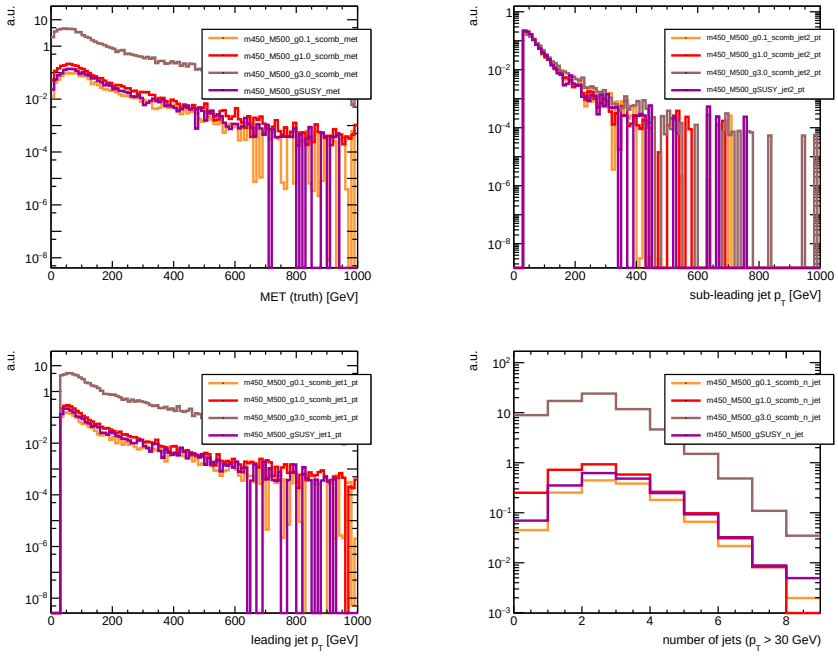

Figure A.10: $E_{\mathrm{T}}^{\mathrm{miss}}$, leading jet p_{T}, sub-leading jet p_{T}, and jet multiplicity distributions for m_{χ} = 450 GeV, M_{η} = 500 GeV. The distributions for the $t-$channel model with several couplings ($g = 0.1$ in orange, $g = 1.0$ in red, $g = 3.0$ in grey) are compared to the distribution for the SUSY model (purple). Spectra are normalized to their cross-section.

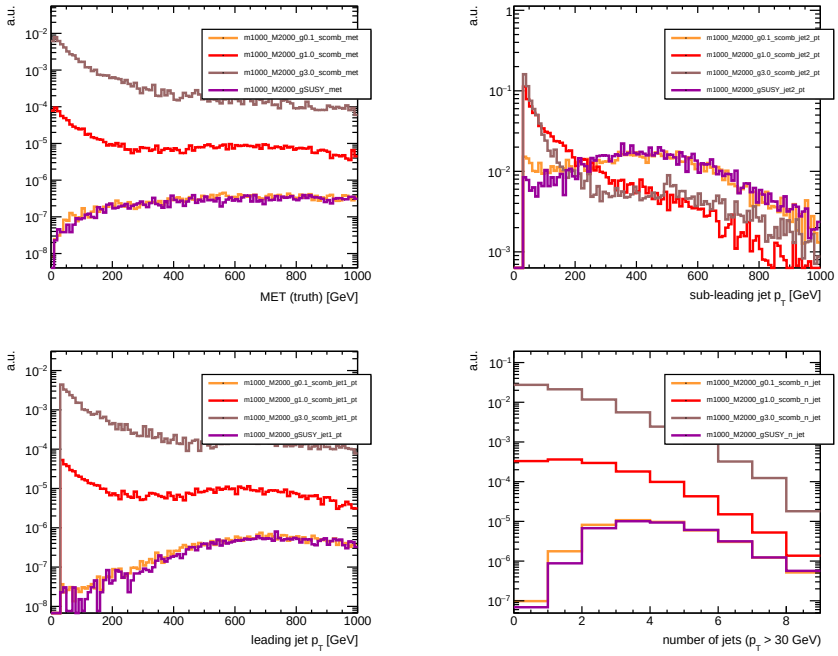

Figure A.11: $E_{\mathrm{T}}^{\mathrm{miss}}$, leading jet p_{T}, sub-leading jet p_{T}, and jet multiplicity distributions for m_{χ} = 1000 GeV, M_{η} = 2000 GeV. The distributions for the $t-$channel model with several couplings ($g = 0.1$ in orange, $g = 1.0$ in red, $g = 3.0$ in grey) are compared to the distribution for the SUSY model (purple). Spectra are normalized to their cross-section.

APPENDIX B

Further results of the mono-jet analysis

This appendix collects further results on the background estimates of the mono-jet analysis.

B.1 Full breakdown of the systematic uncertainties from the shape fit

Tables B.1–B.5 report the effect of each source of uncertainty considered in the analysis in percentage of the total expected background in the SR and in every CRs for all $p_{\mathrm{T}}^{\mathrm{recoil}}$ bins before the fit. The values are calculated as the variation of the expected background when shifting down (first number) and up (second number) each nuisance parameter by one standard deviation.

Table B.6 reports the effect of the variations of each source of uncertainty considered in the analysis in percentage of the total post-fit predicted background in the SR.

B.2 Event yields from the counting experiment fits

In addition to the shape fit described in Section 8.8.2, ten counting experiment fits are performed in the mono-jet analysis in the inclusive $p_{\mathrm{T}}^{\mathrm{recoil}}$ bins, described in Section 8.4, with a simplified likelihood model, as explained in Section 8.5.2.

The predicted yields from these fits are shown in Tables B.7–B.11 for the signal region and the control regions for all the inclusive $p_{\mathrm{T}}^{\mathrm{recoil}}$ bins, along with the background composition, as determined from each fit. The predicted events are in agreement with the observed events. The SM predictions are determined with a total uncertainty of 2% in BIN>250 and 10% in BIN>1000.

SR	BIN_250	BIN_300	BIN_350	BIN_400	BIN_500	BIN_600	BIN_700	BIN_800	BIN_900	BIN_1000
NCB_Sys	(-0.28,0.28)	(-0.13,0.14)	(-0.11,0.11)	(-0.08,0.08)	(-0.06,0.06)	(0.00,0.00)	(0.00,0.00)	(0.00,0.00)	(0.00,0.00)	(0.00,0.00)
PDFcomb	(-1.53,1.53)	(-1.54,1.54)	(-1.84,1.84)	(-2.11,2.11)	(-2.45,2.45)	(-2.85,2.85)	(-3.16,3.16)	(-3.25,3.25)	(-4.36,4.36)	(-6.63,6.63)
ckkw	(-0.76,0.76)	(-0.92,0.92)	(-0.93,0.93)	(-0.92,0.92)	(-0.54,0.54)	(-0.28,0.28)	(-0.41,0.41)	(-0.32,0.32)	(-0.38,0.38)	(-0.64,0.64)
diboson_Sys	(-0.14,0.14)	(-0.16,0.16)	(-0.19,0.19)	(-0.27,0.27)	(-0.43,0.43)	(-0.71,0.71)	(-0.90,0.90)	(-1.30,1.30)	(-1.34,1.34)	(-2.47,2.47)
lumiSys	(-3.17,3.17)	(-3.19,3.19)	(-3.19,3.19)	(-3.20,3.20)	(-3.20,3.20)	(-3.20,3.20)	(-3.20,3.20)	(-3.20,3.20)	(-3.20,3.20)	(-3.20,3.20)
multijet_Sys	(-0.56,0.56)	(-0.31,0.32)	(-0.11,0.11)	(-0.06,0.06)	(-0.08,0.08)	(-0.06,0.06)	(-0.08,0.08)	(-0.15,0.15)	(-0.07,0.07)	(-0.07,0.07)
EG_RESOLUTION_ALL	(0.01,0.00)	(0.00,0.00)	(0.00,0.00)	(0.00,0.00)	(-0.01,0.00)	(-0.02,-0.01)	(0.00,0.00)	(0.02,0.02)	(0.87,-0.81)	(0.03,-0.03)
EG_SCALE_ALL	(0.02,-0.03)	(0.02,-0.01)	(0.01,-0.01)	(0.01,-0.01)	(0.00,-0.01)	(0.01,-0.01)	(0.03,-0.03)	(0.00,0.01)	(0.00,0.00)	(0.02,-0.01)
EL_EFF_ID	(0.17,-0.17)	(0.19,-0.19)	(0.19,-0.20)	(0.20,-0.20)	(0.24,-0.24)	(0.21,-0.21)	(0.15,-0.15)	(0.17,-0.17)	(0.18,-0.18)	(0.16,-0.16)
EL_EFF_Iso	(0.00,0.00)	(0.00,0.00)	(0.00,0.00)	(0.00,0.00)	(0.00,0.00)	(0.00,0.00)	(0.00,0.00)	(0.00,0.00)	(0.00,0.00)	(0.00,0.00)
EL_EFF_Reco	(0.03,-0.03)	(0.03,-0.03)	(0.03,-0.03)	(0.03,-0.03)	(0.03,-0.03)	(0.03,-0.03)	(0.02,-0.02)	(0.02,-0.02)	(0.03,-0.03)	(0.02,-0.02)
EL_EFF_TriggerEff	(0.00,0.00)	(0.00,0.00)	(0.00,0.00)	(0.00,0.00)	(0.00,0.00)	(0.00,0.00)	(0.00,0.00)	(0.00,0.00)	(0.00,0.00)	(0.00,0.00)
EL_EFF_Trigger	(0.00,0.00)	(0.00,0.00)	(0.00,0.00)	(0.00,0.00)	(0.00,0.00)	(0.00,0.00)	(0.00,0.00)	(0.00,0.00)	(0.00,0.00)	(0.00,0.00)
FT_EFF_B_systematics	(0.00,0.00)	(0.00,0.00)	(0.00,0.00)	(0.00,0.00)	(0.00,0.00)	(0.00,0.00)	(0.00,0.00)	(0.00,0.00)	(0.00,0.00)	(0.00,0.00)
FT_EFF_C_systematics	(0.00,0.00)	(0.00,0.00)	(0.00,0.00)	(0.00,0.00)	(0.00,0.00)	(0.00,0.00)	(0.00,0.00)	(0.00,0.00)	(0.00,0.00)	(0.00,0.00)
FT_EFF_Light_systematics	(0.00,0.00)	(0.00,0.00)	(0.00,0.00)	(0.00,0.00)	(0.00,0.00)	(0.00,0.00)	(0.00,0.00)	(0.00,0.00)	(0.00,0.00)	(0.00,0.00)
FT_EFF_extrapolation	(0.00,0.00)	(0.00,0.00)	(0.00,0.00)	(0.00,0.00)	(0.00,0.00)	(0.00,0.00)	(0.00,0.00)	(0.00,0.00)	(0.00,0.00)	(0.00,0.00)
FT_EFF_extrapolation_from_charm	(0.00,0.00)	(0.00,0.00)	(0.00,0.00)	(0.00,0.00)	(0.00,0.00)	(0.00,0.00)	(0.00,0.00)	(0.00,0.00)	(0.00,0.00)	(0.00,0.00)
JET_EtaIntercalibration_NonClosure	(0.80,-0.68)	(0.88,-0.97)	(0.70,-0.48)	(0.31,-0.56)	(0.52,-0.70)	(0.44,-0.31)	(0.76,-0.28)	(-0.03,-0.74)	(0.68,-0.68)	(0.59,-0.10)
JET_GroupedNP_1	(-0.15,0.32)	(-3.10,1.81)	(-0.63,2.35)	(-2.93,2.30)	(-2.67,2.43)	(-1.49,2.18)	(-3.23,2.57)	(-0.65,1.96)	(-1.80,1.84)	(-2.58,2.52)
JET_GroupedNP_2	(-1.39,1.64)	(-1.84,1.71)	(-1.72,1.99)	(-2.31,1.80)	(-2.53,2.73)	(-2.28,2.30)	(-3.49,3.77)	(-2.37,2.76)	(-3.61,3.87)	(-5.31,5.33)
JET_GroupedNP_3	(-0.28,0.39)	(-0.77,0.60)	(-0.67,1.08)	(-1.26,0.88)	(-1.15,1.00)	(-0.71,0.84)	(-1.35,1.15)	(-0.47,1.82)	(-1.16,1.34)	(-1.17,1.67)
JET_JER_SINGLE_NP	(0.02,-0.02)	(-0.70,0.70)	(-0.86,0.86)	(0.05,-0.05)	(-0.52,0.52)	(-0.71,0.71)	(-0.77,0.77)	(0.53,-0.53)	(1.10,-1.10)	(-1.92,1.93)
MET_SoftTrk_ResoPara	(0.06,-0.06)	(0.43,-0.43)	(0.40,-0.40)	(0.11,-0.11)	(0.12,-0.12)	(0.13,-0.13)	(0.40,-0.40)	(-0.48,0.48)	(-0.01,0.01)	(0.05,-0.05)
MET_SoftTrk_ResoPerp	(0.04,-0.04)	(0.34,-0.34)	(0.31,-0.31)	(0.29,-0.29)	(0.24,-0.24)	(0.02,-0.02)	(0.37,-0.37)	(-0.03,0.03)	(0.33,-0.33)	(0.05,-0.05)
MET_SoftTrk_Scale	(0.09,0.03)	(0.16,-0.32)	(0.61,-0.34)	(0.17,-0.33)	(0.25,-0.21)	(0.08,-0.21)	(0.61,-0.20)	(-0.08,0.02)	(0.45,-0.15)	(0.16,-0.25)
MUON_BADMUON_STAT	(0.00,0.00)	(0.00,0.00)	(0.00,0.00)	(0.00,0.00)	(0.00,0.00)	(0.00,0.00)	(0.00,0.00)	(0.00,0.00)	(0.00,0.00)	(0.00,0.00)
MUON_BADMUON_SYS	(0.00,0.00)	(0.00,0.00)	(0.00,0.00)	(0.00,0.00)	(0.00,0.00)	(0.00,0.00)	(0.00,0.00)	(0.00,0.00)	(0.00,0.00)	(0.00,0.00)
MUON_EFF_STAT	(0.03,-0.03)	(0.04,-0.04)	(0.04,-0.04)	(0.03,-0.03)	(0.04,-0.04)	(0.04,-0.04)	(0.04,-0.04)	(0.03,-0.03)	(0.03,-0.03)	(0.04,-0.04)
MUON_EFF_STAT_LOWPT	(0.00,0.00)	(0.00,0.00)	(0.00,0.00)	(0.00,0.00)	(0.00,0.00)	(0.00,0.00)	(0.00,0.00)	(0.00,0.00)	(0.00,0.00)	(0.00,0.00)
MUON_EFF_SYS	(0.15,-0.15)	(0.16,-0.16)	(0.19,-0.19)	(0.19,-0.19)	(0.23,-0.23)	(0.22,-0.22)	(0.23,-0.23)	(0.18,-0.18)	(0.22,-0.22)	(0.29,-0.30)
MUON_EFF_SYS_LOWPT	(0.00,0.00)	(0.00,0.00)	(0.00,0.00)	(0.00,0.00)	(0.00,0.00)	(0.00,0.00)	(0.00,0.00)	(0.00,0.00)	(0.00,0.00)	(0.00,0.00)
MUON_ID	(0.00,0.00)	(0.00,0.00)	(0.00,0.01)	(0.00,-0.01)	(0.00,0.01)	(0.02,-0.03)	(-0.01,0.01)	(-0.01,0.02)	(0.00,0.00)	(0.00,0.05)
MUON_MS	(0.00,0.00)	(0.00,0.00)	(0.01,-0.01)	(0.00,0.00)	(0.00,0.00)	(0.02,-0.03)	(-0.03,0.04)	(0.01,0.04)	(0.00,-0.01)	(0.00,0.00)
MUON_SAGITTA_RESBIAS	(0.00,0.00)	(0.00,0.00)	(0.00,0.00)	(0.00,0.00)	(0.00,0.00)	(0.00,0.00)	(0.00,0.00)	(0.00,0.00)	(0.00,0.00)	(0.00,0.00)
MUON_SAGITTA_RHO	(0.00,0.00)	(0.00,0.00)	(0.00,0.00)	(0.00,0.00)	(0.00,0.00)	(0.00,0.00)	(0.00,0.00)	(0.00,0.00)	(0.00,0.00)	(0.00,0.00)
MUON_SCALE	(-0.01,0.00)	(0.00,0.00)	(0.00,0.00)	(0.00,0.00)	(0.00,0.00)	(0.00,0.00)	(-0.02,0.02)	(0.03,-0.03)	(0.00,0.00)	(0.00,0.00)
MUON_TTVA_STAT	(0.00,0.00)	(0.00,0.00)	(0.00,0.00)	(0.00,0.00)	(0.00,0.00)	(0.00,0.00)	(0.00,0.00)	(0.00,0.00)	(0.00,0.00)	(0.00,0.00)
MUON_TTVA_SYS	(0.00,0.00)	(0.00,0.00)	(0.00,0.00)	(0.00,0.00)	(0.00,0.00)	(0.00,0.00)	(0.00,0.00)	(0.00,0.00)	(0.00,0.00)	(0.00,0.00)
PRW_DATASF	(-0.08,0.20)	(-0.03,0.06)	(-1.02,0.94)	(-0.48,0.46)	(0.16,-0.43)	(0.09,0.05)	(0.86,0.09)	(-1.43,2.07)	(-0.24,0.19)	(-1.07,1.12)
top_Sys	(-1.06,1.06)	(-1.05,1.05)	(-1.18,1.18)	(-1.19,1.19)	(-1.15,1.15)	(-0.93,0.93)	(-1.09,1.09)	(-0.81,0.81)	(-0.79,0.79)	(-1.21,1.21)
vjets_QCDSmoothing	(-0.34,0.32)	(-0.33,0.37)	(-0.36,0.36)	(-0.39,0.41)	(-0.45,0.43)	(-0.49,0.48)	(-0.56,0.56)	(-0.67,0.67)	(-1.54,1.55)	(-9.05,9.05)
vjets_d1K_NLO	(-7.00,6.88)	(-7.23,7.29)	(-7.54,7.51)	(-7.73,7.64)	(-7.94,7.92)	(-8.20,8.18)	(-8.41,8.41)	(-8.61,8.62)	(-8.95,8.95)	(-9.05,9.05)
vjets_d1kappa_EW	(0.00,0.00)	(0.00,0.00)	(-0.02,0.02)	(-0.12,0.08)	(-0.17,0.17)	(-0.26,0.25)	(-0.38,0.38)	(-0.52,0.52)	(-0.71,0.71)	(-1.02,1.03)
vjets_d2K_NLO	(5.06,-5.22)	(4.81,-4.73)	(4.10,-4.12)	(3.23,-3.29)	(1.92,-1.94)	(0.58,-0.58)	(-0.68,0.68)	(-1.85,1.85)	(-2.93,2.92)	(-4.16,4.16)
vjets_d2kappa_EW_eej	(-0.15,0.14)	(-0.19,0.24)	(-0.28,0.29)	(-0.38,0.39)	(-0.51,0.47)	(-0.63,0.63)	(-0.75,0.75)	(-0.90,0.90)	(-0.98,0.98)	(-1.16,1.16)
vjets_d2kappa_EW_evj	(-0.20,0.20)	(-0.22,0.22)	(-0.25,0.24)	(-0.26,0.26)	(-0.28,0.28)	(-0.29,0.29)	(-0.31,0.31)	(-0.30,0.30)	(-0.38,0.38)	(-0.39,0.39)
vjets_d3K_NLO	(-0.52,0.52)	(-0.44,0.43)	(-0.43,0.42)	(-0.41,0.39)	(-0.41,0.41)	(-0.37,0.36)	(-0.40,0.40)	(-0.42,0.42)	(-0.45,0.44)	(-0.45,0.45)
vjets_d3kappa_EW_eej	(-0.13,0.10)	(-0.15,0.19)	(-0.22,0.22)	(-0.31,0.33)	(-0.44,0.41)	(-0.57,0.57)	(-0.71,0.71)	(-0.91,0.91)	(-1.02,1.02)	(-1.25,1.25)
vjets_d3kappa_EW_evj	(0.00,0.00)	(0.00,0.00)	(-0.02,0.02)	(-0.04,0.05)	(-0.06,0.06)	(-0.08,0.08)	(-0.10,0.10)	(-0.11,0.11)	(-0.14,0.14)	(-0.14,0.14)
vjets_dK_NLO_mix	(-0.24,0.21)	(-0.27,0.30)	(-0.34,0.33)	(-0.40,0.41)	(-0.50,0.48)	(-0.57,0.56)	(-0.65,0.65)	(-0.72,0.73)	(-0.83,0.82)	(-0.93,0.93)

Table B.1: Breakdown of the systematic uncertainties on the background estimates before the fit in the SR. The percentages show the size of the uncertainty relative to the total expected background, when varying the nuisance parameter by -1σ and $+1\sigma$.

CR1mu0b	BIN_250	BIN_300	BIN_350	BIN_400	BIN_500	BIN_600	BIN_700	BIN_800	BIN_900	BIN_1000
NCB_Sys	(0.00,0.00)	(0.00,0.00)	(0.00,0.00)	(0.00,0.00)	(0.00,0.00)	(0.00,0.00)	(0.00,0.00)	(0.00,0.00)	(0.00,0.00)	(0.00,0.00)
PDFcomb	(-1.40,1.40)	(-1.66,1.66)	(-1.62,1.62)	(-1.92,1.92)	(-2.25,2.25)	(-3.45,3.45)	(-2.92,2.92)	(-3.91,3.91)	(-4.09,4.09)	(-5.91,5.91)
ckkw	(0.00,0.00)	(0.00,0.00)	(0.00,0.00)	(0.00,0.00)	(0.00,0.00)	(0.00,0.00)	(0.00,0.00)	(0.00,0.00)	(0.00,0.00)	(0.00,0.00)
diboson_Sys	(-0.15,0.15)	(-0.20,0.20)	(-0.26,0.26)	(-0.32,0.32)	(-0.37,0.37)	(-0.49,0.49)	(-0.46,0.46)	(-0.49,0.49)	(-0.56,0.56)	(-0.59,0.59)
lumiSys	(-3.20,3.20)	(-3.20,3.20)	(-3.20,3.20)	(-3.20,3.20)	(-3.20,3.20)	(-3.20,3.20)	(-3.20,3.20)	(-3.20,3.20)	(-3.20,3.20)	(-3.20,3.20)
multijet_Sys	(0.00,0.00)	(0.00,0.00)	(0.00,0.00)	(0.00,0.00)	(0.00,0.00)	(0.00,0.00)	(0.00,0.00)	(0.00,0.00)	(0.00,0.00)	(0.00,0.00)
EG_RESOLUTION_ALL	(-0.00,0.00)	(0.00,0.00)	(-0.00,0.00)	(-0.01,0.01)	(0.00,0.00)	(0.00,-0.00)	(0.00,0.00)	(0.00,0.00)	(0.00,0.00)	(0.00,0.00)
EG_SCALE_ALL	(0.01,-0.00)	(0.00,0.00)	(0.00,-0.00)	(-0.01,0.01)	(0.00,0.00)	(0.00,-0.00)	(0.05,-0.05)	(0.00,0.00)	(0.00,0.00)	(0.00,0.00)
EL_EFF_ID_TOTAL	(0.04,-0.04)	(0.05,-0.05)	(0.06,-0.06)	(0.07,-0.07)	(0.07,-0.07)	(0.08,-0.08)	(0.09,-0.09)	(0.08,-0.08)	(0.08,-0.08)	(0.10,-0.10)
EL_EFF_Iso_TOTAL	(0.00,0.00)	(0.00,0.00)	(0.00,0.00)	(0.00,0.00)	(-0.00,0.00)	(0.00,0.00)	(0.00,0.00)	(0.00,0.00)	(0.00,0.00)	(0.00,0.00)
EL_EFF_Reco_TOTAL	(0.00,-0.00)	(0.00,-0.00)	(0.00,-0.00)	(0.00,0.00)	(0.00,0.00)	(0.00,0.00)	(0.01,-0.01)	(0.01,-0.01)	(0.00,-0.00)	(0.02,-0.02)
EL_EFF_TriggerEff_TOTAL	(0.00,0.00)	(0.00,0.00)	(0.00,0.00)	(0.00,0.00)	(-0.00,0.00)	(0.00,0.00)	(0.00,0.00)	(0.00,0.00)	(0.00,0.00)	(0.00,0.00)
EL_EFF_Trigger_TOTAL	(0.00,0.00)	(0.00,0.00)	(0.00,0.00)	(0.00,0.00)	(-0.00,0.00)	(0.00,0.00)	(0.00,0.00)	(0.00,0.00)	(0.00,0.00)	(0.00,0.00)
FT_EFF_B_systematics	(0.25,-0.25)	(0.28,-0.28)	(0.43,-0.42)	(0.44,-0.43)	(0.40,-0.39)	(0.43,-0.42)	(0.51,-0.50)	(0.44,-0.43)	(0.47,-0.46)	(0.50,-0.49)
FT_EFF_C_systematics	(0.69,-0.69)	(0.76,-0.76)	(0.84,-0.83)	(0.87,-0.86)	(0.93,-0.92)	(1.05,-1.04)	(1.01,-1.00)	(0.97,-0.97)	(1.08,-1.07)	(1.04,-1.03)
FT_EFF_Light_systematics	(0.00,0.00)	(0.00,-0.00)	(0.00,0.00)	(0.00,0.00)	(0.00,0.00)	(0.11,-0.11)	(0.12,-0.12)	(0.12,-0.12)	(0.13,-0.13)	(0.13,-0.13)
FT_EFF_extrapolation	(0.02,-0.02)	(0.03,-0.03)	(0.04,-0.04)	(0.06,-0.06)	(0.08,-0.08)	(0.21,-0.21)	(0.32,-0.32)	(0.44,-0.44)	(0.60,-0.60)	(0.83,-0.83)
FT_EFF_extrapolation_from_charm	(0.00,0.00)	(0.00,0.00)	(0.00,0.00)	(0.00,0.00)	(0.00,0.00)	(0.00,0.00)	(0.00,0.00)	(0.00,0.00)	(0.00,0.00)	(0.00,0.00)
JET_EtaIntercalibration_NonClosure	(0.85,-0.73)	(0.88,-0.72)	(0.64,-1.16)	(0.44,-0.18)	(0.75,-0.68)	(0.15,-0.55)	(0.01,-0.37)	(1.18,-1.66)	(0.12,0.36)	(-0.14,-0.82)
JET_GroupedNP_1	(-0.09,0.19)	(-1.95,1.41)	(-2.83,3.30)	(-2.52,2.20)	(-2.16,2.61)	(-3.68,2.26)	(-2.17,1.85)	(-2.09,-1.47)	(-2.39,3.32)	(-3.24,1.96)
JET_GroupedNP_2	(-1.58,1.53)	(-1.57,1.64)	(-2.19,1.96)	(-1.83,2.13)	(-2.30,3.02)	(-3.83,2.32)	(-2.08,3.25)	(-3.43,1.63)	(-5.21,4.65)	(-5.04,4.56)
JET_GroupedNP_3	(-0.24,-0.01)	(-0.40,0.65)	(-1.20,1.02)	(-0.83,1.10)	(-0.65,1.10)	(-1.11,0.84)	(-1.47,1.29)	(-1.22,0.12)	(-0.49,2.32)	(-1.75,0.57)
JET_JER_SINGLE_NP	(0.19,-0.19)	(-0.04,0.04)	(-0.27,0.27)	(0.25,-0.25)	(0.06,-0.06)	(-0.76,0.76)	(0.56,-0.56)	(2.84,-2.84)	(-2.39,2.39)	(3.20,-3.20)
MET_SoftTrk_ResoPara	(-0.47,0.47)	(-0.43,0.43)	(0.15,-0.15)	(-0.43,0.43)	(-0.31,0.32)	(0.05,-0.05)	(1.00,-1.00)	(-0.34,0.34)	(-1.12,1.12)	(0.11,-0.11)
MET_SoftTrk_ResoPerp	(-0.25,0.25)	(-0.29,0.29)	(0.31,-0.31)	(-0.28,0.28)	(-0.50,0.50)	(0.33,-0.33)	(-0.73,0.73)	(-0.84,0.84)	(-0.75,0.75)	(0.80,-0.80)
MET_SoftTrk_Scale	(-0.64,0.43)	(0.03,0.26)	(0.07,-0.05)	(-0.10,0.34)	(-0.19,0.55)	(-1.10,-0.48)	(0.19,0.19)	(-0.30,0.71)	(0.70,-0.20)	(-0.63,-0.02)
MUON_BADMUON_STAT	(0.00,-0.00)	(0.00,-0.00)	(0.00,-0.00)	(0.00,-0.00)	(0.01,-0.01)	(0.00,-0.00)	(0.02,-0.02)	(0.01,-0.01)	(0.01,-0.01)	(0.04,-0.04)
MUON_BADMUON_SYS	(0.00,-0.00)	(0.00,-0.00)	(0.00,-0.00)	(0.00,-0.00)	(0.01,-0.01)	(0.00,-0.00)	(0.02,-0.02)	(0.01,-0.01)	(0.01,-0.01)	(0.04,-0.04)
MUON_EFF_STAT	(-0.26,0.11)	(-0.26,0.11)	(-0.26,0.12)	(-0.26,0.12)	(-0.28,0.10)	(-0.26,0.12)	(-0.29,0.11)	(-0.28,0.12)	(-0.28,0.12)	(-0.32,0.13)
MUON_EFF_STAT_LOWPT	(-0.00,0.00)	(-0.00,-0.00)	(-0.01,-0.01)	(-0.00,-0.00)	(-0.01,-0.01)	(-0.00,-0.00)	(-0.03,-0.02)	(-0.01,-0.01)	(0.01,-0.01)	(-0.01,-0.04)
MUON_EFF_SYS	(-1.18,1.04)	(-1.27,1.13)	(-1.34,1.20)	(-1.42,1.28)	(-1.53,1.37)	(-1.62,1.50)	(-1.72,1.56)	(-1.78,1.63)	(-1.82,1.68)	(-2.05,1.88)
MUON_EFF_SYS_LOWPT	(-0.01,-0.00)	(-0.00,-0.00)	(-0.01,-0.01)	(-0.00,-0.00)	(-0.01,-0.01)	(-0.01,-0.01)	(-0.03,-0.02)	(-0.01,-0.01)	(0.01,-0.01)	(-0.01,-0.04)
MUON_ID	(0.32,0.08)	(0.23,-0.10)	(0.09,-0.05)	(0.21,-0.35)	(0.12,-0.02)	(-0.12,-0.33)	(0.50,0.02)	(0.80,-0.29)	(2.91,-0.08)	(-0.16,-0.46)
MUON_MS	(-0.02,-0.01)	(0.07,-0.15)	(0.10,-0.12)	(0.10,-0.08)	(-0.04,-0.14)	(-0.02,-0.23)	(0.22,0.03)	(-0.09,-0.12)	(0.28,-0.17)	(-0.33,-0.30)
MUON_SAGITTA_RESBIAS	(0.00,-0.00)	(0.00,-0.00)	(0.00,-0.00)	(0.00,-0.00)	(0.01,-0.01)	(0.00,-0.00)	(0.02,-0.02)	(0.01,-0.01)	(0.01,-0.01)	(0.04,-0.04)
MUON_SAGITTA_RHO	(0.00,-0.00)	(0.00,-0.00)	(0.00,-0.00)	(0.00,-0.00)	(0.01,-0.01)	(0.00,-0.00)	(0.02,-0.02)	(0.01,-0.01)	(0.01,-0.01)	(0.04,-0.04)
MUON_SCALE	(-0.00,-0.01)	(-0.00,-0.01)	(-0.01,-0.01)	(-0.01,0.01)	(-0.14,-0.02)	(-0.03,0.00)	(-0.15,0.04)	(-0.01,-0.01)	(0.00,-0.02)	(-0.12,-0.10)
MUON_TTVA_STAT	(-0.19,0.04)	(-0.18,0.03)	(-0.18,0.03)	(-0.18,0.03)	(-0.19,0.01)	(-0.16,0.03)	(-0.18,0.01)	(-0.18,0.01)	(-0.17,0.01)	(-0.19,-0.00)
MUON_TTVA_SYS	(-0.14,-0.01)	(-0.14,-0.01)	(-0.14,-0.00)	(-0.15,-0.00)	(-0.16,-0.01)	(-0.15,0.02)	(-0.18,0.00)	(-0.17,0.01)	(-0.19,0.03)	(-0.20,0.01)
PRW_DATASF	(1.02,-1.09)	(0.85,-0.90)	(0.59,-0.49)	(0.33,-0.29)	(0.63,-1.20)	(-0.89,-0.65)	(0.37,-0.98)	(-0.18,-1.64)	(-3.99,-0.76)	(-0.02,1.11)
top_Sys	(-1.05,1.05)	(-1.29,1.29)	(-1.56,1.56)	(-1.80,1.80)	(-1.91,1.91)	(-2.33,2.33)	(-3.16,3.16)	(-2.73,2.73)	(-2.53,2.53)	(-4.98,4.98)
vjets_QCDSmoothing	(-0.37,0.38)	(-0.39,0.39)	(-0.41,0.40)	(-0.43,0.43)	(-0.48,0.48)	(-0.56,0.56)	(-0.71,0.71)	(-0.96,0.96)	(-1.84,1.85)	(-8.44,8.44)
vjets_d1K_NLO	(-7.15,7.18)	(-7.34,7.38)	(-7.43,7.42)	(-7.54,7.54)	(-7.76,7.76)	(-7.78,7.78)	(-7.93,7.93)	(-8.23,8.23)	(-8.44,8.44)	(-8.50,8.50)
vjets_d1kappa_EW	(0.00,0.00)	(-0.01,0.01)	(-0.01,0.01)	(-0.12,0.12)	(-0.21,0.21)	(-0.32,0.32)	(-0.46,0.46)	(-0.64,0.64)	(-0.84,0.84)	(-1.19,1.19)
vjets_d2K_NLO	(5.38,-5.36)	(4.82,-4.81)	(4.10,-4.10)	(3.16,-3.16)	(1.84,-1.84)	(0.50,-0.50)	(-0.74,0.74)	(-1.85,1.85)	(-2.78,2.78)	(-3.93,3.93)
vjets_d2kappa_EW_eej	(-0.01,0.01)	(-0.01,0.01)	(-0.01,0.01)	(-0.01,0.01)	(-0.01,0.01)	(-0.01,0.01)	(-0.02,0.02)	(-0.02,0.02)	(-0.02,0.02)	(-0.02,0.02)
vjets_d2kappa_EW_evj	(-0.43,0.43)	(-0.54,0.54)	(-0.62,0.62)	(-0.74,0.74)	(-0.89,0.89)	(-1.03,1.03)	(-1.18,1.18)	(-1.34,1.34)	(-1.49,1.49)	(-1.68,1.68)
vjets_d3K_NLO	(-1.16,1.17)	(-1.09,1.09)	(-0.98,0.98)	(-0.92,0.92)	(-0.87,0.87)	(-0.69,0.69)	(-0.65,0.66)	(-0.58,0.58)	(-0.60,0.60)	(-0.64,0.64)
vjets_d3kappa_EW_eej	(-0.00,0.00)	(-0.00,0.00)	(-0.00,0.00)	(-0.00,0.00)	(-0.01,0.01)	(-0.01,0.01)	(-0.01,0.01)	(-0.02,0.02)	(-0.02,0.02)	(-0.03,0.03)
vjets_d3kappa_EW_evj	(0.00,0.00)	(-0.01,0.01)	(-0.01,0.01)	(-0.13,0.13)	(-0.20,0.20)	(-0.27,0.27)	(-0.36,0.36)	(-0.48,0.48)	(-0.53,0.53)	(-0.59,0.60)
vjets_dK_NLO_mix	(-0.29,0.29)	(-0.36,0.36)	(-0.41,0.41)	(-0.48,0.48)	(-0.58,0.58)	(-0.65,0.66)	(-0.74,0.74)	(-0.84,0.84)	(-0.93,0.93)	(-1.04,1.04)

Table B.2: Breakdown of the systematic uncertainties on the background estimates before the fit in the CR1mu0b. The percentages show the size of the uncertainty relative to the total expected background, when varying the nuisance parameter by -1σ and $+1\sigma$.

CR1mu1b	BIN_250	BIN_300	BIN_350	BIN_400	BIN_500	BIN_600	BIN_700	BIN_800	BIN_900	BIN_1000
NCB_Sys	(0.00,0.00)	(0.00,0.00)	(0.00,0.00)	(0.00,0.00)	(0.00,0.00)	(0.00,0.00)	(0.00,0.00)	(0.00,0.00)	(0.00,0.00)	(0.00,0.00)
PDFcomb	(-0.34,0.34)	(-0.43,0.43)	(-0.41,0.41)	(-0.51,0.51)	(-0.69,0.69)	(-1.37,1.37)	(-1.24,1.24)	(-2.07,2.07)	(-2.39,2.39)	(-2.88,2.88)
ckkw	(0.00,0.00)	(0.00,0.00)	(0.00,0.00)	(0.00,0.00)	(0.00,0.00)	(0.00,0.00)	(0.00,0.00)	(0.00,0.00)	(0.00,0.00)	(0.00,0.00)
diboson_Sys	(-0.06,0.06)	(-0.08,0.08)	(-0.09,0.09)	(-0.17,0.17)	(-0.18,0.18)	(-0.31,0.31)	(-0.30,0.30)	(-0.73,0.73)	(-0.71,0.71)	(0.00,0.00)
lumiSys	(-3.20,3.20)	(-3.20,3.20)	(-3.20,3.20)	(-3.20,3.20)	(-3.20,3.20)	(-3.20,3.20)	(-3.20,3.20)	(-3.20,3.20)	(-3.18,3.18)	(-3.20,3.20)
multijet_Sys	(0.00,0.00)	(0.00,0.00)	(0.00,0.00)	(0.00,0.00)	(0.00,0.00)	(0.00,0.00)	(0.00,0.00)	(0.00,0.00)	(0.00,0.00)	(0.00,0.00)
EG_RESOLUTION_ALL	(-0.00,0.01)	(0.00,-0.00)	(0.00,0.00)	(0.00,0.00)	(0.17,0.06)	(-0.18,0.18)	(0.01,-0.01)	(0.00,0.00)	(0.00,0.00)	(0.00,0.00)
EG_SCALE_ALL	(0.00,0.00)	(0.00,0.00)	(0.00,0.00)	(0.00,0.00)	(-0.00,0.00)	(0.00,0.00)	(-0.01,0.01)	(0.00,0.00)	(0.00,0.00)	(0.00,0.00)
EL_EFF_ID_TOTAL	(0.37,-0.37)	(0.37,-0.37)	(0.38,-0.39)	(0.39,-0.39)	(0.38,-0.38)	(0.34,-0.35)	(0.35,-0.35)	(0.30,-0.30)	(0.24,-0.24)	(0.36,-0.36)
EL_EFF_Iso_TOTAL	(0.00,0.00)	(0.00,0.00)	(0.00,0.00)	(0.00,0.00)	(0.00,0.00)	(0.00,0.00)	(0.00,0.00)	(0.00,0.00)	(0.00,0.00)	(0.00,0.00)
EL_EFF_Reco_TOTAL	(0.00,0.00)	(0.00,-0.00)	(0.00,0.00)	(0.00,0.00)	(0.00,-0.00)	(0.00,-0.00)	(0.06,-0.06)	(0.05,-0.05)	(0.00,-0.00)	(0.07,-0.07)
EL_EFF_TriggerEff_TOTAL	(0.00,0.00)	(0.00,0.00)	(0.00,0.00)	(0.00,0.00)	(0.00,0.00)	(0.00,0.00)	(0.00,0.00)	(0.00,0.00)	(0.00,0.00)	(0.00,0.00)
EL_EFF_Trigger_TOTAL	(0.00,0.00)	(0.00,0.00)	(0.00,0.00)	(0.00,0.00)	(0.00,0.00)	(0.00,0.00)	(0.00,0.00)	(0.00,0.00)	(0.00,0.00)	(0.00,0.00)
FT_EFF_B_systematics	(-3.27,3.19)	(-3.44,3.37)	(-3.56,3.49)	(-3.46,3.39)	(-3.53,3.46)	(-3.34,3.25)	(-3.79,3.76)	(-2.92,2.78)	(-2.70,2.59)	(-3.14,3.09)
FT_EFF_C_systematics	(-7.97,7.93)	(-8.15,8.11)	(-5.34,5.28)	(-6.71,6.69)	(-4.19,4.41)	(-5.79,5.75)	(-7.89,7.83)	(-10.09,10.07)	(-14.61,14.32)	(-5.18,5.03)
FT_EFF_Light_systematics	(-0.81,0.81)	(-0.86,0.86)	(-0.72,0.72)	(-0.69,0.69)	(-0.84,0.84)	(-1.27,1.27)	(-0.26,0.26)	(-1.11,1.11)	(-2.10,2.10)	(-1.86,1.86)
FT_EFF_extrapolation	(-0.50,0.50)	(-0.67,0.67)	(-0.67,0.67)	(-0.83,0.83)	(-0.93,0.92)	(-1.17,1.17)	(-1.76,1.75)	(-1.66,1.65)	(-1.89,1.88)	(-0.95,0.95)
FT_EFF_extrapolation_from_charm	(-0.00,0.00)	(0.00,0.00)	(0.00,0.00)	(0.00,0.00)	(0.00,0.00)	(0.00,0.00)	(0.00,0.00)	(0.00,0.00)	(0.00,0.00)	(0.00,0.00)
JET_EtaIntercalibration_NonClosure	(0.10,-0.78)	(0.88,-0.88)	(0.69,-0.41)	(0.29,-0.71)	(1.28,-0.02)	(-1.93,-0.58)	(-0.51,1.40)	(2.46,5.65)	(0.91,-11.46)	(0.43,-0.20)
JET_GroupedNP_1	(-0.05,-0.93)	(-0.10,0.85)	(-0.76,0.32)	(-1.82,1.33)	(-3.93,3.90)	(-5.82,0.98)	(-0.94,0.35)	(10.37,18.49)	(-7.79,2.52)	(-0.90,-4.29)
JET_GroupedNP_2	(-1.50,0.85)	(-1.57,1.70)	(-1.29,2.31)	(-2.69,2.55)	(-2.52,3.26)	(-3.06,2.61)	(-2.71,2.20)	(3.82,8.21)	(-15.85,11.57)	(-0.58,1.36)
JET_GroupedNP_3	(-0.28,-0.26)	(-0.23,0.35)	(0.01,1.04)	(-1.07,0.20)	(-0.62,4.92)	(-2.52,0.45)	(0.91,2.64)	(2.92,-0.79)	(-8.76,11.88)	(-4.60,-12.19)
JET_JER_SINGLE_NP	(-0.29,0.29)	(-0.81,0.81)	(2.65,-2.65)	(1.28,-1.28)	(-0.72,0.72)	(6.04,-6.04)	(0.59,-0.59)	(-12.96,12.97)	(-22.36,22.55)	(10.03,-9.94)
MET_SoftTrk_ResoPara	(-0.21,0.21)	(0.12,-0.12)	(-0.08,0.08)	(-0.55,0.55)	(-0.54,0.54)	(-0.01,0.01)	(-0.91,0.91)	(-7.50,7.50)	(5.86,-5.86)	(0.12,-0.12)
MET_SoftTrk_ResoPerp	(-0.28,0.28)	(-0.09,0.09)	(-0.15,0.15)	(0.06,-0.06)	(1.04,-1.04)	(0.97,-0.97)	(-2.98,2.98)	(-4.40,4.40)	(-0.98,0.98)	(-0.16,0.21)
MET_SoftTrk_Scale	(-0.78,0.25)	(0.01,-0.15)	(0.09,0.37)	(-0.03,-0.14)	(0.04,-0.45)	(1.05,-0.24)	(-1.22,0.06)	(1.95,-0.59)	(0.19,-4.41)	(-0.20,0.36)
MUON_BADMUON_STAT	(0.00,-0.00)	(0.00,-0.00)	(0.02,-0.02)	(-0.00,0.00)	(0.00,0.00)	(0.09,-0.09)	(0.15,-0.15)	(0.09,-0.09)	(0.12,-0.12)	(0.19,-0.19)
MUON_BADMUON_SYS	(0.00,-0.00)	(0.00,-0.00)	(0.02,-0.02)	(-0.00,0.00)	(0.00,0.00)	(0.09,-0.09)	(0.15,-0.15)	(0.09,-0.09)	(0.12,-0.12)	(0.19,-0.19)
MUON_EFF_STAT	(-0.27,0.11)	(-0.28,0.10)	(-0.27,0.10)	(-0.27,0.12)	(-0.27,0.14)	(-0.32,0.07)	(-0.33,0.03)	(-0.28,0.14)	(-0.31,0.06)	(-0.42,-0.02)
MUON_EFF_STAT_LOWPT	(-0.00,-0.00)	(-0.01,-0.00)	(-0.03,-0.02)	(-0.00,-0.00)	(0.00,0.00)	(-0.13,-0.12)	(-0.13,-0.15)	(-0.09,-0.08)	(0.12,-0.12)	(0.18,-0.19)
MUON_EFF_SYS	(-1.08,0.92)	(-1.21,1.04)	(-1.31,1.15)	(-1.42,1.28)	(-1.56,1.44)	(-1.73,1.49)	(-1.84,1.55)	(-1.75,1.63)	(-1.90,1.66)	(-2.27,1.85)
MUON_EFF_SYS_LOWPT	(-0.00,-0.00)	(-0.08,-0.06)	(-0.03,-0.02)	(-0.00,-0.00)	(-0.00,0.00)	(-0.14,-0.11)	(-0.13,-0.15)	(-0.09,-0.08)	(0.12,-0.12)	(0.18,-0.19)
MUON_ID	(0.09,-0.26)	(-0.04,0.05)	(-0.15,-0.23)	(-0.22,-0.53)	(-0.35,-0.10)	(0.18,-0.00)	(-2.10,-0.54)	(0.02,0.05)	(5.78,1.64)	(0.35,0.13)
MUON_MS	(-0.13,-0.04)	(-0.04,-0.03)	(0.12,-0.18)	(-0.26,-0.27)	(-0.59,-0.27)	(-0.24,-0.16)	(-0.80,-0.70)	(0.53,-0.09)	(0.21,1.70)	(-0.26,-0.22)
MUON_SAGITTA_RESBIAS	(0.00,-0.00)	(0.00,-0.00)	(0.02,-0.02)	(-0.00,0.00)	(0.00,0.00)	(0.09,-0.09)	(0.15,-0.15)	(0.09,-0.09)	(0.12,-0.12)	(0.19,-0.19)
MUON_SAGITTA_RHO	(0.00,-0.00)	(0.00,-0.00)	(0.02,-0.02)	(-0.00,0.00)	(0.00,0.00)	(0.09,-0.09)	(0.15,-0.15)	(0.09,-0.09)	(0.12,-0.12)	(0.19,-0.19)
MUON_SCALE	(-0.11,-0.10)	(-0.11,0.00)	(-0.09,0.04)	(-0.12,-0.04)	(-0.22,0.07)	(0.07,-0.09)	(0.08,-0.30)	(0.12,-0.16)	(0.21,-0.12)	(-0.07,-0.22)
MUON_TTVA_STAT	(-0.19,0.03)	(-0.19,0.02)	(-0.19,0.02)	(-0.17,0.02)	(-0.16,0.02)	(-0.22,-0.03)	(-0.25,-0.06)	(-0.17,0.03)	(-0.22,-0.03)	(-0.32,-0.13)
MUON_TTVA_SYS	(-0.16,0.00)	(-0.17,-0.00)	(-0.17,0.00)	(-0.16,0.01)	(-0.16,0.02)	(-0.22,-0.03)	(-0.26,-0.04)	(-0.17,0.04)	(-0.23,-0.01)	(-0.32,-0.12)
PRW_DATASF	(0.50,-0.94)	(1.09,-1.85)	(0.71,-1.26)	(1.71,-2.02)	(0.36,-1.88)	(0.29,-1.36)	(0.23,2.44)	(2.34,-4.48)	(0.49,0.73)	(7.36,15.49)
top_Sys	(-18.28,18.28)	(-19.42,19.42)	(-21.23,21.23)	(-22.97,22.97)	(-25.56,25.56)	(-26.25,26.25)	(-28.66,28.66)	(-25.78,25.78)	(-24.28,24.28)	(-42.86,42.86)
vjets_QCDSmoothing	(-0.09,0.09)	(-0.10,0.10)	(-0.10,0.10)	(-0.12,0.12)	(-0.15,0.15)	(-0.23,0.22)	(-0.29,0.29)	(-0.58,0.58)	(-0.76,0.76)	(-4.05,4.05)
vjets_d1K_NLO	(-1.76,1.76)	(-1.93,1.93)	(-1.89,1.89)	(-2.01,2.01)	(-2.37,2.37)	(-3.12,3.12)	(-3.38,3.38)	(-4.35,4.35)	(-5.18,5.18)	(-4.08,4.08)
vjets_d1kappa_EW	(0.00,0.00)	(-0.00,0.00)	(-0.00,0.00)	(-0.03,0.03)	(-0.07,0.07)	(-0.14,0.14)	(-0.20,0.20)	(-0.35,0.35)	(-0.50,0.50)	(-0.58,0.58)
vjets_d2K_NLO	(1.30,-1.30)	(1.25,-1.25)	(1.03,-1.03)	(0.82,-0.82)	(0.54,-0.54)	(0.13,-0.13)	(-0.35,0.35)	(-1.01,1.01)	(-1.68,1.68)	(-1.91,1.91)
vjets_d2kappa_EW_eej	(-0.00,0.00)	(-0.00,0.00)	(-0.00,0.00)	(-0.00,0.00)	(-0.00,0.00)	(-0.01,0.01)	(-0.01,0.01)	(-0.01,0.01)	(-0.00,0.00)	(-0.01,0.01)
vjets_d2kappa_EW_evj	(-0.11,0.11)	(-0.14,0.14)	(-0.16,0.16)	(-0.20,0.20)	(-0.27,0.27)	(-0.42,0.42)	(-0.50,0.50)	(-0.72,0.72)	(-0.92,0.92)	(-0.81,0.81)
vjets_d3K_NLO	(-0.28,0.28)	(-0.28,0.28)	(-0.25,0.25)	(-0.24,0.24)	(-0.26,0.26)	(-0.27,0.27)	(-0.27,0.27)	(-0.31,0.31)	(-0.37,0.37)	(-0.31,0.31)
vjets_d3kappa_EW_eej	(-0.00,0.00)	(-0.00,0.00)	(-0.00,0.00)	(-0.00,0.00)	(-0.00,0.00)	(-0.00,0.00)	(-0.01,0.01)	(-0.01,0.01)	(-0.00,0.00)	(-0.01,0.01)
vjets_d3kappa_EW_evj	(0.00,0.00)	(-0.00,0.00)	(-0.00,0.00)	(-0.04,0.04)	(-0.06,0.06)	(-0.11,0.11)	(-0.16,0.16)	(-0.25,0.25)	(-0.33,0.33)	(-0.29,0.29)
vjets_dK_NLO_mix	(-0.07,0.07)	(-0.09,0.09)	(-0.11,0.11)	(-0.13,0.13)	(-0.18,0.18)	(-0.27,0.27)	(-0.32,0.32)	(-0.45,0.45)	(-0.57,0.57)	(-0.50,0.50)

Table B.3: Breakdown of the systematic uncertainties on the background estimates before the fit in the CR1mu1b. The percentages show the size of the uncertainty relative to the total expected background, when varying the nuisance parameter by -1σ and $+1\sigma$.

CR2mu	BIN_250	BIN_300	BIN_350	BIN_400	BIN_500	BIN_600	BIN_700	BIN_800	BIN_900	BIN_1000
NCB_Sys	(0.00,0.00)	(0.00,0.00)	(0.00,0.00)	(0.00,0.00)	(0.00,0.00)	(0.00,0.00)	(0.00,0.00)	(0.00,0.00)	(0.00,0.00)	(0.00,0.00)
PDFcomb	(-1.57,1.57)	(-1.76,1.76)	(-2.01,2.01)	(-2.14,2.14)	(-2.51,2.51)	(-2.93,2.93)	(-3.66,3.66)	(-3.76,3.76)	(-5.04,5.04)	(-4.41,4.41)
ckkw	(0.00,0.00)	(0.00,0.00)	(0.00,0.00)	(0.00,0.00)	(0.00,0.00)	(0.00,0.00)	(0.00,0.00)	(0.00,0.00)	(0.00,0.00)	(0.00,0.00)
diboson_Sys	(-0.17,0.17)	(-0.21,0.21)	(-0.27,0.27)	(-0.30,0.30)	(-0.39,0.39)	(-0.64,0.64)	(-0.50,0.50)	(-0.64,0.63)	(-0.53,0.53)	(-0.75,0.75)
lumiSys	(-3.20,3.20)	(-3.20,3.20)	(-3.20,3.20)	(-3.20,3.20)	(-3.20,3.20)	(-3.20,3.20)	(-3.20,3.20)	(-3.20,3.20)	(-3.15,3.15)	(-3.03,3.03)
multijet_Sys	(0.00,0.00)	(0.00,0.00)	(0.00,0.00)	(0.00,0.00)	(0.00,0.00)	(0.00,0.00)	(0.00,0.00)	(0.00,0.00)	(0.00,0.00)	(0.00,0.00)
EG_RESOLUTION_ALL	(0.00,0.00)	(0.00,0.00)	(0.00,0.00)	(0.00,0.00)	(0.00,0.00)	(0.00,0.00)	(-0.01,0.01)	(0.00,0.00)	(-0.01,0.01)	(0.00,0.00)
EG_SCALE_ALL	(0.00,0.00)	(0.00,0.00)	(0.00,-0.00)	(0.00,0.00)	(0.00,0.00)	(0.00,0.00)	(0.00,0.00)	(0.00,0.00)	(0.00,0.00)	(0.00,0.00)
EL_EFF_ID_TOTAL	(0.04,-0.04)	(0.04,-0.04)	(0.05,-0.05)	(0.05,-0.05)	(0.06,-0.06)	(0.07,-0.07)	(0.06,-0.06)	(0.06,-0.06)	(0.07,-0.07)	(0.07,-0.07)
EL_EFF_Iso_TOTAL	(0.00,0.00)	(0.00,0.00)	(0.00,0.00)	(0.00,0.00)	(0.00,0.00)	(0.00,0.00)	(0.00,0.00)	(0.00,0.00)	(0.00,0.00)	(0.00,0.00)
EL_EFF_Reco_TOTAL	(0.00,-0.00)	(0.00,-0.00)	(0.01,-0.01)	(0.01,-0.01)	(0.01,-0.01)	(0.01,-0.01)	(0.01,-0.01)	(0.01,-0.01)	(0.01,-0.01)	(0.01,-0.01)
EL_EFF_TriggerEff_TOTAL	(0.00,0.00)	(0.00,0.00)	(0.00,0.00)	(0.00,0.00)	(0.00,0.00)	(0.00,0.00)	(0.00,0.00)	(0.00,0.00)	(0.00,0.00)	(0.00,0.00)
EL_EFF_Trigger_TOTAL	(0.00,0.00)	(0.00,0.00)	(0.00,0.00)	(0.00,0.00)	(0.00,0.00)	(0.00,0.00)	(0.00,0.00)	(0.00,0.00)	(0.00,0.00)	(0.00,0.00)
FT_EFF_B_systematics	(0.00,0.00)	(0.00,0.00)	(0.00,0.00)	(0.00,0.00)	(0.00,0.00)	(0.00,0.00)	(0.00,0.00)	(0.00,0.00)	(0.00,0.00)	(0.00,0.00)
FT_EFF_C_systematics	(0.00,0.00)	(0.00,0.00)	(0.00,0.00)	(0.00,0.00)	(0.00,0.00)	(0.00,0.00)	(0.00,0.00)	(0.00,0.00)	(0.00,0.00)	(0.00,0.00)
FT_EFF_Light_systematics	(0.00,0.00)	(0.00,0.00)	(0.00,0.00)	(0.00,0.00)	(0.00,0.00)	(0.00,0.00)	(0.00,0.00)	(0.00,0.00)	(0.00,0.00)	(0.00,0.00)
FT_EFF_extrapolation	(0.00,0.00)	(0.00,0.00)	(0.00,0.00)	(0.00,0.00)	(0.00,0.00)	(0.00,0.00)	(0.00,0.00)	(0.00,0.00)	(0.00,0.00)	(0.00,0.00)
FT_EFF_extrapolation_from_charm	(0.00,0.00)	(0.00,0.00)	(0.00,0.00)	(0.00,0.00)	(0.00,0.00)	(0.00,0.00)	(0.00,0.00)	(0.00,0.00)	(0.00,0.00)	(0.00,0.00)
JET_EtaIntercalibration_NonClosure	(0.68,-0.80)	(0.79,-1.02)	(0.38,-0.31)	(0.57,-0.22)	(0.39,-0.59)	(0.33,-0.15)	(0.56,-0.49)	(0.15,-0.31)	(0.09,0.57)	(0.50,-0.35)
JET_GroupedNP_1	(-0.04,-0.47)	(-2.50,1.77)	(-1.67,2.23)	(-2.52,1.79)	(-2.73,3.27)	(-1.48,0.94)	(-1.13,1.37)	(-4.92,1.03)	(1.06,1.55)	(-2.14,0.53)
JET_GroupedNP_2	(-1.10,1.21)	(-1.93,1.59)	(-1.70,1.88)	(-1.84,1.54)	(-2.13,3.06)	(-2.22,2.15)	(-2.83,3.49)	(-3.60,2.13)	(-3.92,7.14)	(-5.00,4.08)
JET_GroupedNP_3	(-0.19,0.16)	(-0.96,0.59)	(-0.73,0.91)	(-0.38,0.76)	(-0.91,1.24)	(-0.95,0.74)	(-1.20,0.80)	(-0.64,1.23)	(-2.61,0.62)	(-1.20,1.55)
JET_JER_SINGLE_NP	(0.36,-0.36)	(0.02,-0.02)	(-0.08,0.08)	(0.09,-0.09)	(-1.33,1.33)	(0.52,-0.52)	(-1.55,1.55)	(2.45,-2.45)	(-4.35,4.35)	(0.63,-0.63)
MET_SoftTrk_ResoPara	(0.25,-0.25)	(0.37,-0.37)	(-0.24,0.24)	(-0.03,0.03)	(0.13,-0.13)	(-0.93,0.93)	(0.98,-0.98)	(-0.66,0.66)	(-0.04,0.04)	(0.03,-0.03)
MET_SoftTrk_ResoPerp	(0.00,-0.00)	(0.54,-0.54)	(-0.26,0.26)	(0.05,-0.05)	(0.05,-0.05)	(-0.49,0.49)	(0.53,-0.53)	(-1.23,1.23)	(1.54,-1.54)	(0.19,-0.19)
MET_SoftTrk_Scale	(-0.04,-0.00)	(0.17,-0.11)	(-0.17,-0.24)	(0.33,-0.02)	(0.14,-0.16)	(-0.02,0.42)	(-0.04,-0.61)	(-0.24,0.57)	(-0.53,-0.02)	(0.29,0.11)
MUON_BADMUON_STAT	(0.15,-0.15)	(0.15,-0.15)	(0.15,-0.15)	(0.14,-0.14)	(0.17,-0.17)	(0.13,-0.13)	(0.18,-0.18)	(0.16,-0.16)	(0.20,-0.20)	(0.19,-0.19)
MUON_BADMUON_SYS	(0.15,-0.15)	(0.15,-0.15)	(0.15,-0.15)	(0.14,-0.14)	(0.17,-0.17)	(0.13,-0.13)	(0.18,-0.18)	(0.16,-0.16)	(0.20,-0.20)	(0.19,-0.19)
MUON_EFF_STAT	(-0.52,0.23)	(-0.53,0.22)	(-0.52,0.22)	(-0.52,0.24)	(-0.55,0.22)	(-0.51,0.24)	(-0.58,0.21)	(-0.55,0.23)	(-0.59,0.20)	(-0.53,0.15)
MUON_EFF_STAT_LOWPT	(-0.17,-0.13)	(-0.17,-0.14)	(-0.16,-0.13)	(-0.15,-0.13)	(-0.18,-0.16)	(-0.14,-0.13)	(-0.18,-0.17)	(-0.17,-0.15)	(-0.21,-0.20)	(-0.20,-0.19)
MUON_EFF_SYS	(-2.51,2.25)	(-2.76,2.49)	(-2.93,2.68)	(-3.15,2.92)	(-3.41,3.15)	(-3.56,3.37)	(-3.86,3.59)	(-3.95,3.74)	(-4.09,3.81)	(-4.29,4.03)
MUON_EFF_SYS_LOWPT	(-0.18,-0.11)	(-0.18,-0.13)	(-0.17,-0.12)	(-0.16,-0.12)	(-0.18,-0.15)	(-0.15,-0.12)	(-0.19,-0.17)	(-0.18,-0.14)	(-0.21,-0.19)	(-0.20,-0.18)
MUON_ID	(-0.00,-0.01)	(-0.09,-0.16)	(-0.07,-0.21)	(-0.08,-0.25)	(-0.06,-0.19)	(-0.07,-0.34)	(0.27,-0.59)	(0.56,-0.21)	(-0.26,-0.31)	(-0.07,-0.90)
MUON_MS	(-0.17,-0.15)	(-0.13,-0.13)	(-0.11,-0.17)	(-0.14,-0.13)	(-0.10,-0.14)	(-0.09,-0.15)	(-0.26,-0.21)	(0.09,-0.20)	(0.04,-0.41)	(0.05,-0.37)
MUON_SAGITTA_RESBIAS	(0.15,-0.15)	(0.15,-0.15)	(0.15,-0.15)	(0.14,-0.14)	(0.17,-0.17)	(0.13,-0.13)	(0.18,-0.18)	(0.16,-0.16)	(0.20,-0.20)	(0.19,-0.19)
MUON_SAGITTA_RHO	(0.15,-0.15)	(0.15,-0.15)	(0.15,-0.15)	(0.14,-0.14)	(0.17,-0.17)	(0.13,-0.13)	(0.18,-0.18)	(0.16,-0.16)	(0.20,-0.20)	(0.19,-0.19)
MUON_SCALE	(-0.11,-0.15)	(-0.17,-0.15)	(-0.12,-0.19)	(-0.12,-0.14)	(-0.14,-0.15)	(-0.12,-0.14)	(-0.23,-0.14)	(-0.13,-0.11)	(-0.20,-0.17)	(0.19,-0.19)
MUON_TTVA_STAT	(-0.36,0.07)	(-0.36,0.05)	(-0.34,0.05)	(-0.33,0.05)	(-0.35,0.02)	(-0.32,0.05)	(-0.37,0.00)	(-0.35,0.03)	(-0.38,-0.01)	(-0.37,-0.01)
MUON_TTVA_SYS	(-0.29,-0.01)	(-0.29,-0.02)	(-0.29,-0.01)	(-0.28,-0.00)	(-0.31,-0.02)	(-0.29,0.02)	(-0.35,-0.02)	(-0.35,0.04)	(-0.38,-0.01)	(-0.40,0.01)
PRW_DATASF	(0.71,-0.82)	(1.16,-1.38)	(0.26,-0.36)	(0.48,-0.71)	(0.36,0.57)	(0.46,1.93)	(1.86,-0.32)	(-1.08,0.03)	(0.39,5.64)	(3.14,-1.84)
top_Sys	(-0.85,0.85)	(-0.79,0.79)	(-0.94,0.94)	(-0.94,0.94)	(-1.07,1.07)	(-0.48,0.48)	(-0.78,0.78)	(0.00,0.00)	(0.00,0.00)	(0.00,0.00)
vjets_QCDSmoothing	(-0.65,0.65)	(-0.69,0.69)	(-0.72,0.72)	(-0.77,0.77)	(-0.84,0.84)	(-0.92,0.92)	(-1.05,1.05)	(-1.19,1.19)	(-2.30,2.29)	(-8.46,8.46)
vjets_d1K_NLO	(-6.92,6.91)	(-7.25,7.24)	(-7.38,7.38)	(-7.60,7.60)	(-7.76,7.76)	(-7.83,7.83)	(-8.22,8.22)	(-8.40,8.40)	(-8.66,8.66)	(-8.42,8.42)
vjets_d1kappa_EW	(0.00,0.00)	(-0.00,0.00)	(-0.00,0.00)	(-0.10,0.10)	(-0.16,0.16)	(-0.25,0.25)	(-0.36,0.36)	(-0.49,0.49)	(-0.65,0.65)	(-0.88,0.88)
vjets_d2K_NLO	(5.21,-5.21)	(4.77,-4.78)	(4.11,-4.11)	(3.24,-3.24)	(1.89,-1.89)	(0.47,-0.47)	(-0.78,0.78)	(-1.84,1.84)	(-2.92,2.92)	(-3.93,3.93)
vjets_d2kappa_EW_eej	(-0.40,0.40)	(-0.49,0.49)	(-0.56,0.56)	(-0.66,0.66)	(-0.78,0.78)	(-0.89,0.89)	(-1.03,1.03)	(-1.14,1.14)	(-1.27,1.27)	(-1.35,1.35)
vjets_d2kappa_EW_evj	(-0.00,0.00)	(-0.00,0.00)	(-0.00,0.00)	(-0.00,0.00)	(-0.00,0.00)	(0.00,0.00)	(-0.00,0.00)	(-0.01,0.01)	(-0.00,0.00)	(-0.00,0.00)
vjets_d3K_NLO	(-0.00,0.00)	(-0.00,0.00)	(-0.00,0.00)	(-0.00,0.00)	(-0.00,0.00)	(0.00,0.00)	(-0.00,0.00)	(-0.00,0.00)	(-0.00,0.00)	(-0.00,0.00)
vjets_d3kappa_EW_eej	(-0.00,0.00)	(-0.12,0.12)	(-0.18,0.18)	(-0.28,0.28)	(-0.44,0.43)	(-0.61,0.61)	(-0.83,0.83)	(-1.05,1.05)	(-1.33,1.33)	(-1.64,1.64)
vjets_d3kappa_EW_evj	(0.00,0.00)	(-0.00,0.00)	(-0.00,0.00)	(-0.00,0.00)	(-0.00,0.00)	(0.00,0.00)	(-0.00,0.00)	(-0.00,0.00)	(-0.00,0.00)	(-0.00,0.00)
vjets_dK_NLO_mix	(-0.26,0.25)	(-0.31,0.31)	(-0.36,0.36)	(-0.42,0.41)	(-0.49,0.49)	(-0.55,0.55)	(-0.63,0.63)	(-0.69,0.69)	(-0.76,0.76)	(-0.80,0.80)

Table B.4: Breakdown of the systematic uncertainties on the background estimates before the fit in the CR2mu. The percentages show the size of the uncertainty relative to the total expected background, when varying the nuisance parameter by -1σ and $+1\sigma$.

CR1e	BIN_250	BIN_300	BIN_350	BIN_400	BIN_500	BIN_600	BIN_700	BIN_800	BIN_900	BIN_1000
NCB_Sys	(0.00,0.00)	(0.00,0.00)	(0.00,0.00)	(0.00,0.00)	(0.00,0.00)	(0.00,0.00)	(0.00,0.00)	(0.00,0.00)	(0.00,0.00)	(0.00,0.00)
PDFcomb	(-1.24,1.24)	(-1.31,1.31)	(-1.57,1.57)	(-1.72,1.72)	(-2.07,2.07)	(-2.44,2.44)	(-2.91,2.91)	(-3.06,3.06)	(-4.03,4.03)	(-5.85,5.85)
ckkw	(0.00,0.00)	(0.00,0.00)	(0.00,0.00)	(0.00,0.00)	(0.00,0.00)	(0.00,0.00)	(0.00,0.00)	(0.00,0.00)	(0.00,0.00)	(0.00,0.00)
diboson_Sys	(-0.16,0.16)	(-0.20,0.20)	(-0.23,0.23)	(-0.31,0.31)	(-0.47,0.47)	(-0.77,0.77)	(-1.21,1.21)	(-1.18,1.18)	(-1.23,1.23)	(-3.45,3.45)
lumiSys	(-3.20,3.20)	(-3.20,3.20)	(-3.20,3.20)	(-3.20,3.20)	(-3.20,3.20)	(-3.20,3.20)	(-3.20,3.20)	(-3.20,3.20)	(-3.20,3.20)	(-3.20,3.20)
multijet_Sys	(0.00,0.00)	(0.00,0.00)	(0.00,0.00)	(0.00,0.00)	(0.00,0.00)	(0.00,0.00)	(0.00,0.00)	(0.00,0.00)	(0.00,0.00)	(0.00,0.00)
EG_RESOLUTION_ALL	(-0.02,-0.08)	(-0.04,-0.01)	(-0.14,-0.05)	(0.04,0.01)	(0.05,0.03)	(-0.01,-0.18)	(-0.13,0.14)	(0.50,-0.35)	(0.56,-0.18)	(-0.26,-0.04)
EG_SCALE_ALL	(0.41,-0.70)	(0.62,-0.64)	(0.52,-0.74)	(0.71,-0.65)	(0.58,-0.60)	(0.46,-0.57)	(0.73,-0.22)	(0.61,-0.41)	(0.34,-0.47)	(0.05,-0.42)
EL_EFF_ID_TOTAL	(-1.11,0.97)	(-1.21,1.11)	(-1.24,1.17)	(-1.27,1.19)	(-1.26,1.23)	(-1.27,1.22)	(-1.26,1.27)	(-1.27,1.24)	(-1.26,1.26)	(-1.29,1.17)
EL_EFF_Iso_TOTAL	(-0.56,0.43)	(-0.81,0.71)	(-0.96,0.89)	(-1.12,1.04)	(-1.27,1.24)	(-1.47,1.41)	(-1.79,1.80)	(-2.08,2.05)	(-2.34,2.34)	(-2.53,2.40)
EL_EFF_Reco_TOTAL	(-0.25,0.11)	(-0.24,0.14)	(-0.22,0.16)	(-0.23,0.16)	(-0.21,0.18)	(-0.22,0.16)	(-0.19,0.20)	(-0.20,0.17)	(-0.20,0.20)	(-0.26,0.13)
EL_EFF_TriggerEff_TOTAL	(0.00,-0.00)	(0.01,-0.01)	(-0.01,0.01)	(0.01,-0.01)	(0.01,-0.01)	(0.00,0.00)	(-0.01,0.01)	(0.00,-0.00)	(0.00,0.00)	(0.00,0.00)
EL_EFF_Trigger_TOTAL	(-0.28,0.14)	(-0.26,0.16)	(-0.24,0.17)	(-0.23,0.16)	(-0.20,0.17)	(-0.20,0.15)	(-0.17,0.18)	(-0.17,0.15)	(-0.16,0.16)	(-0.22,0.09)
FT_EFF_B_systematics	(0.00,0.00)	(0.01,-0.01)	(-0.01,0.01)	(0.00,0.00)	(0.01,-0.01)	(0.00,0.00)	(-0.01,0.01)	(0.00,0.00)	(0.00,0.00)	(0.00,0.00)
FT_EFF_C_systematics	(0.00,0.00)	(0.01,-0.01)	(-0.01,0.01)	(0.00,0.00)	(0.01,-0.01)	(0.00,0.00)	(-0.01,0.01)	(0.00,0.00)	(0.00,0.00)	(0.00,0.00)
FT_EFF_Light_systematics	(0.00,0.00)	(0.01,-0.01)	(-0.01,0.01)	(0.00,0.00)	(0.01,-0.01)	(0.00,0.00)	(-0.01,0.01)	(0.00,0.00)	(0.00,0.00)	(0.00,0.00)
FT_EFF_extrapolation	(0.00,0.00)	(0.01,-0.01)	(-0.01,0.01)	(0.00,0.00)	(0.01,-0.01)	(0.00,0.00)	(-0.01,0.01)	(0.00,0.00)	(0.00,0.00)	(0.00,0.00)
FT_EFF_extrapolation_from_charm	(0.00,0.00)	(0.01,-0.01)	(-0.01,0.01)	(0.00,0.00)	(0.01,-0.01)	(0.00,0.00)	(-0.01,0.01)	(0.00,0.00)	(0.00,0.00)	(0.00,0.00)
JET_EtaIntercalibration_NonClosure	(0.56,-1.03)	(1.20,-0.55)	(0.74,-0.74)	(0.37,-0.41)	(0.83,-1.03)	(0.42,-0.26)	(0.68,-1.14)	(1.79,-0.41)	(1.05,0.17)	(-0.03,-0.77)
JET_GroupedNP_1	(-0.41,0.29)	(-2.18,2.70)	(-2.67,2.93)	(-2.59,2.36)	(-3.21,2.42)	(-1.82,3.71)	(-3.11,1.46)	(-1.75,5.29)	(2.12,-0.26)	(-12.17,0.89)
JET_GroupedNP_2	(-1.84,1.33)	(-1.82,2.19)	(-2.02,1.94)	(-2.10,1.96)	(-2.65,2.44)	(-2.34,2.93)	(-4.56,2.34)	(-1.79,6.61)	(2.11,2.23)	(-11.32,4.04)
JET_GroupedNP_3	(-0.43,0.34)	(-0.52,0.90)	(-0.70,0.71)	(-0.79,0.68)	(-1.27,1.32)	(-0.73,0.59)	(-1.56,0.95)	(0.07,1.80)	(-0.68,2.23)	(-3.00,-0.55)
JET_JER_SINGLE_NP	(1.00,-1.00)	(-0.75,0.75)	(0.32,-0.31)	(-0.56,0.56)	(-0.47,0.47)	(-0.47,0.47)	(0.31,-0.31)	(0.58,-0.58)	(-6.81,8.74)	(8.75,-8.75)
MET_SoftTrk_ResoPara	(-0.25,0.25)	(0.10,-0.10)	(-0.07,0.07)	(-0.11,0.11)	(-0.31,0.31)	(-0.72,0.72)	(0.22,-0.22)	(0.12,-0.12)	(-0.98,0.98)	(-0.32,0.32)
MET_SoftTrk_ResoPerp	(-0.02,0.02)	(-0.19,0.19)	(-0.11,0.11)	(0.21,-0.21)	(0.28,-0.28)	(-1.28,1.28)	(0.83,-0.83)	(-0.09,0.09)	(-7.20,7.93)	(6.16,-6.16)
MET_SoftTrk_Scale	(-0.31,0.15)	(0.14,0.11)	(-0.05,-0.05)	(-0.17,-0.04)	(-0.29,-0.09)	(0.05,0.41)	(-0.32,0.49)	(0.67,1.32)	(-0.83,6.28)	(0.49,-5.79)
MUON_BADMUON_STAT	(0.00,0.00)	(0.01,-0.01)	(-0.01,0.01)	(0.00,0.00)	(0.01,-0.01)	(0.00,0.00)	(-0.01,0.01)	(0.00,0.00)	(0.00,0.00)	(0.00,0.00)
MUON_BADMUON_SYS	(0.00,0.00)	(0.01,-0.01)	(-0.01,0.01)	(0.00,0.00)	(0.01,-0.01)	(0.00,0.00)	(-0.01,0.01)	(0.00,0.00)	(0.00,0.00)	(0.00,0.00)
MUON_EFF_STAT	(0.01,-0.02)	(-0.00,-0.04)	(0.03,-0.01)	(0.02,-0.03)	(0.02,-0.03)	(0.02,-0.03)	(0.03,-0.02)	(0.02,-0.02)	(0.02,-0.02)	(0.03,-0.03)
MUON_EFF_STAT_LOWPT	(0.00,0.00)	(-0.01,-0.02)	(0.01,0.01)	(0.00,0.00)	(-0.01,-0.01)	(0.00,0.00)	(0.01,0.01)	(0.00,0.00)	(0.00,0.00)	(0.00,0.00)
MUON_EFF_SYS	(0.06,-0.08)	(0.06,-0.10)	(0.10,-0.09)	(0.11,-0.11)	(0.11,-0.12)	(0.12,-0.12)	(0.13,-0.11)	(0.11,-0.11)	(0.12,-0.12)	(0.14,-0.14)
MUON_EFF_SYS_LOWPT	(0.00,0.00)	(-0.01,-0.02)	(0.01,0.01)	(0.00,0.00)	(-0.01,-0.01)	(0.00,0.00)	(0.01,0.01)	(0.00,0.00)	(0.00,0.00)	(0.00,0.00)
MUON_ID	(0.00,0.00)	(-0.01,-0.02)	(0.01,0.01)	(0.00,0.00)	(-0.01,-0.01)	(0.02,-0.02)	(-0.06,0.06)	(0.14,-0.14)	(0.00,0.00)	(-0.08,-0.05)
MUON_MS	(0.00,0.00)	(-0.01,-0.01)	(0.01,0.01)	(0.01,-0.00)	(-0.04,0.03)	(0.00,0.00)	(0.04,-0.04)	(0.14,-0.14)	(0.00,0.00)	(0.02,-0.02)
MUON_SAGITTA_RESBIAS	(0.00,0.00)	(0.01,-0.01)	(-0.01,0.01)	(0.00,0.00)	(0.01,-0.01)	(0.00,0.00)	(-0.01,0.01)	(0.00,0.00)	(0.00,0.00)	(0.00,0.00)
MUON_SAGITTA_RHO	(0.00,0.00)	(0.01,-0.01)	(-0.01,0.01)	(0.00,0.00)	(0.01,-0.01)	(0.00,0.00)	(-0.01,0.01)	(0.00,0.00)	(0.00,0.00)	(0.00,0.00)
MUON_SCALE	(0.00,0.00)	(-0.00,-0.01)	(-0.01,0.01)	(0.00,0.00)	(-0.02,0.01)	(0.00,0.00)	(-0.01,0.01)	(0.00,0.00)	(0.00,0.00)	(0.00,0.00)
MUON_TTVA_STAT	(0.00,0.00)	(0.01,-0.01)	(-0.01,0.01)	(0.00,0.00)	(0.01,-0.01)	(0.00,0.00)	(-0.01,0.01)	(0.00,0.00)	(0.00,0.00)	(0.00,0.00)
MUON_TTVA_SYS	(0.00,0.00)	(0.01,-0.01)	(-0.01,0.01)	(0.00,0.00)	(0.01,-0.01)	(0.00,0.00)	(-0.01,0.01)	(0.00,0.00)	(0.00,0.00)	(0.00,0.00)
PRW_DATASF	(1.06,-0.96)	(-0.02,-0.48)	(-0.14,-0.00)	(0.13,-0.22)	(0.51,-1.38)	(0.07,-0.79)	(1.28,-2.59)	(1.54,-2.87)	(2.80,-2.59)	(3.17,-2.50)
top_Sys	(-2.87,2.87)	(-3.51,3.51)	(-4.29,4.29)	(-5.18,5.18)	(-5.59,5.59)	(-6.25,6.25)	(-5.77,5.77)	(-5.77,5.77)	(-7.50,7.50)	(-7.53,7.53)
vjets_QCDSmoothing	(-0.34,0.34)	(-0.35,0.35)	(-0.36,0.36)	(-0.38,0.38)	(-0.42,0.42)	(-0.52,0.52)	(-0.63,0.63)	(-0.82,0.83)	(-1.67,1.67)	(-7.47,7.47)
vjets_d1K_NLO	(-6.58,6.58)	(-6.68,6.67)	(-6.68,6.68)	(-6.68,6.67)	(-6.90,6.90)	(-6.99,6.99)	(-7.21,7.21)	(-7.68,7.68)	(-7.79,7.79)	(-7.52,7.52)
vjets_d1kappa_EW	(0.00,0.00)	(-0.01,0.01)	(-0.01,0.01)	(-0.11,0.11)	(-0.19,0.19)	(-0.29,0.30)	(-0.42,0.42)	(-0.60,0.60)	(-0.78,0.78)	(-1.06,1.06)
vjets_d2K_NLO	(4.90,-4.90)	(4.33,-4.34)	(3.67,-3.67)	(2.77,-2.77)	(1.63,-1.63)	(0.38,-0.38)	(-0.67,0.67)	(-1.71,1.71)	(-2.61,2.61)	(-3.49,3.49)
vjets_d2kappa_EW_eej	(-0.00,0.00)	(-0.00,0.00)	(-0.00,0.00)	(-0.00,0.00)	(-0.00,0.00)	(-0.00,0.00)	(-0.00,0.00)	(-0.00,0.00)	(-0.00,0.00)	(-0.00,0.00)
vjets_d2kappa_EW_evj	(-0.41,0.41)	(-0.50,0.50)	(-0.57,0.57)	(-0.66,0.66)	(-0.80,0.80)	(-0.94,0.94)	(-1.08,1.08)	(-1.27,1.27)	(-1.40,1.40)	(-1.51,1.51)
vjets_d3K_NLO	(-1.09,1.09)	(-1.01,1.00)	(-0.90,0.89)	(-0.82,0.82)	(-0.78,0.78)	(-0.62,0.62)	(-0.60,0.60)	(-0.54,0.54)	(-0.56,0.56)	(-0.58,0.58)
vjets_d3kappa_EW_eej	(-0.00,0.00)	(-0.00,0.00)	(-0.00,0.00)	(-0.00,0.00)	(-0.00,0.00)	(-0.00,0.00)	(-0.00,0.00)	(-0.00,0.00)	(-0.00,0.00)	(-0.00,0.00)
vjets_d3kappa_EW_evj	(0.00,0.00)	(-0.01,0.01)	(-0.01,0.01)	(-0.12,0.11)	(-0.18,0.18)	(-0.25,0.25)	(-0.33,0.34)	(-0.45,0.45)	(-0.50,0.50)	(-0.53,0.53)
vjets_dK_NLO_mix	(-0.27,0.27)	(-0.33,0.32)	(-0.37,0.37)	(-0.43,0.43)	(-0.51,0.51)	(-0.59,0.59)	(-0.67,0.68)	(-0.78,0.78)	(-0.86,0.86)	(-0.92,0.92)

Table B.5: Breakdown of the systematic uncertainties on the background estimates before the fit in the CR1e. The percentages show the size of the uncertainty relative to the total expected background, when varying the nuisance parameter by -1σ and $+1\sigma$.

SR	BIN_250	BIN_300	BIN_350	BIN_400	BIN_500	BIN_600	BIN_700	BIN_800	BIN_900	BIN_1000
NCB_Sys	(-0.22,0.22)	(-0.11,0.11)	(-0.08,0.09)	(-0.06,0.07)	(-0.05,0.05)	(0.00,0.00)	(0.00,0.00)	(0.00,0.00)	(0.00,0.00)	(0.00,0.00)
PDFcomb	(0.15,-0.45)	(-0.12,0.48)	(0.19,-1.02)	(0.04,0.08)	(0.03,-0.01)	(0.08,-0.55)	(-0.03,-0.34)	(-0.13,-0.79)	(0.45,-1.35)	(1.29,-2.92)
ckkw	(-0.75,0.75)	(-0.92,0.92)	(-0.92,0.92)	(-0.92,0.92)	(-0.55,0.55)	(-0.29,0.29)	(-0.41,0.41)	(-0.33,0.33)	(-0.39,0.39)	(-0.65,0.65)
diboson_Sys	(-0.09,0.48)	(-0.06,0.54)	(-0.14,0.37)	(-0.10,0.54)	(-0.03,0.50)	(0.12,0.38)	(0.23,0.40)	(0.58,0.05)	(0.41,0.14)	(1.02,-0.89)
lumiSys	(0.19,-0.24)	(0.18,0.54)	(0.22,-0.82)	(0.19,0.32)	(0.19,0.15)	(0.24,-0.43)	(0.23,-0.27)	(0.33,-1.04)	(0.25,-0.81)	(0.24,-1.19)
multijet_Sys	(-0.44,0.44)	(-0.24,0.25)	(-0.09,0.09)	(-0.05,0.05)	(-0.06,0.06)	(-0.04,0.04)	(-0.06,0.06)	(-0.11,0.11)	(-0.05,0.05)	(-0.05,0.05)
EG_RESOLUTION_ALL	(0.04,0.18)	(0.00,0.17)	(0.04,-0.01)	(0.03,0.14)	(0.04,0.02)	(0.04,-0.03)	(0.05,0.10)	(0.13,0.17)	(-0.58,0.84)	(-0.03,0.02)
EG_SCALE_ALL	(0.41,-0.26)	(0.38,-0.29)	(0.49,-0.31)	(0.44,-0.31)	(0.35,-0.28)	(0.40,-0.29)	(0.45,-0.35)	(0.60,-0.37)	(0.53,-0.39)	(0.47,-0.41)
EL_EFF_ID	(-1.09,1.13)	(-1.20,1.62)	(-1.27,0.73)	(-1.29,1.48)	(-1.33,1.33)	(-1.36,1.03)	(-1.44,1.30)	(-1.42,0.81)	(-1.53,0.90)	(-1.74,0.76)
EL_EFF_Iso	(-0.04,0.03)	(-0.26,0.93)	(-0.42,-0.38)	(-0.34,0.78)	(-0.50,0.76)	(-0.62,0.31)	(-0.67,0.53)	(-0.52,-0.32)	(-0.78,0.02)	(-1.65,0.15)
EL_EFF_Reco	(-0.13,0.16)	(-0.19,0.10)	(-0.14,0.18)	(-0.20,0.12)	(-0.21,0.12)	(-0.19,0.14)	(-0.24,0.10)	(-0.19,0.17)	(-0.28,0.10)	(-0.17,0.08)
EL_EFF_TriggerEff	(0.00,-0.00)	(0.04,0.04)	(0.00,-0.03)	(0.03,0.04)	(0.04,0.04)	(0.02,0.02)	(0.03,0.05)	(-0.01,0.00)	(0.03,0.07)	(0.12,0.00)
EL_EFF_Trigger	(-0.08,0.10)	(-0.02,0.03)	(-0.11,0.13)	(-0.04,0.04)	(-0.03,0.03)	(-0.06,0.05)	(-0.04,0.02)	(-0.09,0.07)	(-0.03,0.02)	(-0.12,0.14)
FT_EFF_B	(0.08,-0.26)	(0.95,-0.38)	(-0.32,-0.69)	(0.89,-0.52)	(0.72,-0.56)	(0.23,-0.73)	(0.41,-0.73)	(-0.23,-0.91)	(-0.09,-0.89)	(-1.02,-0.90)
FT_EFF_C	(0.23,-0.28)	(1.04,-0.37)	(-0.20,-0.62)	(0.99,-0.54)	(0.81,-0.53)	(0.28,-0.57)	(0.31,-0.58)	(-0.23,-0.70)	(-0.15,-0.69)	(-1.43,-0.30)
FT_EFF_Light	(0.02,-0.07)	(0.05,-0.13)	(0.03,-0.08)	(0.06,-0.14)	(0.08,-0.17)	(0.10,-0.19)	(0.14,-0.26)	(0.12,-0.22)	(0.18,-0.33)	(0.18,-0.35)
FT_EFF_extrapolation	(0.02,-0.03)	(0.05,-0.10)	(0.05,-0.06)	(0.10,-0.14)	(0.14,-0.17)	(0.18,-0.22)	(0.26,-0.29)	(0.27,-0.28)	(0.39,-0.46)	(0.48,-0.62)
FT_EFF_extrapolation_from_charm	(-0.34,-0.02)	(0.45,-0.06)	(-0.91,-0.02)	(0.26,-0.06)	(0.09,-0.07)	(-0.50,-0.06)	(-0.39,-0.09)	(-1.14,-0.05)	(-0.93,-0.13)	(-1.52,-0.12)
JET_EtaIntercalibration_NonClosure	(-0.01,0.25)	(0.72,0.33)	(-0.43,-0.06)	(0.78,0.15)	(0.56,0.16)	(0.11,0.11)	(0.39,0.44)	(-0.99,0.33)	(-0.41,0.40)	(-1.72,-0.06)
JET_GroupedNP_1	(-0.44,0.62)	(0.39,-0.50)	(-0.82,1.42)	(0.48,-0.06)	(0.28,0.21)	(-0.49,0.87)	(-0.68,0.42)	(-1.15,1.89)	(-0.90,1.47)	(-2.46,1.55)
JET_GroupedNP_2	(0.48,-0.09)	(0.30,0.62)	(0.18,-0.63)	(0.15,0.38)	(0.52,0.30)	(0.14,-0.08)	(0.82,-0.40)	(0.10,-0.68)	(0.66,-0.51)	(0.89,-1.23)
JET_GroupedNP_3	(0.50,0.09)	(-0.16,0.69)	(0.65,-0.36)	(0.07,0.35)	(0.12,0.30)	(0.26,0.11)	(-0.10,-0.08)	(1.31,0.02)	(0.61,-0.17)	(1.07,-1.64)
JET_JER_SINGLE_NP	(0.30,-0.38)	(0.25,0.18)	(0.41,-1.05)	(-0.15,0.57)	(0.17,0.07)	(0.39,-0.63)	(0.07,-0.46)	(-0.17,-0.61)	(-0.31,-0.38)	(1.81,-3.74)
MET_SoftTrk_ResoPara	(-0.58,0.46)	(0.04,0.61)	(-1.25,0.38)	(0.18,0.32)	(-0.03,0.34)	(-0.73,0.42)	(-0.87,0.74)	(-0.68,-0.13)	(-1.13,0.41)	(-1.95,0.14)
MET_SoftTrk_ResoPerp	(-0.50,0.36)	(0.19,0.25)	(-1.24,0.70)	(-0.13,0.50)	(-0.25,0.51)	(-0.80,0.60)	(-0.89,0.77)	(-1.83,1.24)	(-1.60,1.17)	(-0.51,-0.56)
MET_SoftTrk_Scale	(-0.38,0.58)	(0.24,-0.03)	(-1.09,1.07)	(-0.10,0.17)	(-0.19,0.35)	(-0.82,0.53)	(-0.63,0.67)	(-1.53,0.84)	(-1.27,1.01)	(-0.54,0.79)
MUON_BADMUON_STAT	(-0.00,0.02)	(-0.06,0.04)	(0.03,-0.02)	(-0.06,0.05)	(-0.05,0.04)	(-0.01,0.02)	(-0.07,0.03)	(-0.03,0.03)	(-0.10,0.01)	(-0.02,-0.25)
MUON_BADMUON_SYS	(-0.01,0.01)	(0.00,0.05)	(-0.02,-0.02)	(0.01,0.05)	(0.00,0.05)	(0.00,0.02)	(0.03,0.05)	(0.00,0.02)	(0.03,0.05)	(-0.05,-0.07)
MUON_EFF_STAT	(-0.14,0.26)	(-0.19,0.29)	(-0.14,0.27)	(-0.18,0.27)	(-0.19,0.29)	(-0.18,0.27)	(-0.20,0.27)	(-0.16,0.21)	(-0.23,0.25)	(-0.19,0.22)
MUON_EFF_STAT_LOWPT	(0.01,-0.00)	(-0.06,0.01)	(0.06,-0.00)	(-0.04,0.01)	(-0.03,0.00)	(0.02,-0.01)	(-0.02,0.01)	(0.05,-0.03)	(-0.00,0.01)	(0.15,-0.06)
MUON_EFF_SYS	(-1.75,1.98)	(-2.04,2.16)	(-2.01,2.36)	(-2.25,2.45)	(-2.40,2.63)	(-2.52,2.85)	(-2.79,3.01)	(-2.72,3.09)	(-2.98,3.36)	(-3.58,3.97)
MUON_EFF_SYS_LOWPT	(0.01,0.03)	(0.06,0.06)	(0.01,0.03)	(0.05,0.05)	(0.06,0.07)	(0.04,0.06)	(0.09,0.09)	(0.02,0.04)	(0.10,0.10)	(0.05,-0.06)
MUON_ID	(-0.15,-0.45)	(0.58,0.40)	(-0.59,-0.92)	(0.65,0.26)	(0.47,0.03)	(-0.01,-0.58)	(0.27,-0.46)	(-0.03,-1.23)	(-0.02,-1.01)	(-0.29,-1.86)
MUON_MS	(-0.23,0.19)	(0.60,0.16)	(-0.74,-0.12)	(0.47,0.06)	(0.28,0.06)	(-0.36,0.04)	(-0.18,0.08)	(-0.88,-0.02)	(-0.72,-0.02)	(-1.41,0.03)
MUON_SAGITTA_RESBIAS	(-0.01,-0.23)	(0.03,0.57)	(-0.02,-0.81)	(0.02,0.35)	(0.02,0.23)	(-0.01,-0.32)	(0.01,-0.25)	(-0.05,-0.97)	(0.00,-0.82)	(0.01,-1.83)
MUON_SAGITTA_RHO	(-0.01,0.00)	(0.03,0.03)	(-0.02,-0.03)	(0.01,0.04)	(0.01,0.02)	(-0.01,-0.01)	(0.01,0.02)	(-0.05,0.00)	(0.00,0.05)	(0.01,-0.03)
MUON_SCALE	(0.04,-0.11)	(0.00,-0.11)	(0.06,-0.08)	(-0.01,-0.10)	(-0.02,-0.07)	(-0.00,-0.05)	(-0.01,-0.08)	(-0.07,-0.04)	(-0.09,-0.05)	(0.15,-0.02)
MUON_TTVA_STAT	(-0.03,0.15)	(-0.01,0.18)	(-0.03,0.13)	(-0.00,0.17)	(0.00,0.16)	(-0.00,0.14)	(0.02,0.14)	(0.01,0.10)	(0.04,0.15)	(-0.05,0.05)
MUON_TTVA_SYS	(0.02,0.12)	(0.05,0.16)	(-0.01,0.11)	(0.04,0.16)	(0.05,0.17)	(0.02,0.15)	(0.03,0.18)	(-0.01,0.14)	(0.01,0.18)	(-0.13,0.08)
PRW_DATASF	(1.27,-1.33)	(0.69,-0.29)	(1.53,-2.17)	(0.97,-0.68)	(0.47,-0.18)	(0.96,-1.19)	(1.08,-1.20)	(2.56,-3.35)	(1.25,-1.94)	(1.46,-2.78)
top_Sys	(0.49,-0.44)	(0.32,0.34)	(0.31,-0.95)	(0.10,0.48)	(0.01,0.33)	(0.08,-0.27)	(-0.16,-0.01)	(-0.15,-0.52)	(-0.58,-0.17)	(-0.62,-1.86)
vjets_QCDSmoothing	(-0.48,0.30)	(0.38,0.54)	(-1.08,-0.12)	(-0.06,0.58)	(-0.29,0.55)	(-0.97,0.41)	(-1.06,0.81)	(-1.86,0.46)	(-1.25,0.07)	(5.02,-6.14)
vjets_d1K_NLO	(-0.01,-0.06)	(-0.05,0.69)	(0.20,-0.83)	(0.06,0.29)	(0.13,0.18)	(0.26,-0.37)	(0.22,-0.23)	(0.45,-0.91)	(0.37,-0.79)	(-0.05,-1.29)
vjets_d1kappa_EW	(-0.21,-0.01)	(0.56,-0.02)	(-0.81,0.06)	(0.36,-0.02)	(0.15,0.08)	(-0.43,0.09)	(-0.26,0.03)	(-0.89,-0.05)	(-0.69,-0.08)	(-1.53,-0.04)
vjets_d2K_NLO	(0.61,-0.21)	(0.84,-0.25)	(0.40,-0.27)	(0.91,-0.26)	(1.24,-0.28)	(1.59,-0.34)	(2.00,-0.33)	(2.33,-0.31)	(2.01,-0.28)	(-0.05,-0.21)
vjets_d2kappa_EW_eej	(0.20,-0.23)	(0.23,-0.26)	(0.35,-0.36)	(0.42,-0.49)	(0.53,-0.66)	(0.68,-0.78)	(0.79,-0.91)	(0.96,-1.04)	(0.99,-1.15)	(1.15,-1.42)
vjets_d2kappa_EW_evj	(-0.09,0.02)	(-0.18,0.90)	(-0.46,-0.41)	(-0.38,0.89)	(-0.56,0.92)	(-0.73,0.46)	(-0.75,0.72)	(-0.88,0.03)	(-1.04,0.38)	(-1.52,0.08)
vjets_d3K_NLO	(-1.07,0.01)	(-0.34,-0.08)	(-1.63,0.05)	(-0.53,-0.04)	(-0.61,-0.03)	(-1.06,0.02)	(-0.75,-0.06)	(-1.45,0.06)	(-1.14,0.07)	(-1.53,0.03)
vjets_d3kappa_EW_eej	(0.15,-0.19)	(0.32,-0.26)	(0.24,-0.26)	(0.45,-0.40)	(0.54,-0.55)	(0.67,-0.67)	(0.85,-0.83)	(0.93,-0.92)	(1.17,-1.10)	(1.34,-1.28)
vjets_d3kappa_EW_evj	(-0.12,-0.01)	(0.67,-0.05)	(-0.67,0.04)	(0.36,-0.00)	(0.13,0.09)	(-0.44,0.19)	(-0.35,0.17)	(-1.13,0.27)	(-1.13,0.29)	(-2.02,0.42)
vjets_dK_NLO_mix	(-0.07,-0.24)	(-0.04,0.58)	(-0.01,-0.81)	(-0.02,0.34)	(-0.03,0.17)	(-0.02,-0.39)	(-0.03,-0.29)	(0.00,-1.07)	(0.03,-0.88)	(-0.08,-1.27)

Table B.6: Breakdown of the systematic uncertainties on the background estimates after the fit in the SR. Note that the individual uncertainties can be correlated, and do not add up quadratically to the total background uncertainty. The percentages show the size of the uncertainty relative to the total expected background, when varying the nuisance parameter by -1σ and $+1\sigma$.

SR	BIN_250	BIN_300	BIN_350	BIN_400	BIN_500	BIN_600	BIN_700	BIN_800	BIN_900	BIN_1000
Observed Events	255486	144283	76808	41523	13680	5097	2122	980	468	245
Fitted background	245900±5800	138000±3400	73000±1900	39900±1000	12720±340	4680±160	2017±90	908±55	464±34	238±23
$Z(\nu\nu)+$ jets	137800±3900	82400±2300	45700±1300	25690±770	8580±260	3270±130	1458±76	671±47	341±28	176±18
$W(\tau\nu)+$ jets	50300±1500	25370±810	12280±520	6660±190	1880±63	632±26	261±13	104±9	55±5	24±3
$W(\mu\nu)+$ jets	20860±840	10970±520	5380±280	2630±140	750±44	270±19	115±13	47±8	29±4	17±2
$W(e\nu)+$ jets	20600±620	10340±340	4930±220	2368±97	682±33	200±17	63±8	32±3	16±1	7±2
$Z(\tau\tau)+$ jets	812±32	364±15	178±8	88±5	24±1	8±1	3.5±0.5	1.2±0.1	0.7±0.1	0.4±0.1
$Z(\mu\mu)+$ jets	564±32	257±18	107±9	43±3	10±1	3±1	1.8±0.5	1.1±0.3	0.7±0.2	0.2±0.2
$Z(ee)+$ jets	0.11±0.03	0.07±0	0.03±0	0.03±0.03	0±0	0±0	0±0	0±0	0±0	0±0
$t\bar{t}$, single-top	8600±1100	4450±560	2110±280	990±150	269±42	86±18	26±10	7±6	1.14±1.14	0±1
Dibosons	5230±400	3540±260	2220±170	1370±130	507±64	210±34	88±19	44±11	21±6	13±4
Multijets	700±700	220±210	51±50	21±21	8±8	3±3	1±1	1±1	0.2±0.2	0.1±0.1
Non-collision bkgs	360±360	120±120	51±51	22±22	4±4	0±0	0±0	0±0	0±0	0±0
Pre-fit background	197000±19000	110000±11000	57900±5700	31800±3200	10300±1000	3720±380	1520±170	675±79	323±43	161±28

Table B.7: Event yields in SR before and after the counting experiment fits, compared to the observed events. For the predictions, both the statistical and systematic uncertainties are included. The uncertainties for the individual background processes can be correlated, and do not necessarily add in quadrature to the total background uncertainty.

CR1mu0b	BIN_250	BIN_300	BIN_350	BIN_400	BIN_500	BIN_600	BIN_700	BIN_800	BIN_900	BIN_1000
Observed Events	110938	66643	37185	20936	7077	2693	1150	521	263	133
Fitted background	110810±350	66540±260	37110±190	20890±140	7035±75	2654±44	1130±28	510±19	258±14	132±10
$Z(\nu\nu)+$ jets	37±3	21±1	10±1	6±1	2±0.2	0.5±0.2	0.2±0.1	0.08±0.02	0.03±0.01	0.02±0.01
$W(\tau\nu)+$ jets	5860±160	3610±79	2047±53	1165±47	410±12	156±9	79±4	35±2	17±1	8±1
$W(\mu\nu)+$ jets	94940±900	56570±570	31360±340	17610±210	5857±92	2161±54	920±34	423±23	219±15	114±9
$W(e\nu)+$ jets	7±2	3±2	1±1	0.19±0.02	0±0	0.06±0.01	0.07±0.01	0.03±0.01	0.01±0	0.02±0
$Z(\tau\tau)+$ jets	277±21	149±11	79±5	47±3	18±1	8±1	4±1	1.2±0.3	0.5±0.1	0.2±0.1
$Z(\mu\mu)+$ jets	1774±75	914±40	463±24	229±13	67±8	25±1	12±1	5.8±0.5	2.8±0.4	1.8±0.3
$Z(ee)+$ jets	0±0	0±0	0±0	0±0	0±0	0±0	0±0	0±0	0±0	0±0
$t\bar{t}$, single-top	4700±790	2950±480	1600±270	850±150	291±56	135±33	47±20	13±11	2.48±2.48	0±2
Dibosons	3220±230	2310±170	1550±110	988±75	391±33	168±23	69±10	32±6	16±3	8±1
Multijets	0±0	0±0	0±0	0±0	0±0	0±0	0±0	0±0	0±0	0±0
Non-collision bkgs	0±0	0±0	0±0	0±0	0±0	0±0	0±0	0±0	0±0	0±0
Pre-fit background	87500±8700	52700±5300	29300±2900	16700±1700	5690±580	2110±230	862±96	386±47	187±26	94±16

Table B.8: Event yields in CR1mu0b before and after the counting experiment fits, compared to the observed events. For the predictions, both the statistical and systematic uncertainties are included. The uncertainties for the individual background processes can be correlated, and do not necessarily add in quadrature to the total background uncertainty.

CR1e	BIN_250	BIN_300	BIN_350	BIN_400	BIN_500	BIN_600	BIN_700	BIN_800	BIN_900	BIN_1000
Observed Events	68973	44693	26645	15566	5619	2266	1015	462	246	136
Fitted background	69030±260	44740±210	26690±160	15590±120	5650±68	2278±41	1028±26	465±17	246±12	135±11
$Z(\nu\nu)+$ jets	1.8±0.3	1.4±0.1	1.1±0.1	0.9±0.1	0.6±0.1	0.33±0.04	0.17±0.04	0.13±0.03	0.1±0.02	0.05±0.01
$W(\tau\nu)+$ jets	4110±140	2630±86	1552±51	912±33	337±14	136±6	62±4	30±2	15±1	8±1
$W(\mu\nu)+$ jets	7.20±7.20	5±2	4±1	0.98±0.98	0.4±0.2	0.07±0.01	0.2±0.1	0.2±0.1	0.1±0.1	0.04±0.04
$W(e\nu)+$ jets	54500±1000	34860±660	20710±400	12080±250	4330±110	1709±60	804±36	373±23	204±16	110±10
$Z(\tau\tau)+$ jets	212±15	130±9	86±6	48±3	15±1	5±1	2.4±0.5	0.9±0.5	0.35±0.35	0.2±0.1
$Z(\mu\mu)+$ jets	0.4±0.2	0.15±0.02	0.3±0.2	0.3±0.1	0.07±0.01	0.01±0	0±0	0±0	0±0	0±0
$Z(ee)+$ jets	5±4	3±3	1.24±1.24	0.58±0.58	0.2±0.2	0.02±0.02	0.01±0.01	0.01±0.01	0.01±0	0±0
$t\bar{t}$, single-top	8200±1000	5580±670	3280±390	1830±250	648±95	273±54	83±32	26±22	5.11±5.11	0±3
Dibosons	2020±160	1530±110	1050±83	716±64	319±36	155±20	76±13	35±6	21±5	17±10
Multijets	0±0	0±0	0±0	0±0	0±0	0±0	0±0	0±0	0±0	0±0
Non-collision bkgs	0±0	0±0	0±0	0±0	0±0	0±0	0±0	0±0	0±0	0±0
Pre-fit background	56600±5600	36900±3700	22000±2300	13100±1400	4780±530	1850±220	820±100	368±50	190±28	101±23

Table B.9: Event yields in CR1e before and after the counting experiment fits,, compared to the observed events. For the predictions, both the statistical and systematic uncertainties are included. The uncertainties for the individual background processes can be correlated, and do not necessarily add in quadrature to the total background uncertainty.

CR2mu	BIN_250	BIN_300	BIN_350	BIN_400	BIN_500	BIN_600	BIN_700	BIN_800	BIN_900	BIN_1000
Observed Events	17372	10639	6012	3348	1102	371	158	65	31	17
Fitted background	17440±130	10695±95	6052±70	3368±50	1116±25	398±13	166±8	73±4	36±3	18±2
$Z(\nu\nu)+$ jets	0±0	0±0	0±0	0±0	0±0	0±0	0±0	0±0	0±0	0±0
$W(\tau\nu)+$ jets	3±1	1.6±0.4	0.9±0.3	0.2±0.2	0.09±0.01	0.02±0	0.02±0	0.01±0	0±0	0±0
$W(\mu\nu)+$ jets	32±3	17±2	9±1	5.8±0.5	2.1±0.2	0.5±0.1	0.4±0.1	0.3±0.1	0.06±0.02	0.03±0.03
$W(e\nu)+$ jets	0±0	0±0	0±0	0±0	0±0	0±0	0±0	0±0	0±0	0±0
$Z(\tau\tau)+$ jets	16±3	9±3	4±1	2.8±0.3	1.1±0.2	0.3±0.1	0.3±0.1	0.1±0.02	0.01±0	0.01±0
$Z(\mu\mu)+$ jets	16360±160	10010±110	5643±76	3133±53	1025±25	361±13	153±8	67±4	33±3	17±2
$Z(ee)+$ jets	0±0	0±0	0±0	0±0	0±0	0±0	0±0	0±0	0±0	0±0
$t\bar{t}$, single-top	486±64	272±35	141±19	67±10	20±4	5±2	2±1	1±1	0.21±0.21	0±0.2
Dibosons	540±39	383±28	254±19	159±13	68±6	31±3	11±1	5.1±0.5	2.3±0.2	1.3±0.2
Multijets	0±0	0±0	0±0	0±0	0±0	0±0	0±0	0±0	0±0	0±0
Non-collision bkgs	0±0	0±0	0±0	0±0	0±0	0±0	0±0	0±0	0±0	0±0
Pre-fit background	14100±1400	8640±880	4830±490	2700±270	900±94	324±34	126±15	55±7	26±4	13±2

Table B.10: Event yields in CR2mu before and after the counting experiment fits,, compared to the observed events. For the predictions, both the statistical and systematic uncertainties are included. The uncertainties for the individual background processes can be correlated, and do not necessarily add in quadrature to the total background uncertainty.

CR1mu0b	BIN_250	BIN_300	BIN_350	BIN_400	BIN_500	BIN_600	BIN_700	BIN_800	BIN_900	BIN_1000
Observed Events	110938	66643	37185	20936	7077	2693	1150	521	263	133
Fitted background	110810±350	66540±260	37110±190	20890±140	7035±75	2654±44	1130±28	510±19	258±14	132±10
$Z(\nu\nu)+$jets	37±3	21±1	10±1	6±1	2±0.2	0.5±0.2	0.2±0.1	0.08±0.02	0.03±0.01	0.02±0.01
$W(\tau\nu)+$jets	5860±160	3610±79	2047±53	1165±47	410±12	156±9	79±4	35±2	17±1	8±1
$W(\mu\nu)+$jets	94940±900	56570±570	31360±340	17610±210	5857±92	2161±54	920±34	423±23	219±15	114±9
$W(e\nu)+$jets	7±2	3±2	1±1	0.19±0.02	0±0	0.06±0.01	0.07±0.01	0.03±0.01	0.01±0	0.02±0
$Z(\tau\tau)+$jets	277±21	149±11	79±5	47±3	18±1	8±1	4±1	1.2±0.3	0.5±0.1	0.2±0.1
$Z(\mu\mu)+$jets	1774±75	914±40	463±24	229±13	67±8	25±1	12±1	5.8±0.5	2.8±0.4	1.8±0.3
$Z(ee)+$jets	0±0	0±0	0±0	0±0	0±0	0±0	0±0	0±0	0±0	0±0
$t\bar{t}$, single-top	4700±790	2950±480	1600±270	850±150	291±56	135±33	47±20	13±11	2.48±2.48	0±2
Dibosons	3220±230	2310±170	1550±110	988±75	391±33	168±23	69±10	32±6	16±3	8±1
Multijets	0±0	0±0	0±0	0±0	0±0	0±0	0±0	0±0	0±0	0±0
Non-collision bkgs	0±0	0±0	0±0	0±0	0±0	0±0	0±0	0±0	0±0	0±0
Pre-fit background	87500±8700	52700±5300	29300±2900	16700±1700	5690±580	2110±230	862±96	386±47	187±26	94±16

Table B.11: Event yields in CR1mu1b before and after the counting experiment fits,, compared to the observed events. For the predictions, both the statistical and systematic uncertainties are included. The uncertainties for the individual background processes can be correlated, and do not necessarily add in quadrature to the total background uncertainty.

Bibliography

[1] ATLAS Collaboration, *Expected performance of missing transverse momentum reconstruction for the ATLAS detector at $\sqrt{s} = 13$ TeV*, ATL-PHYS-PUB-2015-023, 2015. https://cds.cern.ch/record/2037700.

[2] ATLAS Collaboration, *Performance of missing transverse momentum reconstruction with the ATLAS detector in the first proton–proton collisions at $\sqrt{s} = 13$ TeV*, ATL-PHYS-PUB-2015-027, 2015. https://cds.cern.ch/record/2037904.

[3] ATLAS Collaboration, *Search for new phenomena in events with a photon and missing transverse momentum in pp collisions at $\sqrt{s} = 13$ TeV with the ATLAS detector*, JHEP **06** (2016) 059, arXiv:1604.01306 [hep-ex].

[4] ATLAS Collaboration, *Search for dark matter at $\sqrt{s} = 13$ TeV in final states containing an energetic photon and large missing transverse momentum with the ATLAS detector*, Eur. Phys. J. **C77** (2017) no. 6, 393, arXiv:1704.03848 [hep-ex].

[5] ATLAS Collaboration, *Search for dark matter and other new phenomena in events with an energetic jet and large missing transverse momentum using the ATLAS detector*, arXiv:1711.03301 [hep-ex].

[6] M. E. Peskin and D. V. Schroeder, *An Introduction to quantum field theory*. Addison-Wesley, Reading, USA, 1995. http://www.slac.stanford.edu/~mpeskin/QFT.html.

[7] A. Purcell, *Go on a particle quest at the first CERN webfest*, Tech. Rep. BUL-NA-2012-269, CERN, Geneva, Aug, 2012. https://cds.cern.ch/record/1473657.

[8] P. W. Higgs, *Broken Symmetries and the Masses of Gauge Bosons*, Phys. Rev. Lett. **13** (1964) 508–509.

[9] F. Englert and R. Brout, *Broken Symmetry and the Mass of Gauge Vector Mesons*, Phys. Rev. Lett. **13** (1964) 321–323.

[10] G. Bertone et al., *Particle Dark Matter: Observations, Models and Searches*. Cambridge Univ. Press, Cambridge, 2010.

[11] F. Zwicky, *Die Rotverschiebung von extragalaktischen Nebeln*, Helv. Phys. Acta **6** (1933) 110–127. [Gen. Rel. Grav.41,207(2009)].

[12] V. C. Rubin and W. K. Ford, Jr., *Rotation of the Andromeda Nebula from a Spectroscopic Survey of Emission Regions*, Astrophys. J. **159** (1970) 379–403.

[13] K. G. Begeman, A. H. Broeils, and R. H. Sanders, *Extended rotation curves of spiral galaxies: Dark haloes and modified dynamics*, Mon. Not. Roy. Astron. Soc. **249** (1991) 523.

[14] J. P. Kneib, Y. Mellier, B. Fort, and G. Mathez, *The Distribution of Dark Matter in Distant Cluster Lenses - Modelling A:370*, Astronomy and Astrophysics **273** (June, 1993) 367.

[15] Y. Mellier, *Gravitational lensing and dark matter*, in Bertone [10], pp. 56–82.

[16] M. Markevitch, A. H. Gonzalez, D. Clowe, A. Vikhlinin, W. Forman, C. Jones, S. Murray, and W. Tucker, *Direct Constraints on the Dark Matter Self-Interaction Cross Section from the Merging Galaxy Cluster 1E 0657–56*, The Astrophysical Journal **606** (2004) no. 2, 819. http://stacks.iop.org/0004-637X/606/i=2/a=819.

[17] Space Telescope Science Institute, *v1.0 Data products for Epoch 1 of Abell 370*, Public data, 2016. http://www.stsci.edu/hst/campaigns/frontier-fields/.

[18] D. Clowe, M. Bradač, A. H. Gonzalez, M. Markevitch, S. W. Randall, C. Jones, and D. Zaritsky, *A Direct Empirical Proof of the Existence of Dark Matter*, The Astrophysical Journal Letters **648** (2006) no. 2, L109. http://stacks.iop.org/1538-4357/648/i=2/a=L109.

[19] Planck Collaboration, *Planck 2015 results. I. Overview of products and scientific results*, Astron. Astrophys. **594** (2016) A1, arXiv:1502.01582 [astro-ph.CO].

[20] G. Bertone, D. Hooper, and J. Silk, *Particle dark matter: Evidence, candidates and constraints*, Phys. Rept. **405** (2005) 279–390, arXiv:hep-ph/0404175 [hep-ph].

[21] M. Lisanti, *Lectures on Dark Matter Physics*, in *Proceedings, Theoretical Advanced Study Institute in Elementary Particle Physics: New Frontiers in Fields and Strings (TASI 2015): Boulder, CO, USA, June 1-26, 2015*, pp. 399–446. 2017. arXiv:1603.03797 [hep-ph]. https://inspirehep.net/record/1427360/files/arXiv:1603.03797.pdf.

[22] J. L. Feng, *Dark Matter Candidates from Particle Physics and Methods of Detection*, Ann. Rev. Astron. Astrophys. **48** (2010) 495–545, arXiv:1003.0904 [astro-ph.CO].

[23] EROS-2 Collaboration, P. Tisserand et al., *Limits on the Macho Content of the Galactic Halo from the EROS-2 Survey of the Magellanic Clouds*, Astron. Astrophys. **469** (2007) 387–404, arXiv:astro-ph/0607207 [astro-ph].

[24] MACHO Collaboration, C. Alcock et al., *The MACHO project: Microlensing results from 5.7 years of LMC observations*, Astrophys. J. **542** (2000) 281–307, arXiv:astro-ph/0001272 [astro-ph].

[25] Particle Data Group Collaboration, C. Patrignani et al., *Review of Particle Physics*, Chin. Phys. **C40** (2016) no. 10, 100001.

[26] C. P. Garay, L. Verde, and R. Jimenez, *Neutrino footprint in Large Scale Structure*, Phys. Dark Univ. **15** (2017) 31–34, arXiv:1602.08430 [astro-ph.CO].

[27] G. Servant, *Dark matter at the electroweak scale: non-supersymmetric candidates*, in Bertone [10], pp. 164–189.

[28] N. G. Deshpande and E. Ma, *Pattern of Symmetry Breaking with Two Higgs Doublets*, Phys. Rev. **D18** (1978) 2574.

[29] M. Cirelli, N. Fornengo, and A. Strumia, *Minimal dark matter*, Nucl. Phys. **B753** (2006) 178–194, arXiv:hep-ph/0512090 [hep-ph].

[30] J. L. Feng and J. Kumar, *Dark-Matter Particles without Weak-Scale Masses or Weak Interactions*, Phys. Rev. Lett. **101** (Dec, 2008) 231301. http://link.aps.org/doi/10.1103/PhysRevLett.101.231301.

[31] L. J. Hall, K. Jedamzik, J. March-Russell, and S. M. West, *Freeze-In Production of FIMP Dark Matter*, JHEP **03** (2010) 080, arXiv:0911.1120 [hep-ph].

[32] D. E. Kaplan, M. A. Luty, and K. M. Zurek, *Asymmetric Dark Matter*, Phys. Rev. **D79** (2009) 115016, arXiv:0901.4117 [hep-ph].

[33] J. L. Feng, *Non-WIMP candidates*, in Bertone [10], pp. 190–203.

[34] K. N. Abazajian et al., *Light Sterile Neutrinos: A White Paper*, arXiv:1204.5379 [hep-ph].

[35] P. Sikivie, *Axions*, in Bertone [10], pp. 204–227.

[36] L. Bergstrom, *Nonbaryonic dark matter: Observational evidence and detection methods*, Rept. Prog. Phys. **63** (2000) 793, arXiv:hep-ph/0002126 [hep-ph].

[37] G. Raffelt, *Axion hunting at the turn of the millenium*, Nucl. Phys. Proc. Suppl. **77** (1999) 456–461, arXiv:hep-ph/9806506 [hep-ph].

[38] D. G. Cerdeno and A. M. Green, *Direct detection of WIMPs*, in Bertone [10], pp. 347–369.

[39] T. Saab, *An Introduction to Dark Matter Direct Detection Searches & Techniques*, in *The Dark Secrets of the Terascale: Proceedings, TASI 2011, Boulder, Colorado, USA, Jun 6 - Jul 11, 2011*, pp. 711–738. 2013. arXiv:1203.2566 [physics.ins-det]. https://inspirehep.net/record/1093524/files/arXiv:1203.2566.pdf.

[40] R. Bernabei et al., *Final model independent result of DAMA/LIBRA-phase1*, Eur. Phys. J. **C73** (2013) 2648, arXiv:1308.5109 [astro-ph.GA].

[41] J. Liu, X. Chen, and X. Ji, *Current status of direct dark matter detection experiments*, Nature Phys. **13** (2017) no. 3, 212–216, arXiv:1709.00688 [astro-ph.CO].

[42] LUX Collaboration, D. S. Akerib et al., *Limits on spin-dependent WIMP-nucleon cross section obtained from the complete LUX exposure*, Phys. Rev. Lett. **118** (2017) no. 25, 251302, arXiv:1705.03380 [astro-ph.CO].

[43] G. Bertone and L. Bergstrom, *Gamma rays*, in Bertone [10], pp. 491–506.

[44] Fermi-LAT Collaboration, M. Ackermann et al., *Search for Gamma-ray Spectral Lines with the Fermi Large Area Telescope and Dark Matter Implications*, Phys. Rev. **D88** (2013) 082002, arXiv:1305.5597 [astro-ph.HE].

[45] Fermi-LAT Collaboration, M. Ackermann et al., *The Fermi Galactic Center GeV Excess and Implications for Dark Matter*, Astrophys. J. **840** (2017) no. 1, 43, arXiv:1704.03910 [astro-ph.HE].

[46] A. Achterberg, M. van Beekveld, S. Caron, G. A. Gomez-Vargas, L. Hendriks, and R. Ruiz de Austri, *Implications of the Fermi-LAT Pass 8 Galactic Center Excess on Supersymmetric Dark Matter*, arXiv:1709.10429 [hep-ph].

[47] F. Halzen and D. Hooper, *High-energy neutrinos from WIMP annihilations in the Sun*, in Bertone [10], pp. 507–520.

[48] S. Ting, *The First Five Years of the Alpha Magnetic Spectrometer on the International Space Station*, in *CERN Colloquium*. 2016.

[49] AMS Collaboration, L. Accardo et al., *High Statistics Measurement of the Positron Fraction in Primary Cosmic Rays of 0.5-500 GeV with the Alpha Magnetic Spectrometer on the International Space Station*, Phys. Rev. Lett. **113** (2014) 121101.

[50] AMS Collaboration, M. Aguilar et al., *Antiproton Flux, Antiproton-to-Proton Flux Ratio, and Properties of Elementary Particle Fluxes in Primary Cosmic Rays Measured with the Alpha Magnetic Spectrometer on the International Space Station*, Phys. Rev. Lett. **117** (2016) no. 9, 091103.

[51] C. Balazs and T. Li, *AMS-02 fits Dark Matter*, JHEP **05** (2016) 033, arXiv:1509.02219 [hep-ph].

[52] T. Li, *Simplified dark matter models in the light of AMS-02 antiproton data*, JHEP **04** (2017) 112, arXiv:1612.09501 [hep-ph].

[53] L. Evans and P. Bryant, *LHC Machine*, JINST **3** (2008) S08001.

[54] ATLAS Collaboration, *The ATLAS Experiment at the CERN Large Hadron Collider*, JINST **3** (2008) S08003.

[55] O. S. Bruning, P. Collier, P. Lebrun, S. Myers, R. Ostojic, J. Poole, and P. Proudlock, *LHC Design Report Vol.1: The LHC Main Ring*, .

[56] CERN, *The four main LHC experiments*, CERN Document Server. https://cds.cern.ch/record/40525.

[57] ATLAS Collaboration, *Luminosity determination in pp collisions at $\sqrt{s}$ = 8 TeV using the ATLAS detector at the LHC*, Eur. Phys. J. **C76** (2016) no. 12, 653, arXiv:1608.03953 [hep-ex].

[58] ATLAS Collaboration, *Luminosity Public Results*, ATLAS public plots. https://twiki.cern.ch/twiki/bin/view/AtlasPublic/LuminosityPublicResultsRun2.

[59] https://inspirehep.net/record/1294662/files/Figures_T_Coordinate.png.

[60] ATLAS Collaboration, *ATLAS Photos*, CERN Document Server. http://atlasexperiment.org/photos/index.html.

[61] ATLAS Collaboration, *ATLAS liquid argon calorimeter: Technical design report*, Tech. Rep. CERN-LHCC-96-41, CERN, Geneva, 1996.

[62] ATLAS Collaboration, *Performance of the ATLAS Trigger System in 2015*, Eur. Phys. J. **C77** (2017) no. 5, 317, arXiv:1611.09661 [hep-ex].

[63] W. Lampl, S. Laplace, D. Lelas, P. Loch, H. Ma, S. Menke, S. Rajagopalan, D. Rousseau, S. Snyder, and G. Unal, *Calorimeter clustering algorithms: Description and performance*, tech. rep., 2008.

[64] ATLAS Collaboration, *Performance of the ATLAS Track Reconstruction Algorithms in Dense Environments in LHC run 2*, arXiv:1704.07983 [hep-ex].

[65] M. Cacciari, G. P. Salam, and G. Soyez, *The anti-k_t jet clustering algorithm*, JHEP **04** (2008) 063, arXiv:0802.1189 [hep-ph].

[66] ATLAS Collaboration, *Jet energy scale measurements and their systematic uncertainties in proton-proton collisions at $\sqrt{s} = 13$ TeV with the ATLAS detector*, Phys. Rev. **D96** (2017) no. 7, 072002, arXiv:1703.09665 [hep-ex].

[67] ATLAS Collaboration, *Jet energy measurement with the ATLAS detector in proton-proton collisions at $\sqrt{s} = 7$ TeV*, Eur. Phys. J. **C73** (2013) no. 3, 2304, arXiv:1112.6426 [hep-ex].

[68] ATLAS Collaboration, *Performance of pile-up mitigation techniques for jets in pp collisions at $\sqrt{s} = 8$ TeV using the ATLAS detector*, Eur. Phys. J. **C76** (2016) no. 11, 581, arXiv:1510.03823 [hep-ex].

[69] ATLAS Collaboration, *Tagging and suppression of pileup jets with the ATLAS detector*, ATLAS-CONF-2014-018 . https://cds.cern.ch/record/1700870/.

[70] ATLAS Collaboration, *JVT Public Plots for ICHEP 2016*, ATLAS public plots. https://atlas.web.cern.ch/Atlas/GROUPS/PHYSICS/PLOTS/JETM-2016-011/.

[71] ATLAS Liquid Argon Calorimeter Group Collaboration, O. Simard, *The monitoring and data quality assessment of the ATLAS liquid argon calorimeter*, J. Phys. Conf. Ser. **587** (2015) no. 1, 012008.

[72] ATLAS Collaboration, *Selection of jets produced in 13 TeV proton–proton collisions with the ATLAS detector*, ATLAS-CONF-2015-029, 2015. https://cds.cern.ch/record/2037702.

[73] ATLAS Collaboration, *Expected performance of the ATLAS b-tagging algorithms in Run-2*, ATL-PHYS-PUB-2015-022, 2015. https://cds.cern.ch/record/2037697.

[74] ATLAS Collaboration, *Optimisation of the ATLAS b-tagging performance for the 2016 LHC Run*, ATL-PHYS-PUB-2016-012, 2016. https://cds.cern.ch/record/2160731.

[75] ATLAS Collaboration, *Electron and photon energy calibration with the ATLAS detector using LHC Run 1 data*, Eur. Phys. J. **C74** (2014) no. 10, 3071, arXiv:1407.5063 [hep-ex].

[76] ATLAS Collaboration, *Electron and photon energy calibration with the ATLAS detector using data collected in 2015 at $\sqrt{s} = 13$ TeV*, ATL-PHYS-PUB-2016-015, 2016. https://cds.cern.ch/record/2203514.

[77] ATLAS Collaboration, *Measurement of the photon identification efficiencies with the ATLAS detector using LHC Run-1 data*, Eur. Phys. J. **C76** (2016) no. 12, 666, arXiv:1606.01813 [hep-ex].

[78] ATLAS Collaboration, *Photon identification in 2015 ATLAS data*, ATL-PHYS-PUB-2016-014, 2016. https://cds.cern.ch/record/2203125.

[79] M. Cacciari, G. P. Salam, and G. Soyez, *FastJet user manual*, Eur. Phys. J. C **72** (2012) 1896, arXiv:1111.6097 [hep-ph].

[80] ATLAS Collaboration, *Photon identification efficiencies in 2015 and 2016 data*, 2016. https://atlas.web.cern.ch/Atlas/GROUPS/PHYSICS/PLOTS/EGAM-2017-004/index.html.

[81] ATLAS Collaboration, *Electron efficiency measurements with the ATLAS detector using the 2015 LHC proton–proton collision data*, ATLAS-CONF-2016-024, 2016. https://cds.cern.ch/record/2157687.

[82] ATLAS collaboration, *Muon reconstruction performance of the ATLAS detector in proton–proton collision data at $\sqrt{s}$ =13 TeV*, Eur. Phys. J. **C76** (2016) no. 5, 292, arXiv:1603.05598 [hep-ex].

[83] ATLAS Collaboration, *Performance of missing transverse momentum reconstruction with the ATLAS detector using proton-proton collisions at $\sqrt{s} = 13$ TeV*, to be subitted to EPJC (2018) .

[84] M. Cacciari and G. P. Salam, *Pileup subtraction using jet areas*, Phys. Lett. **B659** (2008) 119–126, arXiv:0707.1378 [hep-ph].

[85] G. Aad et al., *Performance of Missing Transverse Momentum Reconstruction in Proton-Proton Collisions at 7 TeV with ATLAS*, Eur. Phys. J. **C72** (2012) 1844, arXiv:1108.5602 [hep-ex].

[86] ATLAS Collaboration, *Public Plots: Missing Transverse Momentum Distribution and Performance in 2016 data*, ATLAS public plots. https://atlas.web.cern.ch/Atlas/GROUPS/PHYSICS/PLOTS/JETM-2016-008/.

[87] D. Abercrombie et al., *Dark Matter Benchmark Models for Early LHC Run-2 Searches: Report of the ATLAS/CMS Dark Matter Forum*, arXiv:1507.00966 [hep-ex].

[88] G. Busoni, A. De Simone, E. Morgante, and A. Riotto, *On the Validity of the Effective Field Theory for Dark Matter Searches at the LHC*, Phys. Lett. **B728** (2014) 412–421, arXiv:1307.2253 [hep-ph].

[89] I. M. Shoemaker and L. Vecchi, *Unitarity and Monojet Bounds on Models for DAMA, CoGeNT, and CRESST-II*, Phys. Rev. **D86** (2012) 015023, arXiv:1112.5457 [hep-ph].

[90] A. Crivellin, U. Haisch, and A. Hibbs, *LHC constraints on gauge boson couplings to dark matter*, Phys. Rev. **D91** (2015) 074028, arXiv:1501.00907 [hep-ph].

[91] L. M. Carpenter, A. Nelson, C. Shimmin, T. M. P. Tait, and D. Whiteson, *Collider searches for dark matter in events with a Z boson and missing energy*, Phys. Rev. **D87** (2013) no. 7, 074005, arXiv:1212.3352 [hep-ex].

[92] M. Papucci, A. Vichi, and K. M. Zurek, *Monojet versus the rest of the world I: t-channel models*, JHEP **11** (2014) 024, arXiv:1402.2285 [hep-ph].

[93] N. F. Bell, J. B. Dent, A. J. Galea, T. D. Jacques, L. M. Krauss, and T. J. Weiler, *Searching for Dark Matter at the LHC with a Mono-Z*, Phys. Rev. **D86** (2012) 096011, arXiv:1209.0231 [hep-ph].

[94] A. DiFranzo, K. I. Nagao, A. Rajaraman, and T. M. P. Tait, *Simplified Models for Dark Matter Interacting with Quarks*, JHEP **11** (2013) 014, arXiv:1308.2679 [hep-ph]. [Erratum: JHEP01,162(2014)].

[95] J. Alwall, R. Frederix, S. Frixione, V. Hirschi, F. Maltoni, O. Mattelaer, H. S. Shao, T. Stelzer, P. Torrielli, and M. Zaro, *The automated computation of tree-level and next-to-leading order differential cross sections, and their matching to parton shower simulations*, JHEP **07** (2014) 079, arXiv:1405.0301 [hep-ph].

[96] T. Sjöstrand, S. Mrenna, and P. Z. Skands, *PYTHIA 6.4 Physics and Manual*, JHEP **05** (2006) 026, arXiv:hep-ph/0603175.

[97] L. Lönnblad and S. Prestel, *Matching Tree-Level Matrix Elements with Interleaved Showers*, JHEP **03** (2012) 019, arXiv:1109.4829 [hep-ph].

[98] M. Backovic, A. Martini, O. Mattelaer, K. Kong, and G. Mohlabeng, *Direct Detection of Dark Matter with MadDM v.2.0*, Phys. Dark Univ. **9-10** (2015) 37–50, arXiv:1505.04190 [hep-ph].

[99] NNPDF Collaboration, R. D. Ball et al., *Parton distributions for the LHC Run II*, JHEP **04** (2015) 040, arXiv:1410.8849 [hep-ph].

[100] T. Sjostrand, S. Mrenna, and P. Z. Skands, *A Brief Introduction to PYTHIA 8.1*, Comput. Phys. Commun. **178** (2008) 852–867, arXiv:0710.3820 [hep-ph].

[101] R. D. Ball et al., *Parton distributions with LHC data*, Nucl. Phys. B **867** (2013) 244–289, arXiv:1207.1303 [hep-ph].

[102] NNPDF Collaboration, R. D. Ball, V. Bertone, S. Carrazza, L. Del Debbio, S. Forte, A. Guffanti, N. P. Hartland, and J. Rojo, *Parton distributions with QED corrections*, Nucl. Phys. **B877** (2013) 290–320, arXiv:1308.0598 [hep-ph].

[103] ATLAS Collaboration, *ATLAS Run 1 Pythia8 tunes*, Atl-phys-pub-2014-021, 2014. https://cds.cern.ch/record/1966419.

[104] N. Arkani-Hamed, S. Dimopoulos, and G. Dvali, *The Hierarchy problem and new dimensions at a millimeter*, Phys. Lett. B **429** (1998) 263–272, arXiv:hep-ph/9803315 [hep-ph].

[105] T. Gleisberg et al., *Event generation with SHERPA 1.1*, J. High Energy Phys. **02** (2009) 007, arXiv:0811.4622 [hep-ph].

[106] S. Schumann and F. Krauss, *A Parton shower algorithm based on Catani-Seymour dipole factorisation*, JHEP **03** (2008) 038, arXiv:0709.1027 [hep-ph].

[107] S. Höche, F. Krauss, S. Schumann, and F. Siegert, *QCD matrix elements and truncated showers*, JHEP **05** (2009) 053, arXiv:0903.1219 [hep-ph].

[108] H.-L. Lai et al., *New parton distributions for collider physics*, Phys. Rev. D **82** (2010) 074024, arXiv:1007.2241 [hep-ph].

[109] T. Gleisberg and S. Höche, *Comix, a new matrix element generator*, JHEP **12** (2008) 039, arXiv:0808.3674 [hep-ph].

[110] F. Cascioli, P. Maierhofer, and S. Pozzorini, *Scattering Amplitudes with Open Loops*, Phys. Rev. Lett. **108** (2012) 111601, arXiv:1111.5206 [hep-ph].

[111] S. Höche, F. Krauss, M. Schönherr, and F. Siegert, *QCD matrix elements + parton showers: The NLO case*, JHEP **04** (2013) 027, arXiv:1207.5030 [hep-ph].

[112] ATLAS Collaboration, *Monte Carlo Generators for the Production of a W or Z/γ^* Boson in Association with Jets at ATLAS in Run 2*, ATL-PHYS-PUB-2016-003, 2016. https://cds.cern.ch/record/2120133.

[113] D. J. Lange, *The EvtGen particle decay simulation package*, Nucl. Instrum. Meth. A **462** (2001) 152.

[114] S. Alioli, P. Nason, C. Oleari, and E. Re, *A general framework for implementing NLO calculations in shower Monte Carlo programs: the POWHEG BOX*, JHEP **06** (2010) 043, arXiv:1002.2581 [hep-ph].

[115] S. Alioli, P. Nason, C. Oleari, and E. Re, *NLO single-top production matched with shower in POWHEG: s- and t-channel contributions*, JHEP **09** (2009) 111, arXiv:0907.4076 [hep-ph]. [Erratum: JHEP02,011(2010)].

[116] P. Artoisenet, R. Frederix, O. Mattelaer, and R. Rietkerk, *Automatic spin-entangled decays of heavy resonances in Monte Carlo simulations*, JHEP **03** (2013) 015, arXiv:1212.3460 [hep-ph].

[117] T. Sjostrand, S. Mrenna, and P. Skands, *PYTHIA 6.4 physics and manual*, J. High Energy Phys. **05** (2006) 026, arXiv:hep-ph/0603175.

[118] J. Pumplin et al., *New generation of parton distributions with uncertainties from global QCD analysis*, J. High Energy Phys. **07** (2002) 012, arXiv:hep-ph/0201195 [hep-ph].

[119] P. Z. Skands, *Tuning Monte Carlo Generators: The Perugia Tunes*, Phys. Rev. D **82** (2010) 074018, arXiv:1005.3457 [hep-ph].

[120] ATLAS Collaboration, *Further ATLAS tunes of* PYTHIA *6 and Pythia 8*, ATL-PHYS-PUB-2011-014, 2011. https://cds.cern.ch/record/1400677.

[121] A. Martin, W. Stirling, R. Thorne, and G. Watt, *Parton distributions for the LHC*, Eur.Phys.J. **C63** (2009) 189–285, arXiv:0901.0002 [hep-ph].

[122] ATLAS Collaboration, *The ATLAS Simulation Infrastructure*, Eur. Phys. J. C **70** (2010) 823–874, arXiv:1005.4568 [physics.ins-det].

[123] GEANT4 Collaboration, *GEANT4: A Simulation toolkit*, Nucl. Instrum. Methods Phys. Res., Sect. A **506** (2003) 250–303.

[124] D. Adams and others, *Recommendations of the Physics Objects and Analysis Harmonisation Study Groups 2014*, Atlas-phys-int-2014-018. https://cds.cern.ch/record/1743654.

[125] ATLAS Collaboration, *Search for new phenomena in events with a photon and missing transverse momentum in pp collisions at $\sqrt{s} = 8$ TeV with the ATLAS detector*, Phys. Rev. **D91** (2015) no. 1, 012008, arXiv:1411.1559 [hep-ex]. [Erratum: Phys. Rev.D92,no.5,059903(2015)].

[126] M. Baak et al., *HistFitter software framework for statistical data analysis*, Eur.Phys.J. **C75** (2015) 153, arXiv:1410.1280 [hep-ex].

[127] W. Buttinger, *Using Event Weights to account for differences in Instantaneous Luminosity and Trigger Prescale in Monte Carlo and Data*, Atl-com-soft-2015-119, 2015. https://cds.cern.ch/record/2014726.

[128] ATLAS Collaboration, *Characterisation and mitigation of beam-induced backgrounds observed in the ATLAS detector during the 2011 proton-proton run*, JINST **8** (2013) P07004, arXiv:1303.0223 [hep-ex].

[129] ATLAS Collaboration, *Improved luminosity determination in pp collisions at $\sqrt{s}$ = 7 TeV using the ATLAS detector at the LHC*, Eur. Phys. J. C **73** (2013) 2518, arXiv:1302.4393 [hep-ex].

[130] A. Buckley, J. Ferrando, S. Lloyd, K. Nordstroem, B. Page, M. Ruefenacht, M. Schoenherr, and G. Watt, *LHAPDF6: parton density access in the LHC precision era*, Eur. Phys. J. **C75** (2015) 132, arXiv:1412.7420 [hep-ph].

[131] M. Botje et al., *The PDF4LHC Working Group Interim Recommendations*, arXiv:1101.0538 [hep-ph].

[132] A. L. Read, *Presentation of search results: The CL(s) technique*, J. Phys. G **28** (2002) 2693–2704.

[133] T. Junk, *Confidence level computation for combining searches with small statistics*, Nucl. Instrum. Methods Phys. Res., Sect. A **434** (1999) 435–443, arXiv:9902006 [hep-ex].

[134] G. Cowan, K. Cranmer, E. Gross, and O. Vitells, *Asymptotic formulae for likelihood-based tests of new physics*, Eur. Phys. J. **C71** (2011) 1554, arXiv:1007.1727 [physics.data-an]. [Erratum: Eur. Phys. J.C73,2501(2013)].

[135] F. Kahlhoefer et al., *Implications of unitarity and gauge invariance for simplified dark matter models*, JHEP (2016) 016, arXiv:1510.02110 [hep-ph].

[136] PICO-2L Collaboration, *Dark Matter Search Results from the PICO-2L C3F8 Bubble Chamber*, Phys. Rev. Lett. **114** (2015) 231302, arXiv:1503.00008 [astro-ph.CO].

[137] XENON100 Collaboration, *Limits on spin-dependent WIMP-nucleon cross sections from 225 live days of XENON100 data*, arXiv:1301.6620 [astro-ph.CO].

[138] LUX Collaboration, D. S. Akerib et al., *First spin-dependent WIMP-nucleon cross section limits from the LUX experiment*, arXiv:1602.03489 [hep-ex].

[139] D. Racco et al., *Robust collider limits on heavy-mediator Dark Matter.*, J. High Energy Phys. **05** (2015) 009, arXiv:1502.04701 [hep-hp].

[140] J. M. Lindert et al., *Precise predictions for V+jets dark matter backgrounds*, arXiv:1705.04664v1 [hep-ph].

[141] ATLAS Collaboration, *Search for new phenomena in final states with an energetic jet and large missing transverse momentum in pp collisions at $\sqrt{s} = 13$ TeV using the ATLAS detector*, Phys. Rev. **D94** (2016) no. 3, 032005, arXiv:1604.07773 [hep-ex].

[142] CMS collaboration, *Search for new physics in final states with an energetic jet or a hadronically decaying W or Z boson and transverse momentum imbalance at $\sqrt{s} = 13$ TeV*, arXiv:1712.02345 [hep-ex].

[143] S. Frixione, P. Nason, and C. Oleari, *Matching NLO QCD computations with Parton Shower simulations: the POWHEG method*, JHEP **11** (2007) 070, arXiv:0709.2092 [hep-ph].

[144] P. Nason, *A New method for combining NLO QCD with shower Monte Carlo algorithms*, JHEP **11** (2004) 040, arXiv:hep-ph/0409146 [hep-ph].

[145] U. Haisch, F. Kahlhoefer, and E. Re, *QCD effects in mono-jet searches for dark matter*, JHEP **12** (2013) 007, arXiv:1310.4491 [hep-ph].

[146] U. Haisch and E. Re, *Simplified dark matter top-quark interactions at the LHC*, JHEP **06** (2015) 078, arXiv:1503.00691 [hep-ph].

[147] ATLAS Collaboration, *ATLAS Run 1 Pythia8 tunes*, Atl-phys-pub-2014-021, 2014. https://cds.cern.ch/record/1966419.

[148] M. Papucci, A. Vichi, and K. M. Zurek, *Monojet versus the rest of the world I: t-channel models*, JHEP **11** (2014) 024, arXiv:1402.2285 [hep-ph].

[149] L. Lonnblad and S. Prestel, *Matching Tree-Level Matrix Elements with Interleaved Showers*, JHEP **03** (2012) 019, arXiv:1109.4829 [hep-ph].

[150] ATLAS Collaboration, *ATLAS simulation of boson plus jets processes in Run 2*, 2017. https://cds.cern.ch/record/2261937.

[151] ATLAS Collaboration, *Selection of jets produced in proton–proton collisions with the ATLAS detector using 2011 data*, ATLAS-CONF-2012-020, 2012. https://cds.cern.ch/record/1430034.

[152] ATLAS Collaboration, *Search for squarks and gluinos with the ATLAS detector in final states with jets and missing transverse momentum using 4.7 fb^{-1} of $\sqrt{s} = 7$ TeV proton-proton collision data*, Phys. Rev. **D87** (2013) no. 1, 012008, arXiv:1208.0949 [hep-ex].

[153] J. Anders and M. D'Onofrio, *V+Jets theoretical uncertainties estimation via a parameterisation method*, 2016. https://cds.cern.ch/record/2125718.

[154] ATLAS Collaboration, *Multi-boson simulation for 13 TeV ATLAS analyses*, ATL-PHYS-PUB-2016-002, 2016. https://cds.cern.ch/record/2119986.

[155] CMS collaboration, *Search for dark matter produced with an energetic jet or a hadronically decaying W or Z boson at $\sqrt{s} = 13$ TeV*, JHEP **07** (2017) 014, arXiv:1703.01651 [hep-ex].

[156] F. Kahlhoefer, K. Schmidt-Hoberg, T. Schwetz, and S. Vogl, *Implications of unitarity and gauge invariance for simplified dark matter models*, JHEP **02** (2016) 016, arXiv:1510.02110 [hep-ph].

[157] ATLAS Collaboration, *Search for new phenomena in dijet events using 37 fb^{-1} of pp collision data collected at $\sqrt{s}$ =13 TeV with the ATLAS detector*, Phys. Rev. **D96** (2017) no. 5, 052004, arXiv:1703.09127 [hep-ex].

[158] ATLAS Collaboration, *Search for new phenomena in the dijet mass distribution using $p - p$ collision data at $\sqrt{s} = 8$ TeV with the ATLAS detector*, Phys. Rev. **D91** (2015) no. 5, 052007, arXiv:1407.1376 [hep-ex].

[159] ATLAS Collaboration, *Search for new light resonances decaying to jet pairs and produced in association with a photon or a jet in proton–proton collisions at $\sqrt{s} = 13$ TeV with the ATLAS detector*, ATLAS-CONF-2016-070, 2016. https://cds.cern.ch/record/2206221.

[160] ATLAS Collaboration, *Search for light dijet resonances with the ATLAS detector using a Trigger-object Level Analysis in LHC pp collisions at $\sqrt{s} = 13$ TeV*, ATLAS-CONF-2016-030, 2016. https://cds.cern.ch/record/2161135.

[161] A. Albert et al., *Recommendations of the LHC Dark Matter Working Group: Comparing LHC searches for heavy mediators of dark matter production in visible and invisible decay channels*, arXiv:1703.05703 [hep-ex].

[162] A. Boveia et al., *Recommendations on presenting LHC searches for missing transverse energy signals using simplified s-channel models of dark matter*, arXiv:1603.04156 [hep-hp].

Acknowledgments

Many people have helped me to carry out and complete this work at different stages, and therefore I would like to thank them.

First of all, I wish to thank my supervisors, Silvia Resconi and Leonardo Carminati. Your dedication, expertise and professionalism have been an example to me throughout these years and your wise guidance could adjust the course of my efforts every time it was needed. I am especially indebted to Silvia for the non-stop encouragement and support at all times and grateful to Leonardo for the questions he posed along the way.
I am grateful to the Milano ATLAS group as a totality and to my colleagues, individually, for the many useful discussions and for being people I could count on during work and outside.

Among the people who had the largest impact on my formation as a dark matter hunter, I must firstly thank Valerio Ippolito: thank you for involving me in the mono-jet analysis and for your insight on a multitude and diversity of questions. A special thank you to Marie-Hélène Genest for the help at different stages of the PhD, including the reading of this thesis, and for being an inspirational example of physicist. Thank you to Caterina Doglioni, for the lively passion for this subject and for having got me into the study of the t-channel model.

I am grateful to the Exotic conveners and the Jets and Dark Matter sub-conveners, Klaus Mönig, Gabriel Facini, Marco Vanadia and Silvia Resconi, for the stimulating discussions within the mono-jet and mono-photon analyses and for supporting my activity throughout.

Among the mono-jet enthusiasts, I am indebted to Giuliano Gustavino, for his help, patience and positivity and for sharing a year of hard work. Thank you to Cora Fischer and Millie McDonald, for the numerous amount of cross-checks and debugging sessions.

I had the chance to know and work with many great people in the $E_{\mathrm{T}}^{\mathrm{miss}}$ group, in particular I wish to thank Peter Loch, Donatella Cavalli, Silvia Resconi (for a third time), Teng Jian Khoo and Benjamin Brunt.

It would have been impossible to complete this work without the support of the people I dear most, who therefore I want to thank especially.

Thank you very much to my parents, who always encouraged me to follow my inclinations and supported me throughout my choices. Thanks for reminding me not to forget some important aspects of my life.

Thanks a lot, Costanza, for being my sister and my friend, and for the trust we can put into one another during our lives.

Finally thank you so much, Francesco, for your continuous support and encouragement throughout these years. I cannot overestimate how much your understanding and your love are important to me. You have my true gratitude and my heart.